The Source Apportionment of Airborne Particulate Matter Composition on Sable Island, Nova Scotia, Canada

by

Thomas Codey Barnett

Submitted in partial fulfillment of the requirements
for the degree of Master of Applied Science

at

Dalhousie University
Halifax, Nova Scotia
April 2016

TABLE OF CONTENTS

LIST OF TABLES

LIST OF FIGURES

ABSTRACT

Atmospheric particulate matter has been shown to have acute and chronic health impacts, potential to negatively affect ecosystems, and plays an important role in climate forcing through its role in the formation of cloud condensation nuclei. Particle size, morphology, and chemical composition are key in determining the extent of the impacts on populations and the planet. In this study, particulate mass concentration and number counts were measure from October 1 – December 31, 2015 and the United States Environmental Protection Agency Positive Matrix Factorization v5.0 program was used to apportion the particulate matter sources with further evidence provided by air mass back trajectories and satellite observations. It was found that sea spray contributed 43.4% of particulate matter, long range transport from the continent contributed 30.9% of particulate matter, aged biogenic marine emissions/aged marine aerosol contributed 24.3% of particulate matter, and fresh biogenic marine emissions contributed 1.4% of particulate matter.

LIST OF ABBREVIATIONS USED

Al	Aluminum
ANO_3	Ammonium nitrate
AOD	Aerosol optical depth
APCS	Absolute Principal Component Scores
APS	TSI aerodynamic particle sizer model 3321
ASO_4	Ammonium sulphate
AFRG	Atmospheric Forensics Research Group
BC	Black Carbon
CAAQS	Canadian Ambient Air Quality Standards
CCG	Canadian Coast Guard
CCN	Cloud condensation nuclei
CMB	Chemical Mass Balance
CO_2	Carbon dioxide
d_a	Aerodynamic diameter
d_e	Equivalent volume
DMS	Dimethylsulphide
DMA	Differential mobility analyzer
DRX	TSI DustTrak DRX model 8533
EBC	Equivalent black carbon
Fe	Iron
H_2S	Hydrogen sulphide
HBr	Hydrobromic acid
HCl	Hydrochloric acid
HEPA	High efficiency particulate air
HF	Hydrofluoric acid
Hg	Mercury
HYSPLIT	Hybrid Single-Particle Lagrangian Integrated Trajectory
η	Fluid viscosity
IN	Ice nuclei

IPCC	Intergovernmental Panel on Climate Change
IQR	Interquartile range
κ_v	hygroscopicity
LARGE	Langley Aerosol Research Group Experiment
LOSU	Level of scientific understanding
LRT	Long-Range Transport
MODIS	Moderate Resolution Imaging Spectroradiometer
NAAMES	North Atlantic Aerosols and Marine Ecosystems Study
NASA	National Aeronautics and Space Administration
NE US	Northeast United States
Ni	Nickel
NH_3	Ammonia
$(NH_4)_2SO_4$	Ammonium sulphate
NOAA	National Oceanic and Atmospheric Administration
NO_2	Nitrogen dioxide
NO_x	Nitrogen oxides
NS	Nova Scotia
O&G	Oil & gas
O_3	Ozone
OH	Hydroxide
OC	Organic Carbon
PBW	Particle bound water
PCA	Principal Component Analysis
PM	Particulate matter
$PM_{1/2.5/4/10/20}$	Atmospheric particles with a median aerodynamic diameter less than, or equal to, 1.0 µm, 2.5 µm, 4.0 µm, 10 µm, and 20 µm
ρ_0	Density of liquid water
ρ_p	Particle density
RM	Residue matter
Si	Silicon

SIA	Secondary inorganic aerosol
SO_2	Sulphur dioxide
SO_4	Sulphate
SOA	Secondary organic aerosol
SPARTAN	Surface PARTiculate mAtter Network
TEO	Trace elemental oxides
TSP	Total suspended particles
UFP	Ultrafine Particle
UFPM	TSI ultrafine particle monitor model 3031
USEPA	US Environmental Protection Agency
V	Vanadium
VIIRS	Visible Infrared Imaging Radiometer Suite
VOC	Volatile organic compound
WHO	World Health Organization
χ	Particle shape factor
Zn	Zinc

ACKNOWLEDGEMENTS

I am grateful to my supervisor Dr. Mark Gibson for his continued support and guidance and for giving me the opportunity to perform my research on Sable Island. I would also like to thank Haya Qadoumi and the rest of the Atmospheric Forensics Research Group, my supervisory committee members Dr. Susanne Craig, Dr. Rob Jamieson, and Dr. Jan Haelssig. I would like to thank the Environmental Studies Research Funds and Natural Resources Canada for funding the project, Gerry Forbes and Maritime Air Charter for arranging travel to Sable Island. Finally, I would like to acknowledge everyone in Environment Canada and Parks Canada for their help with instrument maintenance and data collecting, as well as Dave Taylor and Eric Theriault for their considerable advice and guidance.

CHAPTER 1 INTRODUCTION

Particulate matter (PM) emitted into the atmosphere from natural and anthropogenic sources is known to adversely affect human health by increasing risk of cardiorespiratory disease, cancer, and mortality (Dockery et al., 1993; Pope et al., 2002; WHO, 2013). Many studies of health effects associated with PM investigate fine airborne particles with a median aerodynamic diameter less than, or equal to, 2.5 µm ($PM_{2.5}$), with a focus on mass concentration. The World Health Organization (WHO) estimated that 3.1 million deaths in 2010 were attributed to $PM_{2.5}$. Recently, more research has been conducted into ultrafine particles (UFPs), that form part of the composition of PM mass, and their impact on health and climate. UFP studies focus on number counts as they contribute very little to particle mass yet dominate number count (Brace et al., 2014). Due to their small size, high number concentration, increased diffusion in the atmosphere (relative to particles > 0.1 µm), and large surface area, UFPs can deposit large amounts of toxic pollutants deep in the lungs (Delfino, Sioutas & Malik, 2005; Oberdörster, 2001). Furthermore, atmospheric PM has a significant impact on climate forcing. The Intergovernmental Panel on Climate Change (IPCC) reports that aerosols can directly and indirectly affect climate, however the magnitude of aerosol impact on climate is largely uncertain (IPCC, 2013). By scattering or absorbing incoming solar radiation, particles directly affect the global radiation balance. Particles also act as cloud condensation nuclei (CCN) by providing condensing surfaces for atmospheric water vapour leading to particle growth and cloud droplet formation. These clouds have a higher albedo and scatter more incoming solar radiation, which results in atmospheric cooling (IPCC, 2013; Kerminen et al., 2012).

Biogenic marine emissions from phytoplankton contribute significant CCN to the marine atmosphere, especially during the spring and fall phytoplankton blooms in the northwest Atlantic Ocean. In the spring, a combination of light, nutrients, and favourable ocean conditions allow for a massive bloom consisting mainly of diatoms. In the summer, these nutrients are depleted and the water column stratifies which allows for a small assemblage of phytoplankton to take the place of the diatoms. In the fall, increased wind and storms causes mixing of the water column and incorporates nutrient rich deeper water into the upper sunlit layer (Craig et al., 2015). There are many competing hypotheses for the spring bloom which include Sverdrup's critical depth hypothesis (Behrenfeld, 2010), the critical turbulence (Huisman et al., 1999) and eddy stratification (Mahadevan et al., 2012) hypotheses, and the disturbance recovery hypothesis (Behrenfeld, 2010; Smith et al., 2015). It has been suggested that a combination of these hypotheses are what allows the spring bloom; however, this uncertainty is one of the drivers behind the recent National Aeronautics and Space Administration (NASA) North Atlantic Aerosols and Marine Ecosystems Study (NAAMES) mission running from November 2015 to August 2020. The NAAMES study will utilize aircraft, ship, and satellite observations to investigate seasonal phytoplankton growth, providing insight into how their trace reactive gas emissions affect remote marine aerosols, CCN abundance, and ultimately their impact on climate (NASA, 2015). It is also known that sea salt aerosols are exceptional CCN and the uncertainty in the contribution of marine emissions to the global aerosol budget corresponds to a large uncertainty in the aerosol number concentration in the marine atmosphere (IPCC, 2013; Petters & Kreidenweis, 2007). Therefore, the measurement of aerosols in the marine environment is paramount to understanding their influence on climate and Earth system processes. Although satellites can provide useful information regarding aerosols in the marine environment, marine aerosol emissions can only be constrained by in situ observations (IPCC, 2013).

Sable Island is a predominantly marine influenced site (Duderstadt et al, 1998) and ideal for continuous long-term measurement of marine emissions. This study will use source apportionment, supplemented with satellite observations of ocean colour and air mass back trajectory analyses to identify the PM sources impacting air quality on Sable Island providing crucial information on how marine emissions impact aerosol composition. Ultimately, this information can be used to help global models predict the climate and ecosystem effects of marine aerosol emissions.

CHAPTER 2 LITERATURE REVIEW

2.1 Airborne Particulate Matter

Airborne PM refers to solid particles and/or liquid droplets suspended in a gaseous medium (Gibson et al., 2009; Wheeler et al., 2014). Collectively, this suspension is called an aerosol. Aerosols are categorized as primary or secondary aerosols and they can be further distinguished based on how they are generated and the physical characteristics of their particulates (Hinds, 1998; Kulkarni, Baron & Willeke, 2011). Primary aerosols are formed when PM is emitted directly into the suspending gas (usually air); examples of primary aerosol formation mechanisms include combustion processes, fragmentation processes, and sea spray (Doohoo et al., 2015; Franklin et al., 2014; MacNeil et al., 2014; Palmer et al., 2013; Snider et al., 2016; Wheeler et al., 2014). Secondary aerosols are formed from gas-to-particle conversions; some examples include cloud droplet formation and the oxidation of volatile organic compounds (VOCs) such as isoprene emitted by phytoplankton (Facchini et al., 2008; Hinds, 1998; IPCC, 2013; Kulkarni, Baron & Willeke, 2011). Aerosols can exist in homogeneous, monodisperse or polydisperse states. Homogeneous aerosols are composed of chemically identical particles, whereas monodisperse aerosols are composed of same sized particles and polydisperse aerosols contain a mixture of particle sizes and chemical compositions. Monodisperse aerosols are not found in the natural environment, they are usually engineered and used as test aerosols for instrument calibration (Berglund & Liu, 1973; Hinds, 1998; Kulkarni, Baron & Willeke, 2011). Atmospheric aerosols are made up of inorganic nitrate, sulphate, ammonium, and sea salt, as well as organic species, mineral species, black carbon, and biological particles (IPCC, 2013).

2.2 Particle Characteristics

Density is one of three traits used to characterize PM. Particulates produced from fragmentation processes will share the density of the parent material, however those produced from combustion (smoke, fumes) can have densities far less than anticipated due to voids created by their aggregate structure (Hinds, 1998). Individual particles can also exist in different phases, which is reflected in their density (DeCarlo et al., 2004; Hinds, 1998). Particle shape is another characteristic to consider when sampling PM. Liquid droplets are usually spherical, however solid particles seldom are and can have complex shapes. Therefore, equivalent diameters are used to apply theories of aerosol properties to non-spherical particles. The most common equivalent diameter used for aerosols is the aerodynamic diameter (d_a), which is the diameter that a spherical particle with a density of 1000 kg m^{-3} would have if it shared the same settling velocity as the non-spherical particle (DeCarlo et al., 2004; Hinds, 1998). That is to say, a particle with an aerodynamic diameter of 5 microns behaves the same as a spherical liquid water droplet with a diameter of 5 microns.

Particle motion is described by Stokes law shown below in equation 1. Stokes law assumes the particle is moving in an incompressible fluid, no other particles are close by, particle motion is constant, fluid velocity at the surface of the particle is zero, and the particle is a rigid sphere to solve the Navier-Stokes equations (DeCarlo et al., 2004; Hinds, 1998; Kulkarni, Baron & Willeke, 2011).

$$F_D = 3\pi\eta V d \qquad (1)$$

Where F_D = resisting force (form force + frictional force) on a spherical particle moving through a fluid, η = viscosity, V = particle velocity, and d = particle diameter. Non-spherical particles have larger surface areas than spherical particles, therefore they experience more drag force. Applying a shape factor (χ) corrects for non-spherical particle shapes (DeCarlo et al., 2004; Hinds, 1998; Kulkarni, Baron & Willeke, 2011).

As shown in equation 2 below, the terminal settling velocity of an airborne particle is proportional to the square of its diameter (Hinds, 1998; DeCarlo et al., 2004).

$$V_{TS} = \frac{\rho_p d_e^2 g}{18\eta\chi} \qquad (2)$$

Where V_{TS} = terminal settling velocity, ρ_p = particle density, d_e = equivalent volume diameter, η = fluid viscosity, and χ = particle shape factor. A spherical particle has a shape factor of 1, and non-spherical particles generally have shape factors larger than 1. For example, cylindrical particles have shape factors ranging from 1.01 – 1.68, a cluster of 3 spherical particles has a shape factor of 1.15, quartz a factor of 1.36, and sand a factor of 1.57 (DeCarlo et al., 2004; Hinds, 1998). Since d_a accounts for particle shape and density, when substituted for d_e (Hinds, 1998; Decarlo et al., 2004), the equation for terminal settling velocity becomes:

$$V_{TS} = \frac{\rho_0 d_a^2 g}{18\eta} \qquad (3)$$

Where ρ_0 = 1000 kg m^{-3}.

This highlights that particle size is usually the most important characteristic affecting particle behavior (Kulkarni, Baron & Willeke, 2011). As such, atmospheric particles, which typically range from 0.01 microns to 100 microns, are segregated into size fractions. Total suspended particles (TSP) or super-coarse particles refers to all particles with a median aerodynamic diameter ≤ 60 µm (Hinds, 1998; Kulmala et al, 2004). Respirable and fine particles are those with median aerodynamic diameters ≤ 10 µm (PM_{10}) and ≤ 4 µm (PM_4), respectively. Coarse particles are found in the size fraction between $PM_{2.5}$ and PM_{10}, UFPs have median aerodynamic diameters ≤ 100 nm. UFPs can be subdivided into nucleation mode (3-20 nm) and Aitken mode (20-90 nm) (Hinds, 1998; Kulmala et al., 2004). Accumulation mode particles are a sub-group of fine particles, having median aerodynamic diameters between 0.1 µm – 1 µm (Kulmala et al., 2004).

2.3 Particle Distributions

Super-coarse and coarse mode particles are not stable in the atmosphere; they have greater settling velocities than fine and ultrafine particle modes and therefore, shorter atmospheric lifetimes (IPCC, 2013). As shown in Figure 1, coarse mode particles tend to dominate PM volume.

Figure 1 shows fine mode particles dominate PM surface area. This is a result of their typically aggregated structure. Smaller (nucleation and accumulation mode) particles coagulate or have atmospheric vapours condense on their surface, causing particle growth (Kulkarni, Baron & Willeke, 2011).

UFPs only account for 1% - 8% of ambient PM mass but dominate particle number counts, as shown in Figure 1. UFPs make up 80% of particle number concentration in urban environments (Zhu et al., 2002). Wichmann et al., 2000 found that 88% of particle number counts in Erfurt, Germany were from UFPs.

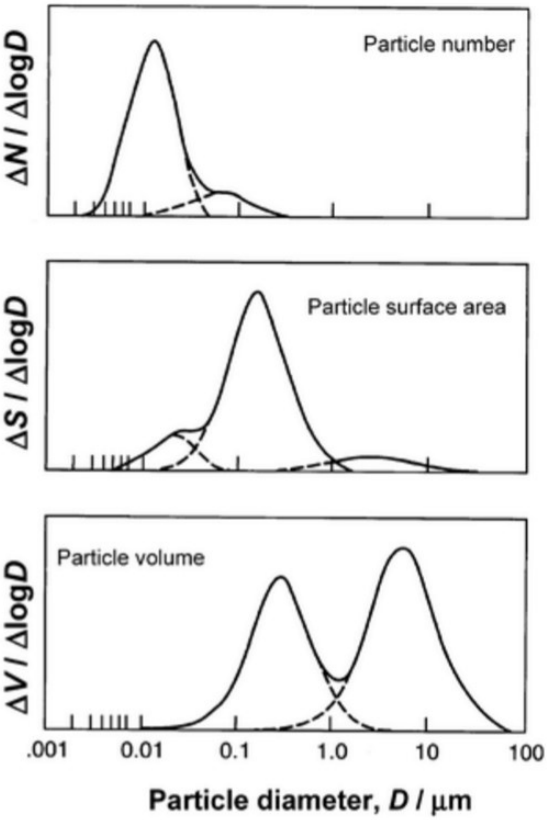

Figure 1. Ambient particle distribution as a function of particle number, surface area, and volume (Royal Society of Chemistry, 2012)

2.4 Species and Sources

Primary sources of PM include sea spray, surface dust, fossil fuel combustion, biomass burning, and volcanoes (Dohoo et al., 2013; Teather et al., 2013). Sea spray is naturogenic and caused by the bursting of sea surface bubbles, breaking waves, and high sea surface winds, and is influenced by sea temperature and composition. Sea spray aerosols are composed of inorganic salt particles (coarse mode), traces of sulphate, and organic aerosols (accumulation mode) derived from biological activity and are responsible for emitting 1400-6800 Tg yr^{-1} of PM to the atmosphere (IPCC, 2013). Manders et al, (2010) found that continental sea salt concentrations in Europe ranged from 0.3 $\mu g\ m^{-3}$ – 13 $\mu g\ m^{-3}$, with concentrations decreasing further inland. In coastal regions sea salt can account for 80% of atmospheric PM mass (European Environment Agency, 2012). Gibson et al. (2009) found at four sampling sites in west-central Scotland, UK, the coastal site PM_{10} was dominated by sea salt and chlorine depletion was noted at the urban sites.

Mineral dust is an important contributor to atmospheric aerosols, especially in dry and semi-arid deserts and regions impacted by human activities and decreased vegetation (Teather et al., 2013). The most significant source of mineral dust is the Sahara Desert (Fuzzi et al., 2015). The magnitude of mineral dust emissions to the atmosphere is a function of surface wind speed and surface characteristics. Naturogenic sources of re-entrained mineral dust (e.g. saltation) are responsible for 75% of global dust emissions and contribute 1000 – 4000 Tg of global aerosol mass per year (Fuzzi et al., 2015; IPCC, 2013). Anthropogenic activities (e.g. agricultural practices and road traffic) contribute the remaining 25% of global dust emissions (Fuzzi et al., 2015). Mineral dust contributes mainly to the coarse mode and less to the super-coarse and fine modes (Fuzzi et al., 2015; IPCC, 2013; Miller-Schulze et al, 2015). Querol et al. (2009) found that mineral dust contributed between 2 μg m^{-3} and 14 μg m^{-3} to the coarse particle mode in Europe and only 0.5 μg m^{-3} to 2 μg m^{-3} to the fine mode.

Combustion processes emit nitrogen and sulphur containing gases, which oxidize in the atmosphere to form nitrates and sulphates of ammonia (Gibson, 2004; Gibson et al., 2012; Gibson, Kundu & Satish, 2013; MacNeil et al., 2013; Palmer et al., 2013). Combustion is also a source of black carbon (BC) and organic carbon (OC), an important source of atmospheric UFPs (Kulkarni, Baron & Willeke, 2011). The most significant source of ultrafine particles in urban environments is vehicle emissions (Krecl et al., 2015; Brace et al., 2014). While measuring ultrafine particle counts at 30, 60, 90, 150, and 300 m downwind of Interstate 405 in Los Angeles, USA, Zhu et al. (2002b) found particle number counts peaking at 160 000 particles cm^{-3} for particles ≤13 nm at 30 m from the interstate. Particles smaller than 13 nm were no longer detected 90 m downwind of the interstate, and at 300 m downwind, ultrafine particle number concentrations were indistinguishable from background concentrations (Zhu et al., 2002b). In a second study, Zhu et al. (2002a) examined UFP number concentrations a 17, 20, 30, 90, 150, and 300 m downwind of freeway 710 in Los Angeles. UFP counts for particles ≤10 nm peaked around 320 000 particles cm^{-3} at 17 m from the freeway, at 20 m the concentration dropped to 240 000 particles cm^{-3} for particles ≤10 nm and at distances greater than 150 m, UFP number concentrations were indistinguishable from background concentrations.

The most significant emissions from volcanoes are in the form of ash (coarse mode) and sulphur gas. Volcanoes also emit carbon dioxide (CO_2), hydrochloric acid (HCl), hydrofluoric acid (HF), hydrobromic acid (HBr), water vapour, and mercury (Hg) at lower concentrations (European Environment Agency, 2012; Glasow, Bobrowski & Kern, 2009). Sulphur gas is emitted predominantly in the form of sulphur dioxide (SO_2); sulphate (SO_4) and hydrogen sulphide (H_2S) account for approximately 1% of sulphur gas emissions from volcanoes (IPCC, 2001; Gibson et al., 2013).

There are between 8 and 15,000 wildfires in North America every year, generating vast amounts of primary and secondary PM that can travel thousands of kilometers and impact downwind populations, ecosystems, and ultimately climate (Palmer et al., 2013; Franklin et al., 2014; MacNeil et al., 2014; Wheeler et al., 2014). Forest fires consumed a median of 17 000 km^2 of land per year in Canada from 1990 – 2011, contributing large amounts of atmospheric PM and trace gases (Palmer et al., 2013; Gibson et al., 2013). Other sources of primary aerosols include industrial processes such as cement manufacturing, metallurgy processes, and waste incineration.

Figure 2 and Figure 3 show source contributions to global $PM_{2.5}$ from the Surface PARTiculate mAtter Network (SPARTAN) and PM_{10} at various urban, rural, and marine ground based sites around the world (Snider et al., 2015)

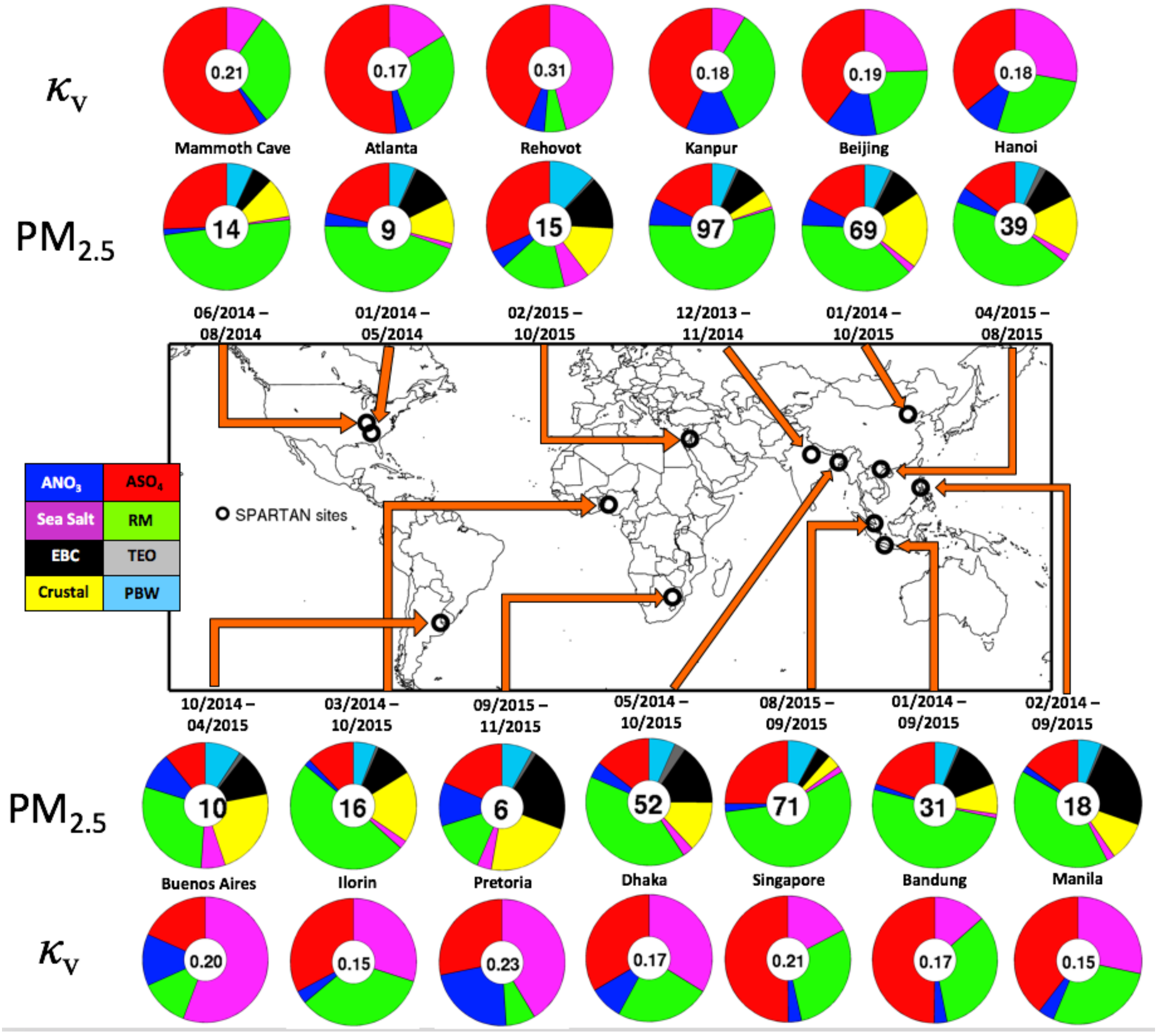

Figure 2. Global $PM_{2.5}$ Speciation from SPARTAN Ground Based Sampling Network (Snider et al., 2016)

In Figure 2, ANO_3 and ASO_4 are ammonium nitrate and ammonium sulfate, respectively. RM is residue matter, EBC is equivalent black carbon, TEO is trace elemental oxides, and PBW is particle bound water. κ_v is hygroscopicity, which describes a particles ability to uptake water. Hygroscopic particles often cause a problem during measurements as they attract excess moisture. This increased particle bound water increases the size and mass of the PM, resulting in a particle that is no longer representative of the original PM emitted or formed. Figure 3 shows PM_{10} speciation at various urban, rural, and marine regions around the world.

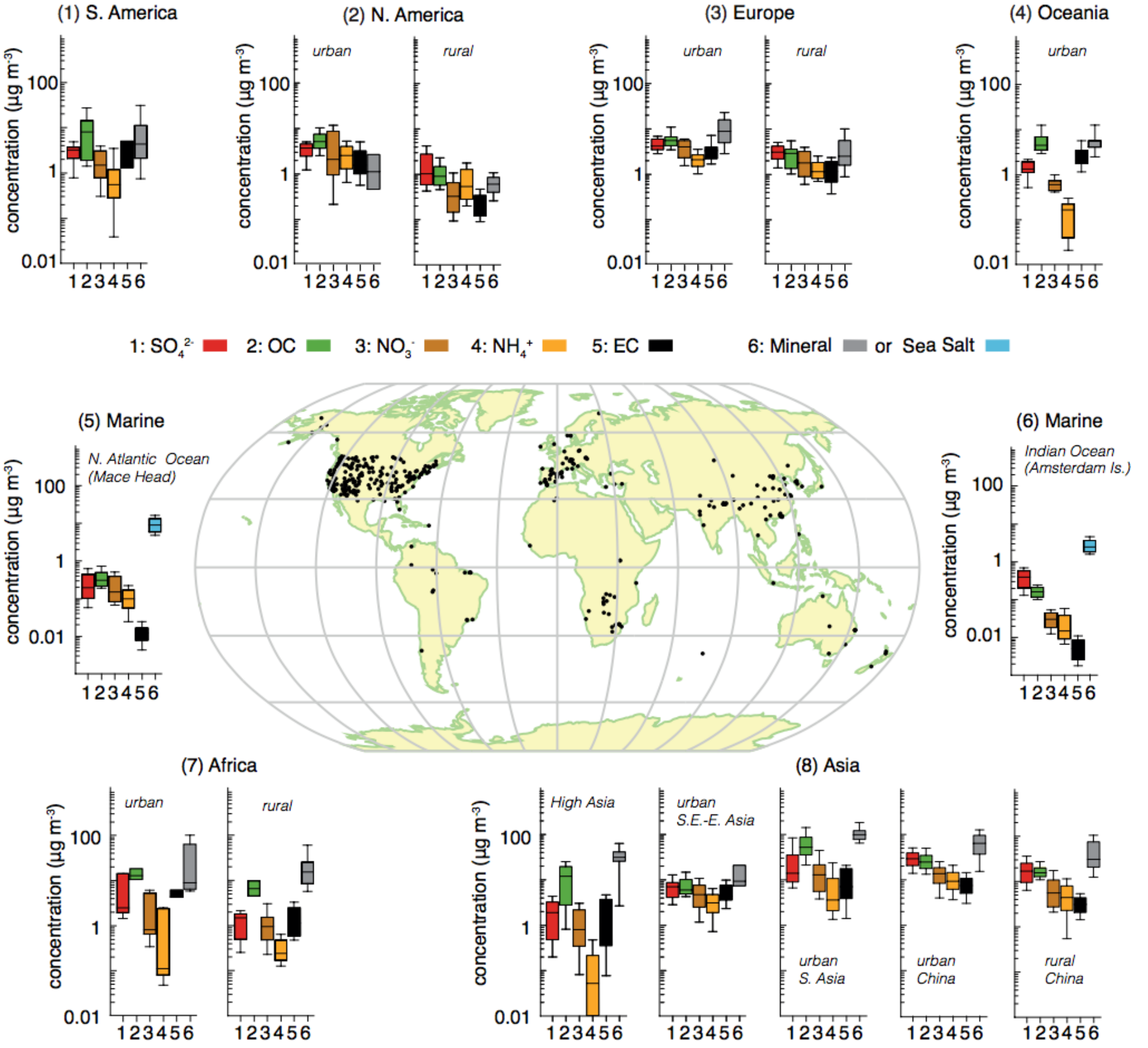

Figure 3. Continental Speciation of PM_{10} (IPCC, 2014)

It is clear from Figure 3 that sea salt is a significant contributor to PM_{10} in the marine environment and mineral (surface dust) heavily impacts PM_{10} in Africa and Asia. Gibson et al. (2009) found that easterly airflow impacting the west coast of Scotland was laden with SO_4-PM_{10} originating form the coal fired power stations in Germany.

Secondary sources of PM are the result of chemical reactions between gas phase precursors and these aerosols have a greater impact on the atmosphere than previously thought (IPCC, 2013; Gibson et al., 2009). The gasses primarily responsible for the formation of secondary particles include SO_2, oxides of nitrogen (NO_x), ammonia (NH_3), and VOCs. SO_2 and NO_x are emitted during combustion processes and react with NH_3, primarily from agricultural processes, to form secondary inorganic aerosol (SIA) (Fuzzi et al., 2015). This process is well understood. Secondary organic aerosol (SOA) formation processes, however, are not well understood mainly due to incomplete emissions inventories of biogenic VOCs (Fuzzi et al., 2015; IPCC, 2013). The formation of SOA occurs from condensation of low-volatility vapours; VOCs are oxidized by atmospheric O_3, the hydroxyl radical (OH), and NO_3, thereby decreasing their volatility and causing them to cluster and condense forming new PM (Fuzzi et al., 2015; Hao, et al, 2009; IPCC, 2013)(Gibson, Guernsey, et al., 2009). On a global scale, the majority of SOA is formed from oxidation of terrestrial biological VOCs and dimethylsulphide (DMS), emitted by phytoplankton (IPCC, 2013; Keller, Bellows & Guillard, 2009). Globally, SOA comprises 60% of organic aerosol mass (Hao, et al., 2009). At northern mid-latitudes SOA production is complemented by anthropogenic NO_x sources (IPCC, 2013). Dimethylsulphide, produced by phytoplankton, is a significant source of atmospheric sulphur (Malin, Turner & Holligan, 1994). Dimethylsulphide is ultimately oxidized to SO_4 which acts as a powerful cloud condensation nuclei and also forms crystals that reflect sun light back into space, contributing to global cooling (IPCC, 2013; Kloster, 2006). Kulmala et al. (2004) suggests that formation of 3 nm UFPs can be up to 10 particles cm^{-3} s^{-1} in the boundary layer and 100 particles cm^{-3} s^{-1} in urban environments. It is also noted that particle growth rate averaged 1-20 nm hr^{-1} in mid-latitudes (depending on temperature and condensable vapour) and reached lows of 0.1 nm hr^{-1} in polar regions. O'Dowd et al. (2002) studied formation and growth of UFPs at Mace Head Atmospheric Research station in the western coast of Ireland and found 3 nm UFP formation rates reached 100 000 particles cm^{-3} s^{-1}.

The most significant source of indoor particulates is smoking. Cooking is the largest contributor to indoor PM in non-smoking households and the second largest in smoking households (Kulkarni, Baron & Willeke, 2011). Stovetop cooking and the use of toaster ovens can lead to UFP number concentrations greater than 100 000 particles cm^{-3} and UFP number concentrations in restaurants can be between 50 000 particles cm^{-3} – 200 000 particles cm^{-3} (Wallace & Ott, 2010). Brace et al. found that median UFP number concentrations measured in a Halifax, Nova Scotia hospital operating theatre and hallway outside the operating theatre were 798 and 668 particles cm^{-3} during electrocautery procedures, respectively. Median outdoor UFP number concentrations in Halifax were 11646 particles cm^{-3} (Brace et al., 2014). Radon, when present indoors, can agglomerate onto existing PM, creating radioactive aerosols (Kulkarni, Baron & Willeke, 2011).

2.5 Health Effects

It has been well documented that exposure to PM is linked to increased risk of cardiovascular and cardiopulmonary disease, lung and other cancers, morbidity, and mortality (Pope et al., 2002; Dockery et al., 1993; WHO, 2013). No evidence exists of a safe level of PM where no health effects may be observed. The World Health Organization estimates that 3% of cardiopulmonary and 5% of lung cancer deaths are caused by PM exposure globally and that in 2010, 3.1 million deaths were attributed to $PM_{2.5}$ (WHO, 2013).

Particle size and chemical composition play major roles in particle toxicity (Dockery et al., 1993; Mirowsky, et al., 2013; Øvrevik et al., 2006). Particle size influences where in the respiratory system particles are deposited. Particles must follow a series of direction changes when inhaled and coarse particles are easily impacted on airway walls due to their inertia. Impaction deposition is of primary concern in extrathoracic region (upper airway) where the majority of inhaled PM mass is deposited (Hinds, 1998; Salma et al, 2002). Samoli et al. (2008) found a 0.2% - 0.6% increase in all-cause mortality associated with a 10 μg m^{-3} increase in PM_{10}. Pope et al. (2002) found that TSP and PM_{10} were not consistently associated with mortality. Kan et al. (2007) also showed no significant effect of PM_{10} on mortality in Shanghai, China where PM_{10} concentrations averaged 52.3 μg m^{-3} over the 10 month study; for reference, the WHO guideline for annual PM_{10} concentration is 20 μg m^{-3} (WHO, 2013) and the annual mean PM_{10} concentration in Canada is 11 μg m^{-3} (WHO, 2014). The literature suggests that coarse particles are less toxic than smaller size fractions. Coarse particles are generally made up of crustal elements and windblown dust, they contain lower concentrations of soluble metals which may contribute to their lower toxicity (Costa & Dreher, 1997).

Fine particles have less inertia than coarse particles, can be breathed deeper into the lungs, and are likely to be more toxic than coarse particles, posing a greater risk to human health. Fine particles are deposited in the alveolar region of the lungs by settling and diffusion. Particles ≤ 0.5 μm in diameter follow diffusion deposition mechanisms rather than settling (Dockery et al., 1993; Hinds, 1998). An increase in $PM_{2.5}$ of 10 μg m^{-3} was found to be associated with a 4% increase in all-cause mortality, a 6% -13% increase in cardiopulmonary mortality, and an 8% increase in lung cancer (Krewski et al., 2009; Pope et al., 2002; WHO, 2013). A study by Boldo et al. (2006) found that in 23 European cities, 1296 lung cancer deaths and 8053 cardiopulmonary deaths could be prevented annually by reducing annual mean $PM_{2.5}$ concentrations to 20 $\mu g\ m^{-3}$. The same study found a further reduction in annual mean $PM_{2.5}$ to 15 $\mu g\ m^{-3}$ would prevent 1901 lung cancer deaths and 11 612 cardiopulmonary deaths annually. Currently, the Canadian Ambient Air Quality Standard (CAAQS) for annual mean $PM_{2.5}$ is 10 $\mu g\ m^{-3}$, the 24-hour mean is 28 $\mu g\ m^{-3}$. The standards for annual and 24-hour mean $PM_{2.5}$ will be reduced to 27 $\mu g\ m^{-3}$ and 8.8 $\mu g\ m^{-3}$, respectively in 2020 (Environment and Climate Change Canada, 2013). From the WHO Ambient Air Pollution Database, annual mean $PM_{2.5}$ measured at Sherbrooke, Nova Scotia was 7 $\mu g\ m^{-3}$ for 2010. Chemical species common to $PM_{2.5}$ include sulphates, nitrates, and elemental and black carbon, organics, iron (Fe), and zinc (Zn), all of which are associated with mortality (Bell et al., 2007). Gibson et al. (2013) found that 47% of $PM_{2.5}$ mass in Halifax, Nova Scotia during a 45-day sampling campaign was attributed to ammonium sulphate and 27.9% to ammonium nitrate/aged marine aerosol mixture. Other species found included Zn, Fe, from vehicles, nickel (Ni) and vanadium (V) from ship emissions, and aluminum (Al) and silicon (Si) from surface dust.

UFPs, due to their small size, have the ability to penetrate membranes in the body when inhaled and within hours of exposure, can translocate to the liver, heart, and nervous system (Geiser, et al., 2005). The health effects of UFPs are not fully defined at present. However, there is growing evidence that UFPs may be linked various morbidities and mortality (Zhu et al., 2002). Many studies linking health effects to particulate exposure examine the mass concentration of PM (specifically PM_{10} and $PM_{2.5}$) and UFPs contribute very little to particle mass. However, UFPs dominate particle number counts and surface area and have a high pulmonary deposition efficiency, therefore they have the ability to transport high concentrations of toxic pollutants, which cause inflammatory responses, deep into the respiratory system (Delfino, Sioutas & Malik, 2005; Oberdörster, 2001)(McNeilly et al., 2004). A report published by Wichmann et al. (2000) evaluated the link between air pollution and morbidity and mortality over a 3.5 year period in Erfurt, Germany. It was noted that ultrafine particle number and fine particle mass concentrations had independent effects on mortality. In a paper published by Peters et al. (1997) respiratory symptoms associated with exposure to ultrafine particles were greater than those associated with fine particles. It was also reported that number of ultrafine particles had a greater impact on peak expiratory flow (the maximum force with which one can exhale) than number of coarse particles (Peters et al., 1997).

2.6 Environmental Effects

Atmospheric heavy loading of particulates can lead to haze events, reducing visibility. The haze formed from particulate matter can have adverse effects on climate, known as the aerosol direct effect which is discussed later in this section, and ecosystems (Cheng et al., 2013). Sulphates are a major component of PM and therefore, haze. Sulphates can react in the atmosphere and form acidic PM, which when deposited at the surface, can cause ecosystem acidification (Bell & Treshow, 2003).

Aerosols also have a significant effect on global climate by influencing the radiation budget; Figure 4 below shows radiative forcing values associated with various anthropogenic pollutants, where a negative sign indicates a cooling effect, and a positive sign, warming. Figure 4 highlights that although the contribution to radiative forcing by aerosols has been quantified, its impact is largely uncertain. It is also noted on Figure 4 that the level of scientific understanding (LOSU) for the aerosol direct effect on radiative forcing has a medium-to-low understanding and the indirect effect (aerosol-cloud albedo) has a low understanding, contrasted by GHGs and ozone, which have high and medium LOSU, respectively.

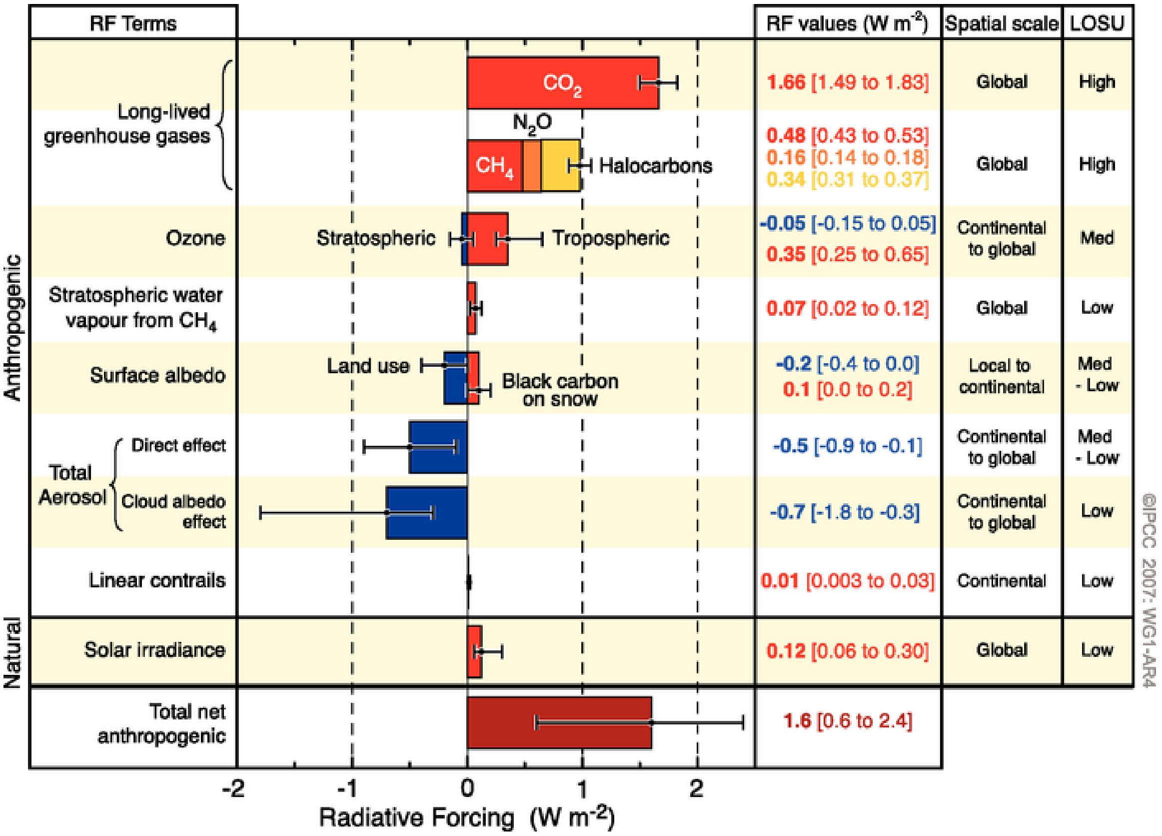

Figure 4. Radiative forcing from anthropogenic pollutants (IPCC, 2007).

2.6.1 Aerosol Indirect Effect

Interactions between aerosols and clouds are responsible for the large uncertainty in knowledge about the aerosol radiative forcing effect on Earth's climate (Kerminen et al., 2012). Particle nucleation followed by condensation of atmospheric vapours plays a major role in the aerosol indirect effect on climate. Cloud droplets can form in the absence of particles; however, saturation ratios, reached almost exclusively in lab experiments, are required (Kulkarni, Baron & Willeke, 2011). CCN are particles on which water vapour can condense (particle activation), causing particle growth and forming cloud droplets (Kerminen, et al., 2012). CCN contribute to an increase in cloud droplet number and decrease in cloud droplet size, which inherently increases surface area. This increase in cloud condensate modifies cloud optical properties, causing an increase in cloud albedo. This is called the cloud albedo effect (IPCC, 2013) and results in an indirect radiative forcing effect between -0.3 W m^{-2} and -1.8 W m^{-2} (Haywood, & Boucher, 2000).

The ability of a particle to activate depends on its size and chemical composition, specifically the presence of water soluble compounds and compounds that affect surface tension. Some studies suggest that particle size is more influential in formation of CCN (Dusek et al., 2006; Orellana et al., 2011). The bulk hygroscopicity parameter, κ, is used to describe the effectiveness of a particle to act as CCN. κ values for hygroscopic atmospheric particles typically range from 0 (non-hygroscopic) – 0.9. Sea salt particles have κ values between 0.5 – 1.4, indicating they are effective for CCN formation (IPCC, 2013; Petters & Kreidenweis, 2007). This is supported by Figure 2, which shows significant hygroscopicity associated with sea salt measured from SPARTAN sampling sites. A minimum particle size of 50 nm – 100 nm is required for particles to act as CCN in the boundary layer, therefore particles formed from gaseous precursors must grow to become CCN (Kerminen, et al., 2012). Sea salt, as mentioned, nitrates and sulphates of ammonia, organic, and inorganic particles can all act as CCN (IPCC, 2013). Insoluble and soluble PM can act as ice nuclei (IN), which modify atmospheric water molecule arrangements thereby increasing their freezing temperature. Twohy & Poellot (2005) sampled IN from anvil cirrus clouds and found that insoluble PM were prevalent in IN collected at warmer cloud temperatures whereas soluble PM prevailed as IN at colder cloud temperatures. This same study found that roughly one third of IN collected were salts, with smaller amounts from sulphates, fossil fuels, industry, and crustal materials (Twohy & Poellot, 2005). IN can cause cloud glaciation which increases the cloud albedo, indirectly affecting the global radiation budget (Pummer, et al., 2014).

2.6.2 Aerosol Direct Effect

Aerosols can directly influence climate through radiation interference. Aerosols can scatter and/or absorb radiation, influencing the global radiation budget; the scattering of solar radiation results in a cooling effect in the atmosphere whereas absorption causes a warming effect. Sulphate aerosols are effective at light scattering and can absorb some near-IR radiation. Global models suggest that radiative forcing from sulphate aerosols ranges from -0.21 W m^{-2} to -0.96 W m^{-2}, depending on atmospheric loading (IPCC, 2007). Organic carbon from the combustion of fossil fuels and forest fires can absorb small amounts of radiation in the UV and visible wavelengths. Studies suggest that OC from high temperature combustion is less absorbing than OC from low temperature combustion. The radiative forcing associated with fossil fuel burning OC aerosols is -0.1 W m^{-2}. BC is the result of incomplete combustion processes and its existence in the atmosphere is mainly from anthropogenic sources. BC is strongly light absorbing; global modelling of atmospheric BC suggests a radiative forcing value of +0.2 W m^{2}. Soot, of which a significant component is BC, has a radiative forcing value of 0.34 W m^{-2}, making it the third greatest contributor to climate warming behind CO_2 and CH_4 (IPCC, 2007). The distribution of BC in the atmospheric column has a significant impact on aerosol optical depth (AOD) and plays a major role in radiative forcing. BC can also have a significant impact on surface albedo, especially when deposited on snow or ice surfaces.

2.7 Air Mass Back Trajectories

Air mass back trajectories are a valuable tool for establishing relationships between a source and receptor. The U.S. National Oceanic and Atmospheric Administration's (NOAA) Hybrid Single-Particle Lagrangian Integrated Trajectory (HYSPLIT) model is the most commonly used dispersion modelling system, with a variety of applications. HYSPLIT it can be used to simulate air parcel transport, dispersion, transformation, and deposition (Stein et al., 2015). Draxler & Rolph (2012) used HYSPLIT to model transport, dispersion, and deposition of cesium-137 and iodine-131 from Fukushima and Stein et al. (2007) looked at benzene dispersion in Houston, Texas. Gibson et al. (2013) used HYSPLIT to investigate source regions of $PM_{2.5}$ measured in Halifax, NS in July and August, 2011. In this thesis, HYSPLIT is used to supplement source apportionment modelling and to examine potential source regions of particulates on Sable Island.

2.8 Source Apportionment

Source apportionment modelling, also known as receptor modelling or source attribution modelling, has been used for a number of decades to help identify sources and their attribution to the total concentration of airborne particulate matter mass or the total VOC concentration at a receptor (Gibson et al., 2009; Hopke, 1991; Kim & Hopke, 2004; Solomon & Hopke, 2008). Source apportionment is a useful tool with which to help our understanding of the potential health and ecosystem impact that upwind sources may have on a receptor. Source apportionment can also help provide insight into the temporal drivers of atmospheric composition and ultimately how changing emissions to the troposphere can impact climate (Gibson et al., 2013; Palmer et al., 2013). One of the most commonly used models is the United States Environmental Protection Agency (USEPA) Chemical Mass Balance (CMB) model v8.2 (Gibson et al., 2010; Jeong et al, 2008; Jeong et al., 2011; Paatero & Trapper, 1994; Ward, Hamilton & Smith, 2004; Ward, Rinehart & Lange, 2006). CMB utilizes $PM_{2.5}$ or VOC chemical species profiles of known emissions sources contained in the USEPA Speciate v 4.2 library. At the heart of the CMB model is a multivariate least squares statistical engine, that first factorizes the sample species composition and then matches these factor species with source species in the USEPA Speciate v 4.2 library (Ward et al., 2012). A good analogy that can be used to describe how the CMB model works is forensic science fingerprint matching. Once the source of the air pollutant is identified, the CMB model then attributes the mass of the source to the total mass of the air pollutant under investigation, e.g. $PM_{2.5}$ or total-VOC (Gibson et al., 2015). While CMB has been successfully used in many source apportionment studies, if the USEPA Speciate library does not contain a chemical species profile of the source impacting the receptor, then it is impossible to apportion that source. An alternative, and much more widely used source apportionment model, is the USEPA Positive Matrix Factorization model (PMF). The USEPA recently released a new version of PMF (version 5.0). The USEPA and research community better supports PMF over CMB. The utility of using PMF is that it does not require source profiles but determines the source contribution by isolating PM chemical species “Factors” which are unique to a particular PM source (Jeong et al., 2011). The source contribution of each “Factor” to the total

$PM_{2.5}$ or total-VOC concentration at the receptor is then quantified from *a priori* information of known source chemical markers (Jeong et al., 2011). Therefore, PMF has much more utility and flexibility than CMB (Gibson et al., 2015; Gibson et al., 2013; Paatero & Trapper, 1994). An older model that is still used in some studies is Absolute Principal Component Scores (APCS). APCS was developed in the 1980's from the popular statistical analysis tool, Principal Component Analysis (PCA) (Thurston & Spengler, 1985). While APCS shares the factorization method of identifying sources with PMF, the final source attribution step can occasionally return negative mass, which is clearly impossible. Therefore, the USEPA created PMF that does not allow negative mass attributions (hence 'positive' in Positive Matrix Factorization). Another very simple model that is often used for apportioning $PM_{2.5}$ or PM_{10} is Pragmatic Mass Closure (PMC) (Gibson et al., 2015; Harrison & Yin, 2008; Yin et al., 2005; Yin & Harrison, 2008). PMC utilizes trace enrichment factors, or simple molar rations, to estimate the chemical compound that was likely found in the original PM sample, e.g. from the post sample analysis of individual NH_4^+ and NO_3^- species, a factor is applied to estimate the original NH_4NO_3 mass that would have likely been present in the $PM_{2.5}$ mass sampled (Gibson et al, 2015). PMC is only useful for determining bulk composition of $PM_{2.5}$, e.g. sea salt, secondary ions, re-entrained surface dust, black carbon, gypsum and organic carbon. PMC is not as source specific as PMF, APCS or CMB. Never the less, PMC does have some utility in air quality management and atmospheric composition studies. PMF was used in this research to identify the particulate sources impacting air quality on Sable Island. This thesis will explore the PM mass and size spectra sampled on Sable Island in order to identify sources and apportion their contribution to the total sample. This data will ultimately provide valuable information for climate models.

CHAPTER 3 MATERIALS AND METHODS

3.1 Site Description

Located approximately 180 km off the coast of Nova Scotia and 290 km east southeast of Halifax, Sable Island is a narrow, crescent-shaped island made up of sand bars and sand dunes. The island has a maximum elevation of 30 m and is approximately 42 km long and 1 km wide at the widest point. The size and shape of the island is affected by the high winds, tides, and currents around the continental shelf (Wang et al, 1996; Friends of Sable Island Society, 2012). Figure 5 shows a map of Nova Scotia, including Sable Island.

Figure 5. Map of Nova Scotia, showing Sable Island adapted from “Source apportionment of the air quality on Sable Island” by Alex Hayes.

All of the instruments used for this study were housed in the air chemistry shed on Sable Island, shown in Figure 6. The air chemistry shed is located on the west side of Sable

Island Main Station (upwind of diesel generators), along with the Parks Canada and Environment and Climate Change Canada buildings. In Figure 6 yellow scaffolding can be seen near the rear of the shed. The scaffolding was erected for the installation of new sampling inlets on the roof of the air chemistry shed, shown in Figure 7.

Figure 6. Exterior of Sable Island air chemistry shed (Barnett, 2015).

Figure 7. Existing (left) and new sampling inlets (center, right) installed on Sable Island air chemistry shed (Barnett, 2015)

Figure 8 shows the interior of the air chemistry shed with the TSI Aerodynamic Particle Sizer (APS) model 3321 (left), the TSI Ultrafine Particle Monitor (UFPM) model 3031 (center), and the TSI DustTrak DRX model 8533 (top right). These instruments are discussed in greater detail later in this chapter.

Figure 8. Interior of Sable Island air chemistry shed (Barnett, 2016)

3.1.1 Site Visits

The three methods of travelling to Sable Island include helicopter, boat, and fixed wing aircraft. Private helicopter operators are not available for trips to Sable Island so helicopters are used at the discretion of the Canadian Coast Guard (CCG) and are subject to operational requirements. A round trip to Sable Island by helicopter costs $12 000 (Gerry Forbes, personal communication, Feb. 1, 2016). The boat that travels to Sable Island is called the Dominion Victory. The boat takes 16 hours to reach Sable Island, 30 hours if it is towing a cargo barge. A round trip to Sable Island aboard the Dominion Victory costs $30 000. The preferred method of travelling to Sable Island is by fixed wing aircraft (Gerry Forbes, personal communication, Feb. 2, 2016). The cost of a round trip to Sable Island by fixed-wing aircraft is $5 500 (Ted Brekelmans, personal communication, Aug. 8, 2015). Both times I travelled to Sable Island were aboard the Britten-Norman Islander aircraft, shown in Figure 9 operated by Ted and Debbie Brekelmans for Maritime Air Charter Limited/Sable Aviation.

Figure 9. Britten-Norman Islander aircraft operated by Maritime Air Charter Ltd. For transport to Sable Island (Barnett, 2015).

The first trip was September 29 – October 3, 2015. The purpose of this trip was to install two new particle sampling instruments and one VOC sampling instrument, as well as assess the condition of two instruments installed previously. The second trip was January 27 – February 2, 2016. The purpose of this trip was to perform maintenance on all instruments, as well as install a new total VOC analyzer.

Travelling to Sable Island has proven to be quite difficult. The major factors affecting the pilot's ability to land/takeoff safely from the island are runway and weather conditions. High crosswinds or low visibility greatly reduce the pilot's ability to safely land on the island. There is no landing strip on Sable Island, the aircraft lands on the beach. Before each flight leaves Halifax, Parks Canada employees stationed on Sable Island explore a 10 km stretch of beach for a potential runway. If a suitable runway is not found, the flight is postponed. One Parks Canada station manager I spoke with said that finding a runway is more of an art than a science, and that Parks Canada employees "make a new airport everyday" (Aaron Carpenter, personal communication, February 1, 2016). Approximately 1 000 ft of runway is needed for the Islander to land and 1 400 ft to takeoff. Sand conditions cannot be too dry or else the aircraft cannot reach a high enough speed for takeoff, the same is true for sand that is too wet. Parks Canada employees drive a truck that weighs more than the aircraft up and down the runway to assess the hardness of the sand. Ideally the runway is oriented parallel to the wind direction (or as close as possible) to reduce shear wind forces on the aircraft. Occasionally the Parks Canada employees have to dig ditches to route water away from runways. Communication via radio helps guide the pilot as they approach the runway, however if radio communication is not possible non-verbal indicators are used to communicate runway orientation to the pilot. The approach end of the runway is marked by two sets of two pylons and the stop end is marked by two sets of three pylons. The Parks Canada truck is parked near the approach end with a beacon light turned on and a windsock attached to the front of the truck to show wind direction (Aaron Carpenter, personal communication, February 1, 2016).

3.2 Particulate Sampling Instruments

During the study, particle number concentrations and mass concentrations were measured in real time in various different size fractions. The instruments used are discussed below.

3.2.1 TSI DustTrak DRX Aerosol Monitor model 8533

The TSI DustTrak DRX Aerosol Monitor model 8533 measures real-time mass concentration of PM_1, $PM_{2.5}$, PM_4 (respirable), PM_{10}, and TSP, simultaneously. As shown in Figure 10 an aerosol sample is drawn into the DRX inlet at 3 L min^{-1} via a diaphragm pump. A fraction of the aerosol sample passes through a high efficiency particulate air (HEPA) filter, becoming sheath air, and a sub-sample of the aerosol continues through the inlet nozzle. The sheath air and aerosol sub-sample merge before entering the detection chamber; the sheath air surrounds the aerosol subsample so that only one particle is illuminated at any one time. The sheath air also aids in keeping the optics and detector clean (Hinds, 1998; TSI, 2012b).

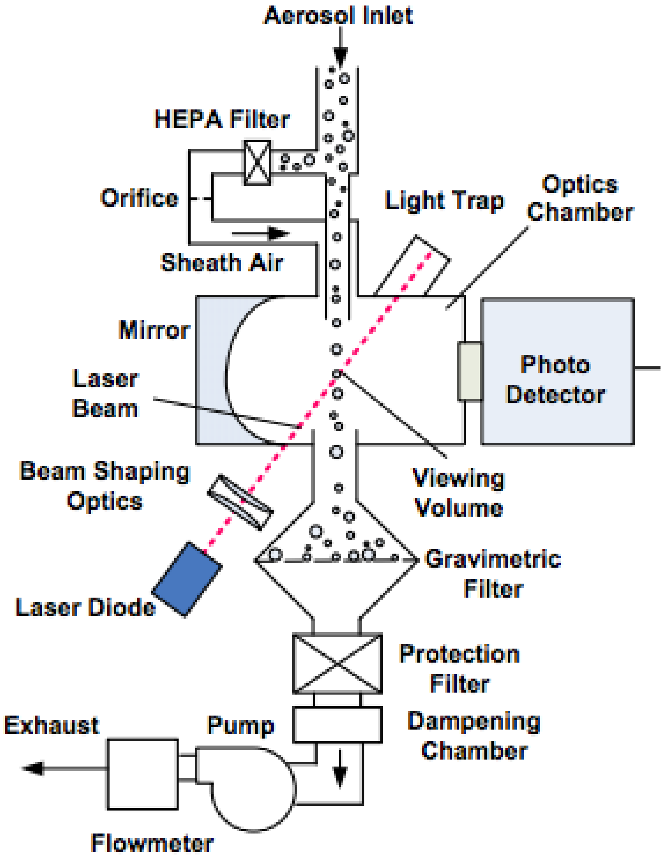

Figure 10. DustTrak DRX schematic diagram (TSI, 2012b)

Inside the detection chamber, a laser diode emits light that passes through a series of beam-shaping optics, sending a sheet of light through the detection chamber. When particles pass through the sheet of light, the refracted light is collected on a spherical mirror that focuses the light on to a photodetector. The photodetector measures voltage across the detector, which is proportional to concentration. The intensity of light scattered from single-particle pulses is used to determine the median aerodynamic diameter of the particles (Szymanski et al., 2009; TSI, 2012b). The particles are then collected on an internal filter that can be analyzed for gravimetric correction, aerosol chemical and biological composition, toxicology and/or morphology if required (TSI, 2012b). It is important to note that particle sizing errors occur when the refractive index of the particles measured is different from the test aerosols used to calibrate the instrument, e.g. Arizona desert dust. Changes in refractive index, aerosol composition, and particle size distributions can cause the instrument to over read by a factor of two or more (Hinds, 1998; Szymanski et al., 2009).

Prior to installing the DustTrak DRX on Sable Island, the instrument was factory calibrated by TSI using ISO 12103-1, A(Arizona)1 test dust (TSI, 2012b). It is recommended that the DRX be factory calibrated every 12 months. Once on the island, the DRX flow rate was set to 3 L min^{-1} using a rotameter and the calibration was tested using the zero-flow calibrator supplied by TSI. To install the DustTrak DRX in the Air Chemistry shed on Sable Island, a hole was drilled (at a downward angle from inside to outside, to mitigate water running into the shed) through the side of the shed. A stainless steel tube runs from the inside of the shed, through the hole, and approximately 60 cm from the outside wall of the shed where the inlet is housed inside a stainless steel weather shelter outfitted with bug screen. The stainless steel tube is insulated to reduce condensation inside the tube. Tygon tubing runs from the inlet of the DRX, through a water trap, and connects to the stainless steel tube. Figure 11 below shows the set-up of the DRX on Sable Island.

Figure 11. TSI DustTrak DRX Aerosol Monitor model 8533 and water trap on Sable Island (Barnett, 2016)

Aerosol data is downloaded by inserting a USB device into the USB drive on the DRX. On the Thursday of each week, an Environment Canada employee stationed on Sable Island will e-mail the data to the Atmospheric Forensics Research Group (AFRG) at Dalhousie University. The raw data is saved as a “level 0” file and is not edited. The data is examined for missing values and formatting before merging with the previous data. This manipulated data is saved as a “level 1” file. After downloading data and before resuming sampling, the flow rate of the DRX is checked and the instrument is calibrated with a zero flow attachment to ensure measurements are accurate.

3.2.2 TSI Aerodynamic Particle Sizer (APS) model 3321

During the project, aerosols with a particle size distribution between 0.5 µm to 20 µm (median aerodynamic diameter) in real-time were measured in different size ranges using a TSI Aerodynamic Particle Sizer (APS) model 3321. The APS spectrometer is capable of measuring particle size distributions in high-resolution via 52 size channels. Applications for the APS include, but are not limited to, inhalation toxicology, atmospheric studies, ambient and indoor air quality monitoring, and powder sizing (Peters & Leith, 2003; TSI, 2012a). The APS is also being used in the NASA NAAMES study that the Sable Island project is now a part of. The NASA APS is housed on the C-130 Hercules aircraft as part of the Langley Aerosol Research Group Experiment (LARGE) instrument package (NASA, 2015).

Figure 12 provides a schematic diagram of the operation of the APS. As can be seen in Figure 12, the APS operates by measuring the time-of-flight of aerosols in an accelerated flow field using a double-crest optical system as well as light-scattering intensity of individual particles (Chen et al, 1985; TSI, 2012a).

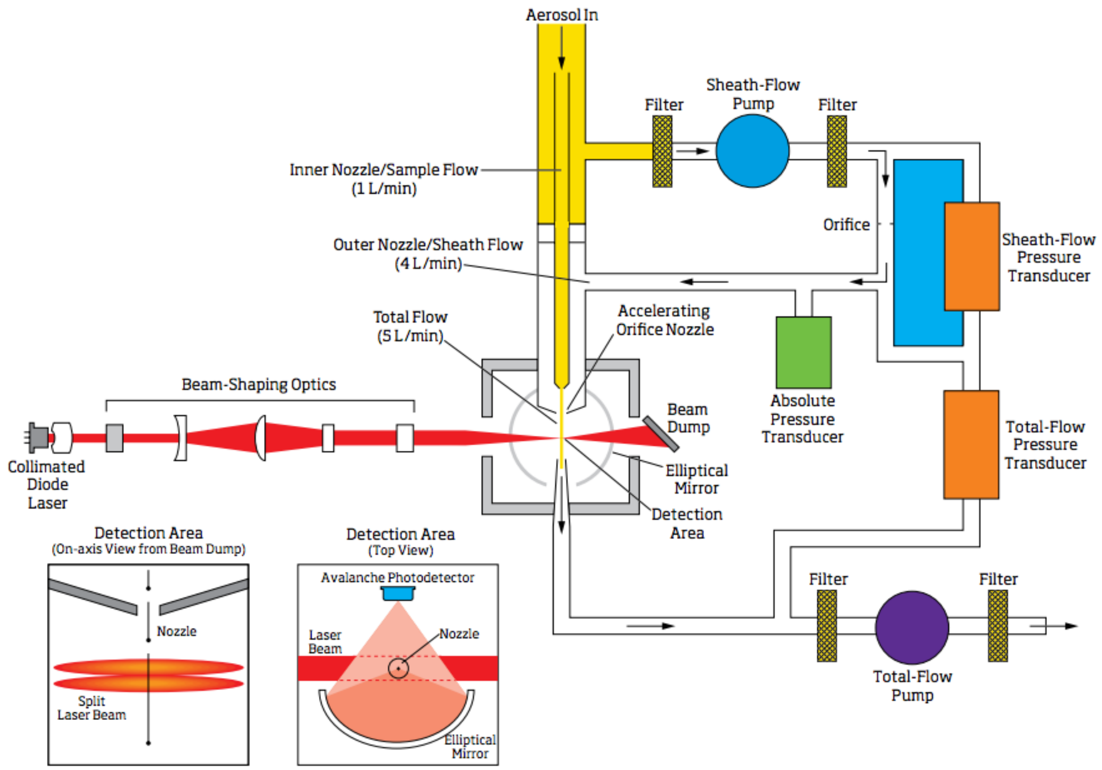

Figure 12. Schematic diagram of APS operation (TSI, 2012a)

As an aerosol sample enters the APS it is split into sheath flow and sample flow. The outer nozzle of the APS directs 4 L min^{-1} of sheath flow through two filters and an absolute pressure transducer to remove particles. The inner nozzle directs 1 L min^{-1} of sample flow toward the detection chamber. The sheath flow and sample flow merge before passing through an accelerating orifice, which separates particles based on inertia (large particles have a greater inertia than smaller particles, causing them to accelerate slower). As with the DRX, the sheath flow helps arrange for only one particle to pass through the detection chamber at a time. The combined sheath and sample flow then enter the detection chamber. A collimated laser diode is focused as it passes through a series of beam-shaping optics and enters the detection chamber. As particles pass through these overlapping laser beams, the refracted light is collected by an elliptical mirror and focused onto a photodetector (Chen et al., 1985; Hinds, 1998; TSI, 2012a). As can be seen in Figure 12, a collimated laser diode interacts with the particles to produce a two-crested peak when the scattered light is detected. The time-of-flight between the two crests is measured and is proportional to the aerodynamic size of the particle. The amplitude of the signal is also logged separately to produce light-scattering intensity measurements. When a signal cannot remain above the detection threshold and only one crest is detected, the event is logged and the particle is counted in the smallest size channel (<0.523 μm). When a signal remains above the detection threshold but only one crest is detected the event is logged but no data is recorded. This event is typically caused by a large particle, where the second crest is outside of the maximum timer range (4.096 μs). When coincidence occurs (more than one particle enters the detector at one time), the signal remains above the detection threshold but 3 or more crests are detected. These events are logged but no data is recorded (Chen et al., 1985; TSI, 2012a; TSI, 2015).

The APS was installed in the Sable Island Air Chemistry shed on Wednesday, September 30, 2015 and is shown in Figure 13. A 1.25 inch diameter hole was drilled through the roof and ceiling of the shed to accommodate a candy cane inlet for the APS. The inlet was levelled and secured to the roof of the Air Chemistry shed by a tripod and stainless steel mounting brackets to hold the feet of the tripod. A weather proof rubber flashing was installed around the inlet at the roof opening and sealed with a weather proof roofing tar to prevent water ingress into the shed. Typical house hold window bug screen was strapped to the inlet entrance to keep bugs, sand, and other debris from entering the APS.

The end of the inlet inside the shed was connected to the inlet of the APS using anti-static tubing supplied by TSI for use with the APS.

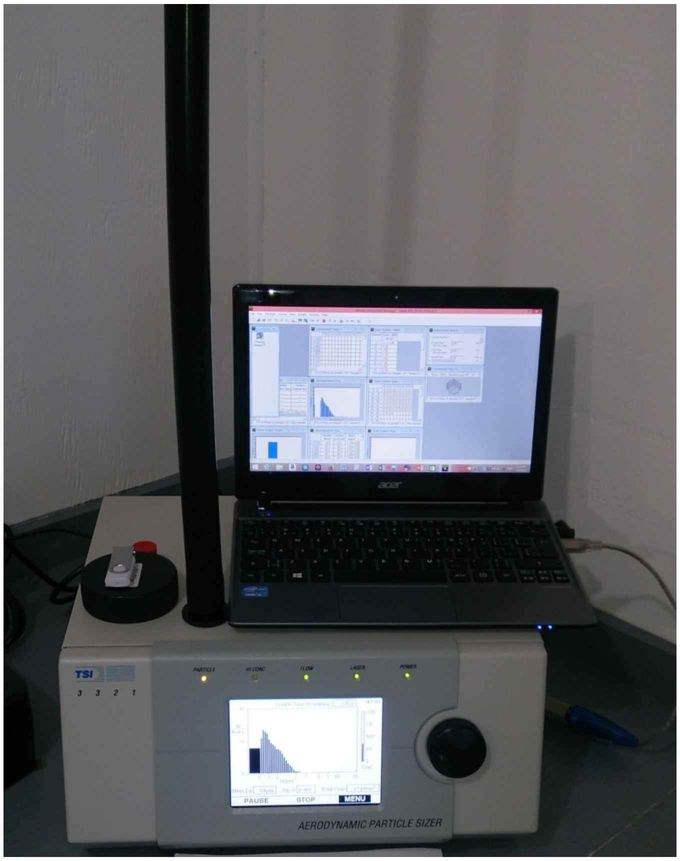

Figure 13. TSI Aerodynamic Particle Sizer model 3321 on Sable Island (Barnett, 2016)

The APS is configured to auto-export sample data to the laptop shown in Figure 13 at 15-minute intervals. The data is stored in a text file on the hard drive. The data handling procedure for APS data is the same as that for the DRX. On January 28, 2016, the inlet and inner and outer nozzles of the APS were cleaned; the internal HEPA filters were also replaced. The internal filters of the APS (blue) are shown below, in Figure 14.

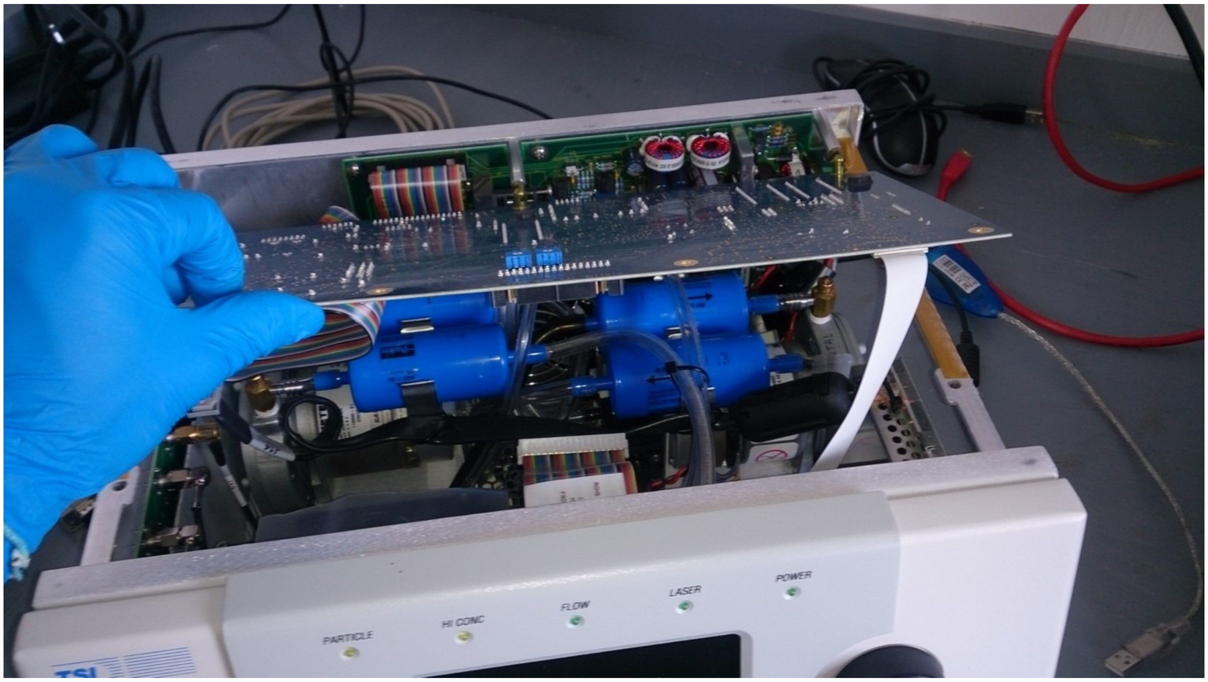

Figure 14. Inner components of the APS, internal HEPA filters are housed in blue cartridges (Barnett, 2016)

3.2.3 TSI Ultrafine Particle Monitor (UFPM) model 3031

Aerosols with a particle size distribution between 20 nm to 800 nm (median aerodynamic diameter) were measured in real time using the TSI Ultrafine Particle Monitor (UFPM) model 3031. The UFPM measures particles in six size channels (20-30 nm, 30-50 nm, 50-70 nm, 70-100 nm, 100-200 nm, 200-800 nm). The UFPM on Sable Island shown below in Figure 15 is equipped with the TSI 3031200 Environmental Sampling System (ESS) that includes a PM_{10} size selective inlet, PM_1 sharp cut cyclone, flow splitter, Nafion dryer, and particle filter (TSI, 2014b).

Figure 15. TSI Ultrafine Particle Monitor model 3031 and TSI 3031200 Environmental Sampling system on Sable Island (Barnett, 2015).

A flow rate of 16.7 L/min through the ESS is achieved using the internal pump from the UFPM (5 L min^{-1}) and an external vacuum pump (11.7 L min^{-1}) shown in Figure 15 to the left of the UFPM. The aerosol sample is drawn into the PM$_{10}$ size selective inlet, through the stainless steel down-tube, and into the PM$_1$ sharp cut cyclone impactor. The cyclone removes particles with a median aerodynamic diameter greater than, or equal to, 1 µm from the aerosol flow. The aerosol then passes through a flow splitter, where a subsample is drawn through a Nafion dryer for conditioning at a flow rate of 5 L min^{-1}. The Nafion dryer serves to reduce the effects of relative humidity on the sample before it passes through a section of anti-static Tygon tubing and enters the UFPM. The vacuum pump siphons 11.7 L min^{-1} (purge flow) through a particle filter before exhausting to the air chemistry shed. The flow rate from the vacuum pump is governed by a needle valve that follows the particle filter (TSI, 2012d). The pump is connected to a pressure gauge on the Nafion dryer; the pressure gauge is used to ensure the dryer is working properly and to test the ESS for leaks. In order for the Nafion dryer to function properly, the purge flow pressure reading should be -0.5 bar or lower. To test for a leak in the ESS, the inlet is removed and the stainless steel down tube is plugged. The Tygon tubing is removed from the bottom of the Nafion dryer and the dryer is plugged. The pump is turned on and the purge flow pressure should read -0.9 bar or lower if there are no leaks (TSI, 2014b). Leak tests performed on October 1, 2015 and January 31, 2016 showed no leaks in the ESS.

As shown by the UFPM schematic in Figure 16, the aerosol sample enters the equalization tank, which reduces short-term fluctuations in the aerosol sample. The aerosol sample is then split into aerosol flow and ion jet flow. The aerosol flow enters the mixing chamber at 4 L min^{-1}. The ion jet flow is passed through carbon and HEPA filters to remove all particles before entering the ionizer. The ionizer used in the UFPM is a Corona-Jet charger that uses a Corona needle with a 2.5 kV charge to generate positive ions (Hillemann et al., 2014; TSI, 2012c). The charged ion jet flow then merges with the aerosol flow in the mixing chamber where the aerosol undergoes diffusion charging. Both the particles and the ions follow Brownian motion and when an ion collides with a particle, it attaches, charging the particle. The charge acquired by a particle is proportional to particle diameter (Hinds, 1998; TSI, 2012c). The charged aerosol then enters the differential mobility analyzer (DMA) shown in section B of Figure 16.

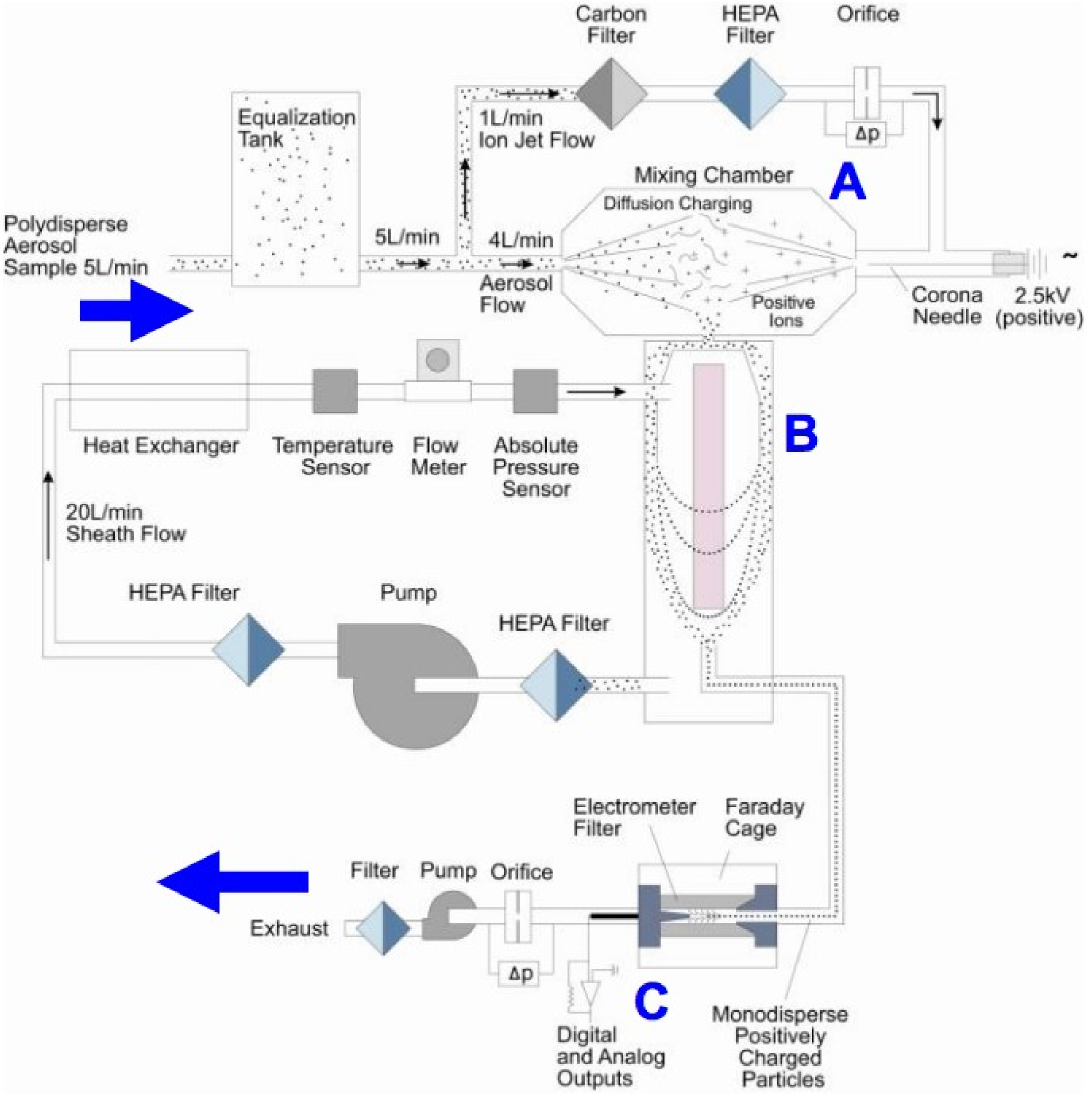

Figure 16. Schematic of UFPM 3031 operation (TSI, 2012c)

The DMA consists of an outer metal cylinder and an inner high voltage cylindrical rod. The outer metal cylinder is electrically grounded and the inner high-voltage rod is kept at a controlled negative voltage (from -0.3 V and -10 000 V with 27 steps in between), creating an electric field between the outer cylinder and inner rod. The sample enters the DMA at the top and flows downwards along the outer metal cylinder while a 20 L min^{-1} sheath flow generated by an internal pump also enters the DMA from the top, flowing downwards between the sample flow and the inner high-voltage rod; the two flows do not mix (Hillemann et al., 2014; Hinds, 1998; TSI, 2012c). The negatively charged rod attracts the positively charged particles through the sheath air. Particles with a greater electrical mobility will collect near the top of the DMA and those with a lesser electrical mobility are collected at the bottom of the DMA where they mix with the sheath flow and are collected on a high efficiency filter; the sheath flow is then recycled through the DMA. Depending on the voltage applied to the inner rod, particles within a certain electrical mobility range will pass through a small slit at the bottom of the inner rod and the aerosol travels to the detector. The charged particles are collected on a conductive filter and an electrometer measures current, which is used to calculate the particle number concentration (Hinds, 1998; Hillemann et al., 2014; TSI, 2012c). The data handling procedure for the UFPM is the same as that for the DRX and APS.

3.4 Instrument Malfunctions

During the visit to Sable Island in January, the DRX was disassembled for maintenance. Upon inspection it was noted that the beam collecting optics were fouled by sand and salt particles. Figure 17 shows the dirty DRX optics. The sand and salt build up would reduce the ability of the beam collecting optics to properly focus the reflected light toward the detector, resulting in the DRX under reporting particulate mass concentration.

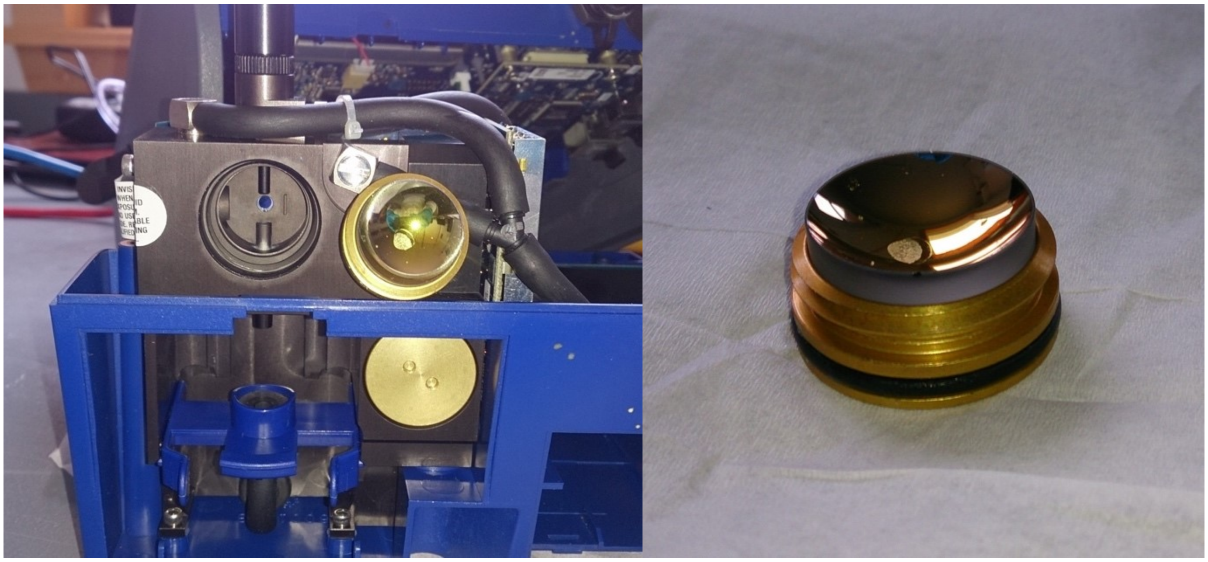

Figure 17. Disassembled DRX showing dirty beam collecting optics (left) and close up of beam collecting optics showing sand/salt build-up (right) (Barnett, 2016)

On October 14, 2015, the backup battery for the APS failed, cutting off the APS power supply. An Environment Canada employee stationed on Sable Island noticed the defective backup battery and replaced it with a spare. Another issue encountered was with the laptop used to log the APS data. The laptop would freeze periodically and require a reboot, resulting in short periods of missing data. The APS laptop was replaced on January 28, 2016 and no data logging issues have been reported since.

On December 8, 2015, the UFPM went into standby mode and stopped logging data. The reason for this is unknown and is currently being investigated. An Environment Canada employee stationed on Sable Island noticed the issue on December 10, 2015 and restarted the UFPM in sampling mode.

3.5 Meteorological Data

The meteorological data in this report was retrieved from the Government of Canada climate website (http://climate.weather.gc.ca/). There are two weather stations on Sable Island; for this report the meteorological data was obtained from Sable Island Airport (ID: 8204703) which is roughly 100 m from the air chemistry shed (Gerry Forbes, personal communication, January 14, 2016). Meteorological data was used to generate wind rose plots as well as pollution rose plots for the DRX, APS, and UFPM.

3.6 HYSPLIT

The NOAA HYSPLIT model uses a Lagrangian approach with a moving frame of reference to model air mass advection and dispersion and a Eulerian method to calculate pollution concentration in a fixed 3D grid system (Stein et al., 2015). HYSPLIT was used to generate 5-day air mass back trajectories for Sable Island during the sampling campaign. Air mass back trajectories longer than 5-days are typically not used as the model error becomes unacceptable. Two back trajectories were generated for each day to account for any dramatic changes in potential upwind source regions due to changing synoptic wind fields, one at 00:00 UTC and the second at 12:00 UTC. The meteorological data used to compute the back trajectories was the Global Data Assimilation System (GDAS) model and the air mass arrival height was set to 500 m (default) to reduce the risk of air masses contacting the surface before arriving at Sable Island (Gibson et al., 2013).

3.7 Satellite Observations

Satellite observations for Sable Island from the NASA Visible Infrared Imaging Radiometer Suite (VIIRS), Aqua and Terra (Moderate Resolution Imaging Spectroradiometer) MODIS satellites were downloaded from the NASA Ocean Color Web (http://oceancolor.gsfc.nasa.gov/cgi/browse.pl?sen=am) database. The MODIS satellites see every point on Earth's surface every 24-48 hours. In 36 discrete spectral bands ranging from 0.4 μm – 14.4 μm, data products are produced that include cloud cover and cloud droplet size, aerosol properties, and terrestrial and marine (i.e. phytoplankton) photosynthetic activity. The MODIS satellites also measure chlorophyll fluorescence, which helps to indicate phytoplankton health as well as distribution (NASA, 2016a; NASA, n.d.). The VIIRS satellite has similar capabilities as the Aqua and Terra MODIS satellites, however the VIIRS satellite has a 750 m spatial resolution, which provides twice the spatial resolution of the MODIS satellites (NASA, 2016b). The chlorophyll-a data products were used to identify phytoplankton blooms around Sable Island, the NE US, and eastern Canada and support the hypothesis of biogenic marine emissions producing UFPs from gas-to-particle conversion. The quasi true colour observations were also used to identify phytoplankton blooms as well as assess cloud cover around Sable Island.

3.8 Positive Matrix Factorization

The US EPA PMF receptor model v5 was used for source apportionment of the size-resolved $PM_{1/2.5/4/10}$ and total mass concentrations and size-resolved particle number sampled during the Sable Island Project. The PMF receptor model has an extensive heritage, having been applied to many $PM_{2.5}$ source apportionment studies (Gugamsetty et al., 2012; Paatero, 1997; Paatero and Trapper, 1994; Henry, 1997; Martello et al., 2008; Jeong et al., 2011; Kim et al., 2004; Chen et al., 2007b; Brown et al., 2007; Larson et al., 2004;J eong et al., 2008; Song et al., 2001; Bari et al., 2009). The PMF model uses a mass balance equation, equation 4, that can be written to account for all m chemical species in the n samples as contributions from p independent sources (Hopke, 1991).

$$X_{ij} = \sum_{k=1}^{p} f_{ik}\, g_{kj} \qquad (4)$$

where χ_{ij} is the i^{th} elemental concentration measured in the j^{th} sample, f_{ik} is the gravimetric concentration (ng mg^{-1}) from the i^{th} element in the material from the k^{th} source, and g_{kj} is the airborne $PM_{2.5}$ mass concentration (mg m^{-3}) of material from the k^{th} source contributing to the j^{th} sample. The following physical constraints are applied to the PMF model: 1) the model must fit the original data as well as possible, 2) no negative source contributions are allowed and intuitively 3) the sum of the source contributions must be less than or equal to the total mass measured (Hopke, 1991).

PMF then uses factor analysis to estimate the number and composition of the sources as well as their contribution to the total variable (e.g. PM or volatile organic compounds) (Gibson et al., 2013). *A priori* information of source chemical markers, meteorological variables and other numerical features, e.g. distance to a road, present in each PMF factor is used to identify the source associated with each factor (e.g. factors containing Al, Ca, Fe, Si, zero precipitation, warm temperatures and high wind speed are likely associated with re-suspended surficial material) (Gibson et al., 2013). Correlation matrices and PCA of the PM mass, PM chemical species, associated VOCs, other gas measurements, air mass back trajectory models and other meteorological variables are often used to aid the identification of the source of the chemical species in each PMF factor (Jeong et al., 2011; Martello et al., 2008; Gibson et al., 2013).

Once the source has been identified with the aid of the meteorology, gaseous species and other pertinent co-varying drivers of the total variable of interest included in the model, PMF is re-run with only the total variable, e.g. $PM_{2.5}$ mass and $PM_{2.5}$ species present. This is the final step in the PMF modelling process. In addition, the chemical species and contributing mass are scrutinized and compared with the air mass back trajectories for any give 24-hr period (and shorter periods), and potentially at coordinates nested around the receptor if one is interested in potential wind shear effects on the airflow during sampling. This can determine the long range transport (LRT) upwind source region, e.g. air mass trajectories crossing the Ohio Valley en route to Halifax associated with $(NH_4)_2SO_4$ laden $PM_{2.5}$ associated with secondary aerosol smog generated from pre-cursor emissions from this upwind source region (Gibson et al., 2013)

The task of PMF is to determine the loss function (Q), defined in equation 5, as follows:

$$Q = \sum_{i=1}^{n} \sum_{j=1}^{m} \left(\frac{e_{ij}}{S_{ij}} \right)^2 \tag{5}$$

where e_{ij} is the residual matrix of the i^{th} element measured in the j^{th} sample, S_{ij} is the uncertainty in the i^{th} element measured in the j^{th} sample. The loss function, Q, should be approximately equal to the degrees of freedom (Martello et al., 2008). When the calculated Q value is below the degrees of freedom then the uncertainty in the overall model fit is smaller than would be expected from random error, providing confidence that the data set is well defined by the model solution (Martello et al., 2008). When calculating Q, PMF ensures that all the species profiles (matrix F) are non-negative and that each source contribution to the total variable mass (e.g. $PM_{2.5}$ mass) is positive (matrix G). The PMF model simultaneously changes the elements of G and F in iterative steps to minimize Q. For the Sable Island Study the measurement uncertainty was set to 20% which is recommended in the PMF user manual (Eberly, 2005). Any component (PM mass or particle number) found to have a low signal-to-noise ratio were down-weighted as described by Paatero & Hopke (2003).

CHAPTER 4 RESULTS AND DISCUSSION

4.1 Meteorological Data

Table 1 contains the descriptive statistics for Sable Island 2015 meteorological data obtained from the Meteorological Services weather station on Sable Island.

Table 1. Meteorological data descriptive statistics

Variable	Temperature *[°C]*	Wind Direction *[°]*	Wind Speed *[km/h]*
n	8443	8760	8711
n missing	317	0	49
Mean	9.04	255	25.39
St Dev	7.20	98.96	12.60
Min	-11.4	0	0
25 pct	4.1	130	17
Median	8.9	-	24
75 pct	14.9	280	34
Max	53.8	360	84
IQR	10.8	150	17
Data Completeness (annual)	96.38%	100.00%	99.44%

From Table 1 it can be seen that the data completeness for temperature, wind direction and wind speed was 96.38%, 100.00% and 99.44% respectively, which can be considered excellent data completeness. It can also been seen from Table 1 that the mean (min : max *units*) temperature and wind speed was found to be 9.04 (-11.4 : 53.8°C), 25.39 km/h (0 : 84 km/h). The maximum temperature of 53.8°C occurred on January 1 at 17:00 UTC; the temperature was 5°C at 13:00 UTC and there are no temperature readings for 14:00-16:00 UTC on January 1. Missing temperature data indicates a sensor failure. If the sensor was repaired or replaced, the 53.8°C reading may have been from an uncalibrated sensor. A faulty relative humidity sensor was replaced on February 1, 2016 (Alan Wilson, personal communication, March 21, 2016) and it is recommended that the other meteorological sensors be checked to determine if they require calibration or replacement. Figure 18 below provides an annual wind rose for the Sable Island weather station.

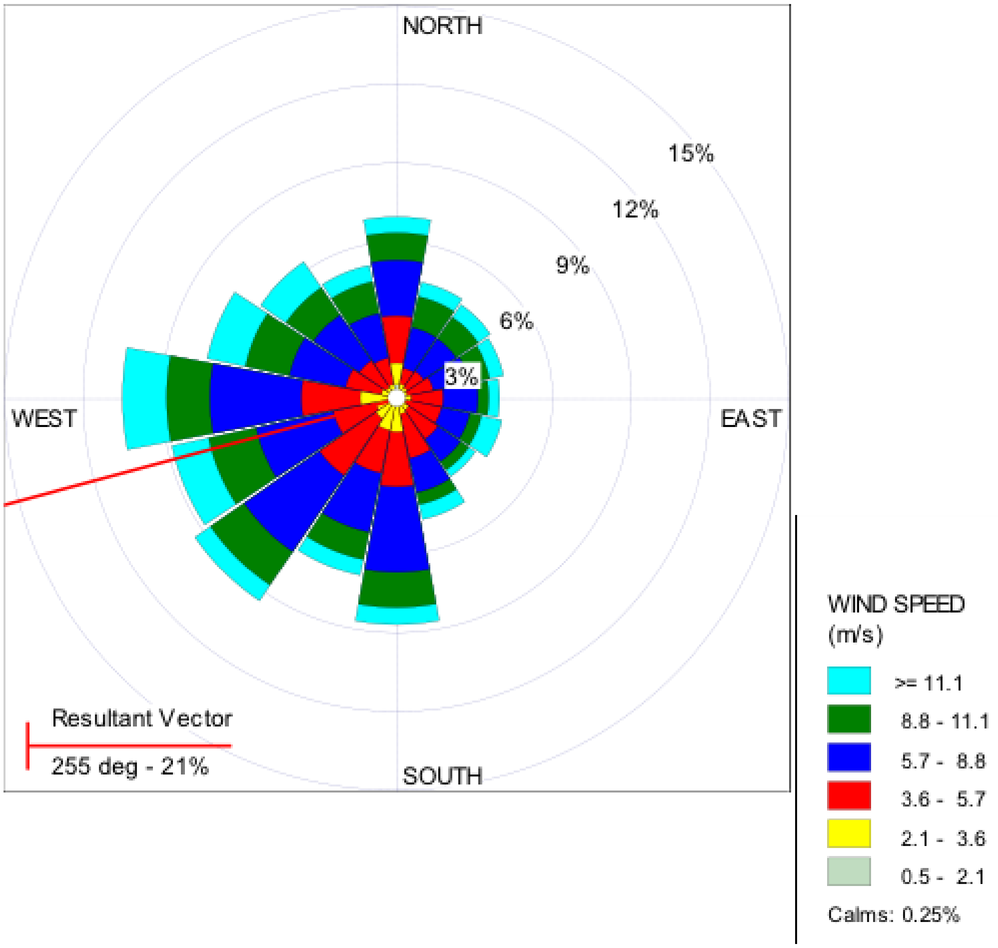

Figure 18. Sable Island 2015 Annual Wind Rose.

As can be seen from Figure 18, prevailing winds on Sable Island are from the WSW with strong winds also from the W, SW, and S directions. Waugh et al. (2010) found the prevailing wind direction on Sable Island from June 2003 – December 2006 to be from the SW. Figure 19 presents a wind rose for the 2015 sampling campaign, October 1, 2015 – December 31, 2015.

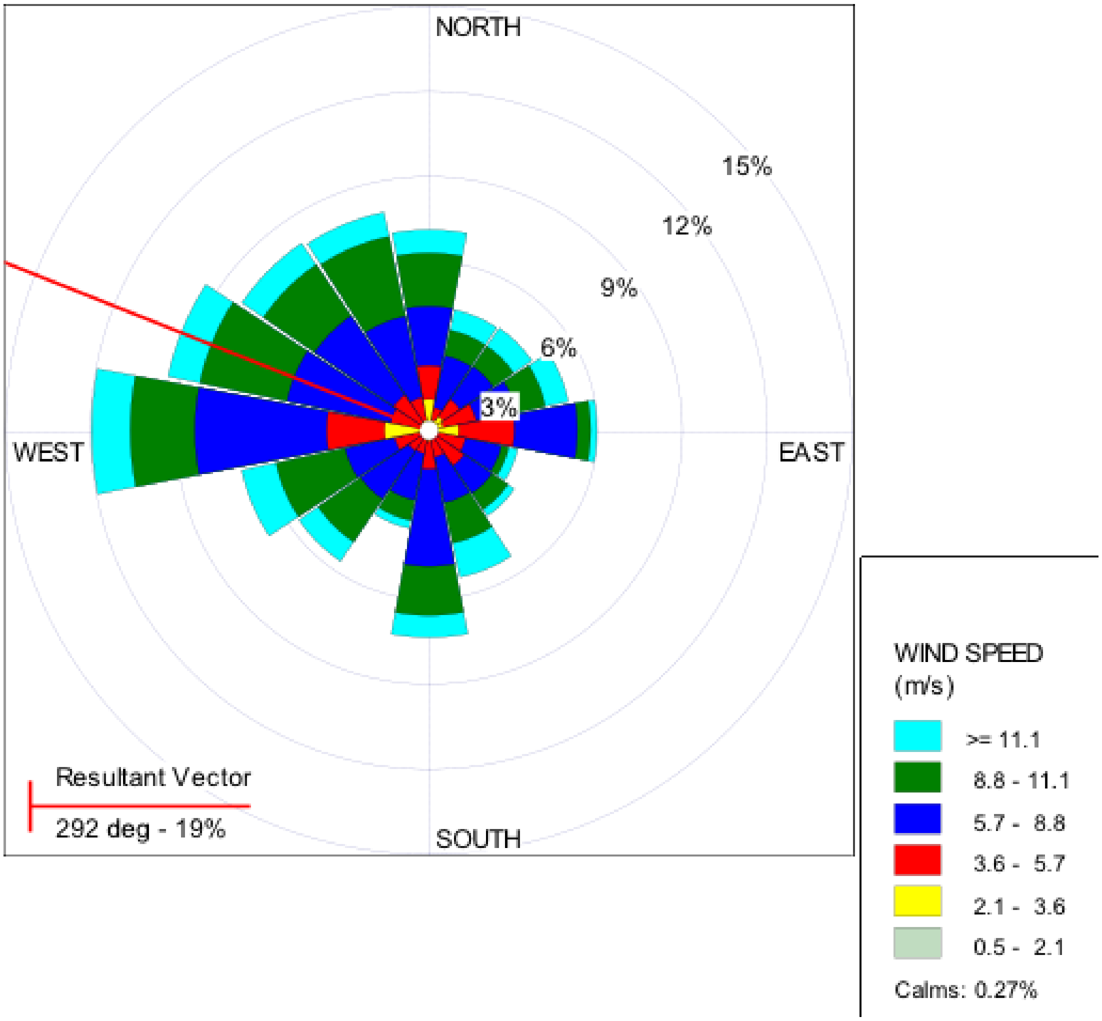

Figure 19. Sable Island wind rose for October 1, 2015, through December 31, 2015

As shown in Figure 19, prevailing winds during the sampling period were from the WNW direction with strong winds also from the W direction. Wind from the NW direction could result in more transboundary pollution from the mainland.

4.2 DustTrak DRX Particulate Mass

Table 2 contains the descriptive statistics for $PM_{1/2.5/4/10}$ and total mass concentrations measured by the TSI DustTrak DRX model 8533.

Table 2. TSI DustTrak DRX descriptive statistics

Variable	PM_1 *[μg/m³]*	$PM_{2.5}$ *[μg/m³]*	PM_4 *[μg/m³]*	PM_{10} *[μg/m³]*	Total *[μg/m³]*
n	1875	1875	1875	1875	1875
n missing	66	66	66	66	66
Mean	13.84	14.32	14.51	14.60	14.61
St Dev	3.85	4.20	4.25	4.27	4.27
Min	9	9	9	9	9
25 pct	11	11.5	11.5	11.5	11.5
Median	13	13	13.5	13.5	13.5
75 pct	15.5	16	16.5	16.5	16.5
Max	34.5	37	37	37.5	37.5
IQR	4.5	4.5	5	5	5
Data Completeness	96.60%	96.60%	96.60%	96.60%	96.60%
Data Completeness (annual)	24.66%	24.66%	24.66%	24.66%	24.66%

From Table 2 it can be seen that the data completeness over the operation period for the DRX $PM_{1/2.5/4.0/10}$ and total mass concentration was 96.6%, and for the entire year was only 24.66%. The lack of data for 75.34% of the year was due to the instrument only being re-deployed on September 30, 2015 after service in July 2015 to repair flood damage. It can also been seen from Table 2 that the mean (min : max µg m^{-3}) for the $PM_{1/2.5/4.0/10}$ and total mass concentration was PM_1 = 13.8 (9 : 34.5 µg m^{-3}), $PM_{2.5}$ = 14.32 (9 : 37.0 µg m^{-3}), PM_4 = 14.50 (9: 37.0 µg m^{-3}), PM_{10} = 14.60 (9 : 37.5 µg m^{-3}) and TSP = 14.60 (9 : 37.5 µg m^{-3}) respectively. The similarity in the PM mass concentration observed for the latter three months of 2015, from the total through to $PM_{1.0}$ size fractions, implies that the aerosol below 10 µm observed on Sable Island is mainly composed of fine aerosols (e.g., gas-to-particle conversion, LRT or fresh local combustion sources). Time series analysis will investigate the peaks and valleys in the $PM_{1/2.5/4.0/10}$ and total mass concentration, to aid in the determination their source.

Figure 20 provides a non-parametric visualization of the PM mass concentration data sampled on Sable Island in the form of a box-whisker plot.

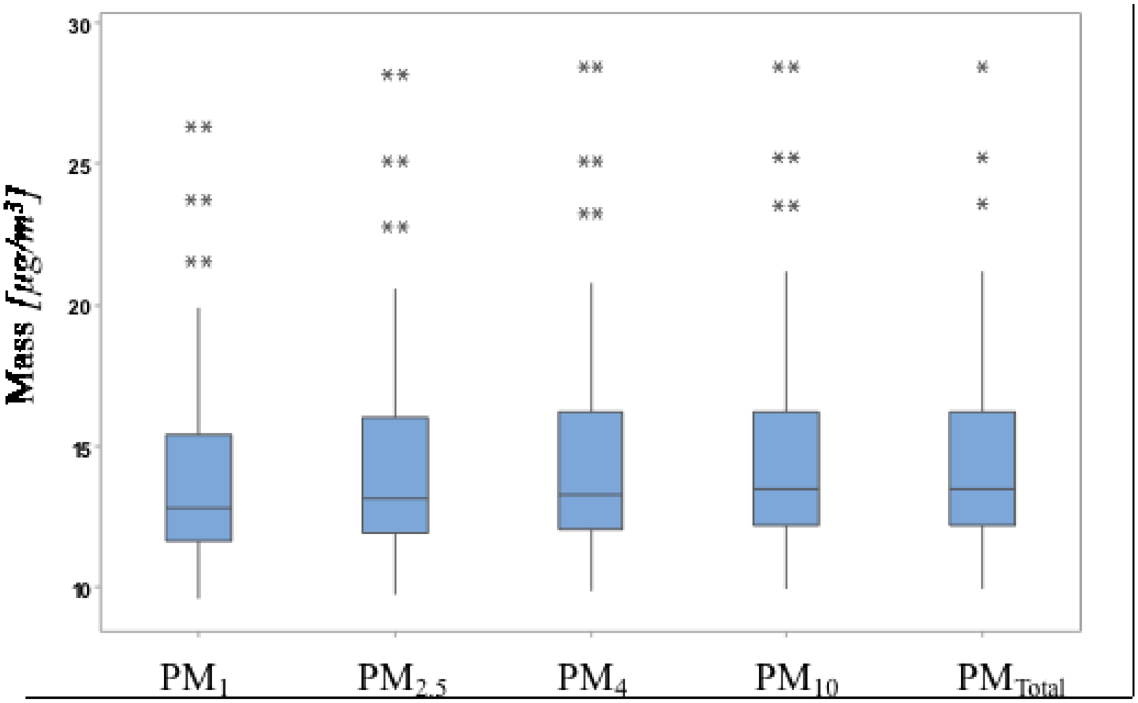

Figure 20. Boxplots of DustTrak DRX $PM_{1.0/2.5/4.0/10}$ and total mass concentrations

In Figure 20, the box represents the interquartile range (IQR) or the 25th and 75th percentiles, respectively and the line is the median. The stars represent outliers, data points that are greater than 1.5 times the IQR from the 75th percentile. The lower and upper whiskers represent the range of data points within 1.5 times the IQR from the 25th and 75th percentiles, respectively. From Figure 20, the $PM_{4/10}$ and total size fractions are nearly identical, highlighting that particle mass on Sable Island from October 1 – December 31 was predominantly from the fine particle mode ($PM_{2.5}$). Figure 21 shows a pollution rose for the DRX $PM_{2.5}$ data.

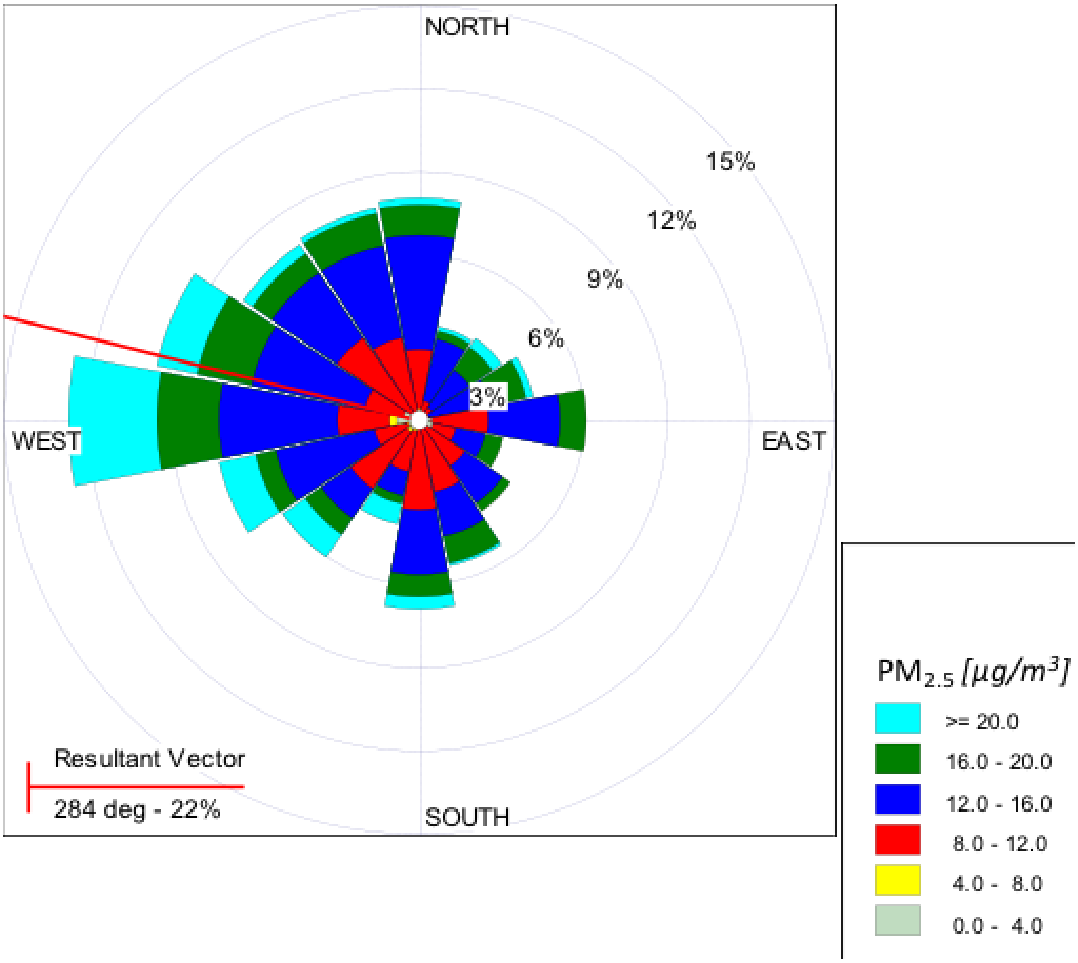

Figure 21. Pollution rose for Sable Island $PM_{2.5}$ measured by the DustTrak DRX

Figure 21 shows a pollution rose for Sable $PM_{2.5}$ mass concentration measured by the DustTrak DRX. The $PM_{2.5}$ size fraction is presented as there was no appreciable increase in particle mass in the size fractions larger than $PM_{2.5}$. A daily time series plot for all PM size fractions measured by the DRX is shown in Figure 22, below. As can be seen from Figure 22, the DRX failed on December 21, 2015. Upon inspection it was found that sand and sea salt crystals entered the optics chamber and fouled the sensor optics. The instrument functioned normally after cleaning and re-calibrating in January, 2016.

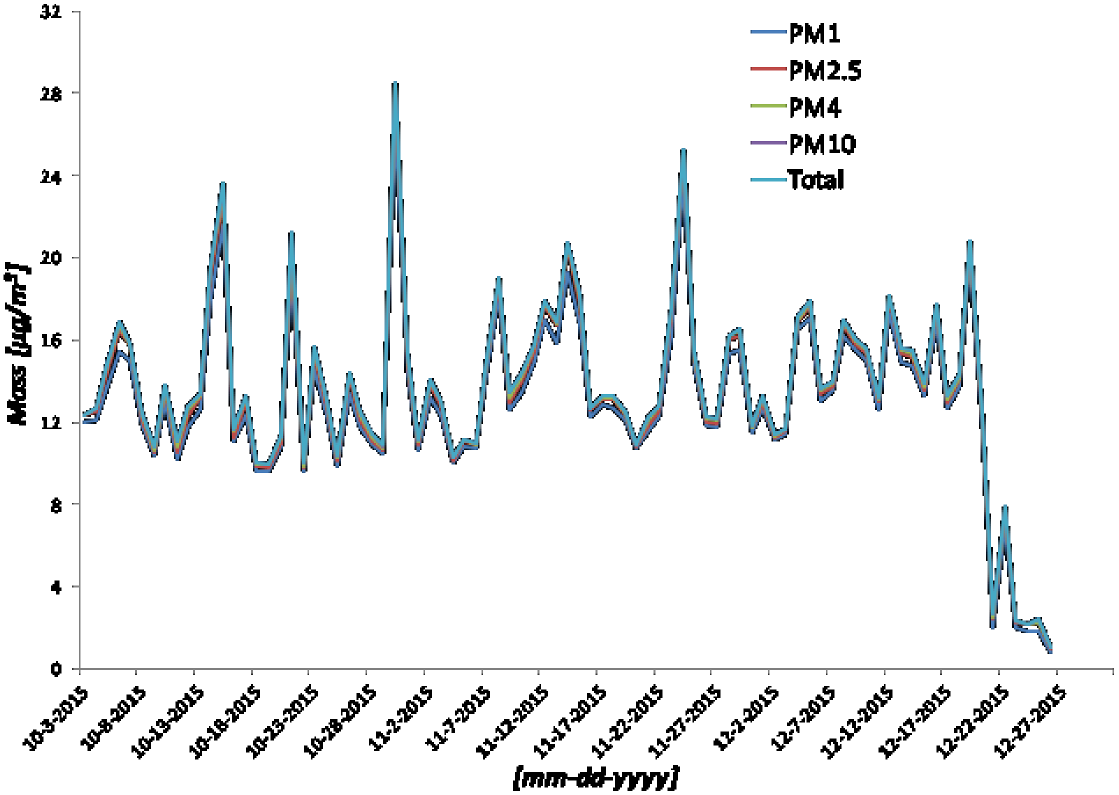

Figure 22. Daily time series of DustTrak DRX $PM_{1.0/2.5/4.0/10}$ and total mass

HYSPLIT and the NASA Terra MODIS, Aqua MODIS, and VIIRS satellites were used to investigate potential source regions for the four largest spikes observed in the DRX $PM_{1/2.5/4/10}$ and total time series. The chlorophyll-a colour bar is presented in Figure 23. The first spike investigated occurred on October 15 at 15:00 UTC where the $PM_{2.5}$ concentration reached 28 µg m^{-3} (24-hour average = 22.83 µg m^{-3}). The chlorophyll-a and quasi true colour satellite images, as well as the 5-day air mass back trajectory for this spike are presented in Figure 24. In the chlorophyll-a images, white pixels indicate missing data due to cloud coverage or other tripped quality control flags and the red dot indicates the location of Sable Island.

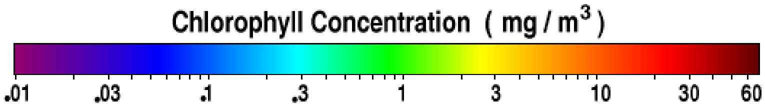

Figure 23. Chlorophyll-a colour key for the NASA Aqua MODIS, Aqua Terra, and VIIRS satellites (http://oceancolor.gsfc.nasa.gov/cms/)

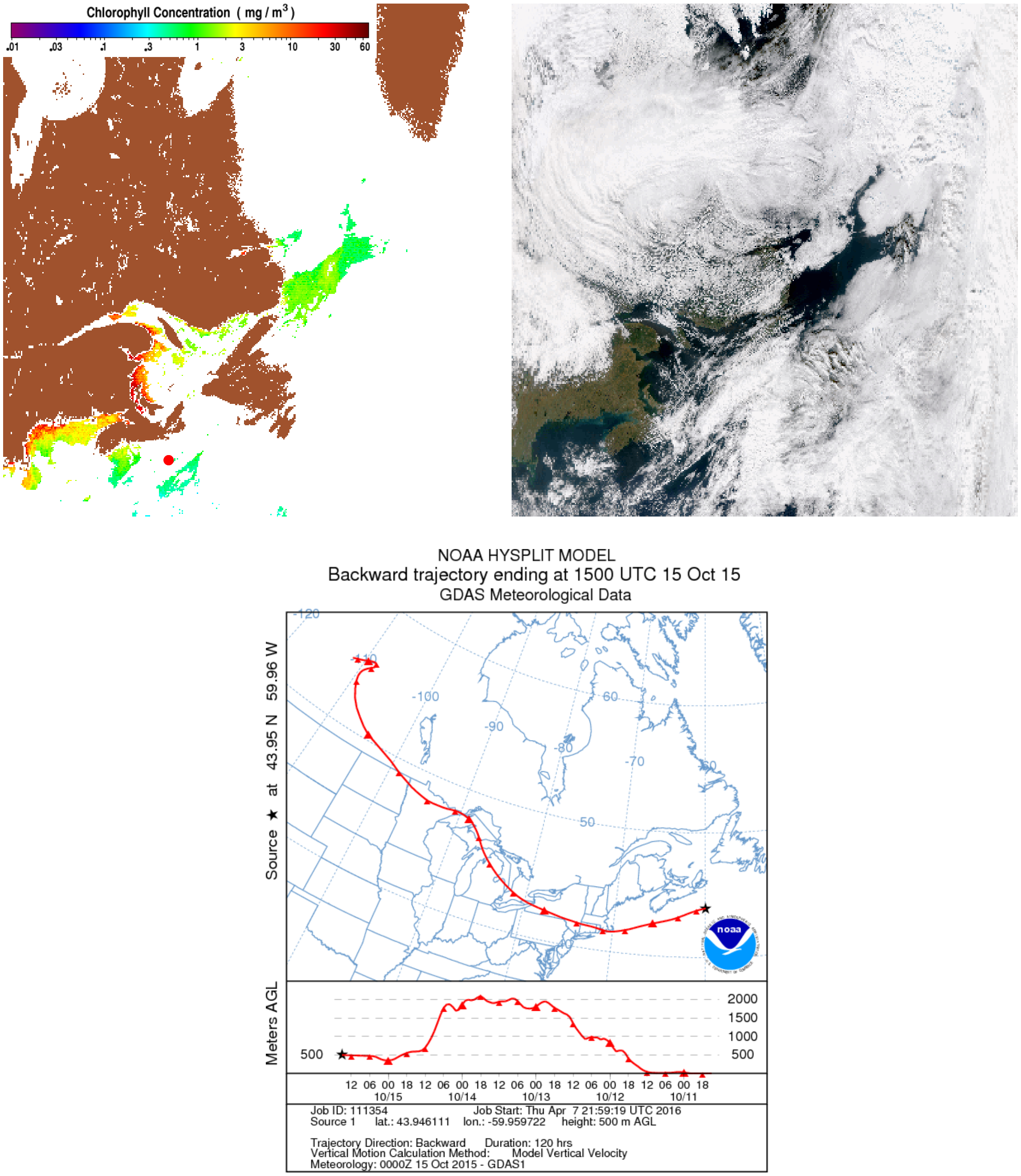

Figure 24. Chlorophyll-a (top left) and quasi true colour (top right) measured by the NASA VIIRS satellite and 5-day air mass back trajectory (bottom) for Sable Island on October 15, 2015

Figure 24 shows the air mass originating in Western Canada, moving along the Canada-United States (US) border to the northeast (NE) US before landing at Sable Island. Pennsylvania, New York, and port areas in Maryland have been identified as potential source regions for Halifax by Jeong et al. (2011) and Gibson et al. (2013), and are known to have many coal-fired power stations, which suggests this spike may be due to LRT from the continent. The air mass reaches an elevation of 2 000 m above the continent and drops to below 500 m over the Atlantic Ocean. The air mass appears to pass the Deep Panuke, Alma, and Thebaud oil and gas (O&G) platforms near Sable Island, indicating O&G as an additional potential source. Locations of the offshore O&G platforms near Sable Island are shown in Figure 25. It is unlikely that UFPs from from biogenic marine emissions are associated with spikes in DRX mass concentration data because UFPs contribute very little to particle mass (Figure 1). Moreover, particles smaller than 300 nm would not be detected by the DRX (Poluboyarov, Korotaeva, & Andryushkova, 2000; Wang et al., 2009).

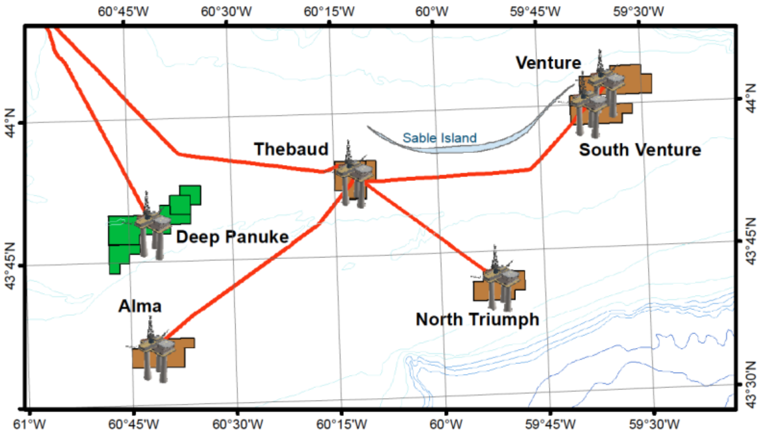

Figure 25. Locations of offshore oil and gas platforms near Sable Island (Canada-Nova Scotia Offshore Petroleum Board, n.d.)

The spike on October 30 occurred at 15:00 UTC, where the measured $PM_{2.5}$ concentration was 36 $\mu g\ m^{-3}$ (24-hour average = 28.17 $\mu g\ m^{-3}$). The chlorophyll-a and quasi true colour satellite images, as well as the 5-day air mass back trajectory for this spike are presented in Figure 26. Figure 26 shows the air mass moved from Alaska, through western Canada and the north east US before impacting Sable Island. The vertical profile shows the air mass approaching the surface as it moves through Ohio; Ohio, Pennsylvania, and western Indiana are known PM source regions due to the use of coal for power generation (Jeong et al., 2011). The air mass also appears to pass the O&G platforms near Sable Island, indicating that the spike may be from LRT, O&G, or a mixture of the two.

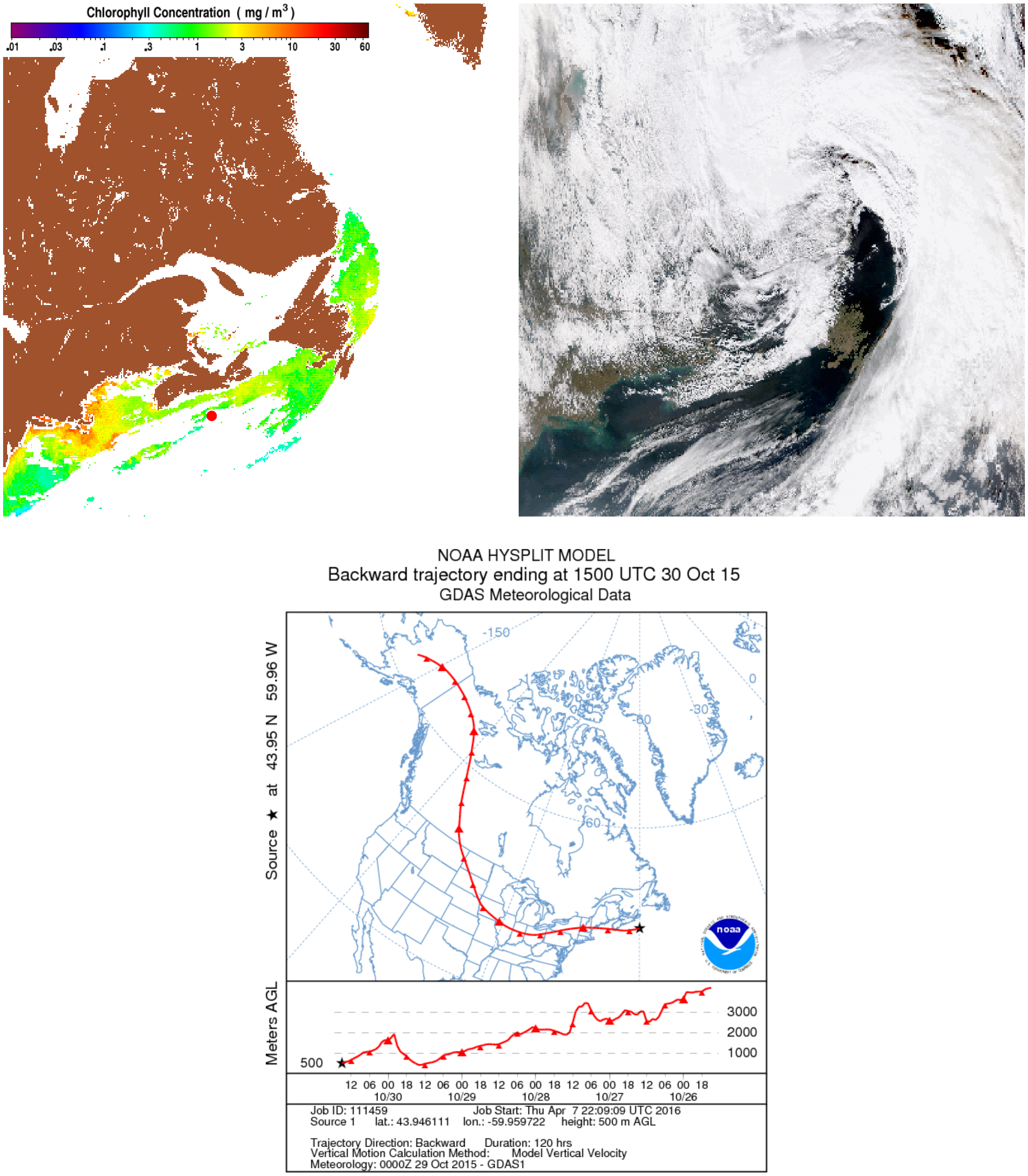

Figure 26. Chlorophyll-a (top left) and quasi true colour (top right) measured by the NASA VIIRS satellite and 5-day air mass back trajectory (bottom) for Sable Island on October 30, 2015

The spike on November 24 occurred at 23:00 UTC, where the measured $PM_{2.5}$ concentration was 37 μg m^{-3} (24-hour average = 25.10 μg m^{-3}). The chlorophyll-a and quasi true colour satellite images, as well as the 5-day air mass back trajectory for this spike are presented in Figure 27. Figure 27 shows the air mass moved along the Canada-US border, through the Windsor-Quebec corridor and Nova Scotia to Sable Island. The Windsor-Quebec corridor is significant industrial area of Canada and heavily populated, making it a source region for SOA and inorganics (Gibson et al., 2013).

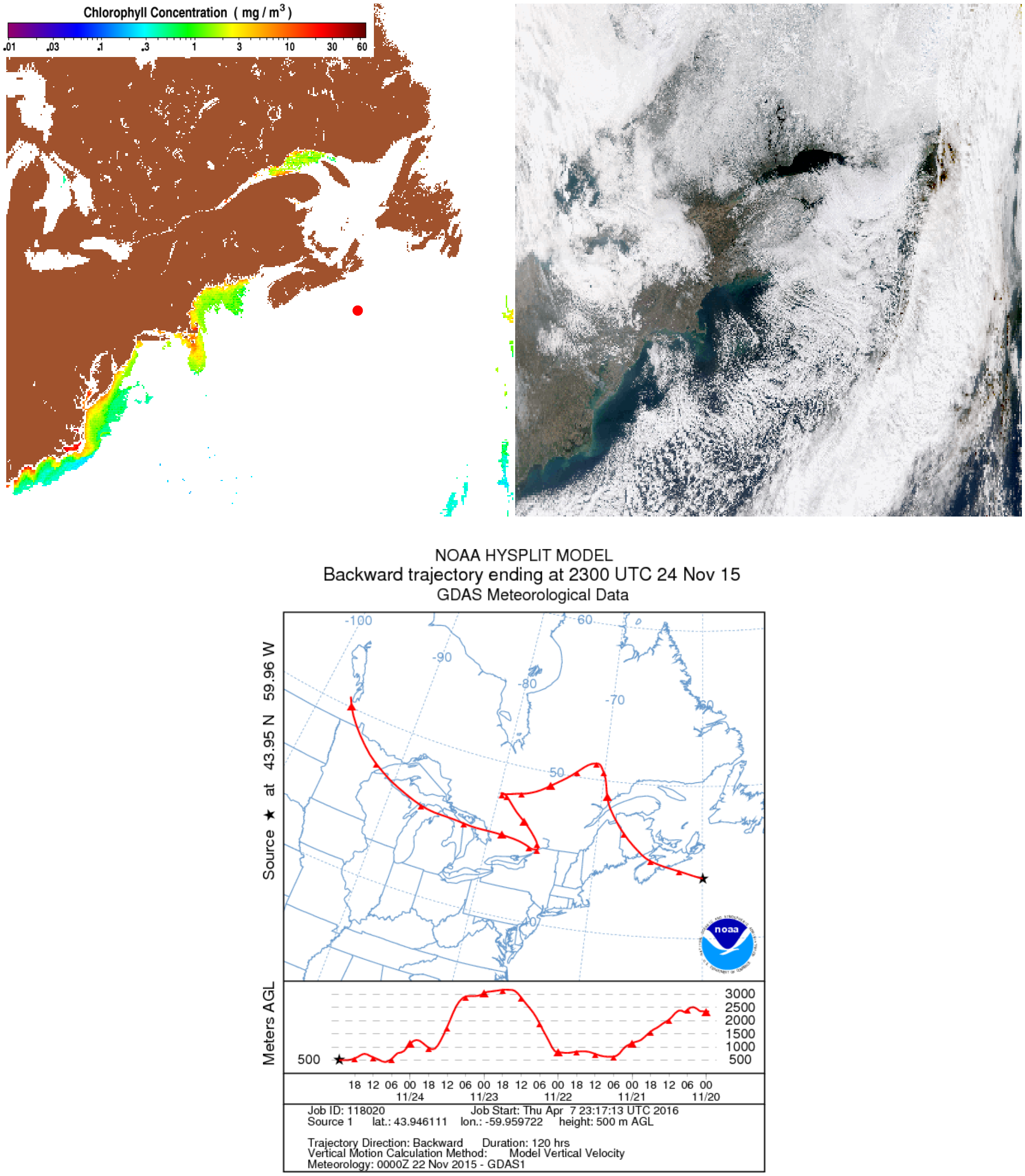

Figure 27. Chlorophyll-a (top left) and quasi true colour (top right) measured by the NASA VIIRS satellite and 5-day air mass back trajectory) (bottom for Sable Island on November 24, 2015

The spike on December 19 occurred at 14:00 UTC, where the measured $PM_{2.5}$ concentration was 26 µg m^{-3} (24-hour average = 20.60 µg m^{-3}). The chlorophyll-a and quasi true colour satellite images, as well as the 5-day air mass back trajectory for this spike are presented in Figure 28. Figure 28 shows the air mass moved through the Ohio Valley (industry and coal fired power stations) and southern NS before impacting Sable Island. The spike on December 9 may be due to LRT from the Ohio valley (Jeong et al., 2011; Gibson et al., 2013; Gibson et al., 2015) and continental outflow of PM from NS.

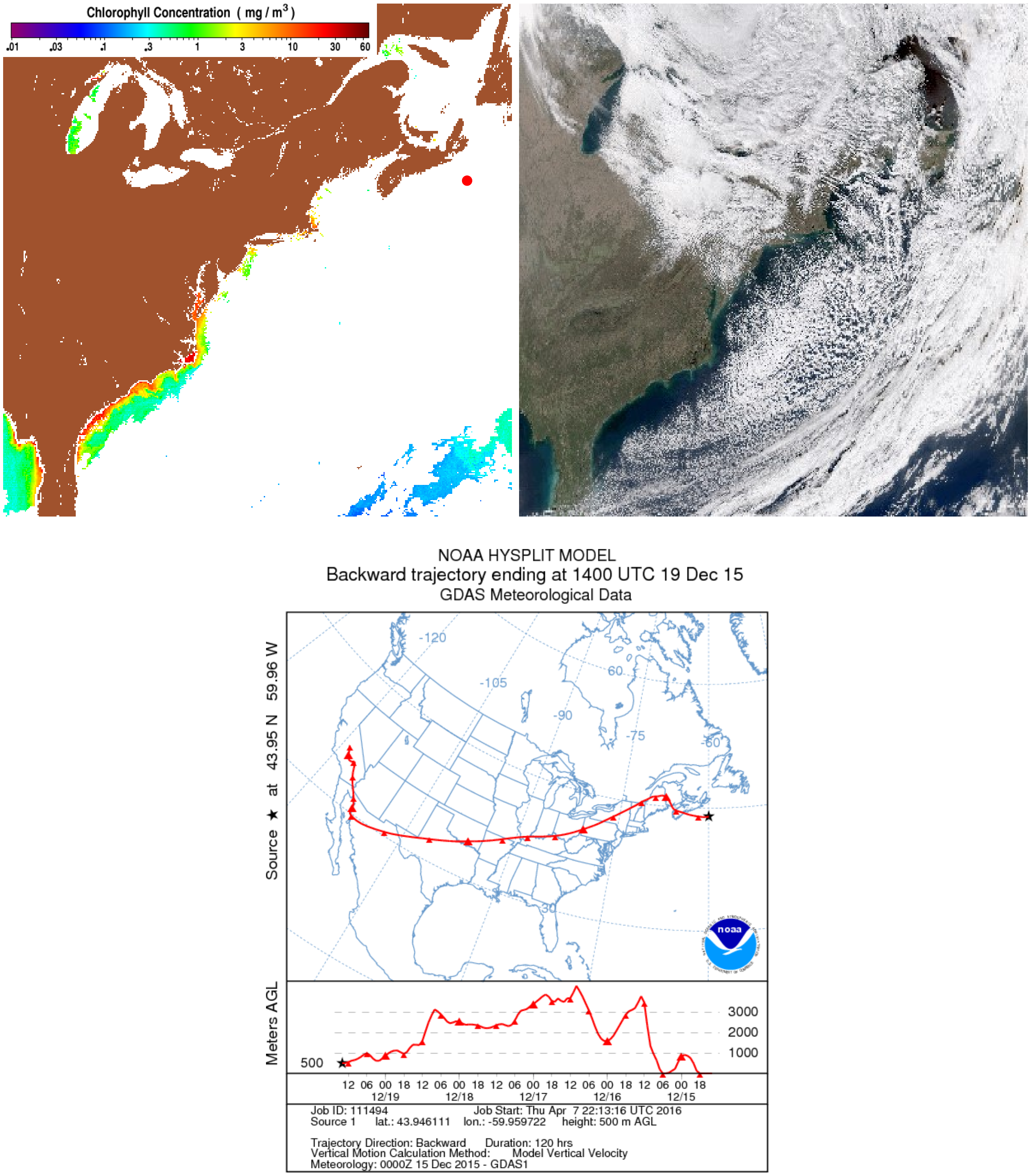

Figure 28. Chlorophyll-a (top left) and quasi true colour (top right) measured by the NASA VIIRS satellite and 5-day air mass back trajectory (bottom) for Sable Island on December 19, 2015

The four days with the least PM mass were also investigated using 5-day air mass back trajectories. The low PM mass on October 11 occurred at 14:00 UTC, where the measured $PM_{2.5}$ concentration was 9.5 μg m^{-3} (24-hour average = 10.56 μg m^{-3}). The chlorophyll-a and quasi true colour satellite images, as well as the 5-day air mass back trajectory for this spike are presented in Figure 29. As shown in Figure 29, the air mass originates from near the north pole and stays at an altitude of 3 000 m – 4 000 m until it reaches Quebec. Northern Canada is a region of low anthropogenic emissions (Gibson et al., 2013), which could explain the low PM mass.

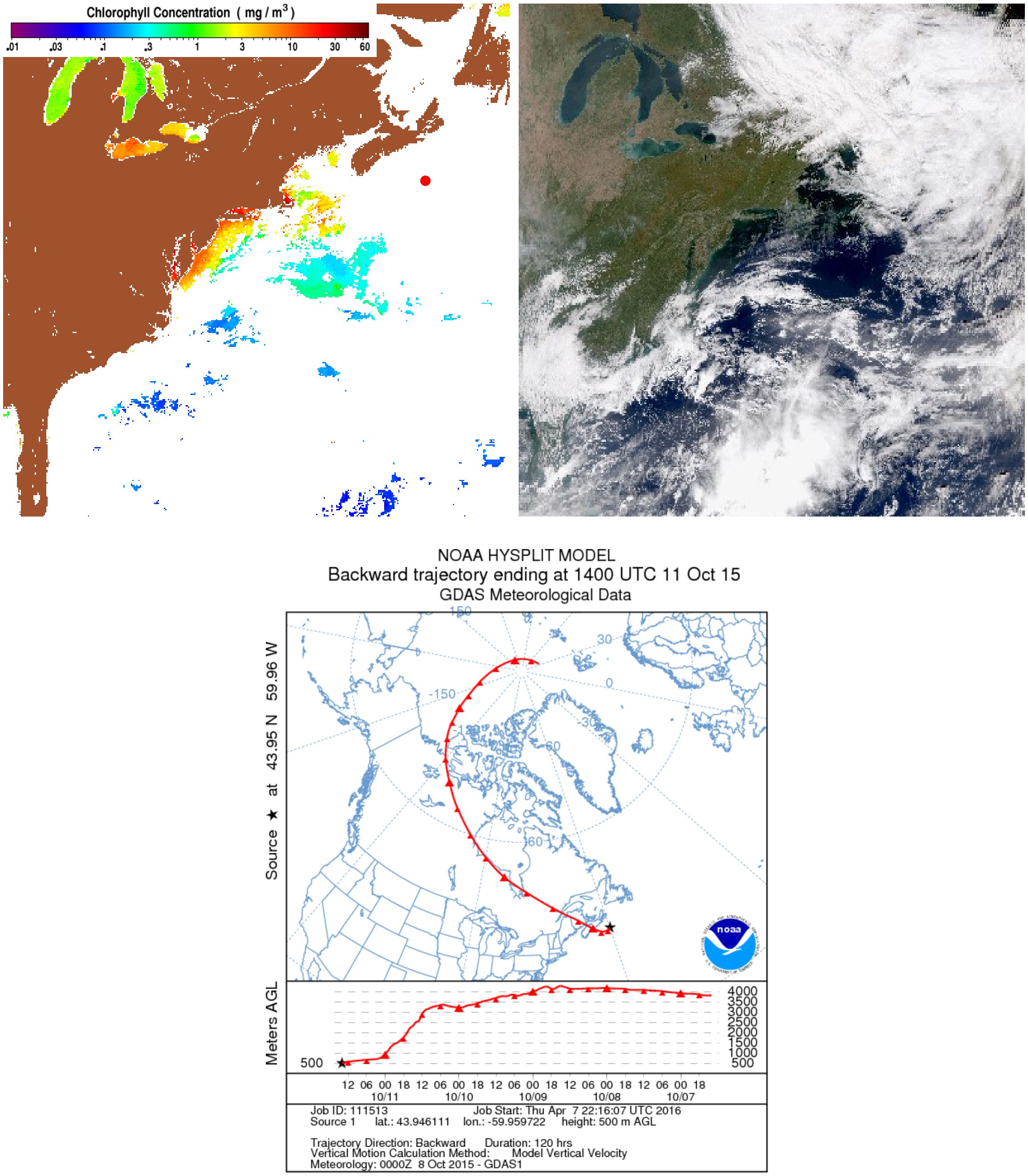

Figure 29. Chlorophyll-a (top left) and quasi true colour (top right) measured by the NASA VIIRS satellite and 5-day air mass back trajectory (bottom) for Sable Island on October 11, 2015

The low PM mass on October 19 occurred at 07:00 UTC, where the measured $PM_{2.5}$ concentration was 9.0 µg m^{-3} (24-hour average = 9.79 µg m^{-3}). The chlorophyll-a and quasi true colour satellite images, as well as the 5-day air mass back trajectory for this spike are presented in Figure 30. From Figure 30 it can be seen that his air mass is also from the north, indicating a clean air mass (Gibson et al., 2013). From the HYSPLIT vertical profile, the air mass altitude increases to 2 000 m before falling on to Sable Island. This may cause the air mass to entrain less surficial PM from the continent before impacting Sable Island.

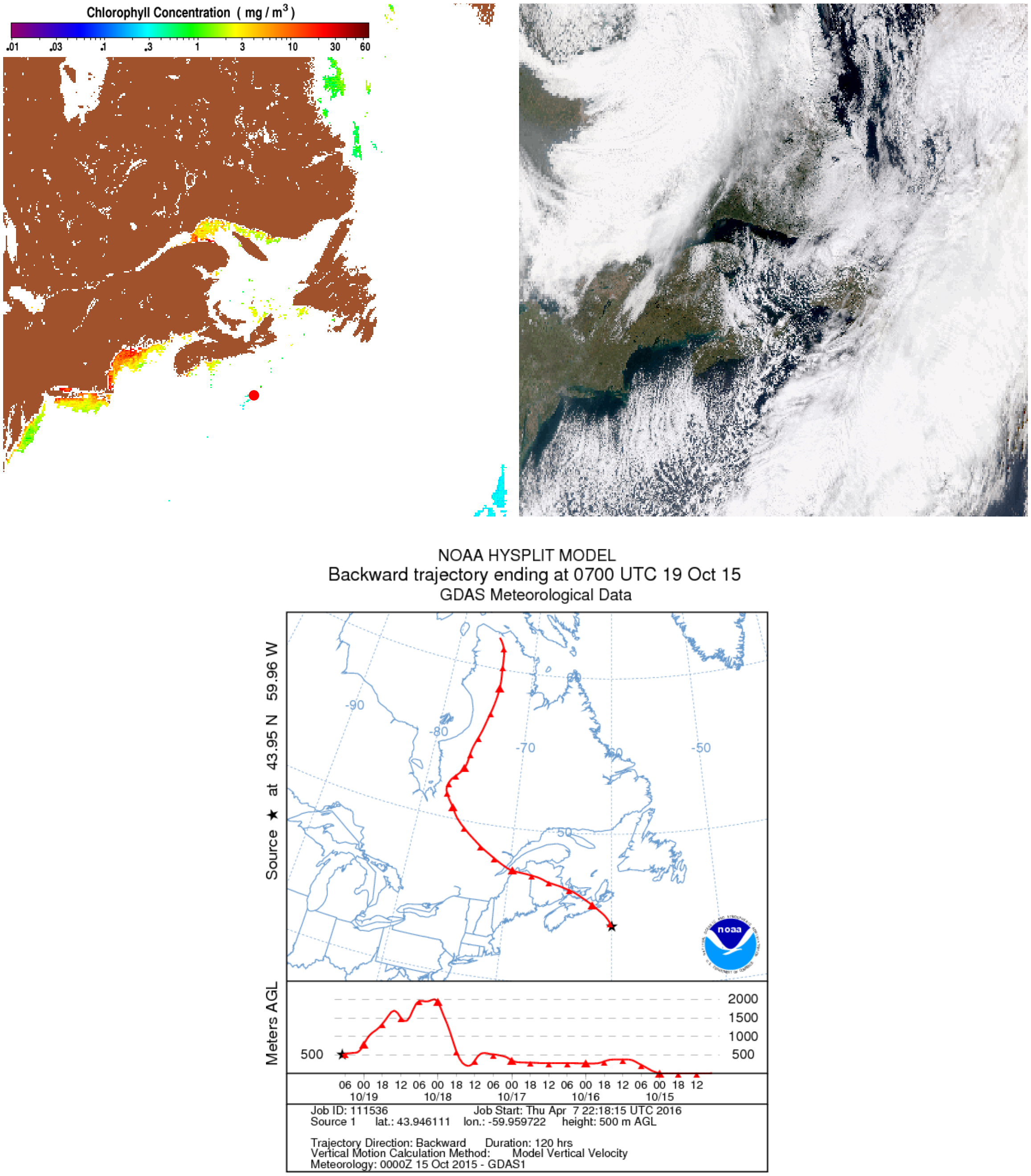

Figure 30. Chlorophyll-a (top left) and quasi true colour (top right) measured by the NASA VIIRS satellite and 5-day air mass back trajectory (bottom) for Sable Island on October 19, 2015

The low PM mass on November 4 occurred at 14:00 UTC, where the measured $PM_{2.5}$ concentration was 9.5 μg m^{-3} (24-hour average = 10.17 μg m^{-3}). The chlorophyll-a and quasi true colour satellite images, as well as the 5-day air mass back trajectory for this spike are presented in Figure 31. Again, the low PM mass is indicative of a clean air from the north (Gibson et al., 2013). The air mass vertical profile in Figure 31 shows the air mass reaching the surface before impacting Sable Island, PM in the air mass may have been scavenged by surface impact.

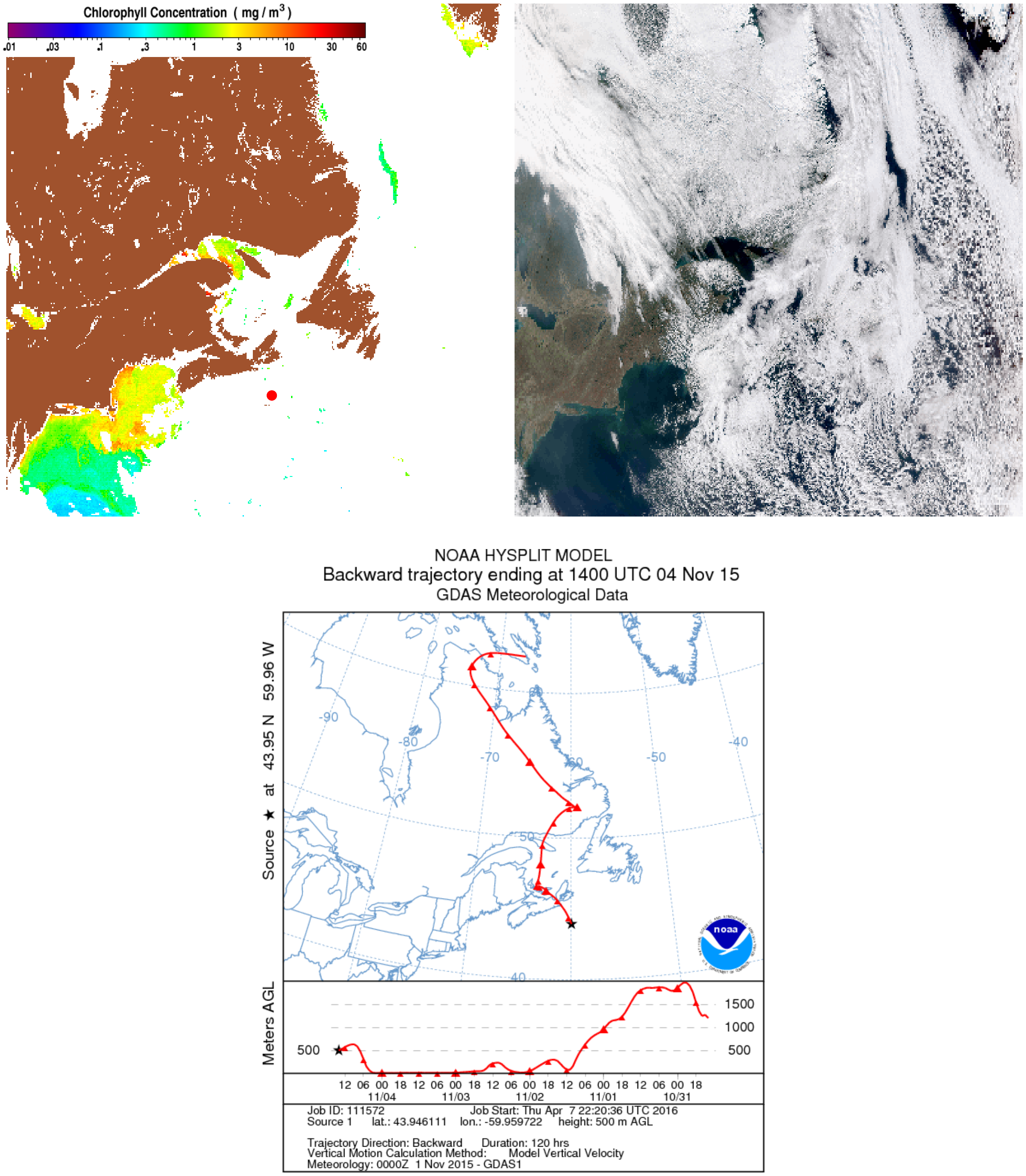

Figure 31. Chlorophyll-a (top left) and quasi true colour (top right) measured by the NASA VIIRS satellite and 5-day air mass back trajectory (bottom) for Sable Island on November 4, 2015

The low mass on November 20 occurred at 17:00 UTC where the measured $PM_{2.5}$ concentration was 10.0 $\mu g\ m^{-3}$ (24-hour average = 10.81 $\mu g\ m^{-3}$), The chlorophyll-a and quasi true colour satellite images, as well as the 5-day air mass back trajectory for this spike are presented in Figure 32. Again, the back trajectory in Figure 32 suggests the low PM mass is due to clean air from the north and a clean marine environment (Gibson et al., 2013).

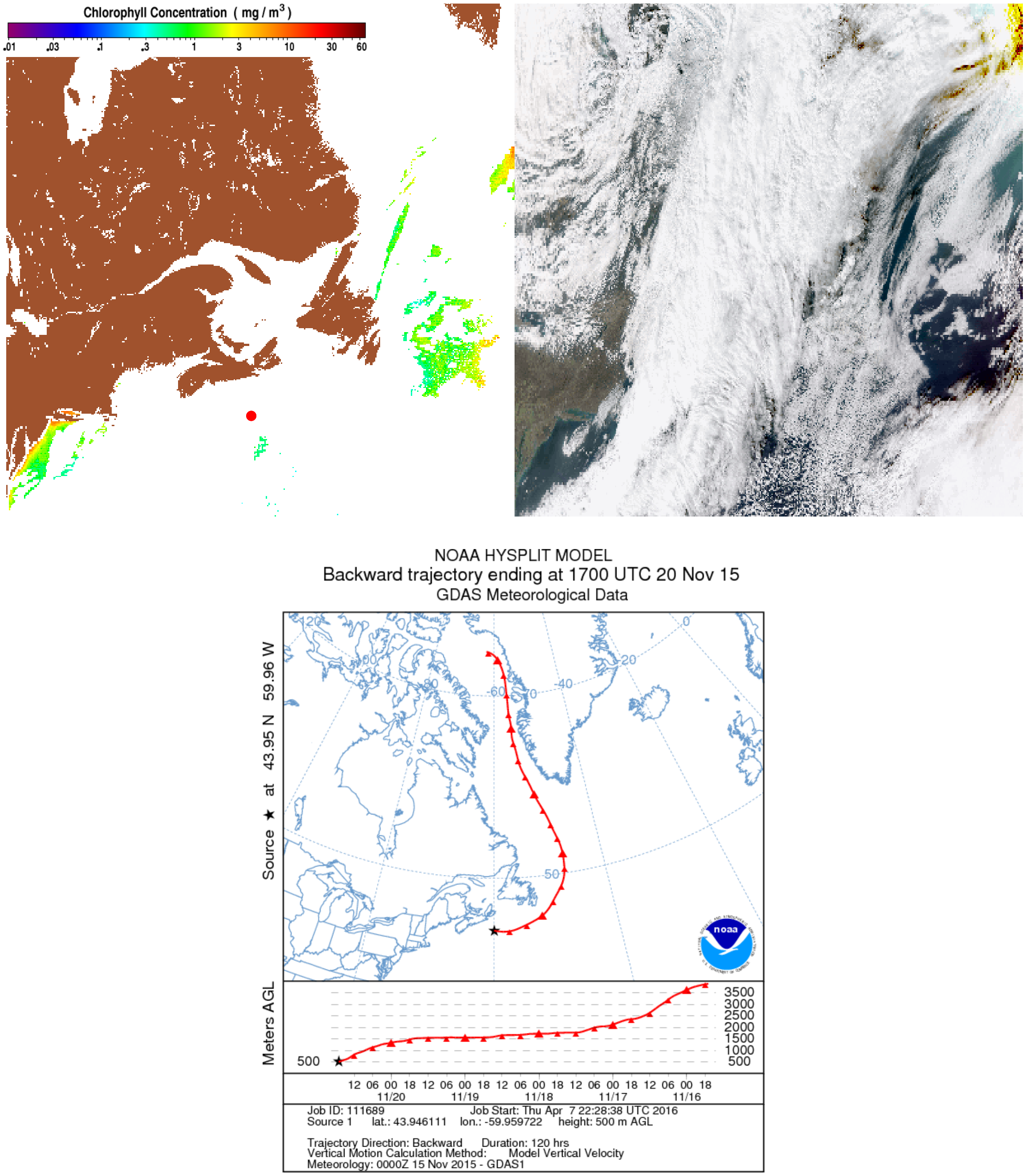

Figure 32. Chlorophyll-a (top left) and quasi true colour (top right) measured by the NASA VIIRS satellite and 5-day air mass back trajectory (bottom) for Sable Island on November 20, 2015

4.3 Ultrafine Particle Monitor Particle Number Counts

Table 3 contains the descriptive statistics for particle number counts for the six size channels of the TSI 3031 Ultrafine Particle Monitor model 3031.

Table 3. TSI 3031 Ultrafine Particle Monitor descriptive statistics.

Variable	**20-30 nm** ***[particle #/cm^3]***	**30-50 nm** ***[particle #/cm^3]***	**50-70 nm** ***[particle #/cm^3]***	**70-100 nm** ***[particle #/cm^3]***	**100-200 nm** ***[particle #/cm^3]***	**200-800 nm** ***[particle #/cm^3]***
n	2122	2122	2122	2122	2122	2122
n missing	88	88	88	88	88	88
Mean	343.1	336.9	179.5	143.47	168.2	25.574
St Dev	530.1	504.1	265.86	208.76	218.91	38.015
Min	0	0	0	0	0	0
25 pct	33.4	20.5	7.44	8.5	18.5	1.25
Median	158.6	159.5	100.25	82.38	120.88	13.75
75 pct	442.2	458.8	245.56	191.06	230.06	34.75
Max	10577.3	9588	4463.75	4195.5	4455.75	503
IQR	408.8	438.3	238.13	182.56	211.56	33.5
Data Completeness	96.02%	96.02%	96.02%	96.02%	96.02%	96.02%
Data Completeness (annual)	24.66%	24.66%	24.66%	24.66%	24.66%	24.66%

From Table 3 it can be seen that the data completeness over the operation period for the particle number counts, in the range 20-30, 30-50, 50-70, 70-100, 100-200, and 200-800 nm was 96.02%, and for the entire year was only 24.66%. The missing data during the operation period is due to an unknown instrument error causing the instrument to enter standby mode and stop logging on December 8. Data logging was resumed on December 10. The low annual data completeness is due to the instrument only being installed on October 1, 2015. It can also been seen from Table 2 that the mean (min : max units = #) particle number counts, in the various size ranges, were as follows: 20-30 nm = 343.1 (0 : 10577.3 #), 30-50 nm = 336.9 (0 : 9588 #), 50-70 nm = 179.5 (0: 4463.75 #), 70-100 = 143.47 nm (0 : 4195.5 #), 100-200 nm = 168.2 (0 : 4455.75 #) and 200-800 nm = 25.57 (0 : 503 #) respectively. The larger mean particle number count for the smaller particle size fits the theory of gas-to-particle conversion to form many ‘small’ particles, e.g. ocean emissions of DMS, isoprene, and halogens reacting to form secondary aerosols and cloud condensation nuclei particles (Pierce & Adams, 2006). In addition, fresh combustion particles can also contribute to the ‘small’ particle size range of 20-50 nm (Krecl et al., 2015). After this size range the number drops considerably, again following the theory of particle physics; particles in aged air masses coagulate to form fewer larger particles, or are washed out by rain (Franklin et al., 2014). Daily and hourly time series analysis will investigate the peaks and valleys in ultrafine particle concentrations to aid in the determination their source. Moreover, UFPs have very little corresponding mass, virtually undetectable using a mass concentration instrument such as a TSI DRX presented in this thesis (Poluboyarov, Korotaeva, & Andryushkova, 2000; Wang et al., 2009; Zhu et al., 2002). Figure 33 provides a non-parametric visualization of the ultrafine (<100 nm) and accumulation mode particle number counts sampled on Sable Island in the form of a box-whisker plot.

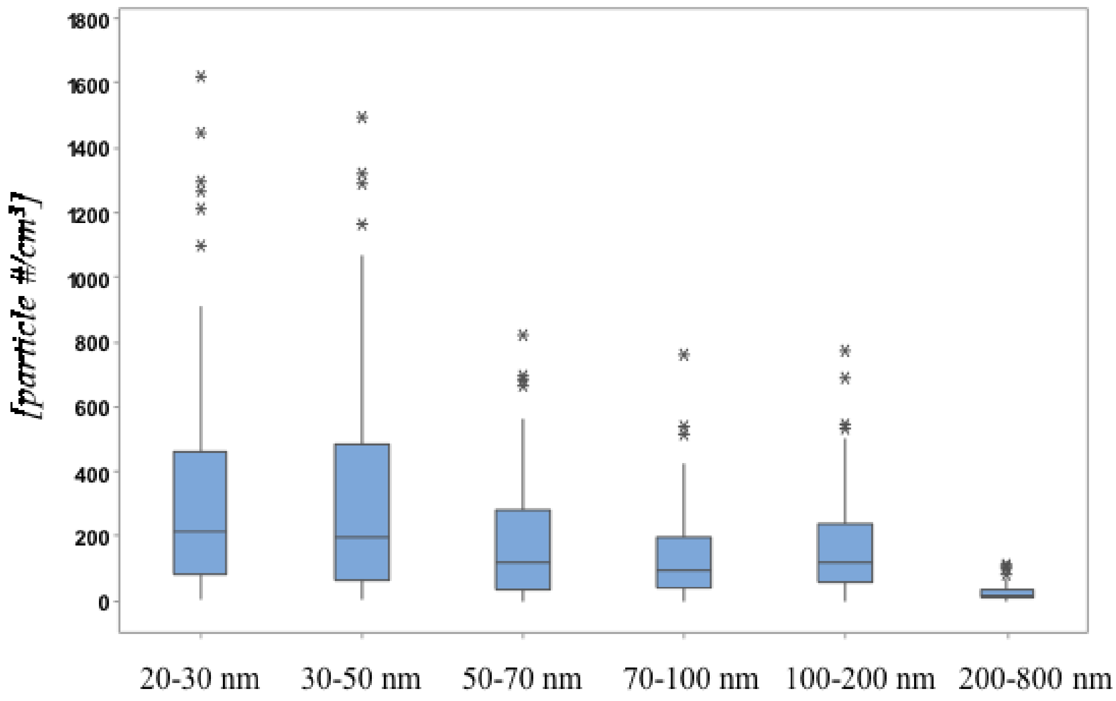

Figure 33. Boxplots of particle number counts for the Ultrafine Particle Monitor model 3031 six size channels.

In Figure 33, the box represents the IQR or the 25th and 75th percentiles, respectively and the line is the median. The stars represent outliers, data points that are greater than 1.5 times the IQR from the 75th percentile. The lower and upper whiskers represent the range of data points within 1.5 times the IQR from the 25th and 75th percentiles, respectively. From Figure 33, it can be seen that the 20-30 nm and 30-50 nm sizes contribute most to particle counts. Figure 33 also shows a general trend of particle number decreasing as size increases. This agrees with the theory of fresh, smaller particles agglomerating to form fewer larger particles. (IPCC, 2013)

Presented in Figure 34 is a pollution rose for UFP number count measure by the UFPM 3031.

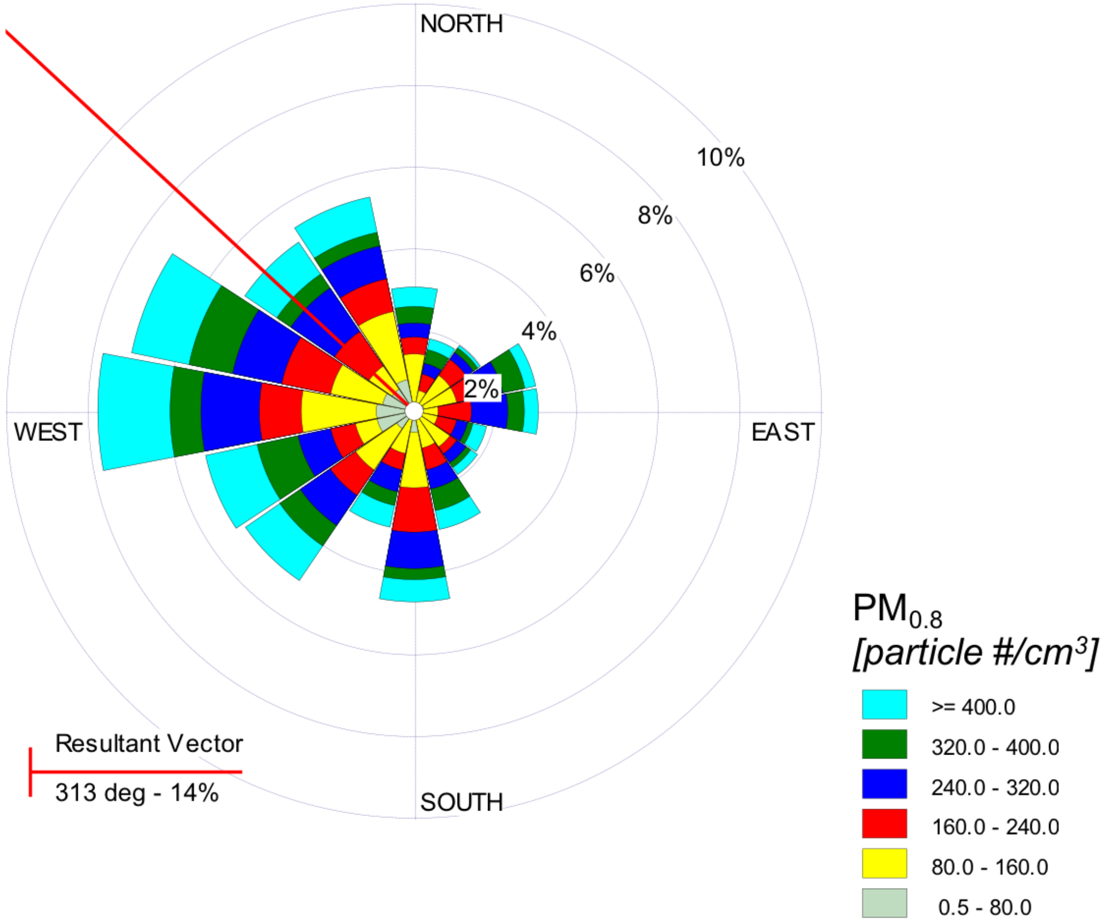

Figure 34. Pollution rose for Sable Island UFP number counts measured by the UFPM 3031.

The pollution rose in Figure 34 shows the majority of UFPs originate from the W, NW, and N directions. UFPs from the W could be a result of fresh combustion from the O&G platforms around Sable Island. UFPs from the NW and N may be from continental outflow, however, UFPs can grow up to 20 nm hr^{-1} (Kulmala et al., 2004) indicating the UFPs are likely from oceanic emissions of VOCs.

Figure 35 presents a daily time series plot of UFP number counts measured by the UFPM 3031.

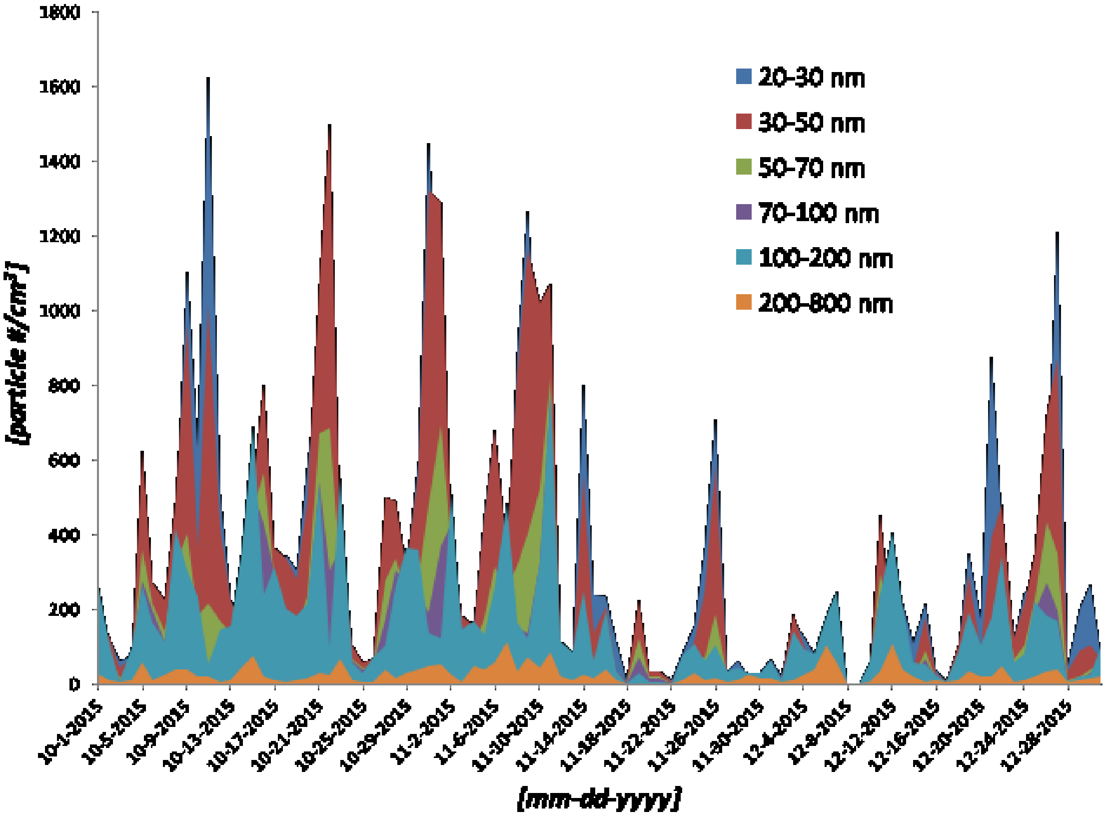

Figure 35. Daily time series of the UFPM 3031 six size channel particle number counts.

Figure 35 shows that the 20-30 nm and 30-50 nm size fractions contributed significantly to spikes in UFP number counts whereas the 200-800 nm size contributed very little. It is also noted that the 20-30 nm and 30-50 nm sizes seem to be inversely correlated with the

100-200 nm and 200-800 nm size fractions e.g. the 20-30 nm and 30-50 nm spikes on October 11, 21, and November 9 correspond to low readings in the 100-200 nm and 200-800 nm size fractions.

HYSPLIT and the NASA Terra MODIS, Aqua MODIS, and VIIRS satellites were used to investigate potential source regions for the four largest spikes observed in the UFPM 3031 daily time series. The first spike investigated occurred on October 11 at 08:00 UTC where the 20-30, 30-50, 50-70, 70-100, 100-200, and 200-800 nm number counts reached 2112, 1209, 191, 8, 45, and 22 particles cm^{-3}, respectively. The 5-day air mass back trajectory for this spike is presented in Figure 36, the chlorophyll-a and quasi true colour satellite images are presented in Figure 29. In Figure 36 the air mass originates in northern Canada and moves from Hudson's Bay through to Nova Scotia while reaching altitudes of 4000 m, before impacting Sable Island. The back trajectory shows the travel time from Nova Scotia to Sable Island to be roughly 6-8 hours for this air mass. Cloud cover over Nova Scotia and Sable Island make it difficult to speculate on marine emissions as a source, although it is expected that fresh combustion from the continent would age during transport and contribute higher particle number counts for particles >100 nm. Chemical speciation of the particle number counts observed would provide greater insight as to the source of this spike.

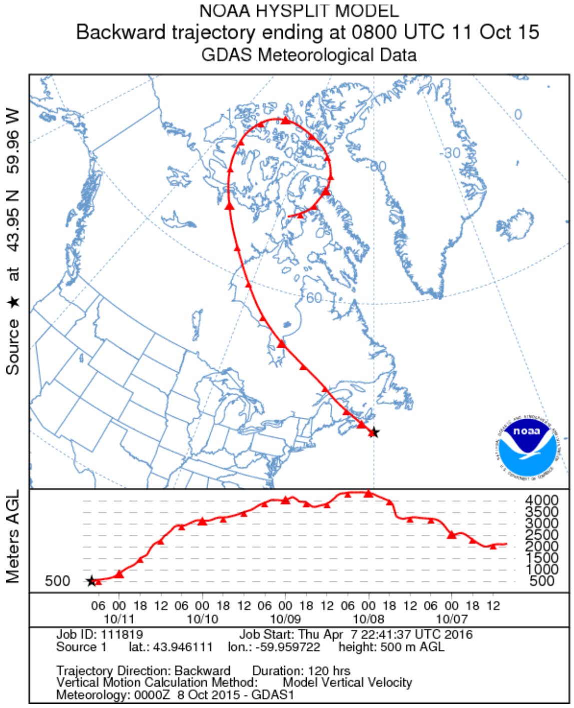

Figure 36. 5-day air mass back trajectory for Sable Island on October 11, 2015

The spike on October 22 occurred at 01:00 UTC where the 20-30, 30-50, 50-70, 70-100, 100-200, and 200-800 nm number counts reached 2947, 2079, 604, 126, 93, and 12 particles cm^{-3}, respectively. The chlorophyll-a and quasi true colour satellite images, as well as the 5-day air mass back trajectory for this spike are presented in Figure 37. From Figure 37 it can be seen that the air mass follows a similar trajectory as that for October 11. The high particle number counts for the 20-30 and 30-50 nm size fractions would suggest marine emissions as the source, however, the elevated number counts in the 50-70, 70-100, and 100-200 nm size fractions could indicate combustion sources from the continent if the particle growth rate was less that 10 nm hr^{-1} (Kulmala et al., 2004). The presence of phytoplankton around Sable Island cannot be determined from these satellite observations.

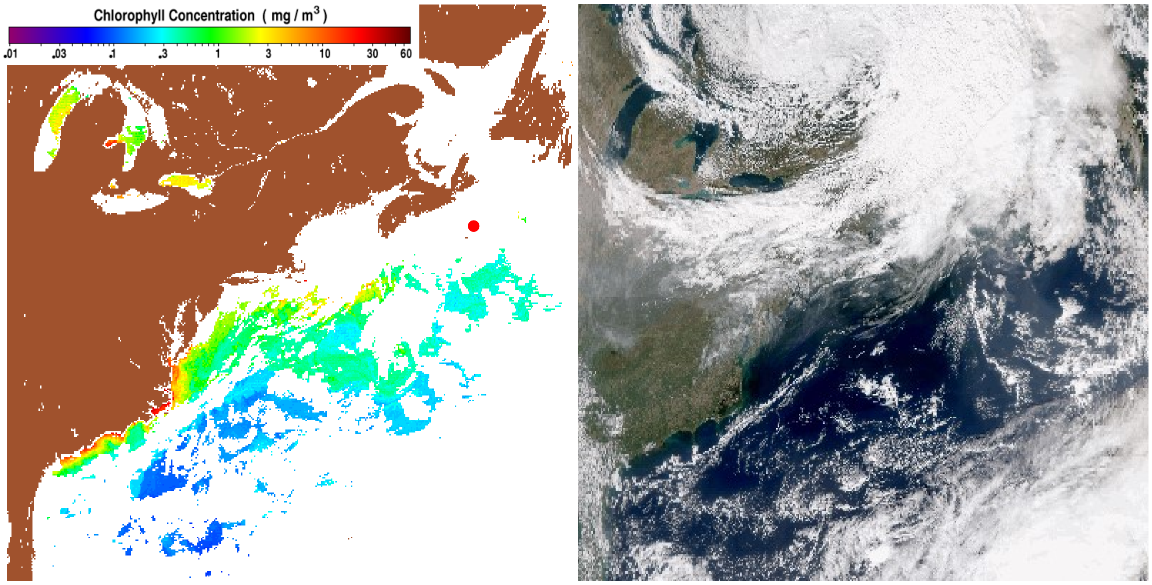

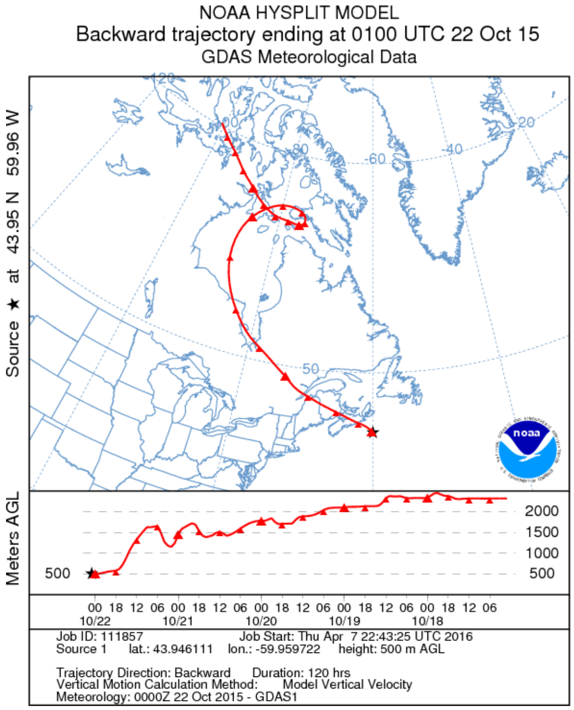

Figure 37. Chlorophyll-a (left) and quasi true colour (right) around Sable Island on October 22, 2015 measured by the NASA VIIRS satellite

The spike on October 31 occurred at 12:00 UTC where the 20-30, 30-50, 50-70, 70-100, 100-200, and 200-800 nm number counts reached 1889, 1321, 307, 37, 83, and 52 particles cm^{-3}, respectively. The chlorophyll-a and quasi true colour satellite images, as well as the 5-day air mass back trajectory for this spike are presented in Figure 38. Although the air mass in Figure 38 originates over the continent and is only over the marine environment for a short time, satellite images show the presence of phytoplankton around Nova Scotia, providing evidence that this spike may be a result of biogenic marine emissions from phytoplankton. Studies from the Scotian Shelf region show that a second, subsidiary phytoplankton bloom occurs in the fall period further supporting this hypothesis (Craig et al., 2015; Li, 2014; Li & Harrison, 2008).

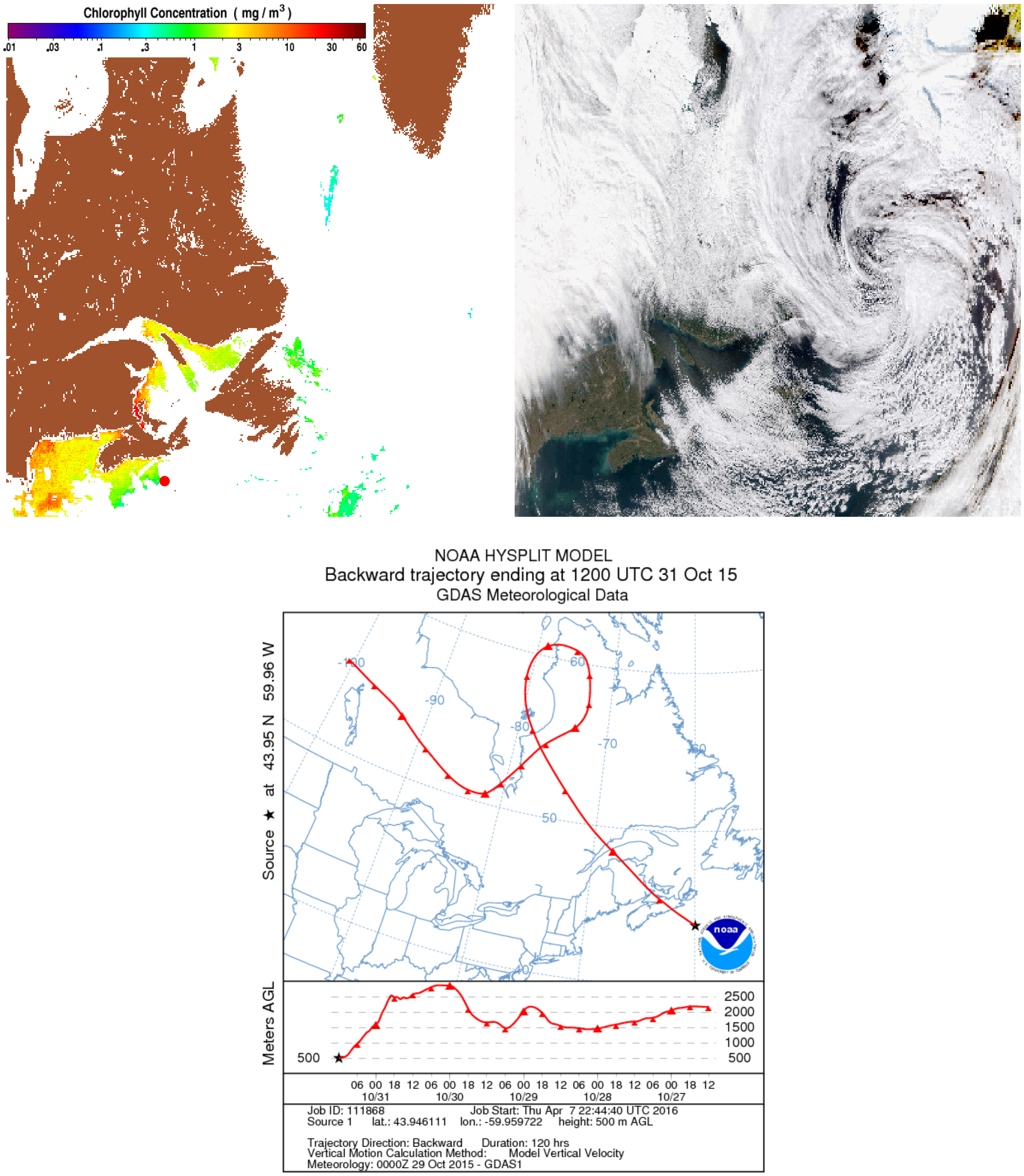

Figure 38. Chlorophyll-a (top left) and quasi true colour (top right) measured by the NASA VIIRS satellite and 5-day air mass back trajectory (bottom) for Sable Island on October 31, 2015

The spike on December 27 occurred at 21:00 UTC where the 20-30, 30-50, 50-70, 70-100, 100-200, and 200-800 nm number counts reached 2939, 1338, 381, 323, 372, and 3 particles cm^{-3}, respectively. The chlorophyll-a and quasi true colour satellite images, as well as the 5-day air mass back trajectory for this spike are presented in Figure 39. As shown in the Figure 39 back trajectory, this air mass was over the ocean for approximately 30 hours before impacting Sable Island. If the slowest particle growth rate reported by Kulmala et al. (2004) is assumed (1 nm hr^{-1}) the particles in the 20-30 nm size fraction could not have originated from the continent. This would suggest this spike in 20-30 nm particles is associated with gas-to-particle conversion from marine emissions. However, phytoplankton presence around Nova Scotia and Sable Island cannot be confirmed with satellite observations due to cloud cover.

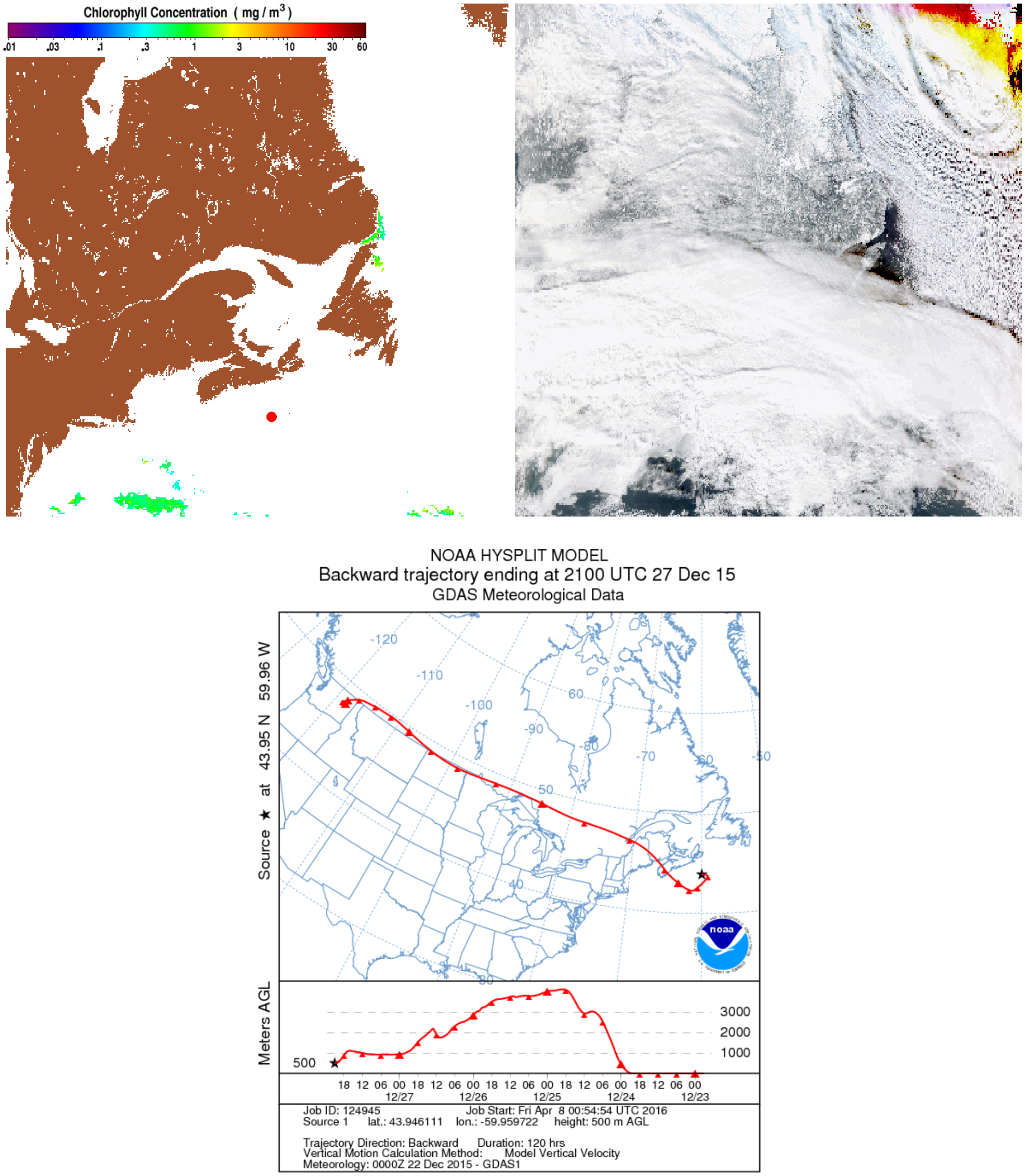

Figure 39. Chlorophyll-a (top left) and quasi true colour (top right) measured by the NASA VIIRS satellite and 5-day air mass back trajectory (bottom) for Sable Island on December 27, 2015

The four days with the lowest particle number counts were also investigated using HYSPLIT. The low on October 25 occurred at 11:00 UTC where the 20-30, 30-50, 50-70, 70-100, 100-200, and 200-800 nm number counts were all 0 particles cm^{-3}, respectively. The chlorophyll-a and quasi true colour satellite images, as well as the 5-day air mass back trajectory for this spike are presented in Figure 40. In Figure 40 it can be seen that the air mass originate in the clean northern region of Canada (Gibson et al. 2013) and moves over the ocean before impacting Sable Island. Cloud cover in the satellite images makes it difficult to speculate on phytoplankton presence, but fall blooms are known to occur in this period (Craig et al., 2015; Li, 2014; Li & Harrison, 2008).

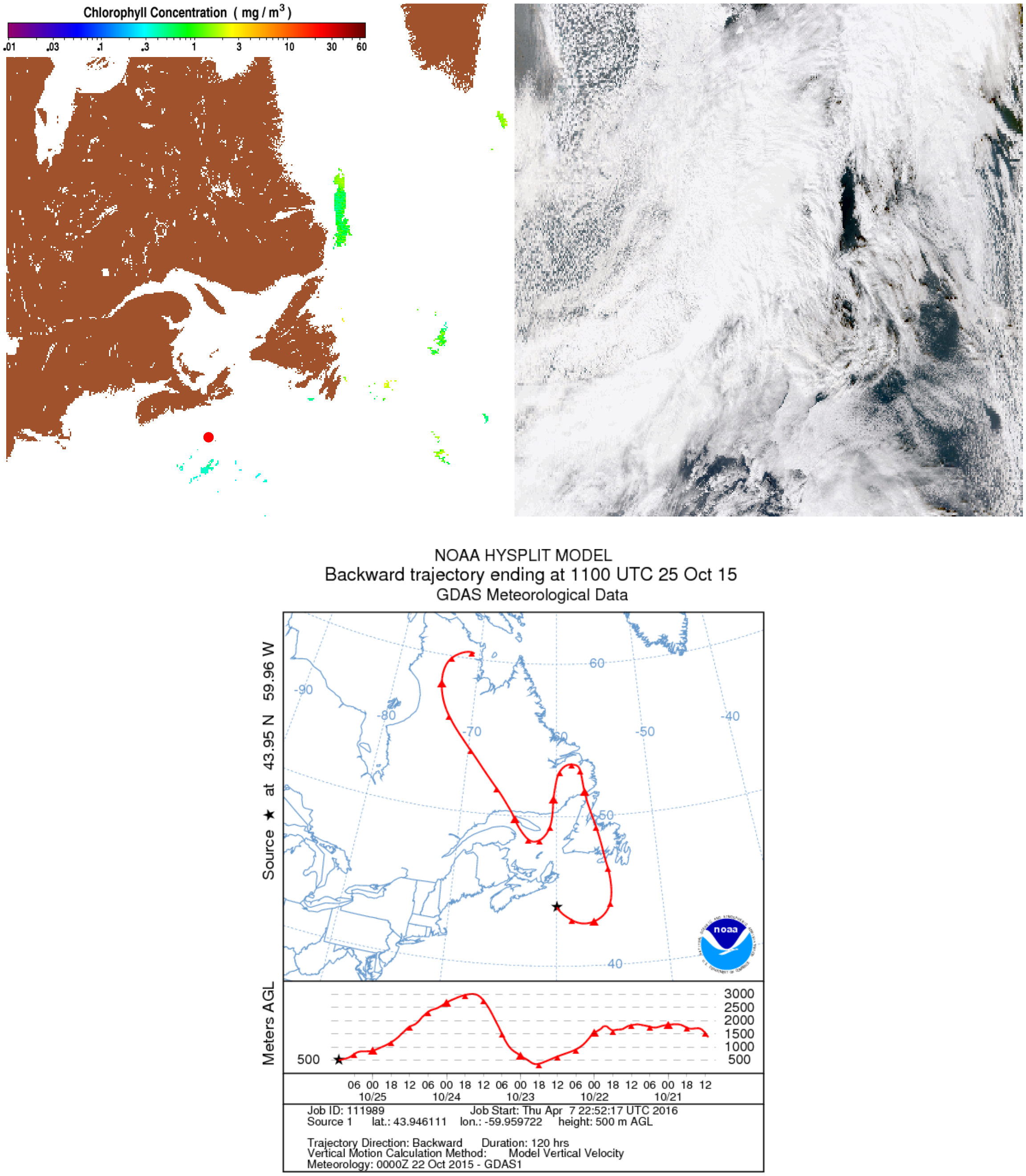

Figure 40. Chlorophyll-a (top left) and quasi true colour (top right) measured by the NASA VIIRS satellite and 5-day air mass back trajectory (bottom) for Sable Island on October 25, 2015

The low on November 13 occurred at 12:00 UTC where the 20-30, 30-50, 50-70, 70-100, 100-200, and 200-800 nm number counts were all 0 particles cm^{-3}, respectively. The chlorophyll-a and quasi true colour satellite images, as well as the 5-day air mass back trajectory for this spike are presented in Figure 41. Figure 41 shows phytoplankton growth around southern Nova Scotia, however phytoplankton around Sable Island cannot be seen due to cloud cover. It is expected that phytoplankton presence would produce UFPs, however this is not the case.

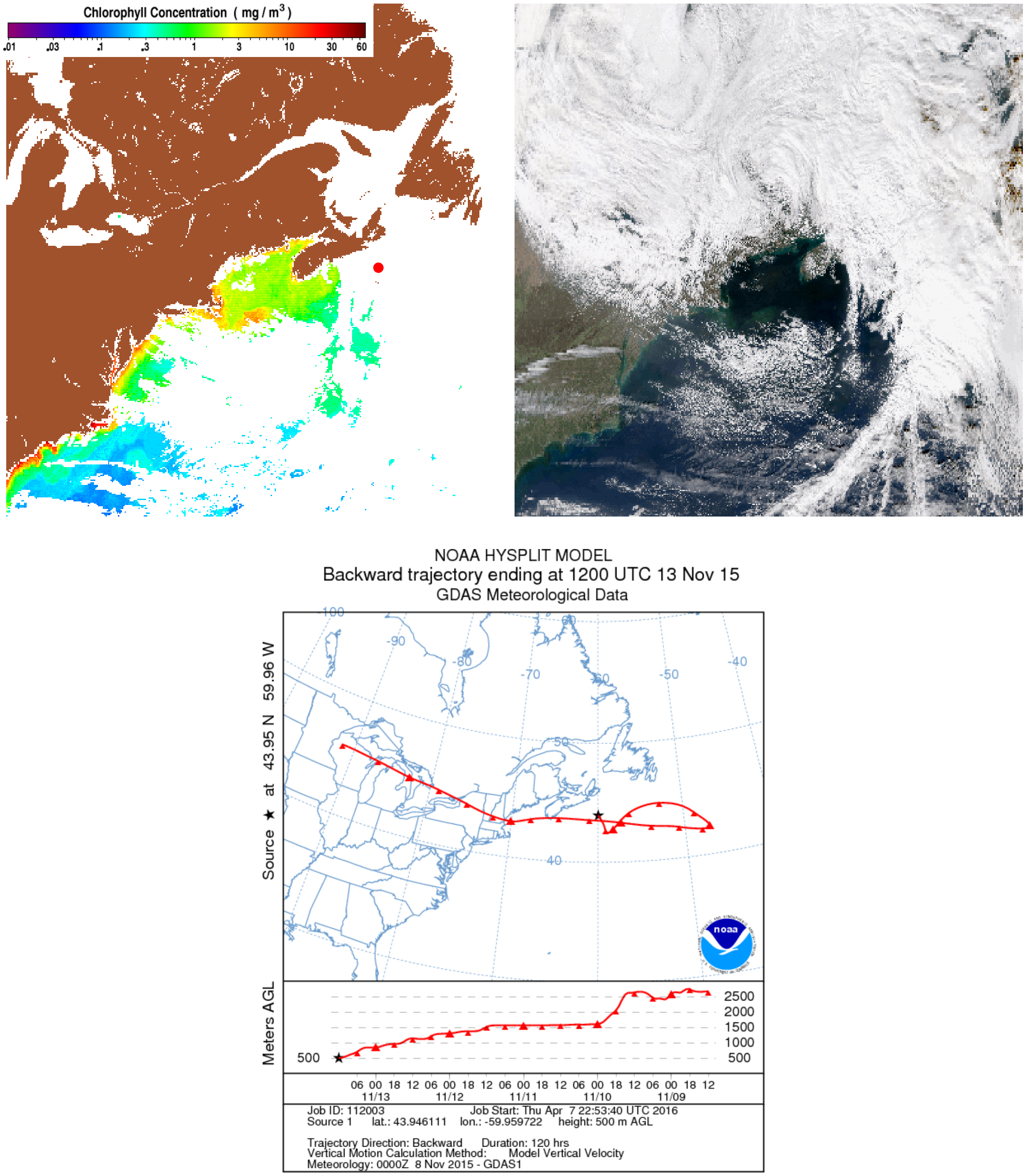

Figure 41. Chlorophyll-a (top left) and quasi true colour (top right) measured by the NASA VIIRS satellite and 5-day air mass back trajectory (bottom) for Sable Island on November 13, 2015

The low on November 22 occurred at 12:00 UTC where the 20-30, 30-50, 50-70, 70-100, 100-200, and 200-800 nm number counts were all 0 particles cm^{-3}, respectively. The chlorophyll-a and quasi true colour satellite images, as well as the 5-day air mass back trajectory for this spike are presented in Figure 42. From Figure 42 it can be seen that the air mass is entirely marine, likely consisting of sea salt particles which would be too large for the UFPM to detect. The satellite images reveal no useful information regarding phytoplankton blooms around Sable Island.

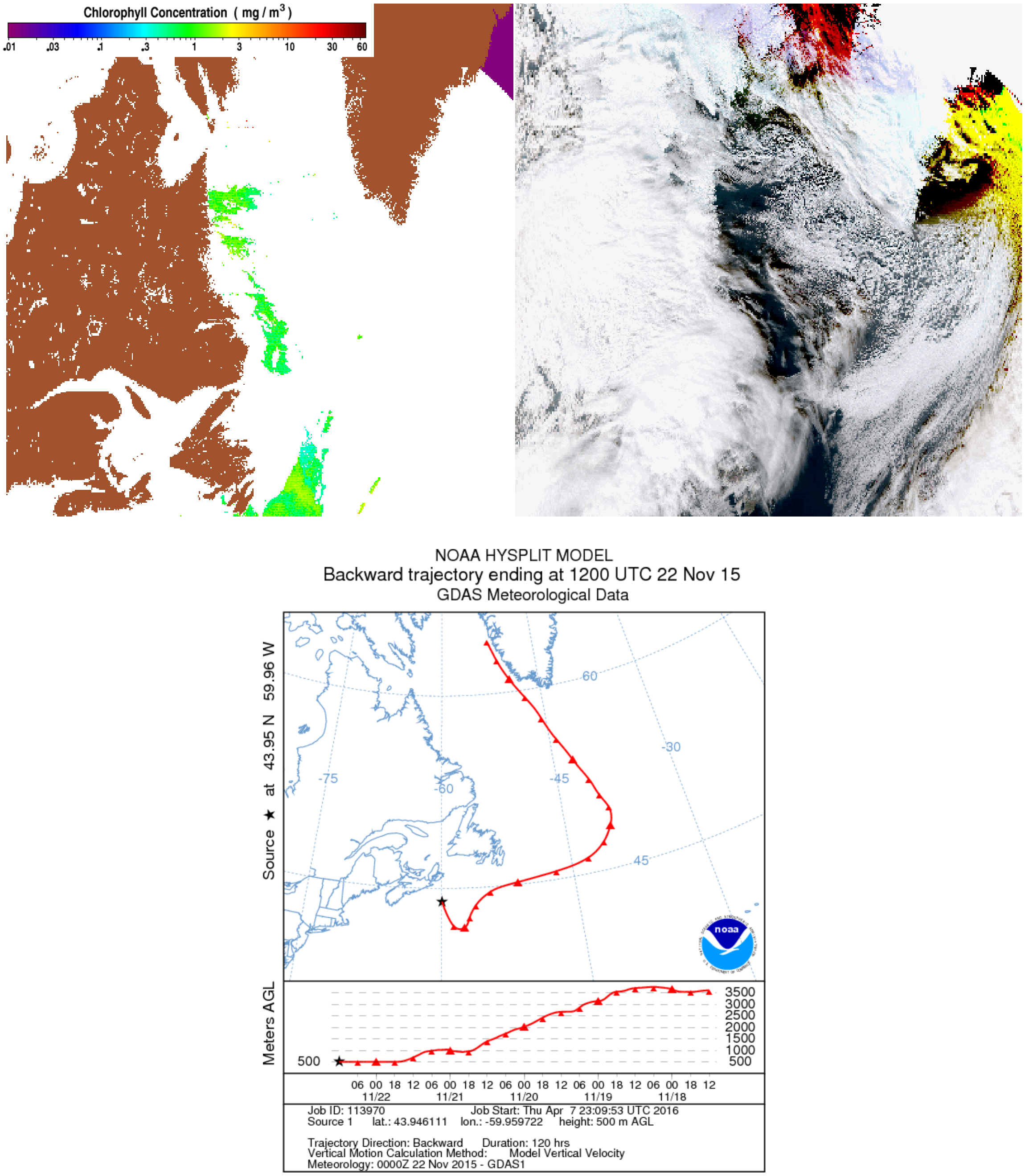

Figure 42. Chlorophyll-a (top left) and quasi true colour (top right) measured by the NASA VIIRS satellite and 5-day air mass back trajectory (bottom) for Sable Island on November 22, 2015

The low on December 17 occurred at 12:00 UTC where the 20-30, 30-50, 50-70, 70-100, 100-200, and 200-800 nm number counts were all 0 particles cm^{-3}, respectively. The chlorophyll-a and quasi true colour satellite images, as well as the 5-day air mass back trajectory for this spike are presented in Figure 43. Figure 43 shows the air mass impacting the surface (ocean) before Sable Island. This would suggest particle deposition in the ocean and very little particle mass and number reaching Sable Island. Again, cloud cover shown in the satellite images make it impossible to determine phytoplankton presence around Sable Island.

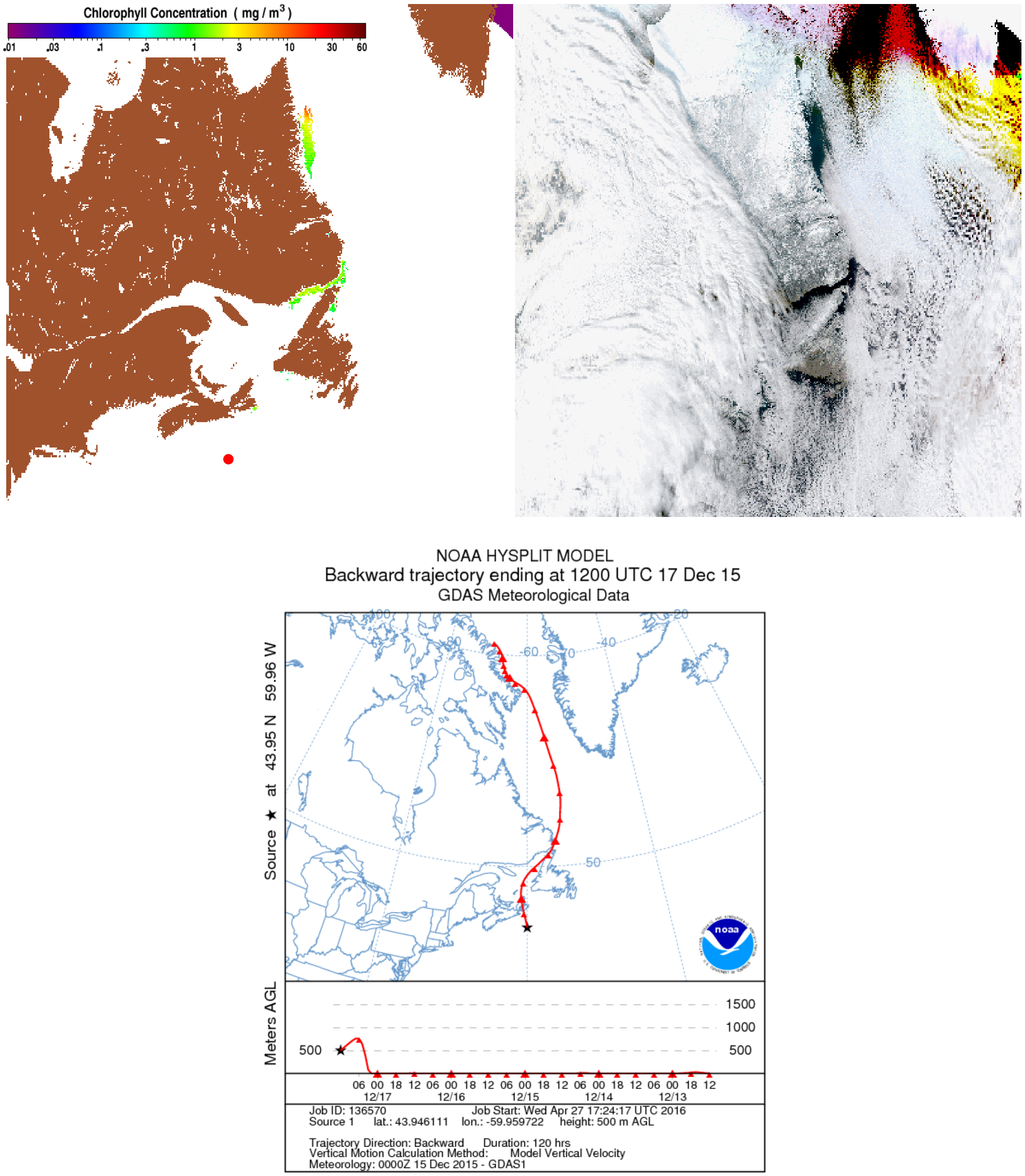

Figure 43. Chlorophyll-a (top left) and quasi true colour (top right) measured by the NASA VIIRS satellite and 5-day air mass back trajectory (bottom) for Sable Island on December 17, 2015

4.4 Aerodynamic Particle Sizer Number Counts

Table 4 contains the descriptive statistics and data completeness for 2015 for the TSI 3321 Aerodynamic Particle Sizer model 3321 particle number counts in the size fractions below 1.0, 2.5, 4.0 10.0 and 20.0 microns. These size fractions were created from averaging the relevant 56 size fractions. The size bins were chosen to correspond with the TSI DustTrak DRX particle mass concentration size fractions.

Table 4. TSI 3321 Aerodynamic Particle Sizer descriptive statistics

Variable	**PM_1** ***[particle #/cm^3]***	**$PM_{2.5}$** ***[particle #/cm^3]***	**PM_4** ***[particle #/cm^3]***	**PM_{10}** ***[particle #/cm^3]***	**PM_{20}** ***[particle #/cm^3]***
n	427	427	427	427	427
n missing	1783	1783	1783	1783	1783
Mean	12.52	15.71	15.92	15.95	15.95
StDev	10.83	12.94	13.11	13.15	13.15
Min	0.97	1.02	1.03	1.03	1.03
25 pct	5.94	7.19	7.29	7.29	7.29
Median	8.81	11.24	11.41	11.53	11.53
75 pct	15.69	19.81	20.14	20.21	20.21
Max	63.94	70.15	71.55	72.14	72.14
IQR	9.75	12.62	12.85	12.92	12.92
Data Completeness	19.32%	19.32%	19.32%	19.32%	19.32%
Data Completeness (annual)	5.75%	5.75%	5.75%	5.75%	5.75%

From Table 4 it can be seen that the data completeness over the operation period for the APS $PM_{1/2.5/4.0/10/20}$ size fraction particle number counts was 19.32%, and for the entire year was only 5.75%. The lack of data for 95.4% of the year was due to the instrument only being installed on October 1, 2015 and some instrument malfunctions faced after deployment. The uninterrupted power supply for the APS failed on October 14, 2015 and the laptop that logs APS data froze on two occasions. Following these failures, it was arranged for Environment Canada employees stationed on the island to perform weekly checks and data downloads on all instruments. I provided step-by-step instructions on how to download data for each instrument in the air chemistry shed and quick system checks to determine if each instrument is functioning properly. During my visit to the island from January 27 – February 1, 2016, the laptop used for logging APS data was replaced. Since implementing the weekly instrument checks and replacing the laptop, no data loss issues have been reported.

It can also been seen from Table 4 that the mean (min : max units = #) for the APS $PM_{1/2.5/4.0/10/20}$ size fraction particle number counts were 1 µm = 12.52 (0.97 : 63.94 #), 2.5 µm = 15.71 (1.02 : 70.15 #), 4.0 µm = 15.92 (1.03: 71.55 #), 10 µm = 15.95 (1.03 : 72.14 #) and 20 µm = 15.95 (1.03 : 72.14 #) respectively. The increase in particle number counts observed from the fine mode (1 µm) to 20 µm fits with the theory that sea spray will impact the larger particle size fractions and this increase is unlikely associated with fresh combustion or O&G operations. Time series analysis will investigate the peaks and valleys in the APS $PM_{1/2.5/4.0/10/20}$ particle number counts to aid in the determination their source. Figure 44 below is a non-parametric visualization of the APS $PM_{1/2.5/4/10/20}$ particle number counts.

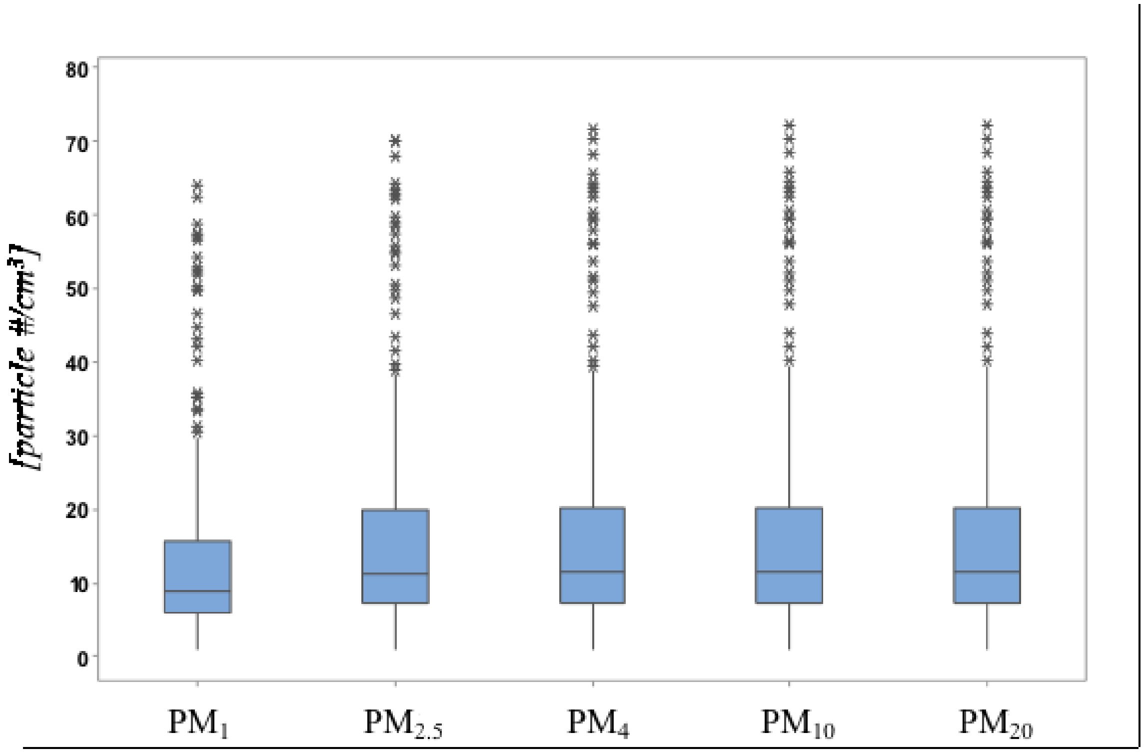

Figure 44. Boxplots of particle number counts from the Aerodynamic Particle Sizer

In Figure 44, the box represents the IQR or the 25th and 75th percentiles, respectively and the line is the median. The stars represent outliers, data points that are greater than 1.5 times the IQR from the 75th percentile. The lower and upper whiskers represent the range of data points within 1.5 times the IQR from the 25th and 75th percentiles, respectively. There are numerous outliers in each size fraction, this may be due to missing data caused by the back-up battery failure. Figure 45 below shows a pollution rose for the APS $PM_{2.5}$ particle number counts.

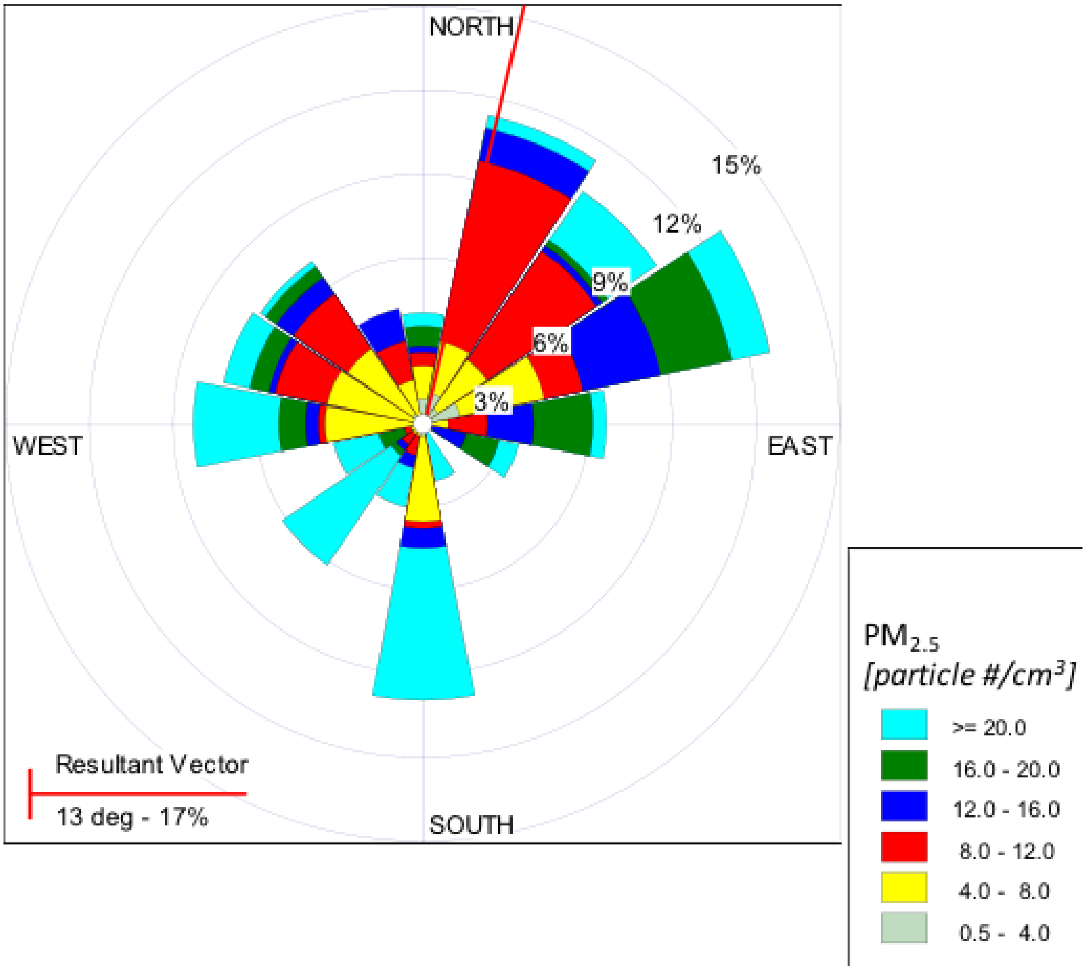

Figure 45. Pollution rose for Sable Island PM$_{2.5}$ particle number counts measured by the APS 3321.

Figure 45 shows that winds were mainly from the NE while the APS was sampling, with significant winds and particle number counts from the south and west. Figure 46 shows daily time series data for 52 particle size channels measured by the APS.

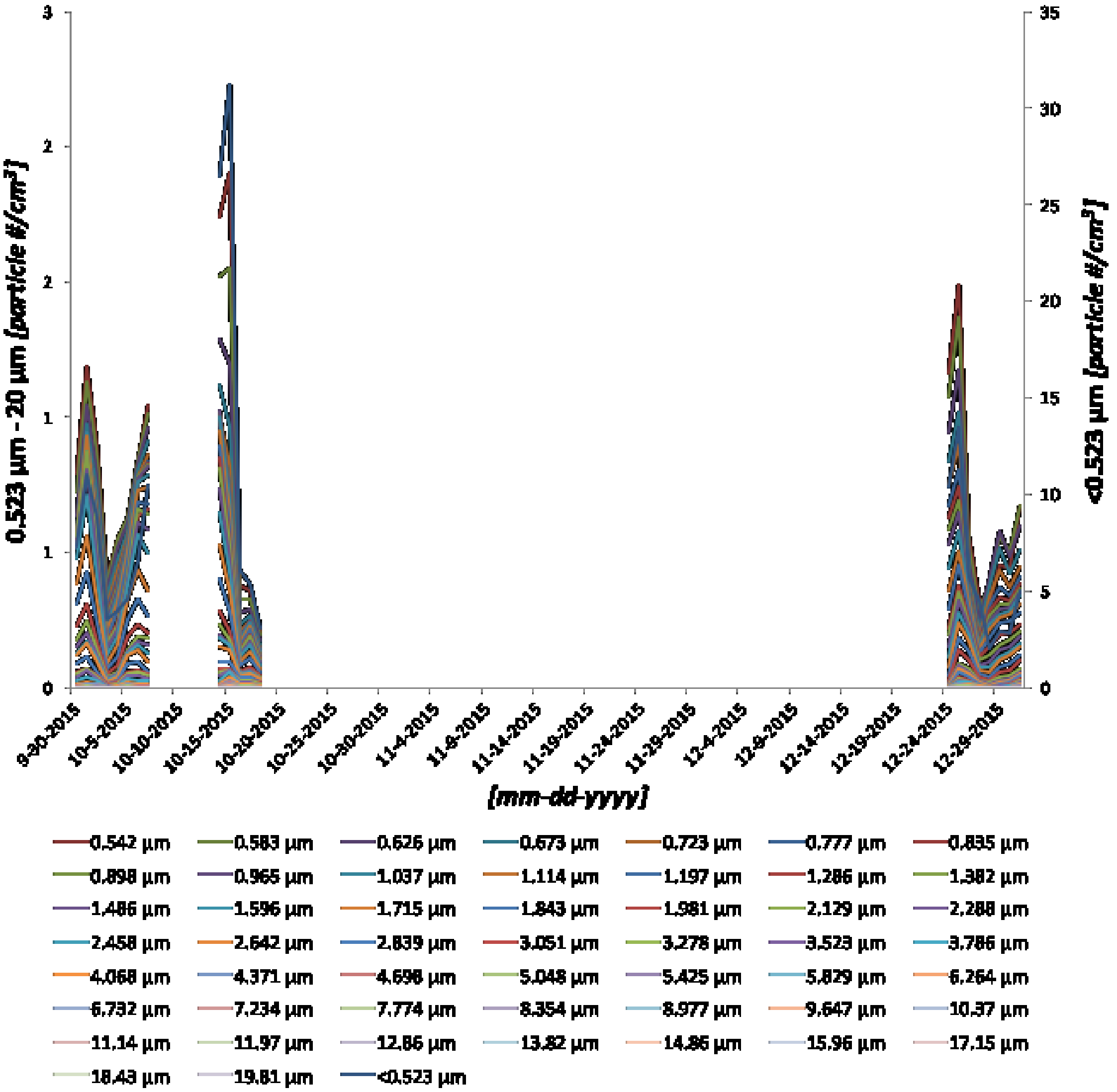

Figure 46. Daily time series of particle number counts for the APS 3321 52 size channels.

The daily time series for the APS in Figure 46 shows missing particle number count data related to laptop issues and a faulty back up battery, however, the three spikes observed were investigated using HYSPLIT and the NASA Terra MODIS, Aqua MODIS, and VIIRS satellites. The first spike occurred on October 1 at 14:00 UTC where particle number counts for the <0.523 μm size fraction reached 15 particles cm^{-3} . The particle number count for all other size fractions totalled 22 particles cm^{-3}. The chlorophyll-a and quasi true colour satellite images, as well as the 5-day air mass back trajectory for this spike are presented in Figure 47. The trajectory in Figure 47 is almost entirely marine, therefore the source for this spike is likely sea spray. Also, the satellite observations show no phytoplankton present in the air mass trajectory which suggests no biogenic marine emissions contributing to this spike.

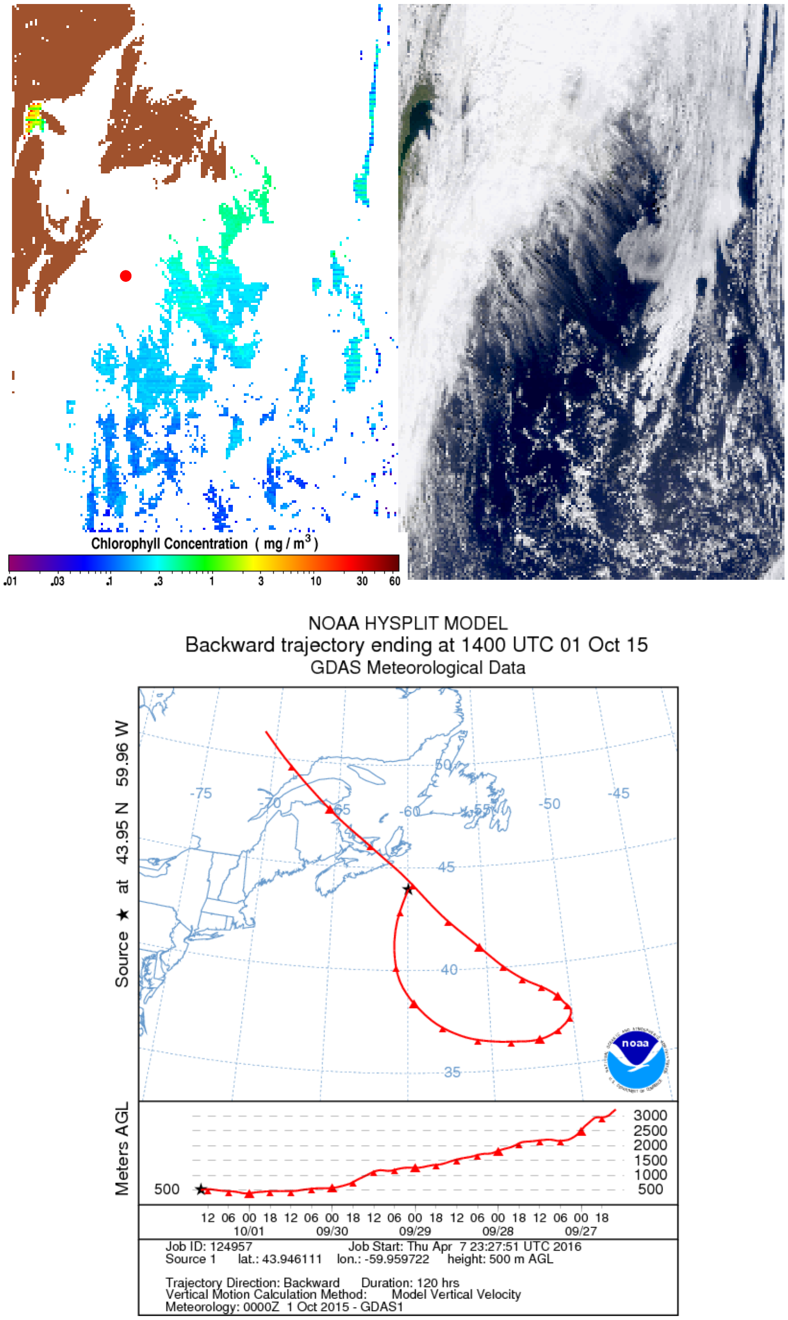

Figure 47. Chlorophyll-a (top left) and quasi true colour (top right) measured by the NASA Aqua TERRA satellite and 5-day air mass back trajectory (bottom) for Sable Island on October 1, 2015

The spike on October 15 occurred at 04:00 UTC where particle number counts for the <0.523 µm size fraction reached 50 particles cm^{-3}. The particle number count for all other size fractions totalled 19 particles cm^{-3}. The 5-day air mass back trajectory for this spike are presented in Figure 48, the chlorophyll-a and quasi true colour images are presented in Figure 24. The air mass in Figure 48 moves through the NE US (known for industry, coal combustion, and agriculture) (Jeong et al., 2011; Gibson et al., 2013) and appears to pass over the O&G platforms near Sable Island Figure 25. The spike on October 15 may be due to LRT from NE US, sea spray, or O&G operations near Sable Island.

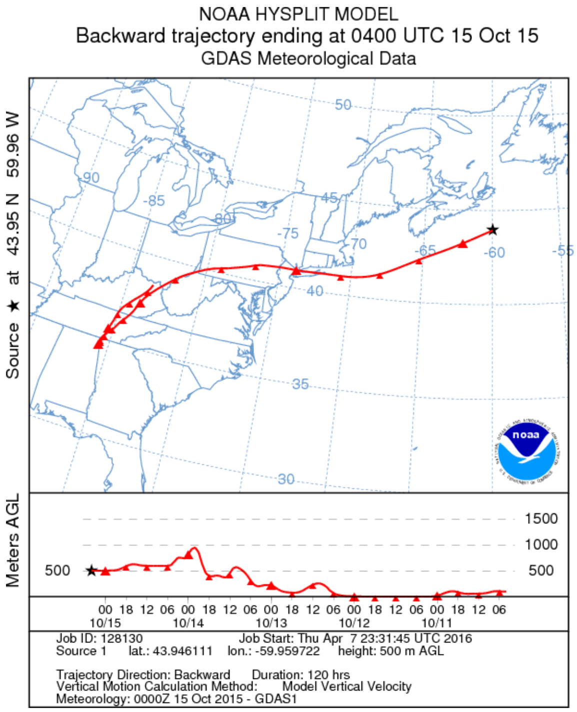

Figure 48. 5-Day air mass back trajectory (bottom) for Sable Island on October 15, 2015

The spike on December 25 occurred at 22:00 UTC where particle number counts for the <0.523 µm size fraction reached 22 particles cm^{-3} . The particle number count for all other size fractions totalled 33.42 particles cm^{-3}. The chlorophyll-a and quasi true colour satellite images, as well as the 5-day air mass back trajectory for this spike are presented in Figure 49. The long trajectory in Figure 49 indicates a fast moving air mass which could indicate high sea surface wind speeds, resulting in re-entrained sand/surface dust and/or sea spray contributing to the coarse mode particle counts. The trajectory shows the air mass moving through the Quebec-Windsor corridor (industrial sources) (Gibson et al., 2013) and the NE US before impacting Sable, which suggests LRT may be the source for the spike on December 25, 2015.

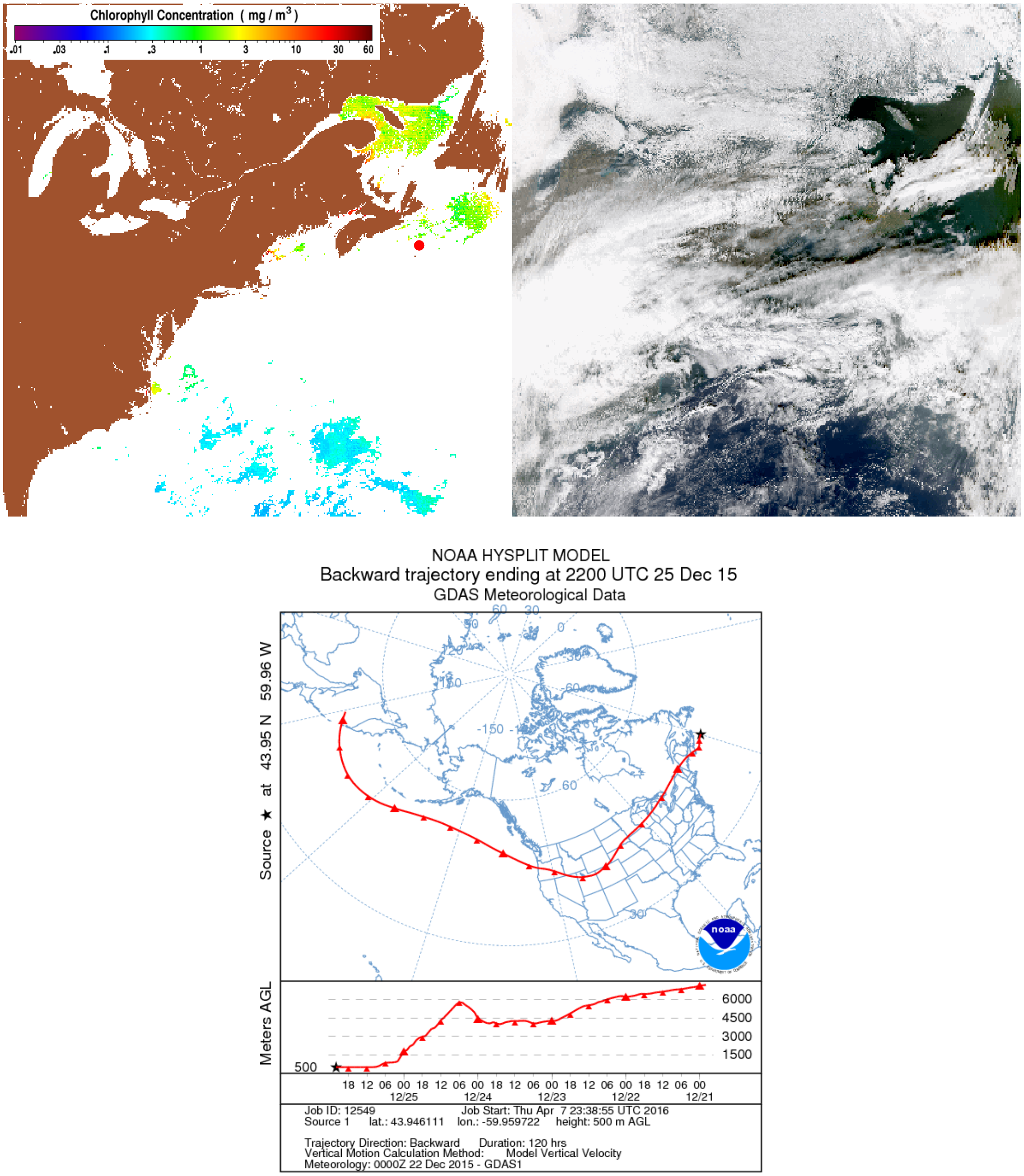

Figure 49. Chlorophyll-a (top left) and quasi true colour (top right) measured by the NASA VIIRS satellite and 5-day air mass back trajectory (bottom) for Sable Island on December 25, 2015

The first low occurred on October 3 at 02:00 UTC where particle number counts for the <0.523 μm size fraction reached 2 particles cm^{-3} . The particle number count for all other size fractions totalled 2 particles cm^{-3}. The chlorophyll-a and quasi true colour satellite images, as well as the 5-day air mass back trajectory for this spike are presented in Figure 50. This is clearly a completely marine air mass impacting Sable on October 3. Low wind speed (short trajectory) means little wave action and wave generated particles, supported by the low particle number observed.

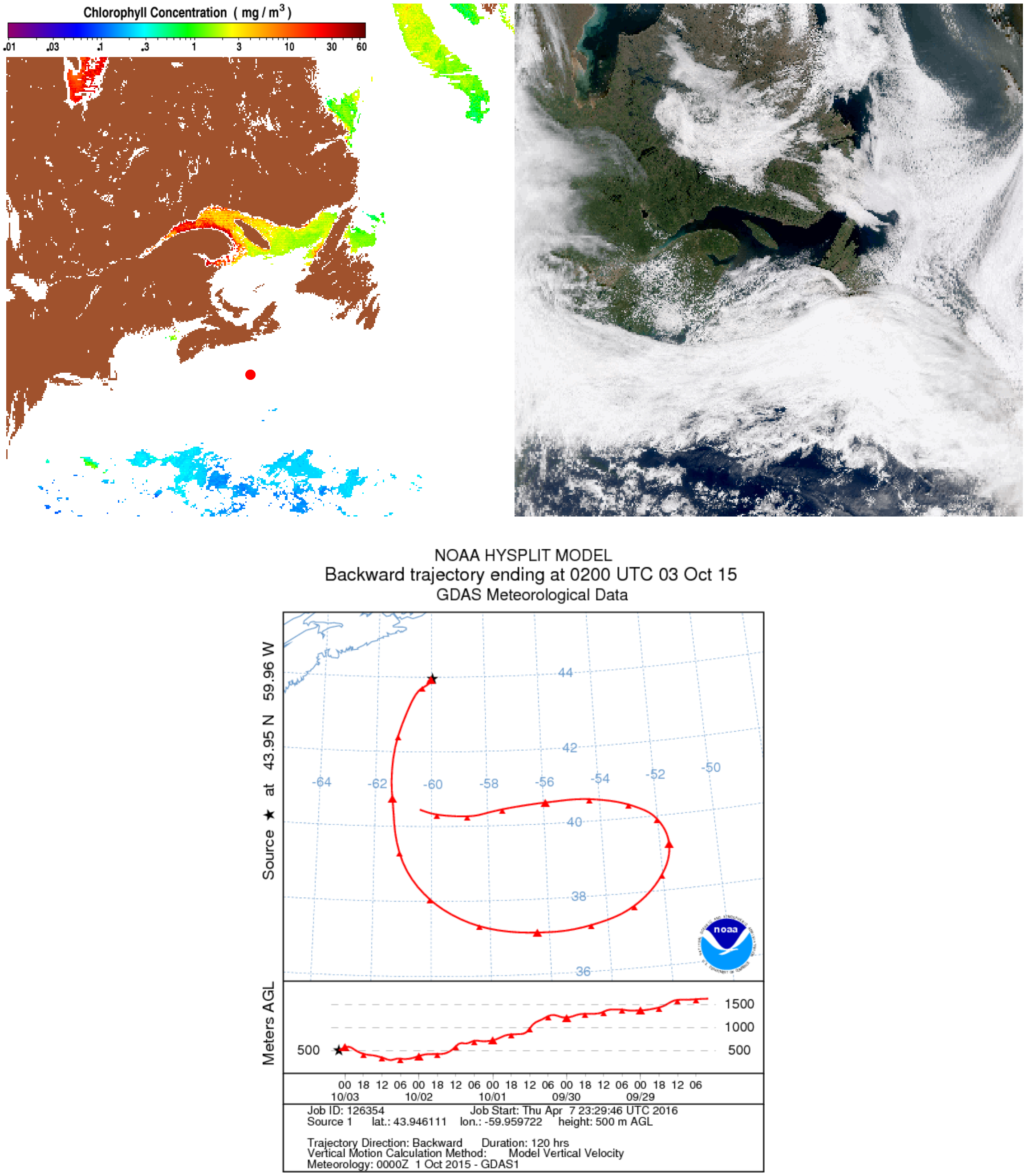

Figure 50. Chlorophyll-a (top left) and quasi true colour (top right) measured by the NASA VIIRS satellite and 5-day air mass back trajectory (bottom) for Sable Island on October 3, 2015

The low on October 17 occurred at 20:00 UTC where particle number counts for the <0.523 µm size fraction reached 1 particles cm^{-3}. The particle number count for all other size fractions totalled 1 particles cm^{-3}. The chlorophyll-a and quasi true colour satellite images, as well as the 5-day air mass back trajectory for this spike are presented in Figure 51. The air mass in Figure 51 originates in Canada's west coast and moves almost directly across the country before impacting Sable Island. The reason for low particle number counts in this air mass is unclear, although the air mass remained at high altitudes throughout the trajectory which could indicate less re-entrained PM from the surface. Particles could have been scavenged by a rainfall event during the trajectory although no rain was reported on Sable Island on October 17. The satellite images show phytoplankton blooms around Nova Scotia which would expectedly give rise to UFPs formed from gas-to-particle conversion, however this was not observed.

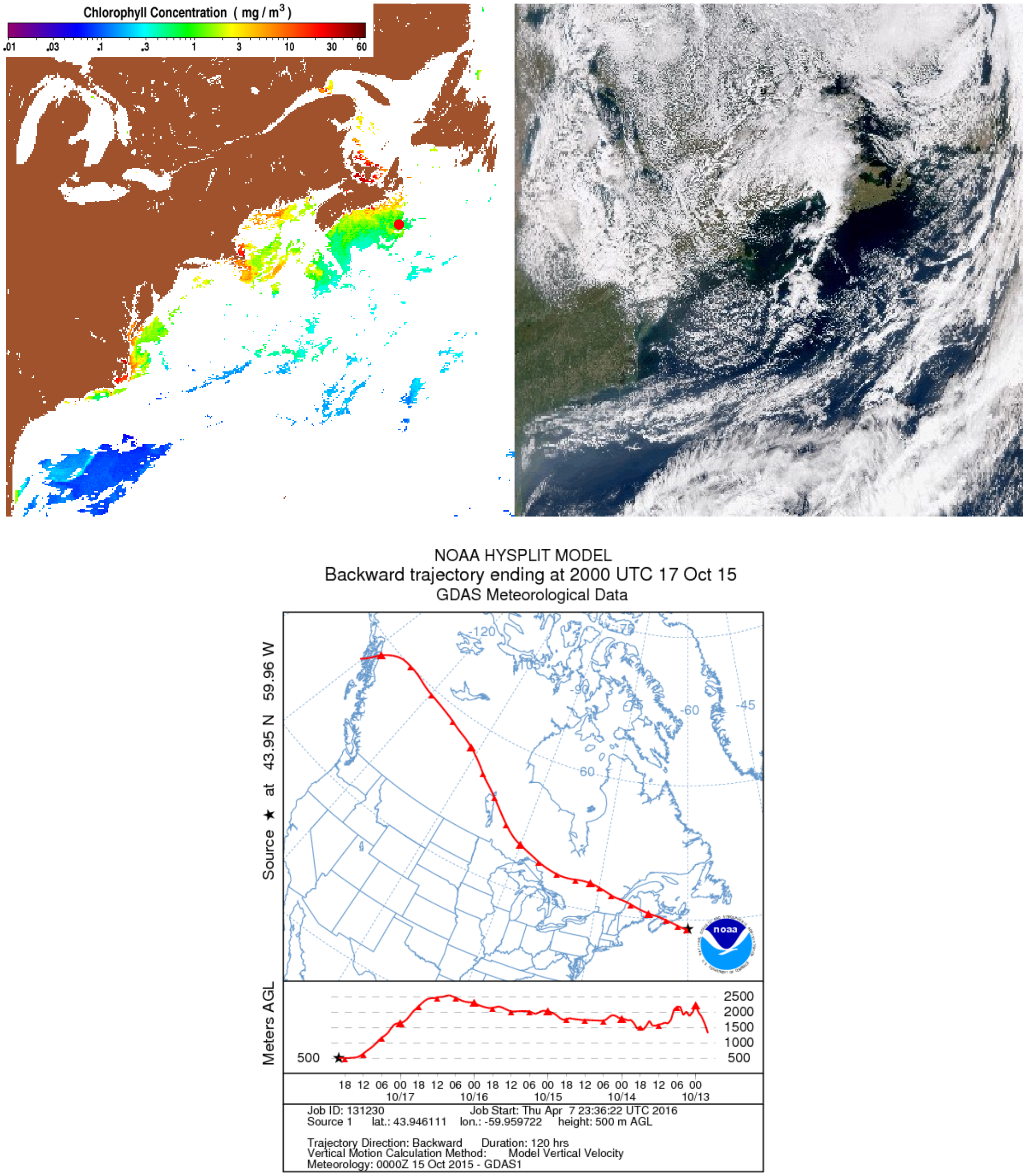

Figure 51. Chlorophyll-a (top left) and quasi true colour (top right) measured by the NASA VIIRS satellite and 5-day air mass back trajectory (bottom) for Sable Island on October 17, 2015

The low on December 28 occurred at 06:00 UTC where particle number counts for the <0.523 μm size fraction reached 0 particles cm^{-3}. The particle number count for all other size fractions totalled 1 particles cm^{-3}. The chlorophyll-a and quasi true colour satellite images, as well as the 5-day air mass back trajectory for this spike are presented in Figure 52. The vertical trajectory in Figure 52 shows the air mass contacting the surface between New Brunswick and Nova Scotia, scavenging particles from the air mass. Rain and snow were reported on Sable Island on December 28, which may have contributed to particle scavenging.

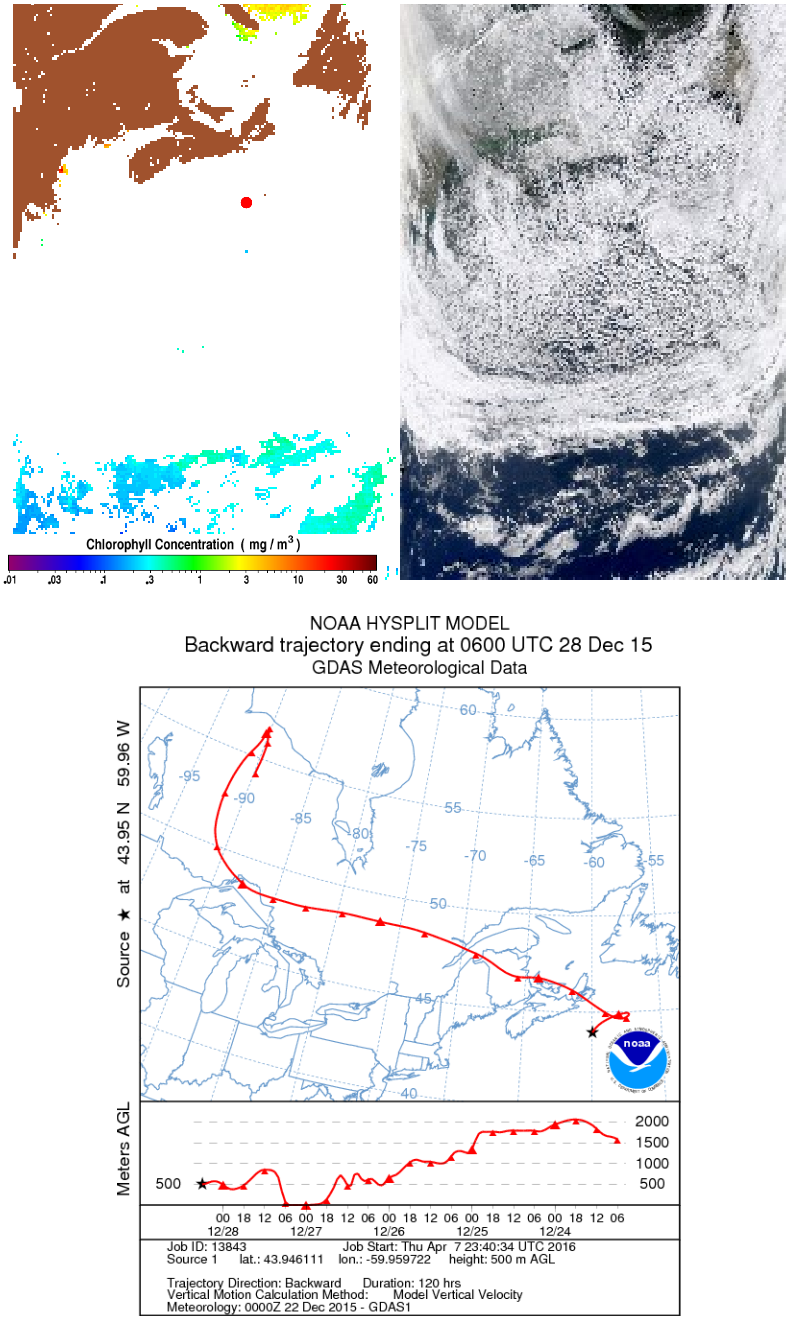

Figure 52. Chlorophyll-a (top left) and quasi true colour (top right) measured by the NASA VIIRS satellite and 5-day air mass back trajectory (bottom) for Sable Island on December 28, 2015

4.5 Positive Matrix Factorization Modelling

The USEPA Positive Matrix Factorization model v5.0 (https://www.epa.gov/air-research/positive-matrix-factorization-model-environmental-data-analyses) was used to investigate the percentage and concentration contribution from various emissions sources to the observed size-resolved particle number counts and PM mass impacting Sable Island between October 1, 2015 and December 31, 2015. The first step in running the model is to create a concentration species file and a corresponding uncertainty file. In this research the species concentration file contained the date in the first column and the associated particle variables in the remaining columns, e.g. the DRX mass data (PM_1, $PM_{2.5}$, PM_4, PM_{10}, and TSP size fractions), the UFPM 3031 particle number counts associated with the six ultrafine particle size bins (20-30 nm, 30-50 nm, 50-70 nm, 70-100 nm, 100-200 nm, and 200-800 nm) and the APS 3321 particle number counts associated with the 52 size bins (500 nm to 20 μm). The uncertainty file was constructed as described in the PMF user guide with the default 20% uncertainty applied. As recommended in the model user guide, the default settings were used, e.g. 20 random start points and 6 factors. All of the 20 runs converged. After running the PMF model approximately 30 times with differing numbers of factors (ranging from 3 to 7), 5 factors were chosen based on the number of likely sources of the aerosol species observed on Sable Island, e.g. marine biogenic emissions, fresh combustion sources, sea salt/spray, long-range transport aerosol, and aged aerosol. The parity plot in Figure 53, and the corresponding time series graph in Figure 54 compare the observed 0.965 μm size bin with the PMF predicted 0.965 μm size bin. The R^2 was found to be 0.99. The R^2 did not drop below 0.9 for the remaining PM variables used in the model, demonstrating that PMF can almost perfectly predict the sample vriables found on Sable Island. This is a highly significant result demonstrating high quality data and a parsimonious model.

Figure 53 provides a parity plot of observed versus predicted particle number counts for the 0.965 µm size fraction.

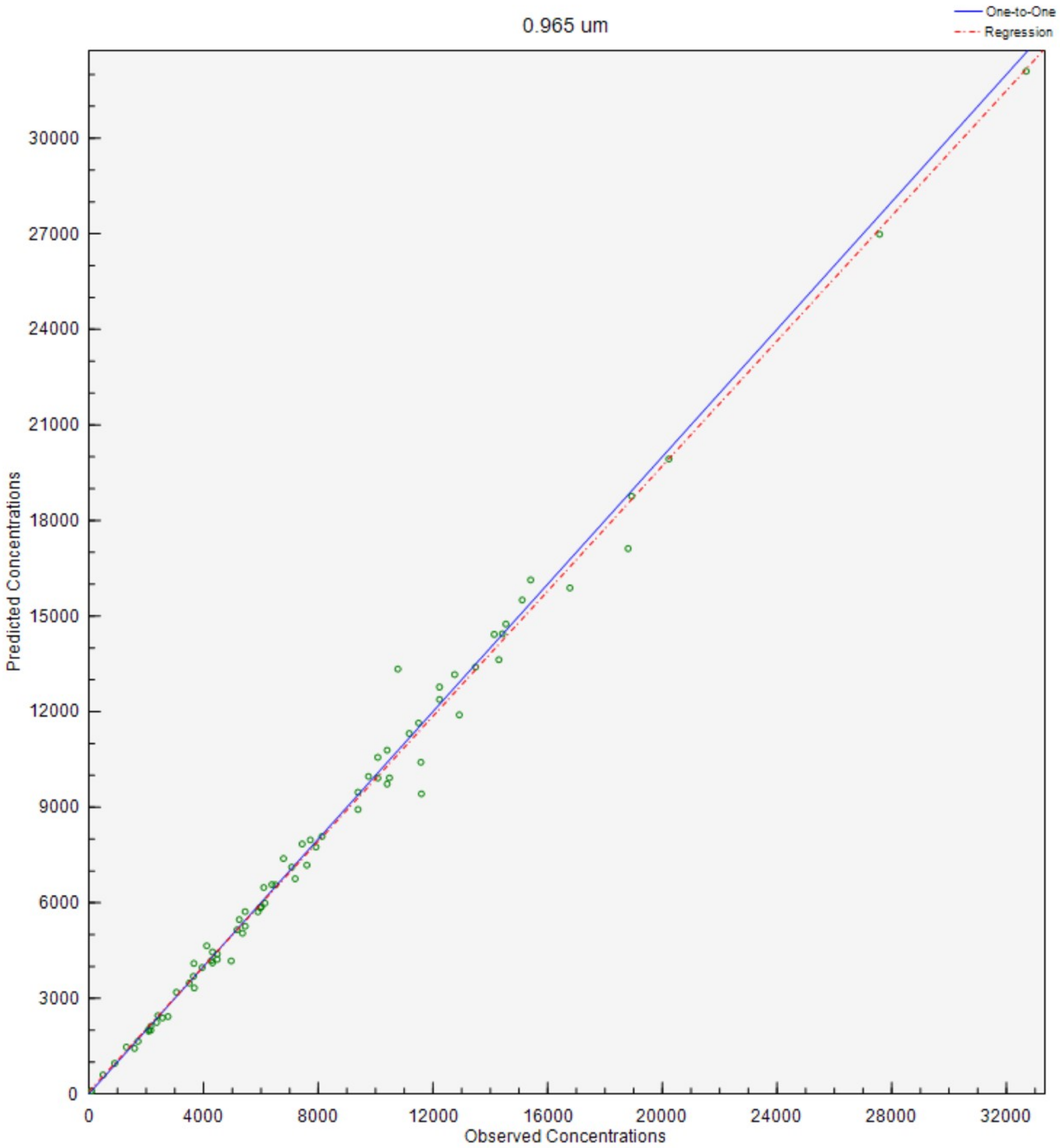

Figure 53. Parity plot of observed versus predicted particle number counts for the 0.965 µm size fraction

Figure 54 provides a time series plot of observed versus predicted particle number counts for the 0.965 µm size fraction.

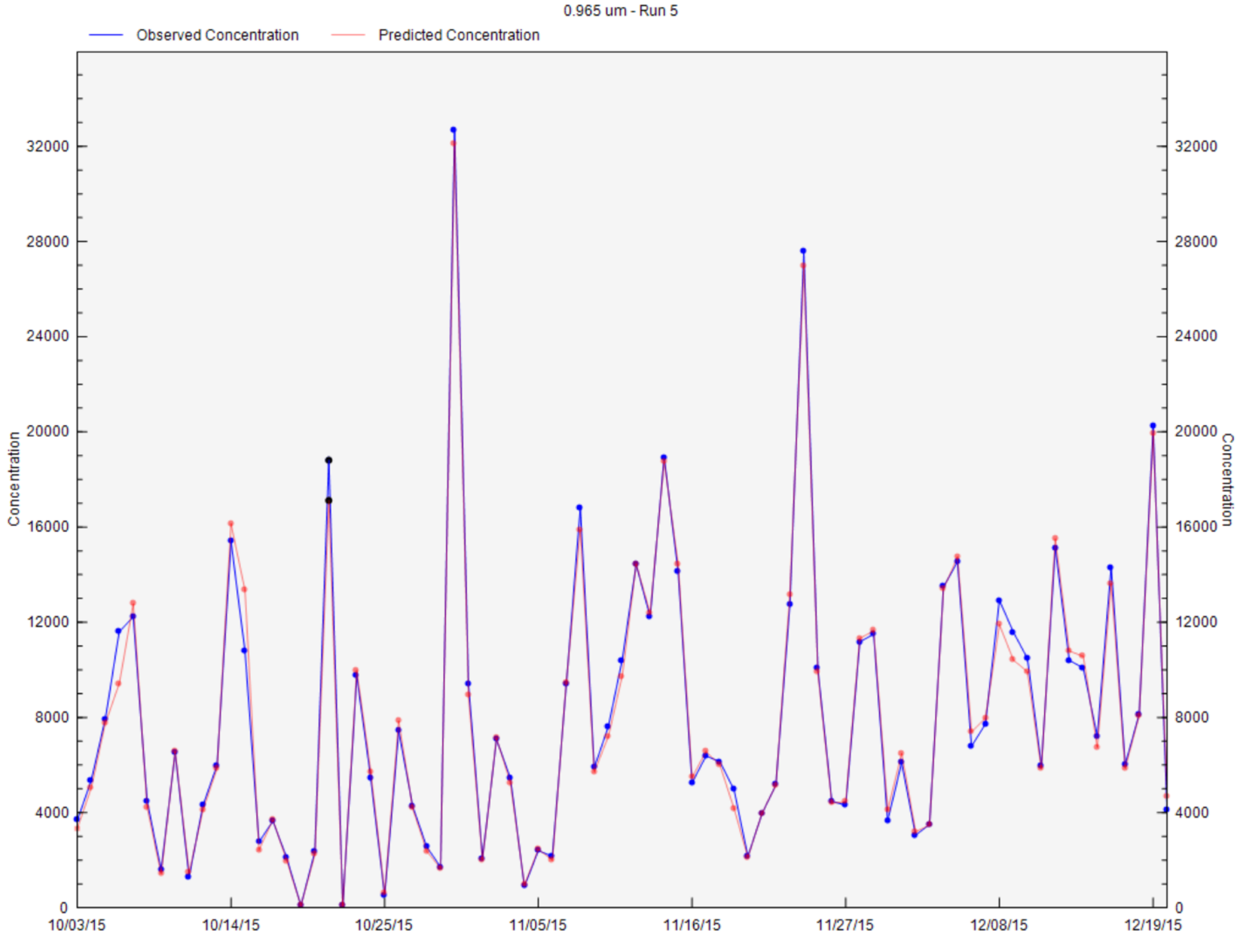

Figure 54. Times series of observed versus predicted particle number counts for the 0.965 µm size fraction

One of the pre-run model checks is on the scaled residuals. None of the scaled residuals for a model variable should be outside ± 3 standard deviations. As can be seen in Figure 55 for the 0.542 µm bin, the scaled residuals are well within the required ± 3 standard deviations. This result was maintained for the other sample variables.

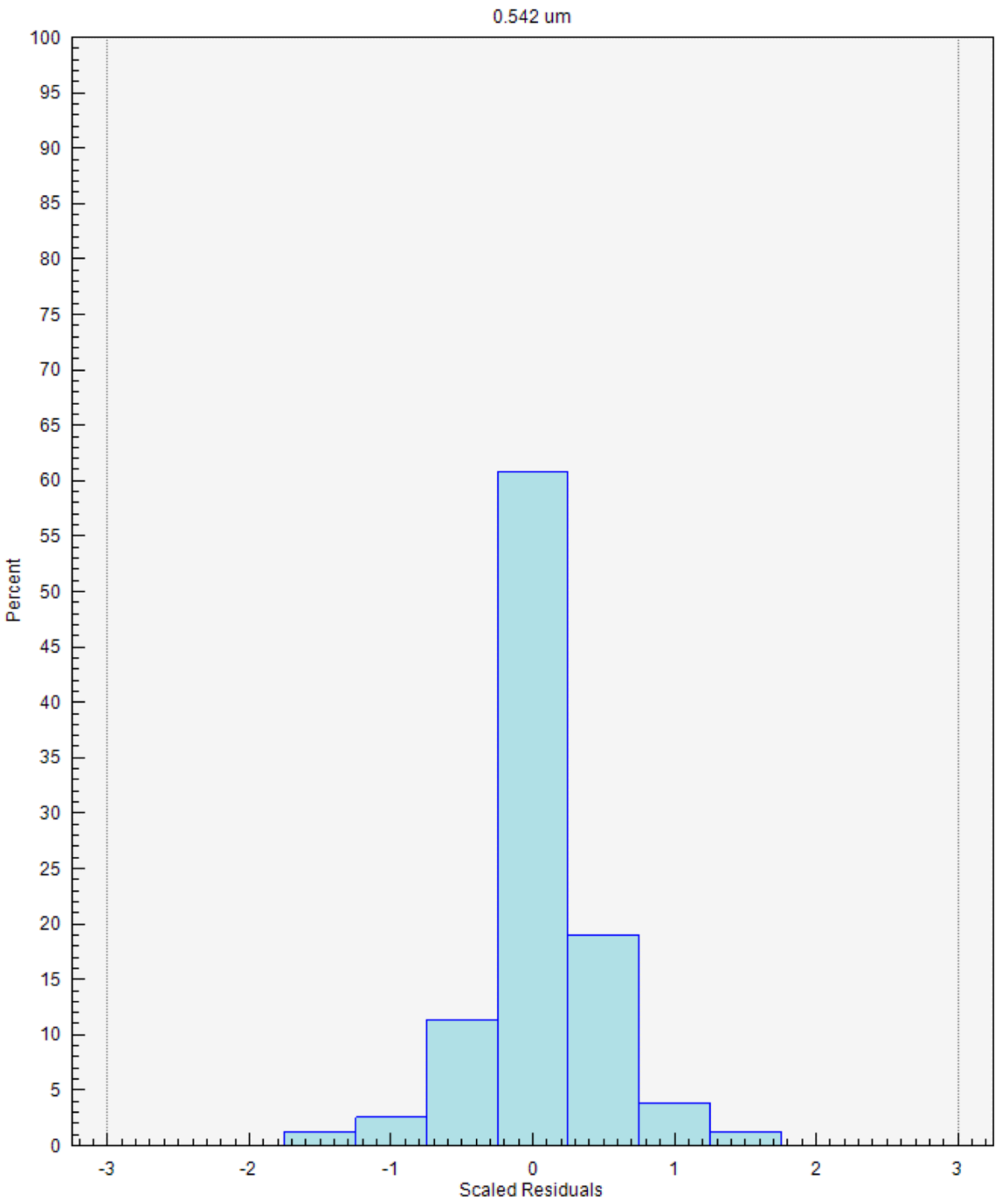

Figure 55. Scaled residuals for the 0.542 μm particle size bin

After passing the pre-model checks, the model is run, and two plots are produced for each factor. The first plot is the factor profile for Factor 1 (Figure 56). The second plot is the corresponding factor contributions associated with Factor 1 (Figure 57). In Figure 56, the primary y-axis represents the particle mass concentration or particle number (blue bars) that is associated with the species found within this factor. In Figure 56, the secondary y-axis represents the percentage of a sample variable, covering the entire data set that falls within this factor (red box). For example, if the red box aligned with 100% on the secondary y-axis, then all of that sample metric, in all of the samples, is associated with this factor and no other. Prior knowledge of source chemical markers, aerosol physics, and augmented by air mass back trajectories, meteorological variables, and remote sensing, can then be used to assign a source name to this factor. The primary y-axis units for each factor profile for each of the species are as follows: the $PM_{1/2.5/4/10}$ and PM total species have units of μg m^{-3}, the 20-30 nm, 30-50 nm, 50-70 nm, 70-100 nm, 100-200 nm, and 200-800 nm species have units of particle # cm^{-3}, and the <0.523 μm through to 19.81 μm species have units of particle #. The factor contributions plots have y-axes that are normalized so that the average of all contributions for each factor is 1.

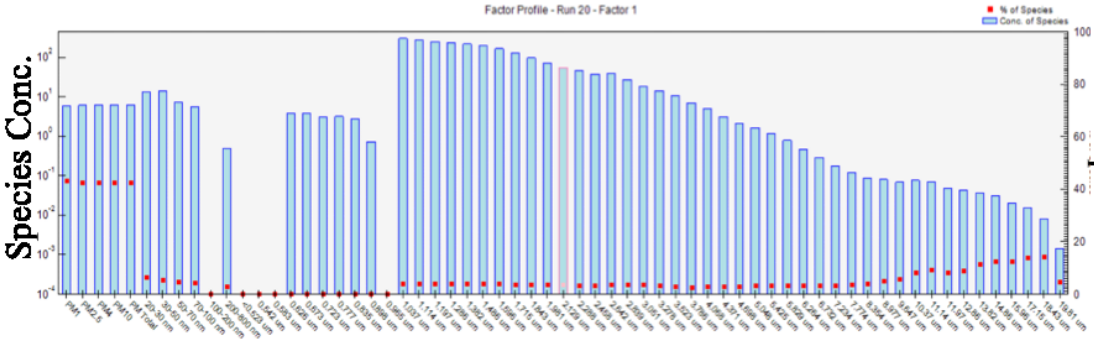

Figure 56. Factor profile for Factor 1

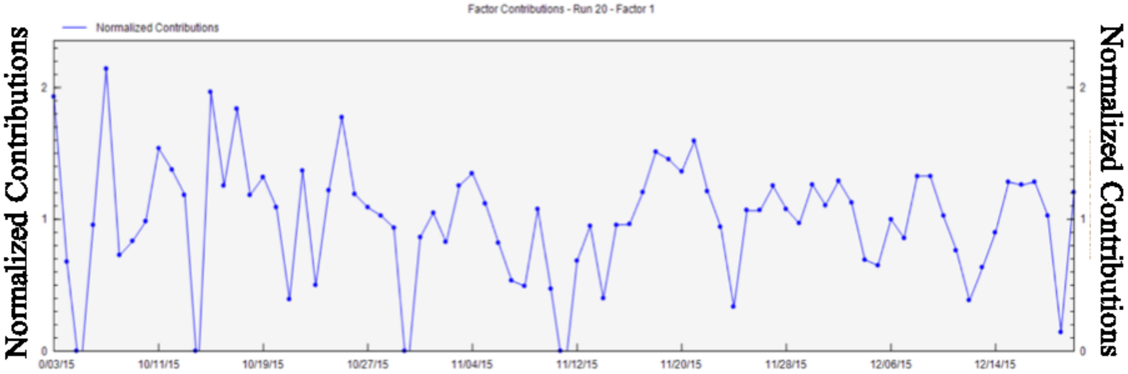

Figure 57. Factor contributions associated with Factor 1

As can be seen in Figure 56, 47% of the PM mass (PM_1 through to TSP) is found within Factor 1. In addition, in Figure 56, it can be seen that there is little contribution from the UFP size fractions through to the fine particle size fractions. The particle size number does not increase from ~5% contribution until reaching 8.99 µm where it rises steeply in number concentration and percentage contribution for the remaining large size fractions. Therefore, Factor 1 cannot be associated with fresh gas-to-particle converted aerosol or with fresh combustion sources that typically give rise to numerous UFPs. Typical long-range aged aerosols have a median particle size-fraction of 1 µm, with no ultrafine or coarse particles above 2.5 µm (Jeong et al., 2011; Gibson et al., 2013). In Figure 57 above, the three spikes investigated using HYSPLIT air mass back trajectories occurred on October 7, 17, and 25. These air mass back trajectories are presented in Figure 58. It can be seen in Figure 58 that the October 7 and December 25 back trajectories are predominantly marine, however, the trajectories for October 15 and 17 are associated with transboundary air flow from eastern Canada and the NE US. Given that 45% of the mass is associated with this factor and it is only the coarse and super-coarse particle size distributions that contribute significant mass, it is with some confidence that this factor can be named sea spray or sea salt. Another local source could be re-suspended sand and weathered material (biological and mineral) on Sable Island. Over the next 3 years, research into the aerosol chemical species will also be investigated together with aerosol mass and number to aid in identification of aerosol sources.

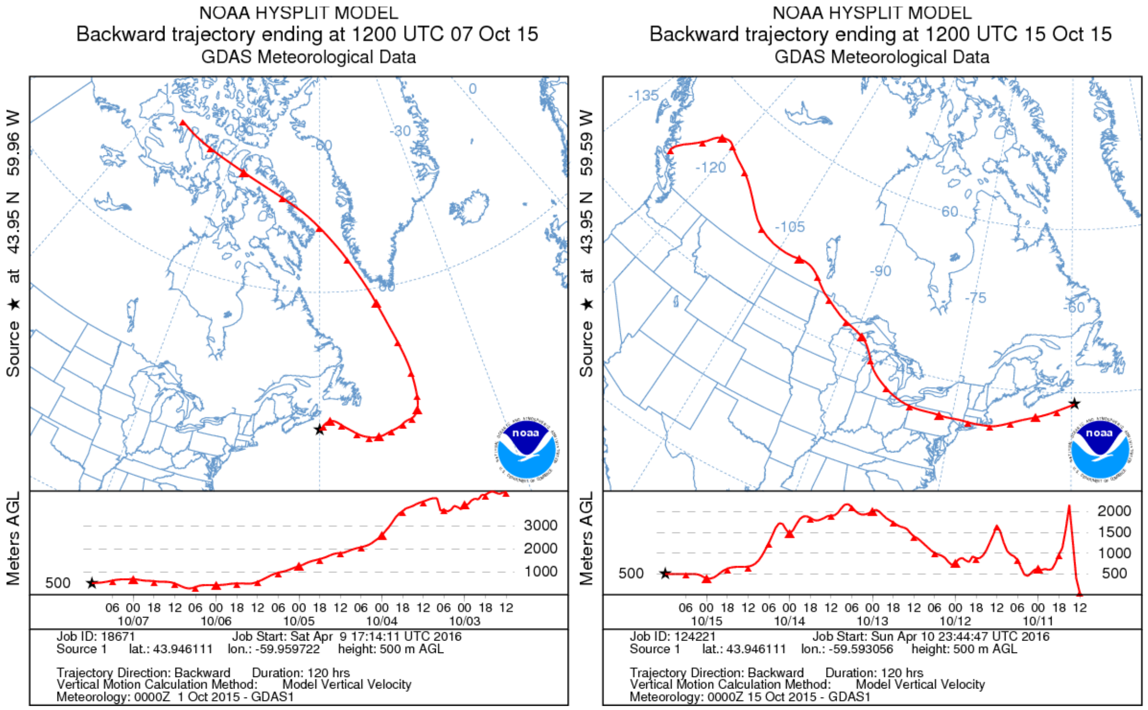

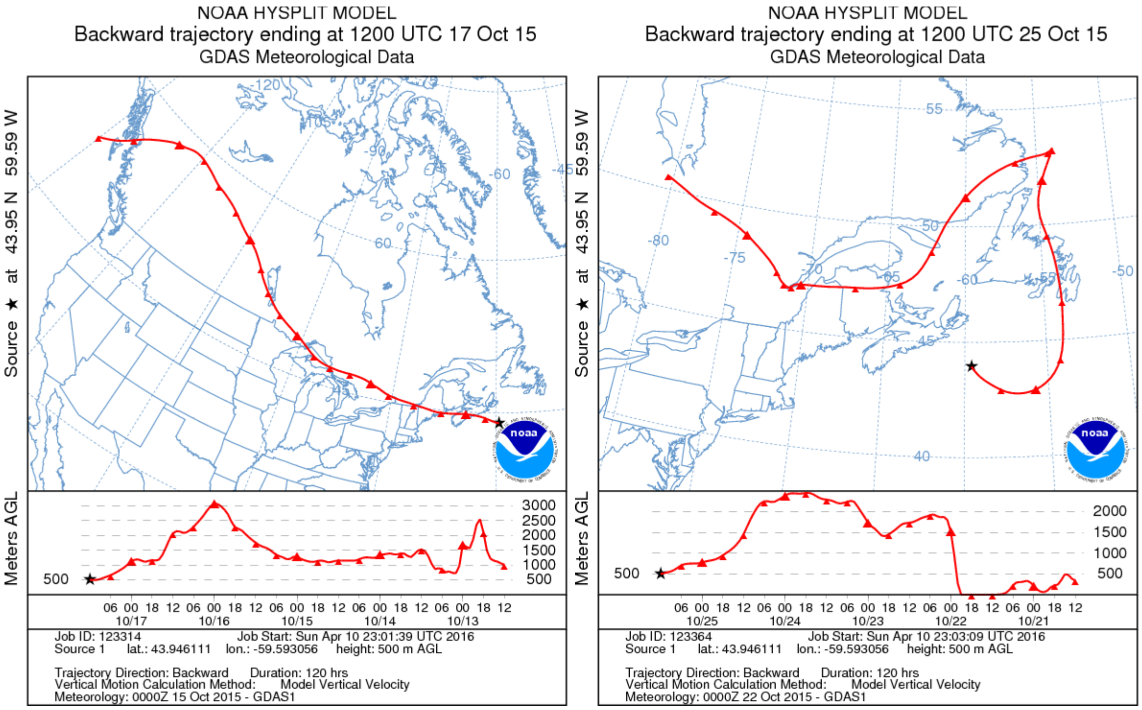

Figure 58. 5-Day air mass back trajectories for Sable Island on October 7 (top left), October 15 (top right), October 17 (bottom left) and October 25, 2015 (bottom right)

Figure 59 below provides the factor profile for Factor 2, with Figure 60 providing the corresponding factor contributions associated with Factor 2.

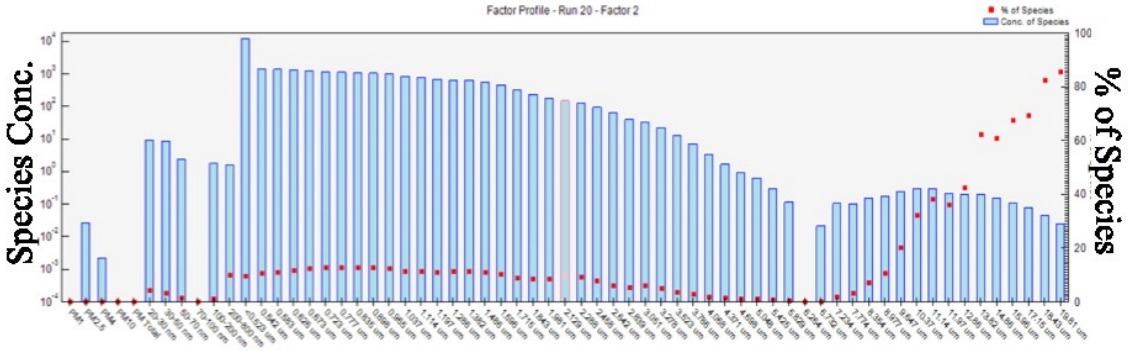

Figure 59. Factor profile for Factor 2

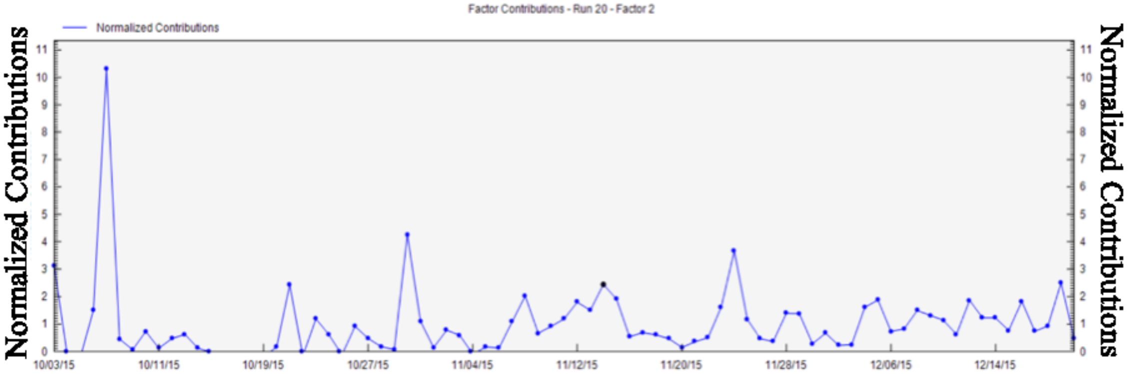

Figure 60. Factor contributions associated with Factor 2

As can be seen in Figure 59, there was very little PM mass found within Factor 2. In addition, in Figure 59, it can be seen that there is little contribution (red boxes) from the ultrafine particle size fractions up to 200 nm. The particle size number jumps to a 10% contribution (red boxes) between 200 nm to 2.458 µm, dropping to zero contribution at 6.264 µm. The particle number climbs sharply from 6.732 µm to 85% when reaching the 19.81 µm size fraction. This is the classic bi-modal distribution associated with aged aerosol that also contains a coarse mode (e.g. sea spray or re-suspended surficial dust)

(Zhu et al., 2002b). Therefore, Factor 2 cannot be associated with fresh gas-to-particle converted aerosol or with fresh combustion sources that typically give rise to numerous ultrafine particles. However, scrutiny of the concentration on the primary y-axis shows very little mass, and thus only a very few particles were associated with the coarse mode above 6.732 nm. The increase in super-coarse particle number counts may be associated with high winds causing re-entrainment of surface dust or sea salt and it is expected that particle mass would be associated super-coarse mode particles. However, the inlet for the DRX instrument that measures particle mass has a 90 degree elbow and super-coarse mode particles could have too much inertia to follow the streamlines and make it to the detector. Therefore, it is with some confidence that this factor can be named island surface dust/sand. Again, 5-day air mass back trajectories and visible satellite images were scrutinized to support the identification of the source related to Factor 2. Figure 61 presents chlorophyll-a and quasi true colour satellite observations as well as 5-day air mass back trajectories for the spike in Factor 2 occurring on October 7. However, as shown in Figure 76 (factor pie chart), this factor contributed less than 0.05% and as such is removed for the final source apportionment model output by PMF.

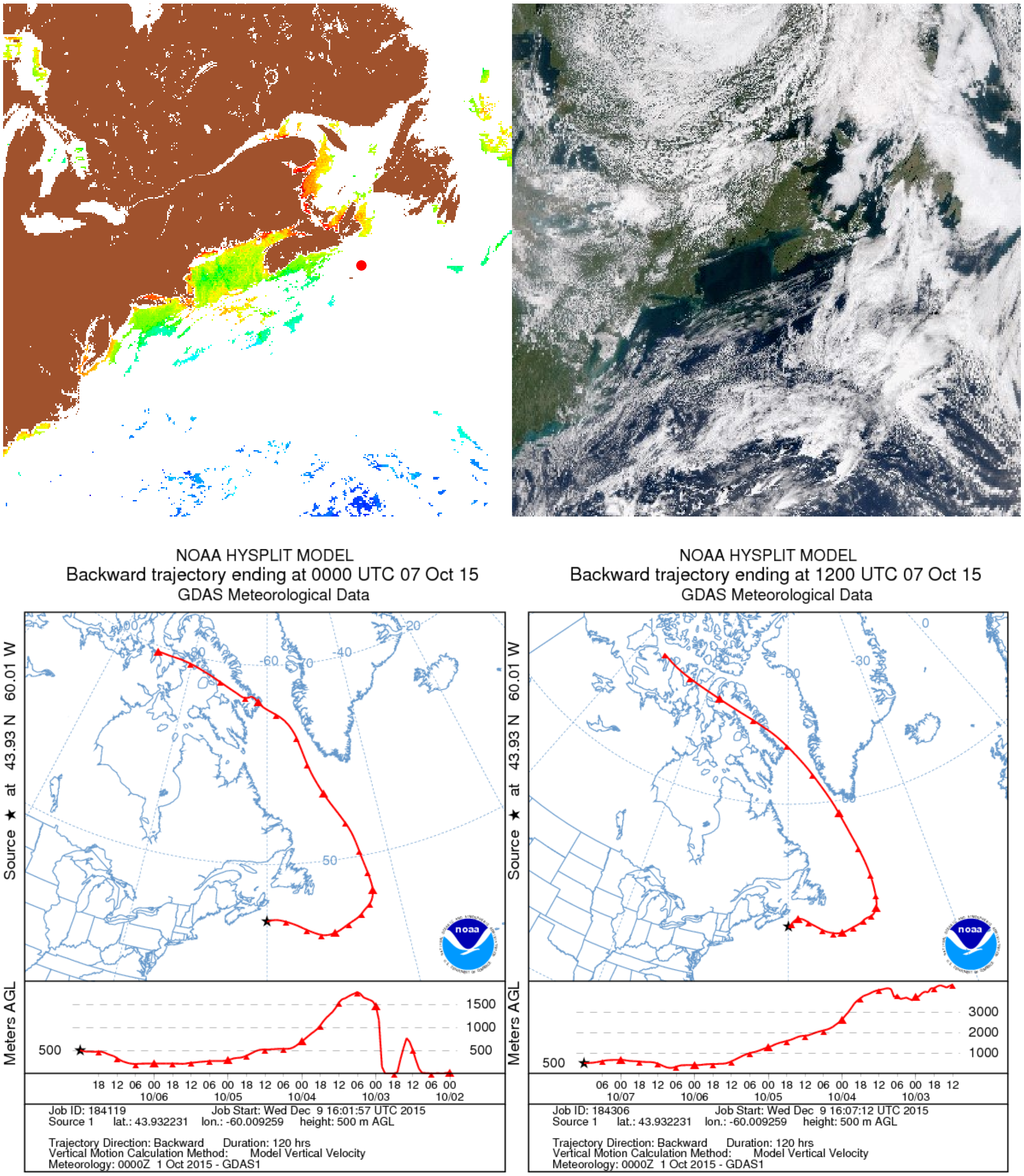

Figure 61. Chlorophyll-a (top left) and quasi true colour (top right) measured by the NASA VIIRS satellite and 5-day air mass back trajectories (bottom) for Sable Island on October 7, 2015

The back trajectories and satellite images associated with the spikes occurring on October 30 and November 24 are found in Figure 26 and Figure 27, respectively. They show air masses originating over the continent and would suggest LRT.

Figure 62 provides the factor profile for Factor 3, with Figure 63 providing the corresponding factor contributions associated with Factor 3.

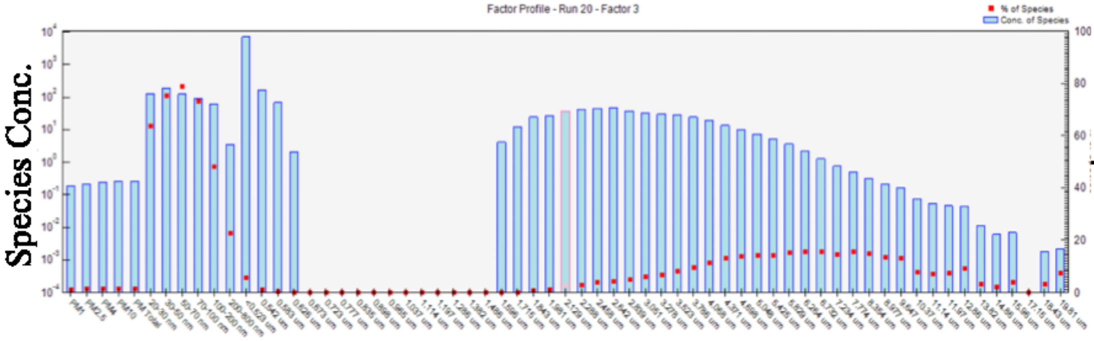

Figure 62. Factor profile for Factor 3

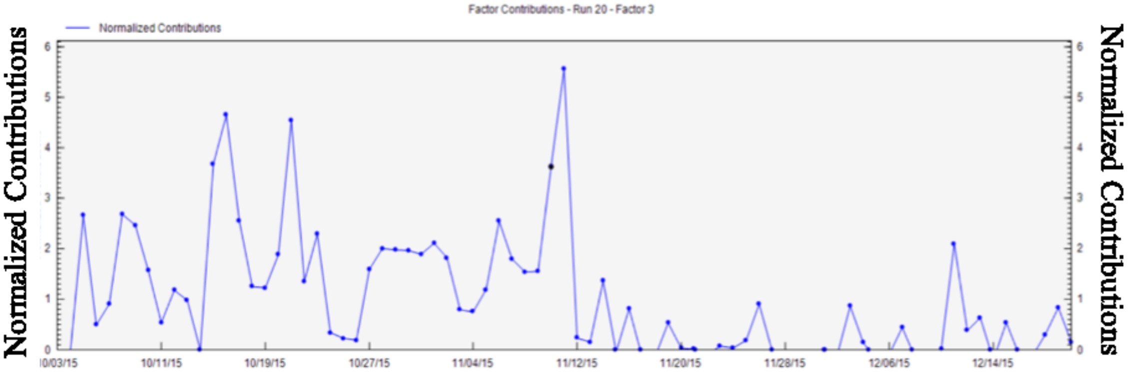

Figure 63. Factor contribution for Factor 3

From Figure 62 it can be seen that 70-80% of the UFP number counts for the 20-30 nm, 30-50 nm, 50-70 nm, and, 70-100 nm and no particle mass is attributed to Factor 3. This clearly indicates either fresh combustion or gas-to-particle conversion as the source for Factor 3. Futhermore, non sea salt sulphate emitted from the oceans appears in the accumulation mode (20 nm – 90 nm) (IPCC, 2013), which provides evidence for Factor 3 being of marine origin. In Figure 63, spikes are seen for October 5, 8, 16, and 21, and November 6 and 11. For the November 6 and 11 spikes, the Scotian Shelf was cloud covered and no useful satellite images could be retrieved from any of the NASA Aqua MODIS, Terra MODIS, and VIIRA satellites. HYSPLIT back trajectories for these dates (Appendix) show the air masses originating over the continent with only a short time spent over the marine environment before impacting Sable Island. The back trajectories for October 21 show the air mass that impacted Sable Island at 12:00 UTC was largely continent-influenced, however the air mass impacting Sable Island at 00:00 UTC travelled over the Atlantic Ocean for its final 24 hours. The chlorophyll-a, quasi true colour, and 5-day air mass back trajectory for October 21 are shown in Figure 64. The Aqua MODIS satellite images provide evidence of a phytoplankton bloom around Nova Scotia and the NE US, this would support the theory of gas-to-particle conversion (biogenic marine emissions forming SOA). In addition, the quasi true colour image shows evidence of continental smog outflow (blue-gray in amongst the clouds (white)). Therefore, the air mass likely had continental smog outflow and also entrained some phytoplankton biogenic secondary aerosol en route to Sable Island. Without further chemical speciation it is difficult to determine if the UFPs on this date are related to secondary marine biogenic emissions or smog outflow from fresh combustion sources. But given that ultrafine particles in this size range can only exist for a few hours it is probable that it is marine biogenic emissions contributing to this factor as fall phytoplankton blooms are known to occur during this period (Craig et al., 2015; Li, 2014; Li & Harrison, 2008).

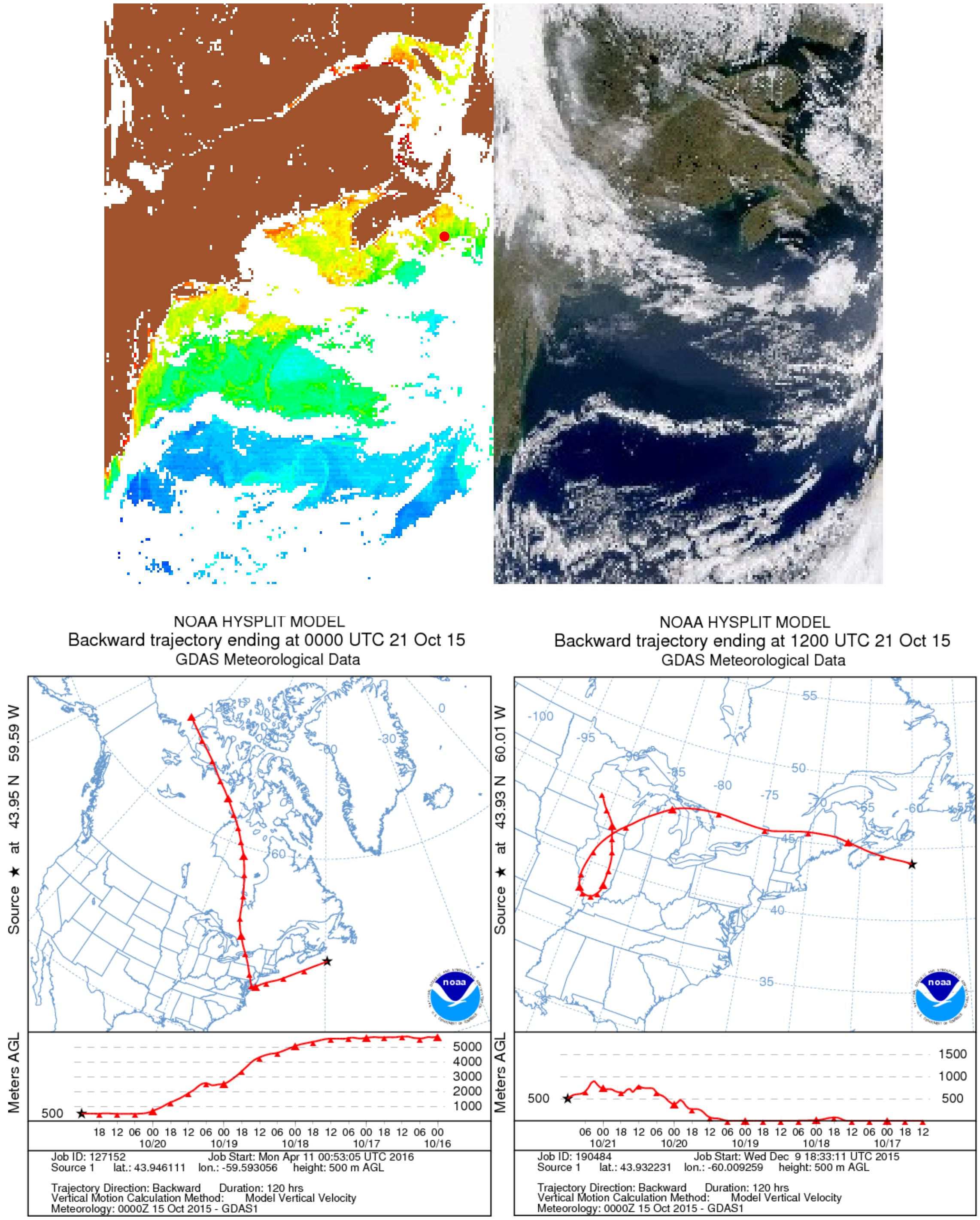

Figure 64. Chlorophyll-a (top left) and quasi true colour (top right) measured by the NASA Aqua MODIS satellite and 5-day air mass back trajectories (bottom) for Sable Island on October 21, 2015

Figure 65 provides the factor profile for Factor 4, with Figure 66 providing the corresponding factor contributions associated with Factor 4.

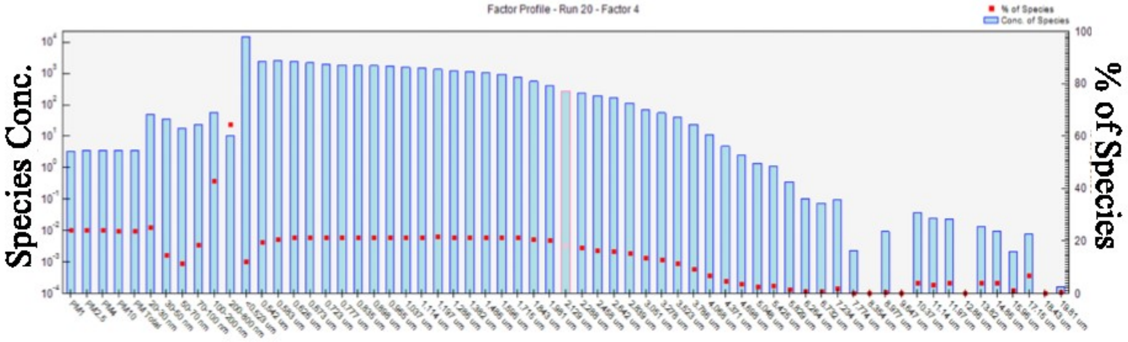

Figure 65. Factor profile for Factor 4

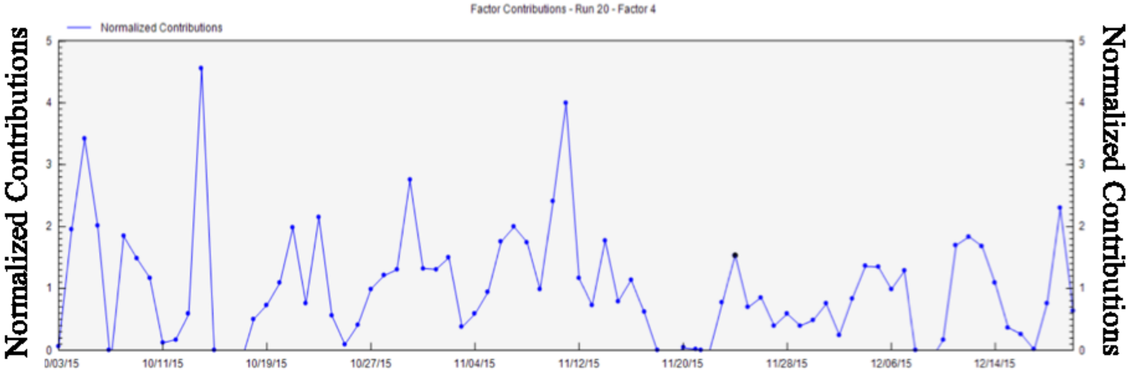

Figure 66. Factor contribution for Factor 4

It can bee seen in Figure 65 that roughly 50% and 70% of 100-200 nm and 200-800nm sized UFPs are associated with Factor 4, along with 30% mass contribution and 20% of particle sizes 0.542- 1.981 µm. As shown in Figure 67, Figure 68, Figure 69, andFigure 70, the satellite images all indicate phytoplankton presence and the air mass back trajectories are mainly marine (October 5 and 14) and/or continental (October 30, November 13); also the trajectories on October 5 and 30 originate in the north, an area of low anthropogenic emissions ("clean" air) (Gibson et al., 2013). Fresh gas-to-particle conversion produces particles as small as 1 nm, therefore the presence of particles between 100-800 nm would indicate a slightly aged marine aerosol (fresh gas-to-particle conversion would produce smaller particles, which would coagulate and grow by condensation) (Kulkarni, Baron & Willeke, 2011). Research shows clean marine aerosols are dominated by volatile sulphate species (e.g. DMS) smaller than 1 μm (Blot et al., 2013). This would suggest that Factor 4 is mixture of slightly aged biogenic marine emissions and aged marine aerosol which contributes to the fine particle count and particle mass. However, another potential source for the fine (100 nm – 800 nm) particles associated with Factor 5 is O&G activities around Sable Island. Chemical speciation is needed to determine if the fine particles are related to combustion or biogenic marine emissions

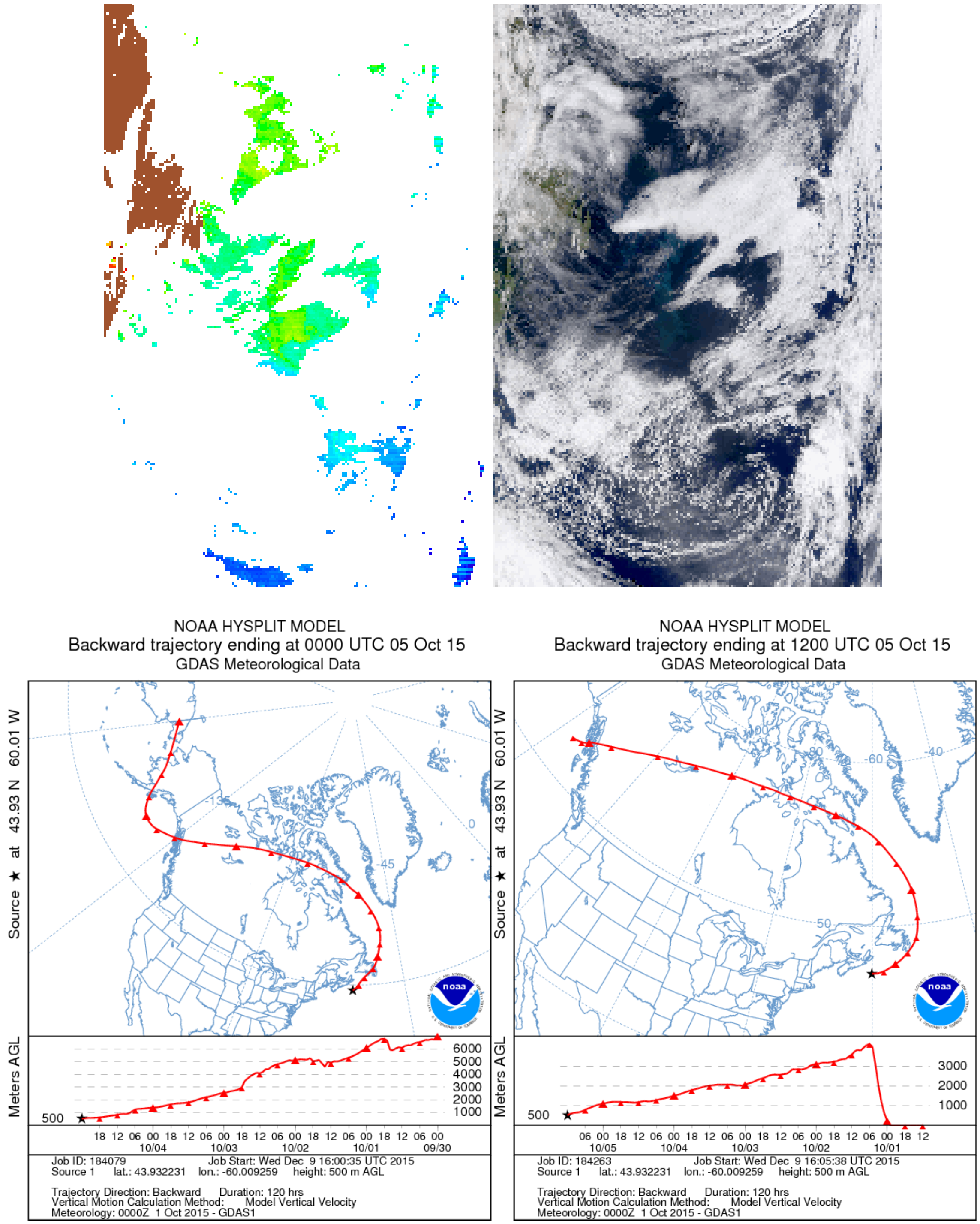

Figure 67. Chlorophyll-a (top left) and quasi true colour (top right) measured by the NASA Terra MODIS satellite and 5-day air mass back trajectories (bottom) for Sable Island on October 5, 2015

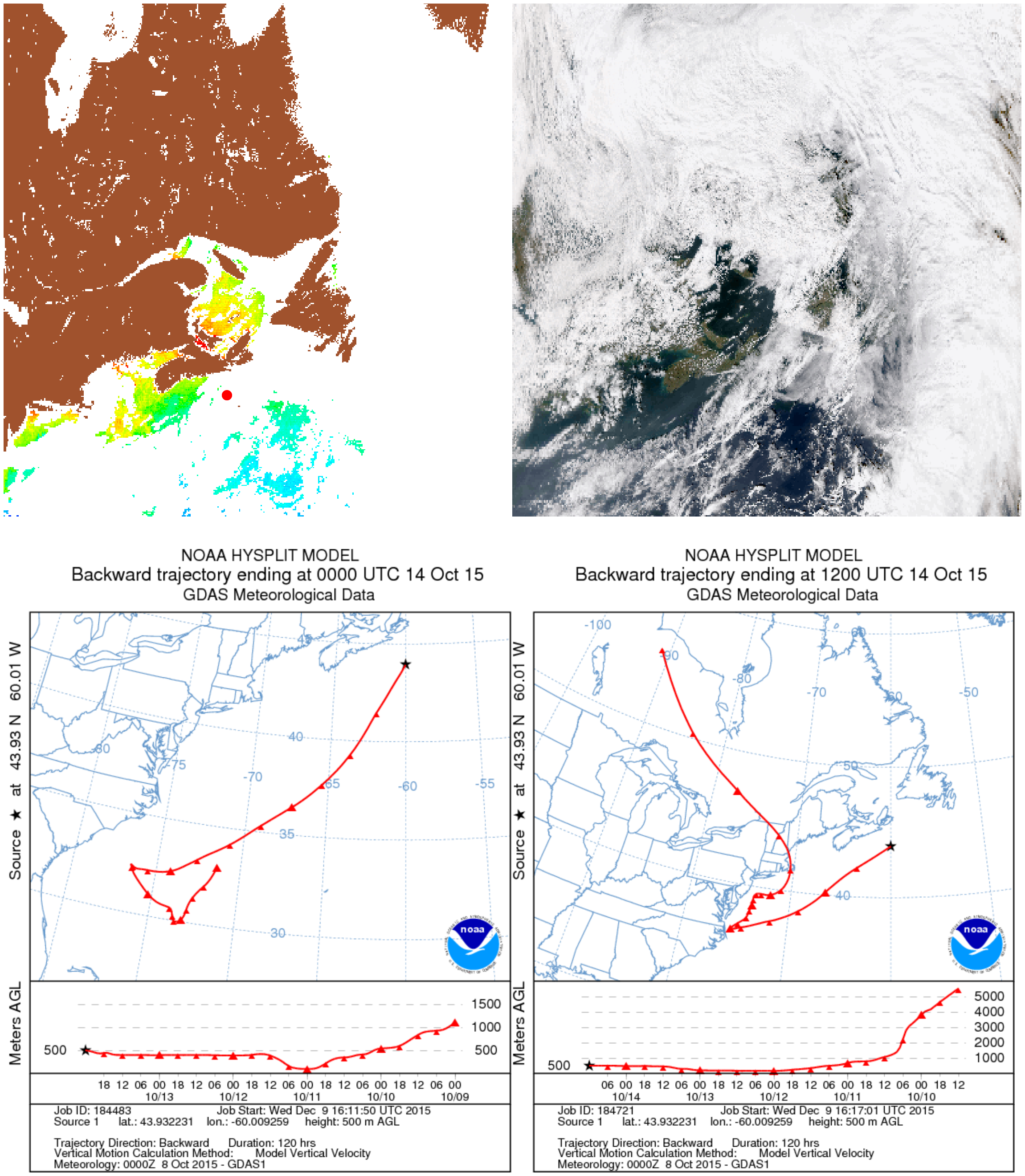

Figure 68. Chlorophyll-a (top left) and quasi true colour (top right) measured by the NASA VIIRS satellite and 5-day air mass back trajectories (bottom) for Sable Island on October 14, 2015

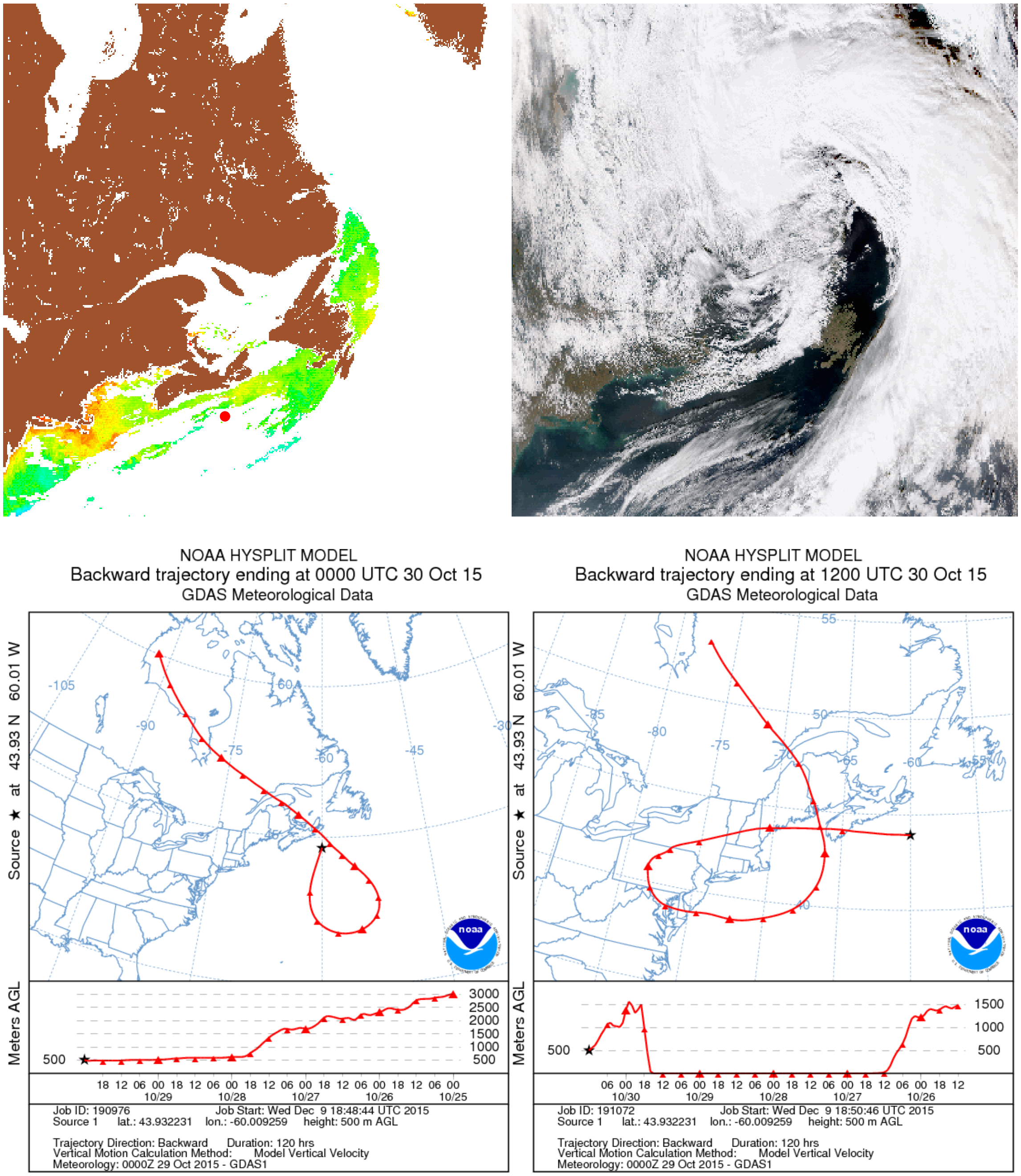

Figure 69. Chlorophyll-a (top left) and quasi true colour (top right) measured by the NASA VIIRS satellite and 5-day air mass back trajectories (bottom) for Sable Island on October 30, 2015

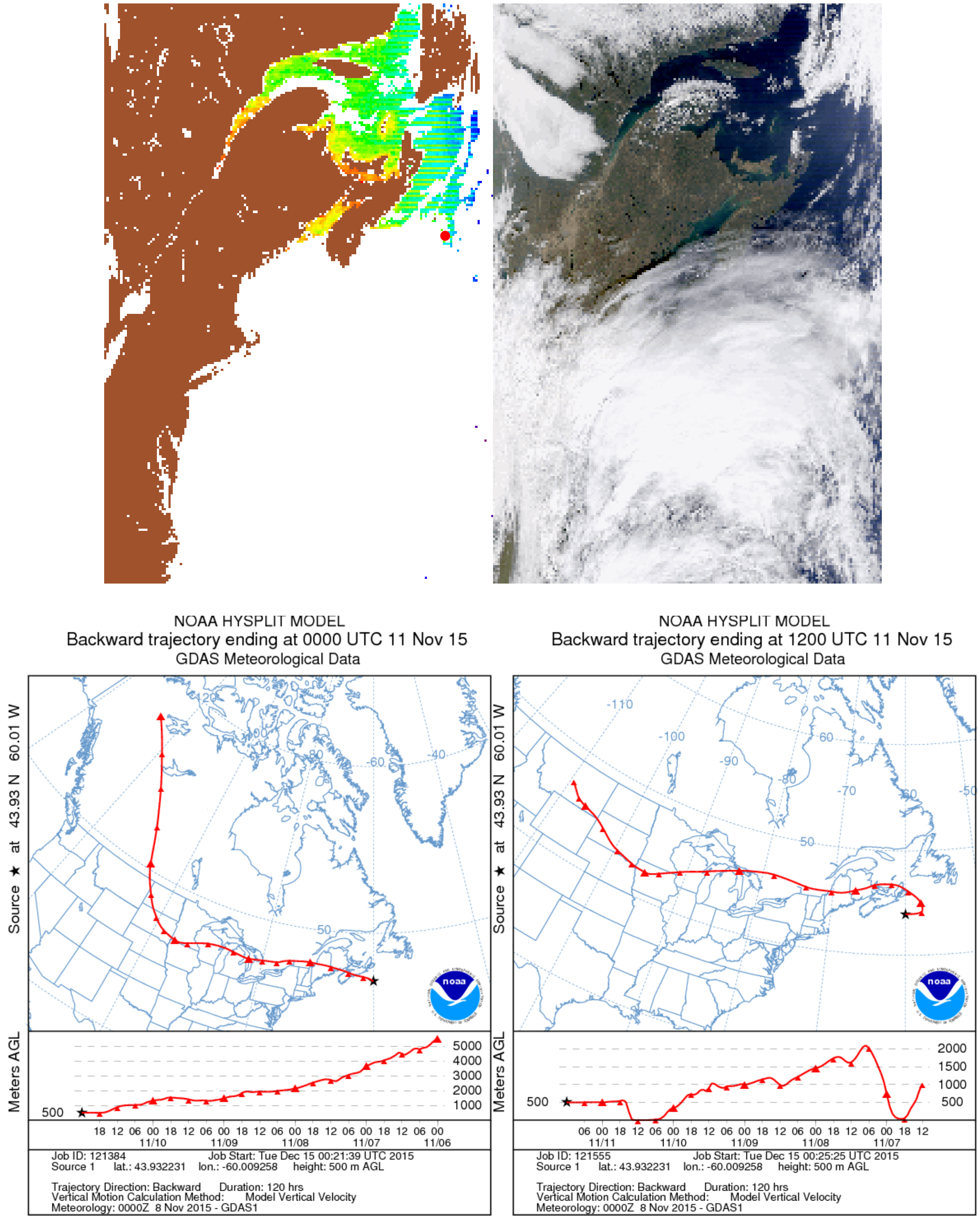

Figure 70. Chlorophyll-a (top left) and quasi true colour (top right) measured by the NASA VIIRS satellite and 5-day air mass back trajectories (bottom) for Sable Island on November 11, 2015

Figure 71 below provides the factor profile for Factor 5, with Figure 72 providing the corresponding factor contributions associated with Factor 5.

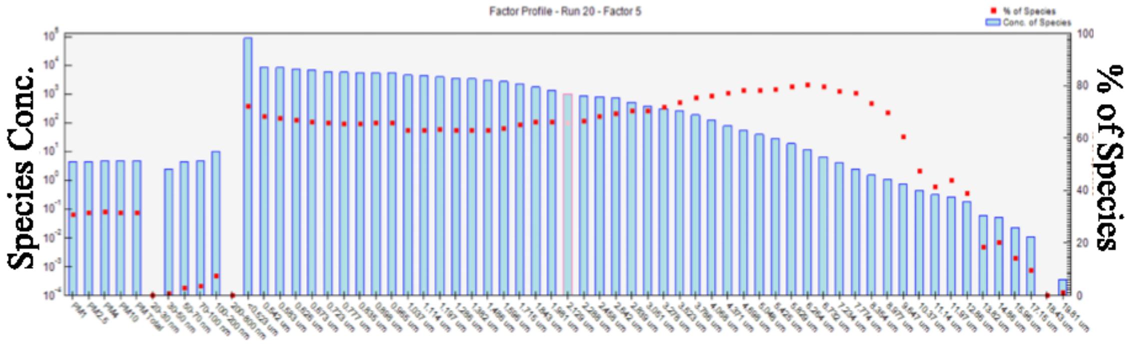

Figure 71. Factor profile for Factor 5

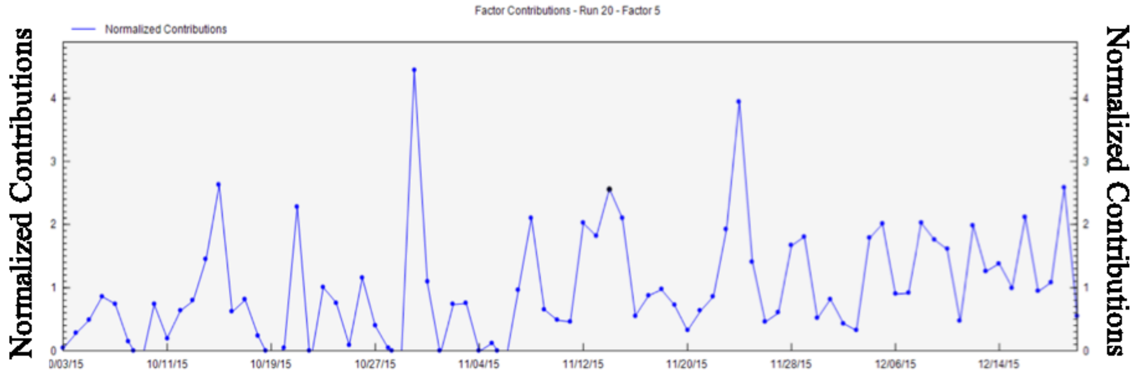

Figure 72. Factor contribution for Factor 5

It can be seen in Figure 71 that 70% - 80% of the species in Factor 5 correspond to the 0.5 µm through to 10 µm size fractions. In addition, there was little species contribution from the ultrafine particles in this factor. Therefore, this factor can not be associated with fresh combustion sources or gas-to-particle conversion. Moreover, the presence of 30% of the aerosol mass within this factor implies larger particles with more mass as opposed to numerous ultrafine particles with virtually no corresponding mass (see Figure 1). This can be supported by the largest species contribution being found in the 6.264 µm size fraction, a fraction that would have far greater mass than the corresponding ultrafine particles that would exhibit little mass. The spikes occurring on October 15 and 30, November 14 and 24, and December 19 were investigated using HYSPLIT air mass back trajectories and NASA satellite observations. Figure 73 shows the chlorophyll-a and quasi true colour for Sable Island as well as air mass back trajectories for November 14. The satellite observations and back trajectories for the other spikes are found in Figure 24, Figure 26, Figure 27, and Figure 28. As shown by these back trajectories, nearly all of the air masses investigated pass through the NE US, a known PM source region for Halifax (Gibson et al., 2013) and therefore, it is with confidence that Factor 5 is LRT. Ammonium sulphate ($(NH_4)_2SO_4$) contributes significantly to LRT from NE US (Gibson et al., 2013) and is highly hygroscopic (Figure 2), therefore the particle mass and high number counts for all fine, coarse, and super-coarse particles may be a result of particle bound water. Missing data in the chlorophyll-a satellite images make it difficult to draw any conclusions regarding phytoplankton contributions to this factor.

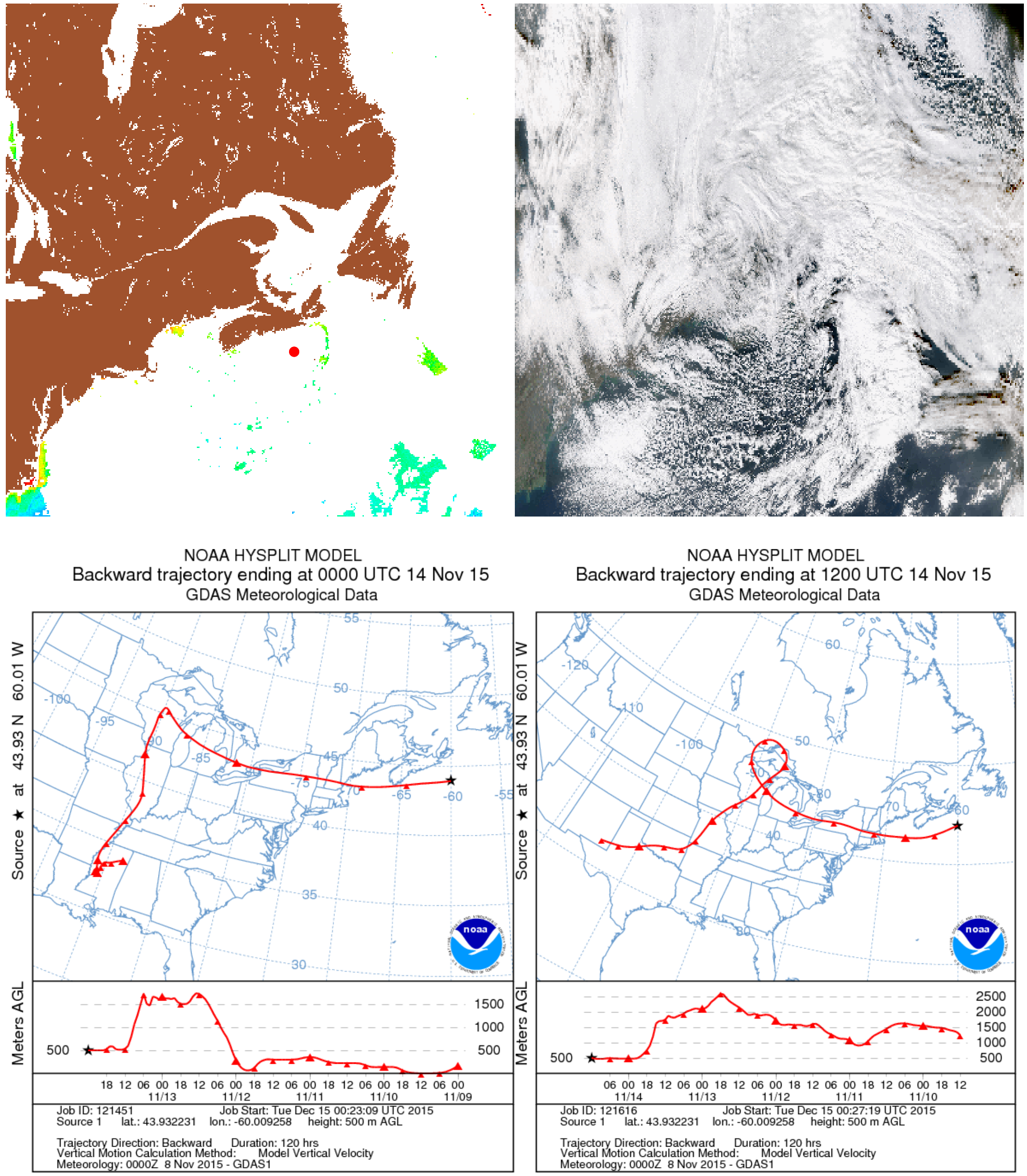

Figure 73. Chlorophyll-a (top left) and quasi true colour (top right) measured by the NASA VIIRS satellite and 5-day air mass back trajectories (bottom) for Sable Island on November 14, 2015

Figure 74 below provides a comparison of the base run factor contribution time series results compared with the factor contributions time series generated by the PMF Fpeak bootstrap model check.

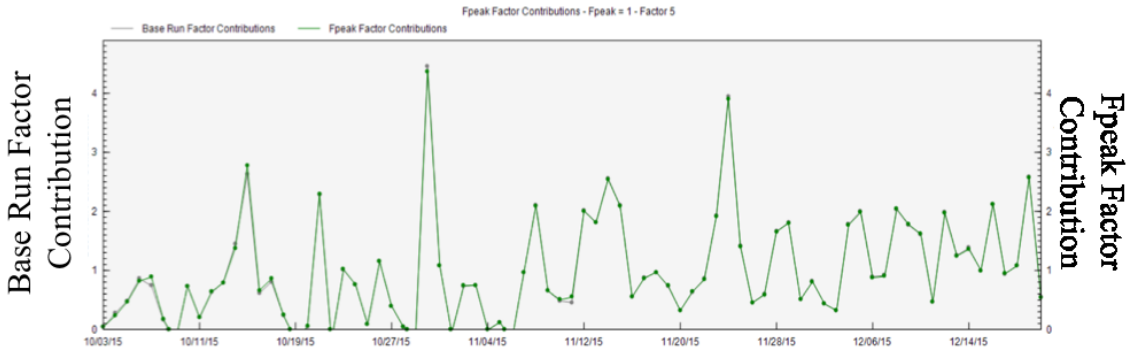

Figure 74. PMF base run time series compared to factor contribution times series

As can be seen in Figure 74, there is almost perfect agreement between the PMF model base run and the factor contributions time series estimated by the Fpeak bootstrapping model check. This demonstrates that the model is extremely robust and that the model output can be treated with confidence. Figure 75 contains the average factor fingerprints of the entire particle mass and number samples. Figure 75 is useful to observe the change in factor contribution as the particle mass and number concentrations change, for example the size fractions from 0.5 µm through to 10 µm are dominated by factor 5 (long-range aged aerosol).

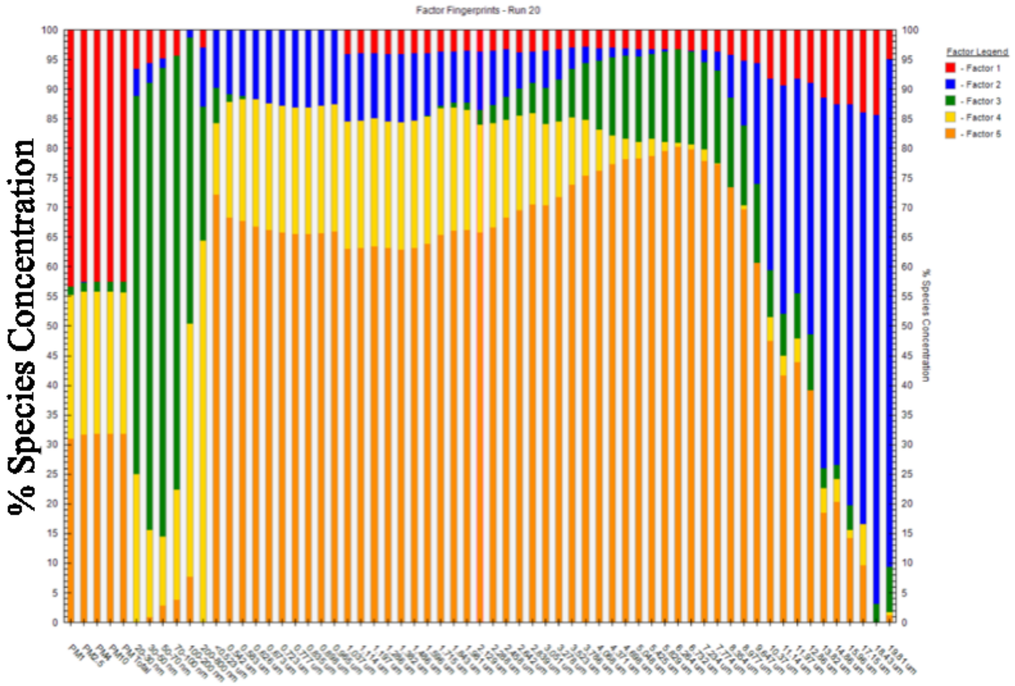

Figure 75. Factor fingerprints

Figure 75 provides a Factor fingerprint, or source finger print for the PM mass and particle number spectra. It gives a quick look at the dominant factors (sources) contribution to the PM mass and number spectra. From Figure 75 it can clearly be seen that Factor 5 (LRT) dominates between 0.523 µm and 10.37 µm. Factor 2 (Island surface dust/sand) dominates above 10.37 µm. Factor 3 (biogenic marine secondary ultrafine particles) dominates between 20 nm and 100 nm and with PM mass dominated by Factors 1 (sea spray), Factor 4 (aged biogenic marine/aged marine aerosol) and Factor 5 (LRT). Figure 76 shows the factor contributions to the PM measured on Sable Island.

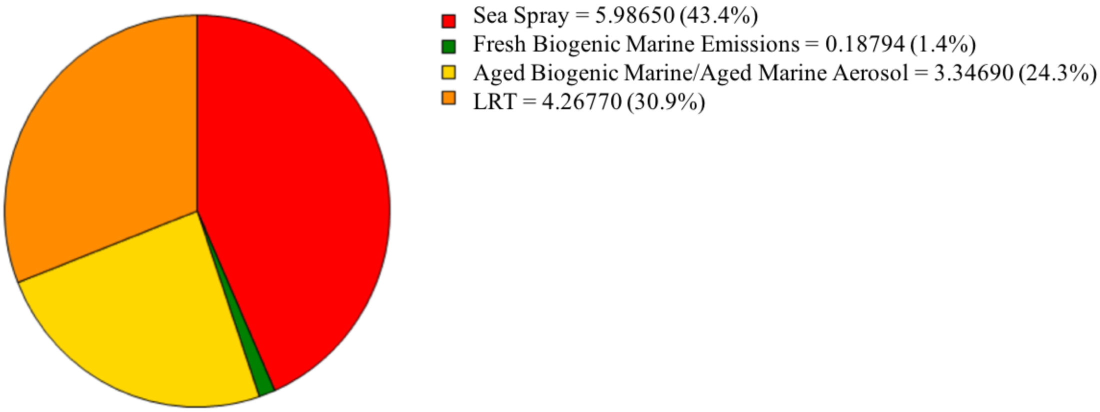

Figure 76. Factor contributions

Figure 76 provides a source attribution pie chart of the percentage and concentration contribution made by each source to the PM mass and particle number spectra sampled. It can be seen that the percentage (%) and concentration (mass/#) for Factor 1 (sea spray) was 43.4% and 5.99 (units, either μg m^{-3}, particle # cm^{-3}, or particle #), for Factor 2 (Island surface dust/sand) the contribution was < 0.05%, and removed from the model, for Factor 3 (biogenic marine emissions) 1.4%, for Factor 4 (aged biogenic marine emissions/aged marine aerosol) was 24.3%, and for Factor 5 (LRT) was 30.9%. The low contribution from biogenic marine emissions is likely due to including particle mass in the model and UFPs contributing very little particle mass.

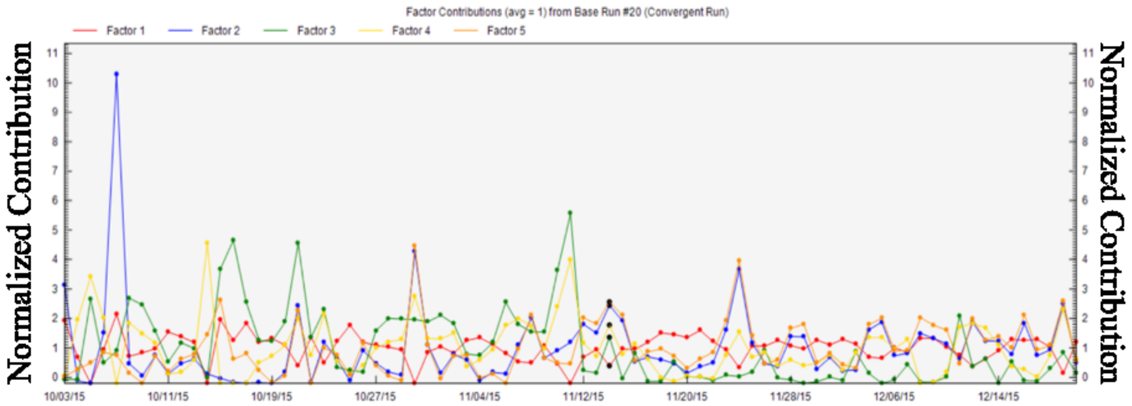

Figure 77. Time series for all Factors

Figure 77 provides a time series of the percentage and concentration from each factor on each sampling day. This is useful for comparing factors to see if there are any relationships or divergence in trends. It can be seen that Factors 3 and 4 are trend quite closely correlated, this is not surprising as Factor 3 is fresh marine biogenic gas-to-particle secondary aerosol and Factor 4 is slightly aged marine emissions/aged marine aerosol. It can be seen from Figure 77 that Factor 5 (LRT) does not trend with either Factor 3 or 4. This would make sense because LRT originated from the continent. The source apportionment time series plot presented in Figure 77 is a very useful tool in understanding the temporal drivers of source contributing to PM mass and particle number on Sable Island.

CHAPTER 5 CONCLUSION AND RECOMMENDATIONS

5.1 Conclusion

A three month particle mass concentration and number count sampling campaign was conducted on Sable Island from October 1 – December 31, 2015 with the goal to apportion particle mass and number to determine their sources. It was found that, for Sable Island, sea spray accounted for 43.4% of the PM. The second greatest contributor was LRT pollution from the continent, likely consisting of coal combustion, agricultural, and industrial sources from the NE US and Windsor-Quebec corridor. Finally, aged biogenic marine emissions/aged marine aerosol and fresh biogenic marine emissions constituted 24.3% and 1.4%, respectively. Future measurements on Sable Island will produce valuable data to help researchers quantify marine emissions inventories, the fate and transport of particulate matter in the marine environment, and their contributions to climate forcing. This thesis explored the source apportionment of PM on Sable Island to identify the marine emission contributions. Marine aerosol composition varies by season and consists of a complex mixture of different species, therefore an opportunity for augmenting the PM data with total VOC and VOC species data would significantly increase the ability to apportion marine emission contributions to atmospheric aerosols. Furthermore, the Sable Island site will provide long term continuous PM mass and number concentration data to a lacking global network of marine aerosol sampling sites. The Sable Island site will also provide important data for climate models and act as a ground validation site for a variety of satellites, but most importantly fill in the gaps between the four intensive NASA NAAMES missions.

5.2 Recommendations

It is recommended that an Aerodyne Aerosol Mass Spectrometer or Aerodyne Chemical Speciation Monitor be deployed on Sable Island to provide real-time PM chemical speciation. A filter based method for collecting particulate mass would provide a gravimetric correction for the DustTrak DRX and allow for post-sample chemical speciation analyses. This way, PM samples can be analyzed for known chemical markers to help in the identification and apportionment of PM sources on Sable Island. Finally, augmenting the PM data with VOC data would support and improve the apportionment of PM on Sable Island.

BIBLIOGRAPHY

Ahlm, L., Liu, S., Day, D.A., Russel, L.M., Weber, R., Gentner, D.R., Goldstein, A.H., DiGangi, J.P., Henry, S.B., Keutsch, F.N., VandenBoer, T.C., Markovic, M.Z., Murphy, J.G., Ren, X., Scheller, S. (2012). Formation and growth of ultrafine particles from secondary sources in Bakersfield, California. *Journal of Geophsical Research – Atmospheres, 117(D21).* doi:10.1029/2011JD017144.

Behrenfeld, M. J. (2010). Abandoning Sverdrup's critical depth hypothesis on phytoplankton blooms. *Ecology*, *91*(4), 977-989.

Bell, J. N. B., & Treshow, M. (2003). Air pollution and plant life (2nd ed.) John Wiley & Sons. doi:9780471490906.

Bell, M.L., Dominici, F., Ebisu, K., Zeger, S.L., Samet, J.M. (2007). Spatial and Temporal Variation in $PM_{2.5}$ Chemical composition in the United States for Heath Effects Studies. *Environmental Health Perspectives, 115(7),* 989-995. Retrieved from http://www.jstor.org/stable/4619499 on April 5, 2016.

Berglund, R.N.& Liu, B.Y.H. (1973). Generation of monodisperse aerosol standards. *Environmental Science and Technology, 7(2),* 147-153. doi:10.1021/es60074a001.

Blot, R., Clarke, A.D., Freitag, S., Kapustin, V., Howell, S.G., Jensen, J.B., Shank, L.M., McNaughton, C.S., Brekhovskikh, V. (2013). Ultrafine sea spray aerosol over the southeastern Pacific: open-ocean contributions to marine boundary layer CCN. *Atmospheric Chemistry and Physics, 13,* 7263-7278. doi:10.5194/acp-13-7263-2013.

Boldo, E., Medina, S., LeTertre, A., Hurley, F., Mücke, H.-G., Ballester, F., Aguilera, I., Eilstein, D. (2006). Apheis: Health impact assessment of long term exposure to

$PM_{2.5}$ in 23 European cites. *European Journal of Epidemiology, 21,* 449-458. doi:10.1007/s10654-006-9014-0.

Brace, M. D., Stevens, E., Taylor, S. M., Butt, S., Sun, Z., Hu, L., Borden, M., Khanna, N., Kuchta, J., Trites, J., Hart, R. & Gibson, M. D. (2014). 'The air that we breathe': assessment of laser and electrosurgical dissection devices on operating theater air quality. *Journal of Otolaryngology - Head & Neck Surgery, 43*(39), 1-9. doi:10.1186/s40463-014-0039-1.

Chen, B.T., Cheng, Y.S., Yeh, H.C. (1985). Performance of a TSI Aerodynamic Particle Sizer, *Aerosol Science and Technology, 4*(1), 89-97. doi:10.1080/02786828508959041.

Cheng, Z., Wang, S., Jiang, J., Fu, Q., Chen, C., Xu, B., Yu, J., Fu, X., Hao, J. (2013). Long-term trend of haze pollution and impact of particulate matter in the Yangtze River Delta, China. *Environmental Pollution, 182,* 101-110. doi:10.1016/j.envpol.2013.06.043.

Costa, D.L., Dreher, K.L. (1997). Bioavailable transition metals in particulate matter mediate cardiopulmonary injury in healthy and compromised animal models. *Environmental Health Perspectives, 105(5),* 1053–1060. Retrieved from http://www.ncbi.nlm.nih.gov/pmc/articles/PMC1470172/ on April 3, 2016.

Craig, S.E., Thomas, H., Jones, C.T., Li, W.K.W., Greenan, B.J.W., Shadwick, E.H., Burt, W.J. (2015). The effect of seasonality in phytoplankton community composition on CO2 uptake on the Scotian Shelf. *J. Mar. Syst. 147*, 52–60. doi:10.1016/j.jmarsys.2014.07.006.

Dockery, D.W., Pope, C.A., Xiping, X., Spengler, J.D., Ware, J.H., Fay, M.E., Ferris Jr., B.G., Speizer, F.E. (1993). An Association between Air Pollution and Mortality in

Six U.S. Cities. *The New England Journal of Medicine, 329,* 1753-1759. doi: 10.1056/NEJM199312093292401.

Dohoo, C., Guernsey, J. R., Gibson, M. D., & VanLeeuwen, J. (2015). Impact of biogas digesters on cookhouse volatile organic compound exposure for rural Kenyan farmwomen. International Society of Exposure Science., 25, 167-174. doi:10.1038/jes.2013.42.

Dohoo, C., VanLeeuwen, J., Guernsey, J., Critchley, K., & Gibson, M. (2013). Impact of biogas digesters on wood utilisation and self-reported back pain for women living on rural Kenyan smallholder dairy farms. *Global Public Health*, 1-15. doi:10.1080/17441692.2012.758299.

DeCarlo, P.F., Slowik, J.G., Worsnop, D.R., Davidovits, P., Jimenez, J.L. (2004). Particle morphology and density characterization by combined mobility and aerodynamic diameter measurements. Part 1: Theory. *Aerosol Science and Technology, 38(12)*, 1185-1205. doi:10.1081/027868290903907.

Delfino, R.J., Sioutas, C. & Malik, S. (2005). Potential Role of Ultrafine Particles in Associations between Airborne Particle Mass and Cardiovascular Health. *Environmental Health Perspectives, 113(8),* 934-946. Retrieved from http://www.jstor.org/stable/3436347 on April 5, 2016.

Draxler, R.R., Rolph, G.D. (2012). Evaluation of the Transfer Coefficient Matrix (TCM) approach to model the atmospheric radionuclide air concentrations from Fukushima. *Journal of Geophysical Research, 117,* D05107. doi:10.1029/2011JD017205.

Duderstadt, K.A., Carroll, M.A., Sillman, S., Wang, T., Albercook, G.M., Feng, L., Parrish, D.D., Holloway, J.S., Fehsenfeld, F.C., Blake, D.R., Blake, N.J., Forbes, G. (1998). Photochemical production and loss rates of ozone at Sable Island, Nova

Scotia during the North Atlantic Regional Experiment (NARE) 1993 summer intensive. *Journal of Geophysical Research, 103*(D11), 13531-13555. Retrieved from http://www.zn903.com/cetwang/_Publications/1998_JGR_Duderstadt.pdf

Dusek, U., Frank, G.P., Hildebrandt, L., Curtius, J., Schneider, J., Walter, S., Chand, D., Drewnick, F., Hings, S., Jung, D., Borrmann, S., Andreae, M.O. (2006). Size Matters More Than Chemistry for Cloud-Nucleating Ability of Aerosol Particles. *Science, 312(5778),* 1375-1378. doi:10.1126/science.1125261.

Environment and Climate Change Canada. (2013). *Canadian Ambient Air Quality Standards.* Retrieved from http://www.ec.gc.ca/default.asp?lang=En&n=56D4043B-1&news=A4B2C28A-2DFB-4BF4-8777-ADF29B4360BD on April 5, 2016.

Environment and Climate Change Canada. (2016). *Air Quality Health Index.* Retrieved from http://www.ec.gc.ca/cas-aqhi/default.asp?Lang=En on April 7, 2015.

European Environment Agency. (2012). *Particulate matter from natural sources and related reporting under the EU Air Quality Directive in 2008 and 2009.* Retrieved from http://www.eea.europa.eu/publications/particulate-matter-from-natural-sources on April 3, 2016.

Facchini, M.A., Decesari, S., Rinaldi, M., Carbone, C., Finessi, E., Mircea, M., Fuzzi, S., Moretti, F., Tagliavini, E., Ceburnis, D., O'Dowd, C.D. (2008). Important Source of Marine Secondary Organic Aerosols from Biogenic Amines, *Environmental Science and Technology, 42*(24), 9116-9121. doi: 10.1021/es8018385.

Franklin, J.E., Drummond, J.R., Griffin, D., Pierce, J.R., Waugh, D.L., Palmer, P.I., Parrington, M.P., Lee, J.D., Lewis, A.C., Rickard, A.R., Taylor, J.W., Allan, J.D., Coe, H., Chisholm, L., Duck, T.J., Hopper, J.T., Gibson, M.D., Curry, K.R., Sakamoto, K.M., Lesins, G., Walker, K.A., Dan, L., Kliever, J., Saha, A. (2014) A case study of aerosol depletion in a biomass burning plume over Eastern Canada during the 2011 BORTAS field experiment. *Atmospheric Chemistry and Physics. 14,* 8449–8460. doi:10.5194/acpd-14-3395-2014.

Friends of Sable Island Society. (2012). *A Brief History of Sable Island.* Retrieved from http://sableislandfriends.ca/?p=148 on March 20, 2016.

Fuzzi, S., Baltensperger, U., Carslaw, K., Decesari, S., Denier van der Gon, H., Facchini, M.C., Fowler, D., Koren, I., Langford, B., Lohmann, U., Nemitz, E., Pandis, S., Riipinen, I., Rudich, Y., Schaap, M., Slowik, J.G., Spracklen, D.V., Vignati, E., Wild, M., Williams, M., Gilardoni, S. (2015). Particulate matter, air quality and climate: lessons learned and future needs. *Atmospheric Chemistry and Physics, 15,* 8217-8299. doi:10.5194/acp-15-8217-2015.

Geiser, M., Rothen-Rutishauser, B., Kapp, N., Schürch, S., Kreyling, W., Schuilz, H., Semmler, M., Hof, V.I., Heyder, J., Gehr, P. (2005). Ultrafine particles cross cellular membranes by nonphagocytic mechanisms in lungs and cultured cells. *Environmental Health Perspectives, 113(11),* 1555-1560. Retrieved from http://www.jstor.org/stable/3436571.

Gibson, M.D. (2004). Source apportionment of PM10 in Glasgow, UK. PhD Thesis, University of Strathclyde, Glasgow, Scotland, UK.

Gibson, M.D., Guernsey, J.R., Beauchamp, S., Waugh, D., Heal, M.R., Brook, J.R., Maher, R., Gagnon, G.A., McPherson, J.P., Bryden, B., Gould, R., Terashima, M. (2009). Quantifying the Spatial and Temporal Variation of Ground-level Ozone in the Rural Annapolis Valley, Nova Scotia, Canada using Nitrite-impregnated Passive Samplers. Journal of the Air & Waste Management Association, 59(3), 310-320.

Gibson, M.D., Haelssig, J., Pierce, J.R., Parrington, M., Franklin, J.E., Hopper, J.T., Li, Z., Ward, T.J. (2015). A comparison of four receptor models used to quantify the boreal wildfire smoke contribution to surface $PM_{2.5}$ in Halifax, Nova Scotia during the BORTAS-B experiment. *Atmospheric Chemistry and Physics, 15,* 815-827. doi:10.5194/acp-15-815-2015

Gibson, M.D., Heal, M.R., Bache, D.H., Hursthouse, A.S., Beverland, I.J., Craig, S.E. Clark, C.F., Jackson. M.H., Guernsey, J., Jones, C. (2009). Using mass reconstruction along a four-site transect as a method to interpret PM10 in west-central Scotland, UK. *Journal of the Air and Waste Management Association, 59(12)*, 1429-1436. doi:10.3155/1047-3289.59.12.1429.

Gibson, M. D., Heal, M. R., Li, Z., Kuchta, J., King, G. H., Hayes, A., & Lambert, S. (2012). The spatial and seasonal variation of nitrogen dioxide and sulfur dioxide in Cape Breton Highlands National Park, Canada and the association with lichen abundance. Atmospheric Envrionment, 64(0), 303-311. doi:10.1016/j.atmosenv.2012.09.068

Gibson, M.D., Kundu, S., & Satish, M. (2013). Dispersion model evaluation of PM2.5, NOx and SO2 from point and major line sources in Nova Scotia, Canada using AERMOD Gaussian plume air dispersion model. Atmospheric Pollution Research, 4(2), 157-167. doi:10.5094/APR.2013.016

Gibson, M.D., Kuchta, J., Chisholm, L., Duck, T., Hopper, J., Beauchamp, S., Waugh, D., King, G., Pierce, J., Li, Z., Leaitch, R., Ward, T.J., Haelssig, J., Palmer, P.I. Source apportionment of speciated $PM_{2.5}$ over Halifax, Nova Scotia, during BORTAS-B, using pragmatic mass closure and principal component analysis. EGU General Assembly, April 7-12, 2013 2013a Vienna, Austria. Geophysical Research Abstracts.

Gibson, M.D., Pierce, J.R., Waugh, D., Kuchta, J.S., Chisholm, L., Duck, T.J., Hopper, J.T., Beauchamp, S., King, G.H., Franklin, J.E., Leaitch, W.R., Wheeler, A.J., Li, Z., Gagnon, G.A., Palmer, P.I. (2013). Identifying the sources driving observed $PM_{2.5}$ temporal variability over Halifax, Nova Scotia, during BORTAS-B. *Atmospheric Chemistry and Physics, 13,* 7199-7213. doi:10.5194/acp-13-7199-2013

Gibson, M.D., Ward, T. J., Wheeler, A.J., Guernsey, J.R., Seaboyer, M.P., Bazinet, P., King, G.H., Brewster, N.B., Kuchta, J., Potter, R., Stieb, D.M. (2010). Woodsmoke source apportionment in the Rural Annapolis Valley, Nova Scotia, Canada. Conference Proceedings of the 103rd Annual Conference of the Air and Waste Management Association, Calgary.

Glasow, R.V., Bobrowski, N. & Kern, C. (2009). The effects of volcanic eruptions on atmospheric chemistry. *Chemical Geology, 264(1-4),* 131-142. doi:10.1016/j.chemgeo.2008.08.020

Hao, L.Q., Yli-Pirilä, P., Tiitta, P., Romakkaniemi, S., Vaattovaara, P., Kajos, M.K., Rinne, J., Heijari, J, Kortelainen, A., Miettinen, P., Kroll, J.H., Holopainen, J.K., Smith, J.N., Joutsensaari, J., Kulmala, M., Worsnop, D.R., Laaksonen, A. (2009). New particle formation from the oxidation of direct emissions of pine seedlings. *Atmopsheric Chemistry and Physics, 9,* 8121-8137. Retrieved from http://www.atmos-chem-phys.net/9/8121/2009/acp-9-8121-2009.pdf on April 4, 2016.

Harrison, R.M. & Yin, J. (2008). Sources and processes affecting carbonaceous aerosol in central England. Atmospheric Environment, 42, 1413-1423.

Hopke, P.K. (1991). An introduction to Receptor Modeling. Chemom. Intell. Lab. System, 10, 21-43.

Haywood, J. & Boucher, O. (2000). Estimates of the direct and indirect radiative forcing due to tropospheric aerosols: A review. *Reviews of Geophysics, 38(4),* 513-543. doi:10.1029/1999RG000078

Hillemann, L., Zschoppe, A., Caldow, R., Sem, G.J., Wiedensohler, A. (2014). An ultrafine particle monitor for size-resolved number concentration measurements in atmospheric aerosols. *Journal of Aerosol Science, 68*, 14-24. doi:10.1016/j.jaerosci.2013.10.007

Hinds, W.C. (1998). *Aerosol Technology: Properties, Behavior, and Measurement of Airborne Particles, Second Edition.* USA: John Wiley & Sons, Inc., 1999.

Huisman, J. E. F., van Oostveen, P., & Weissing, F. J. (1999). Critical depth and critical turbulence: two different mechanisms for the development of phytoplankton blooms. *Limnology and Oceanography*, *44*(7), 1781-1787.

IPCC. (2001). *Climate Change 2001: Working Group I: The Scientific Basis.* Retrieved from http://www.ipcc.ch/ipccreports/tar/wg1/index.php?idp=160 on April 4, 2016.

IPCC. (2007). *Climate Change 2007: Working Group I: The Physical Science Basis.* Retrieved from https://www.ipcc.ch/publications_and_data/ar4/wg1/en/figure-spm-2.html on April 2, 2016.

IPCC. (2013). *Climate Change 2013: The Physical Science Basi*s. Retrieved from https://www.ipcc.ch/pdf/assessment-report/ar5/wg1/WG1AR5_Chapter07_FINAL.pdf on April 2, 2016.

Jaeglé, L., Quinn, P.K., Bates, T.S., Alexander, B., Lin, J.-T. (2011). Global distribution of sea salt aerosols: new constraints from in situ and remote sensing observations. *Atmospheric Chemistry and Physics, 11,* 3137-3157. doi:10.5194/acp-11-3137-2011.

Jeong, C.-H., Evans, G.J., Dann, T., Graham, M., Herod, D., Dabek-Zlotorzynska, E., Mathieu, D., Ding, L., Wang, D. (2008). Influence of biomass burning on wintertime fine particulate matter: Source contribution at a valley site in rural British Columbia. *Atmospheric Environment, 42*, 3684-3699.

Jeong, C.-H., McGuire, M.L., Herod, D., Dann, T., Dabek-Zlotorzynska, E., Wang, D., Ding, L., Celo, V., Mathieu, D., Evans, G. (2011). Receptor model based identification of $PM_{2.5}$ sources in Canadian cities. *Atmospheric Pollution Research, 2(2),* 158-171. doi:10.5094/APR.2011.021.

Kan, H., London, S.J., Chen, G., Zhang, Y., Song, G., Zhao, N., Jiang, L., Chen, B. (2007). Differentiating the effects of fine and coarse particles on daily mortality in Shanghai, China. *Environmental International, 33(3),* 376-384. doi:10.1016/j.envint.2006.12.001.

Keller, M.D., Bellows, W.K. & Guillard, R.L. (2009). Dimethyl Sulfide Production in Marine Phytoplankton. In Saltzman & Copper (Eds.), *Biogenic Sulfur in the Environment* (pp. 167-182). American Chemical Society. doi:10.1021/bk-1989-0393.

Kerminen, V.-M., Paramonov, M., Anttila, T., Riipinen, I., Fountoukis, C., Korhonen, H., Asmi, E., Laakso, L., Lihavainen, H., Swietlicki, E., Svenningsson, B., Asmi, A., Pandis, S.N., Kulmala, M., Petäjä, T. (2012). Cloud condensation nuclei production associated with atmospheric nucleation: a synthesis based on existing literature and new results. *Atmospheric Chemistry and Physics, 12*, 12037-12059. doi: 10.5194/acp-12-12037-2012.

Kim, E., & Hopke, P.K. (2004). Source Apportionment of Fine Particles in Washington, DC, Utilizing Temperature-Resolved Carbon Fractions. Air & Waste Management Association, 54, 773–785.

Kloster, S. (2006). *DMS cycle in the ocean-atmosphere system and its response to anthropogenic perturbations.* Retrieved from https://www.mpimet.mpg.de/fileadmin/publikationen/erdsystem_19.pdf on April 10, 2016.

Krecl, P., Targino, A.C., Johansson, C., Ström, J. (2015). Characterization and Source Apportionment of Submicron Particle Number Size Distributions in a Busy Street Canyon. *Aerosol and Air Quality Research, 15,* 220-233. doi:10.4209/aaqr.2014.06.0108

Krewski,, D., Jerret, M., Burnett, R.T., Ma, R., Hughes, E., Shi, Y., Turner, M.C., Pope III, A., Thurston, G., Calle, E.E., Thun, M.J. (2009). *Extended Follow-Up of Spatial Analysis of the American Cancer Society Study Linking Particulate Air Pollution and Mortality.* Retrieved from http://pubs.healtheffects.org/getfile.php?u=478 on April 3, 2016.

Kuhn, A. M., Fennel, K., & Mattern, J. P. (2015). Model investigations of the North Atlantic spring bloom initiation. *Progress in Oceanography*, *138*, 176-193.

Kulkarni, P., Baron, P.A. & Willeke, K. (2011). Aerosol Measurement: Principles, Techniques, and Applications, Third Edition. doi:10.1002/9781118001684

Kulmala, M., Vehkamäki, H., Petäjä, T., Dal Maso, M., Lauri, A., Kerminen, V.-M., Birmili, W., McMurry, P.H. (2004). Formation and growth rates of ultrafine atmospheric particles: a review of observations. *Journal of Aerosol Science, 35(2),* 143-176. doi:10.1016/j.jaerosci.2003.10.003

Li, W.K.W. (2014). The state of phytoplankton and bacterioplankton on the Scotian Shelf and Slope: Atlantic Zone Monitoring Program 1997-2013. (No. 303), Canadian Technical Report of Hydrography and Ocean Sciences. Bedford Institute of Oceanography.

Li, W.K.W. & Harrison, W.G. (2008). Propagation of an atmospheric signal to phytoplankton in a small basin. Limnol. Oceanogr. 53, 1734–1745.

MacNeill, M., Kearney, J., Wallace, L., Gibson, M., Héroux, M.E., Kuchta, J., Guernsey, J.R., Wheeler, A.J. (2014). Quantifying the contribution of ambient and indoor-generated fine particles to indoor air in residential environments. Indoor Air, 24(4), 362-375. doi:10.1111/ina.12084

Mahadevan, A., D'Asaro, E., Lee, C., & Perry, M. J. (2012). Eddy-driven stratification initiates North Atlantic spring phytoplankton blooms. *Science*, *337*(6090), 54-58.

Malin, L.P.S., Turner, G., Holligan, P. (1994). Dimethyl sulphide and Phaeocystis: A review. *Journal of Marine Systems, 5(1),* 41-53. doi:10.1016/0924-7963(94)90015-9.

Manders, A.M.M., Schaap, M., Querol, X., Albert, M.F.M.A., Vercauteren, J., Kuhlbusch, T.A.J., Hoogerbrugge, R. (2010). Sea salt concentrations across the European continent. *Atmospheric Environment, 44(20)*, 2434-2442. doi:10.1016/j.atmosenv.2010.03.028.

McNeilly, J.D., Heal, M.R., Beverland, I.J., Howe, A., Gibson, M.D., Hibbs, L.R., MacNee, W., Donaldson, K. (2004). Soluble transition metals cause the pro-inflammatory effects of welding fumes in vitro. Toxicology and Applied Pharmacology, 196, 95-107.

Miller-Schulze, J.P., Shafer, M., Schauer, J.J., Heo, J., Soloman, P.A., Lantz, J., Artamonova, M., Chen, B., Imashev, S., Sverdlik, L., Carmichael, G., Deminter, J. (2015). Seasonal contribution of mineral dust and other major components to particulate matter at two remote sites in Central Asia. *Atmospheric Envrionment, 119,* 11-20. doi:10.1016/j.atmosenv.2015.07.011

Mirowsky, J., Hickey, C., Horton, L., Blaustein, M., Galdanes, K., Peltier, R.E., Chillrud, S., Chen, L.C., Ross, J., Nadas, A., Lippmanm, M., Gordon, T. (2013). The effect of particle size, location and season on the toxicity of urban and rural particulate matter. *Inhalation Toxicology, 25(13),* 747-757. doi: 10.3109/08958378.2013.846443

NASA. (2015). *NAAMES Proposal Science.* Retrieved from http://naames.larc.nasa.gov/pdf/NAAMES_Proposal_Science.pdf on April 8, 2016.

NASA. (2016a). *MODIS.* Retrieved from http://terra.nasa.gov/about/terra-instruments/modis on April 10, 2016.

NASA. (2016b.). *Polar Orbiting Missions.* Retrieved from http://npp.gsfc.nasa.gov/viirs.html on April 10, 2016.

NASA. (n.d.). *MODIS Design.* Retrieved from http://modis.gsfc.nasa.gov/about/design.php on April 10, 2016.

Oberdörster, G. (2001). Pulmonary effects of inhaled ultrafine particles. *International Archives of Occupational and Environmental Health, 74(1),* 1-8. Retrieved from http://www.ncbi.nlm.nih.gov/pubmed/11196075 on April 5, 2016.

Oberdörster, G., Oberdörster, E., Oberdörster, J. (2005). Nanotoxicology: An Emerging Discipline Evolving from Studies of Ultrafine Particles. *Environmental Health Perspectives, 113*(7), 823-839. doi:10.1289/ehp.7339

O'Dowd, C.D., Hämeri, K., Mäkelä, J.M., Pirjola, L., Kulmala, M., Jennings, S.G., Berresheim, H., Hansson, H.-C., de Leeuw, G., Kunz, G., Allen, A., Hewitt, C.N., Jackson, A., Viisanen, Y., Hoffman, T. (2002). A dedicated study of New Particle

Formation and Fate in Coastal Environment (PARFORCE): Overview of objectives and achievements. *Journal of Geophysical Research, 107(D19),* 8108. doi:10.1029/2001JD000555.

Orellana, M.V., Matrai, P.A., Leck, C., Rauschenberg, C.D., Lee, A.M., Coz, E. (2011). Marine microgels as a source of cloud condensation nuclei in the high arctic. *Proceedings of the National Academy of Sciences of the United States, 108(33),* 13612-13617. doi: 10.1073/pnas.1102457108.

Øvrevik, J., Låg, M., Refsnes, M., Nafstad, P., Hetlund R.B., Dybing, E. (2006). Particulate matter properties and health effects: consistency of epidemiological and toxicological studies. *Human & Experimental Toxicology, 25(10),* 559-579. doi: 10.1177/096032706072520

Paatero, P. & Trapper, U. (1994). Positive matrix factorization: a non-negative factor model with optimal utilization of error estimates of data values. *Environmetrics, 5*, 111-126.

Palmer, P.I., Parrington, M., Lee, J.D., Lewis, A.C., Rickard, A.R., Bernath, P.F., Duck, T.J., Waugh, D.L., Tarasick, D.W., Andrews, S., Aruffo, E., Bailey, L.J., Barrett, E., Bauguitte, S.J.-B., Vurry, K.R., Di Carlo, P., Chisholm, L., Dan, L., Forster, G., Franklin, J.E., Gibson, M.D., Griffin, D., Helmig, D., Hopkins, J.R., Hopper, J.T., Jenkin, M.E., Kindred, D., Kliever, J., Le Breton, M., Matthiesen, S., Maurice, M., Moller, S., Moore, D.P., Oram, D.E., O'Shea, S.J., Owen, R.C., Pagniello, C.M.L.S., Pawson, S., Percival, C.J., Pierce, J.R., Punjabi, S., Purvis, R.M., Remedios, J.J., Rotermund, K.M., Sakamoto, K.M., da Silva, A.M., Strawbridge, K.B., Strong, K., Taylor, J., Trigwell, R., Tereszchuk, K.A., Walker, K.A., Weaver, D., Whaley, C., Young, J.C. (2013). Quantifying the impact of BOReal forest firels on Tropospheric oxidants over the Atlantic using Aircraft and Satellites (BORTAS) experiment: design, execution and science overview.

Atmospheric Chemistry and Physics, 13, 6239-6261. doi:10.5194/acp-13-6239-2013

Parks Canada. (2013). *Sable Island National Park Reserve.* Retrieved from http://www.pc.gc.ca/eng/pn-np/ns/sable/ne.aspx on March 20, 2016.

Peters, A., Wichmann, H.E., Tuch, T., Heinrich, J., Heyder, J. (1997). Respiratory effects are associated with the number of ultrafine particles. *American Journal of Respiratory and Critical Care Medicine, 155(4),* 1376-1383. doi:10.1164/ajrccm.155.4.9105082.

Peters, T. M., Leith, D. (2003). Concentration measurement and counting efficiency of aerodynamic particle sizer 3321. *Journal of Aerosol Science, 34*(5), 627-634. doi:10.1016/S0021-8502(03)00030-2.

Petters, M.D. & Kreidenweis, S.M. (2007). A single parameter representation of hygroscopic growth and cloud condensation nucleus activity. *Atmospheric Chemistry and Physics, 7,* 1961-1971. doi:10.5194/acp-7-1961-2007.

Pierce, J.R. & Adams, P.J. (2006). Global evaluation of CCN formation by direct emission of sea salt and growth of ultrafine sea salt. *Journal of Geophysical Research-Atmospheres, 111(D6).* doi: 10.1029/2005JD006186

Poluboyarov, V.A., Korotaeva, Z.A. & Andryushkova, O.A. (2000). Preparation of Ultrafine Particles by Mechanical Processing. *Inorganic Materials, 37(5),* 592-595. Retrieved from http://link.springer.com/article/10.1023/A:1017585018929#page-2 on April 9, 2016.

Pope III, C.A., Burnett, R.T., Thun, M.J., Calle, E.E., Krewski, D., Ito, K., Thurston, G.D. (2002). Lung caner, cardiopulmonary mortality, and long-term exposure to fine particulate air pollution. *Journal of the American Medical Association, 287(9),* 1132-1141. doi:10.1001/jama.287.9.1132.

Pummer, B.G., Budke, C., Augustin-Bauditz, S., Niedermeier, D., Felgitsch, L., Kampf, C.J., Huber, R.G., Liedl, K.R., Loerting, T., Moschen, T., Schauperl, M., Tollinger, M., Morris, C.E., Wex, H., Grothe, H., Poschl, U., Koop, T., Frolich-Nowoisky, J. (2014). Ice nucleation by water soluble macromolecules. *Atmospheric Chemistry and Physics, 15*, 4077-4091. doi:10.5194/acp-15-4077-2015

Querol, X., Alastuey, A., Pey, J., Cusack, M., Pérez, N., Mihalopoulos, N., Theodosi, C., Gerasopoulos, E., Kubilay, N., Koçak, M. (2009). Variability in regional background aerosols within the Mediterranean, *Atmospheric Chemistry and Physics*, *9*, 4575–4591. doi:10.5194/acp-9-4575-2009, 2009

Salma, I., Balashazy, I., Winkler-Heil, R., Hofmann, W., Zaray, G. (2002). Effect of particle mass size distribution on the deposition of aerosols in the human respiratory system. *Journal of Aerosol Science, 33(1),* 119-132. doi: 10.1016/S0021-8502(01)00154-9

Smith, M. J., Tittensor, D. P., Lyutsarev, V., & Murphy, E. (2015). Inferred support for disturbance- recovery hypothesis of North Atlantic phytoplankton blooms. *Journal of Geophysical Research: Oceans*, *120*(10), 7067-7090.

Snider, G., Weagle, C. L., Martin, R. V., van Donkelaar, A., Conrad, K., Cunningham, D., Gordon, C., Zwicker, M., Akoshile, C., Artaxo, P., Anh, N.X., Brook, J., Dong, J., Garland, R.M., Greenwald, R., Griffith, D., He, K., Holben, B.N., Kahn, R., Koren, I., Lagrosas, N., Lestari, P., Ma, Z., Vanderlei Martins, J., Quel, E.J., Rudich, Y., Salam, A., Tripathi, S.N., Yu, C., Zhang, Q., Brauer, M., Cohen, A., Gibson, M.D., Liu, Y. (2015). SPARTAN: a global network to evaluate and enhance satellite based estimates of ground-level particulate matter for global health applications. Atmos. Meas. Tech., 8, 505-521.

Snider, G., Weagle, C.L., Murdymootoo, K.K., Ring, A., Ritchie, Y., Walsh, A., Akoshile, C., Anh, N.X., Brook, J., Qonitan, F.D., Dong, J., Griffith, D., He, K., Holben, B.N., Kahn, R., Lagrosas, N., Lestari, P., Ma, Z., Misra, A., Quel, E.J. Salam, A., Schichtel, B., Segev, L., Tripathi, S.N., Wang, C., Yu, C., Zhang, Q., Zhang, Y., Brauer, M., Cohen, A., Gibson, M.D., Liu, Y., Martins, J.V., Rudich, Y., Martin, R.V. (2016). Variation in Global Composition of $PM_{2.5}$: Emerging Results from SPARTAN. *Atmospheric Chemistry and Physics.* Manuscript under review. doi:10.5194/acp-2016-62, 2016

Solomon, P.A. & Hopke, P.K. (2008). The U.S. Environmental Protection Agency's Particulate Matter Supersites Program: An Integrated Synthesis of Scientific Findings and Policy- and Health-Relevant Insights. *Journal of the Air and Waste Management Association, 58*.

Stein, A.F., Draxler, R.R., Rolph, G.D., Stunder, B.J.B., Cohen, M.D., Ngan, F. (2015). *NOAA's HYSPLIT Atmospheric Transport and Dispersion Modeling System.* Retrieved from http://journals.ametsoc.org/doi/pdf/10.1175/BAMS-D-14-00110.1 on March 31, 2016.

Stein, A.F., Isakov, V., Godowitch, J., Draxler, R.R. (2007). A hybrid modeling approach to resolve pollutant concentrations in an urban area. *Atmospheric Environment, 41,* 9410–9426. doi:10.1016/j.atmosenv.2007.09.004

Szymanski, W.W., Nagy, A., Czitrovszky, A. (2009). Optical particle spectrometry – Problems and prospects. *Journal of Quantitative Spectroscopy and Radiative Transfer, 110*(11), 918-929. doi:10.1016/j.jqsrt.2009.02.024

Teather, K., Hogan, N., Critchley, K., Gibson, M. D., Craig, S. E., & Hill, J. (2013). Examining the Links Between Air Quality, Climate Change and Respiratory Health in Qatar Avicenna. doi:10.5339/avi.2013.9

Thurston, G.D. & Spengler, J.D. (1985). A Quantitative Assessment of Source Contributions to Inhalable Particulate Matter Pollution in Metropolitan Boston. *Atmospheric Environment (1967), 19*, 9-25.

TSI. (2012a). *Aerodynamic Particle Sizer Model 3321 Theory of Operation.* Retrieved from http://www.tsi.com/uploadedFiles/_Site_Root/Products/Literature/Brochures/3321%20Operation%20brochure%20US-5001468_WEB.pdf on November 26, 2015.

TSI. (2012b). *DustTrak DRX Aerosol Monitor Theory of Operation.* Retrieved from http://www.tsi.com/uploadedFiles/_Site_Root/Products/Literature/Application_Notes/EXPMN-002_DustTrak_DRX_Theory_of_Operation.pdf on January 2, 2016.

TSI. (2012c). *Ultrafine Particle Monitor Model 3031 and 3031-1 Theory of Operation.* Retrieved from http://www.tsi.com/uploadedFiles/_Site_Root/Products/Literature/Application_Notes/Theory_Of_Operation_3031.pdf on December 6, 2015.

TSI. (2012d). *Ultrafine Particle (UFP) Monitor Model 3031.* Retrieved from http://www.tsi.com/uploadedFiles/_Site_Root/Products/Literature/Spec_Sheets/3031_5001114-spec.pdf on December 6, 2015.

TSI. (2014a). *DustTrak DRX Aerosol Monitors Models 8533, 8533EP and 8534.* Retrieved from http://www.tsi.com/uploadedFiles/_Site_Root/Products/Literature/Spec_Sheets/DustTrak-DRX-6001981_USA-web.pdf on December 29, 2015.

TSI. (2014b). *Model 3031200 Environmental Sampling System Field Setup with Model 3031 Ultrafine Particle Monitor.* Retrieved from http://www.tsi.com/uploadedFiles/_Site_Root/Products/Literature/Application_Notes/UFP-002_Model_3031200_Env_Samp_Sys.pdf on December 6, 2015.

TSI. (2015). *Aerodynamic Particle Sizer Model 3321 High-Resolution Aerodynamic Sizing Plus Light-Scattering Intensity.* Retrieved from http://www.tsi.com/uploadedFiles/_Site_Root/Products/Literature/Spec_Sheets/3321.pdf on November 26, 2015.

Twohy, C.H. & Poellot, M.R. (2005). Chemical characteristics of ice residual nuclei in anvil cirrus clouds: evidence for homogeneous and heterogeneous ice formation. *Atmospheric Chemistry and Physics, 5,* 2289-2297. Retrieved from http://www.atmos-chem-phys.net/5/2289/2005/acp-5-2289-2005.pdf on April 5, 2016.

Wallace, L. & Ott, W. (2010). Personal exposure to ultrafine particles. *Journal of Exposure Science and Environmental Epidemiology, 21,* 20-30. doi:10.1038/jes.2009.59

Wang, T., Carroll, M.A., Albercook, G.M., Owens, K.R., Duderstadt, K.A., Markevitch, A.N., Parrish, D.D., Holloway, J.S., Fehsenfeld, F.C, Forbes, G., Ogren, J. (1996). Ground-based measurements of NO_x and total reactive oxidized nitrogen (NO_y) at Sable Island, Nova Scotia, during the NARE 1993 summer intensive. *Journal of Geophysical Research, 101*(D22), 28991-29004. Retrieved from http://onlinelibrary.wiley.com/doi/10.1029/96JD01090/epdf

Wang, X., Chancellor, G., Evenstad, J., Farnsworth, J.E., Hase, A., Olson, G.M., Screenath, A., Agarwal, J.K. (2009). A Novel Optical Instrument for Estimating Size Segregated Aerosol Mass Concentration in Real Time. *Aerosol Science and Technology, 43(9),* 939-950. doi:10.1080/02786820903045141.

Ward, T.J., Hamilton, J., Raymond F., Smith, G.C. (2004). The Missoula, Montana PM2.5 speciation study - seasonal average concentrations. *Atmospheric Environment, 38*, 6371-6379.

Ward, T.J., Rinehart, L.R. & Lange, T. (2006). The 2003/2004 Libby, Montana PM2.5 Source Apportionment Research Study. *Aerosol Science and Technology, 40,* 166-177.

Ward, T.J., Trost, B., Conner, J., Flanagan, J., Jayanty, R.K.M. (2012). PM2.5 Source Apportionment in a Subarctic Airshed - Fairbanks, Alaska. *Aerosol and Air Quality Research, 12*, 536-543.

Waugh, D., Inkpen, T., Hingston, M., Keast, S., McPherson, J., Worthy, D., Forbes, G. (2010). Sable Island Air Monitoring Program Report: 2003-2006. Environmental Studies Research Funds Report No. 181. Dartmouth. 56 p.

Wheeler, A. J., Gibson, M. D., MacNeill, M., Ward, T. J., Wallace, L.A., Kuchta, J., Seaboyer, M., Dabek, E., Guernsey, J.R., Stieb, D. (2014). Impacts on Indoor Air Quality from using Electrostatic Air Cleaners in Residences with Woodstoves. *Environmental Science & Technology, 48*(20).

WHO. (2013). *Health Effects of Particulate Matter.* Retrieved from http://www.euro.who.int/__data/assets/pdf_file/0006/189051/Health-effects-of-particulate-matter-final-Eng.pdf on April 2, 2016.

WHO. (2014). *Ambient (outdoor) air pollution database, by country and city*. Retrieved from http://www.who.int/phe/health_topics/outdoorair/databases/cities/en/ on April 5, 2016.

Wichmann, H.E., Spix, C., Tuch, T., Wölke, G., Peters, A., Heinrich, J., Kreyling, W.G., Heyder, J. (2000). *Daily mortality and fine and ultrafine particles in Erfurt,* *Germany part 1: role of particle number and particle mass.* Retrieved from http://europepmc.org/abstract/med/11918089 on March 31, 2016

Yin, J., Allen, A.G., Harrison, R.M., Jennings, S.G., Wright, E., Fitzpatrick, M., Healy, T., Barry, E., Ceburnis, D., Mccusker, D. (2005). Major component composition of urban PM10 and PM2.5 in Ireland. *Atmopsheric Research, 78*, 149-165.

Yin, J. & Harrison, R.M. (2008). Pragmatic mass closure study for PM1.0, PM2.5 and PM10 at roadside, urban background and rural sites. *Atmospheric Environment, 42,* 980-988.

Zhu, Y., Hinds, W., Kim, S., Shen, S., Sioutas, C. (2002a). Study of ultrafine particles near a major highway with heavy-duty diesel traffic. *Atmospheric Environment, 36(27),* 4323-4335. doi:10.1016/S1352-2310(02)00354-0

Zhu, Y., Hinds, W., Kim, S., Sioutas, C. (2002b). Concentration and Size Distribution of Ultrafine Particles Near a Major Highway. *Journal of the Air & Waste Management Association, 52(9)*, 1032-1042. doi: 10.1080/10473289.2002.10470842

APPENDIX: HYSPLIT Air Mass Back Trajectories

NOAA HYSPLIT MODEL
Backward trajectory ending at 0000 UTC 01 Oct 15
GDAS Meteorological Data

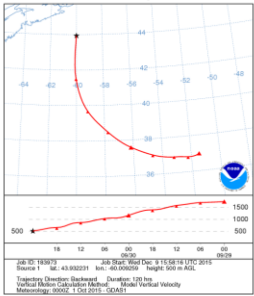

NOAA HYSPLIT MODEL
Backward trajectory ending at 1200 UTC 01 Oct 15
GDAS Meteorological Data

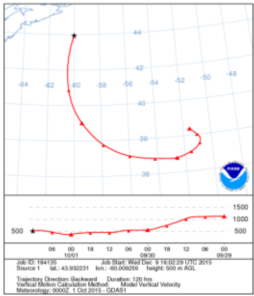

NOAA HYSPLIT MODEL
Backward trajectory ending at 0000 UTC 02 Oct 15
GDAS Meteorological Data

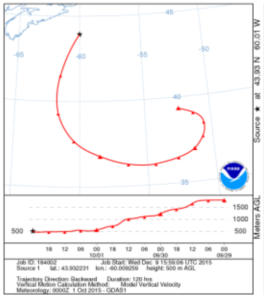

NOAA HYSPLIT MODEL
Backward trajectory ending at 1200 UTC 02 Oct 15
GDAS Meteorological Data

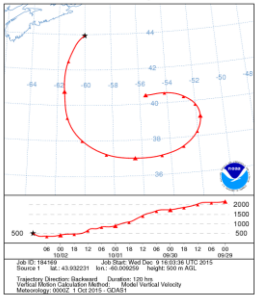

NOAA HYSPLIT MODEL
Backward trajectory ending at 0000 UTC 03 Oct 15
GDAS Meteorological Data

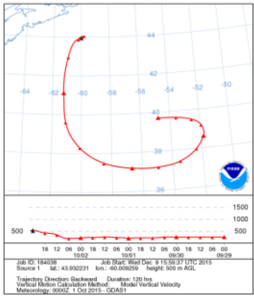

NOAA HYSPLIT MODEL
Backward trajectory ending at 1200 UTC 03 Oct 15
GDAS Meteorological Data

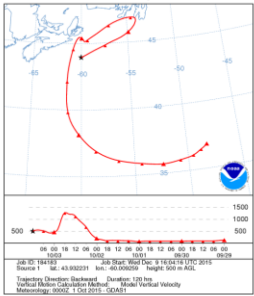

NOAA HYSPLIT MODEL
Backward trajectory ending at 0000 UTC 04 Oct 15
GDAS Meteorological Data

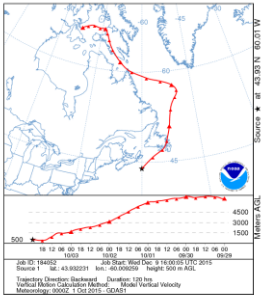

NOAA HYSPLIT MODEL
Backward trajectory ending at 1200 UTC 04 Oct 15
GDAS Meteorological Data

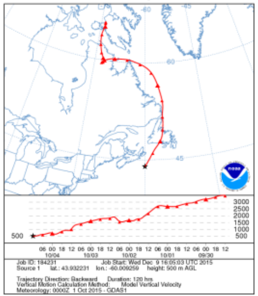

NOAA HYSPLIT MODEL
Backward trajectory ending at 0000 UTC 05 Oct 15
GDAS Meteorological Data

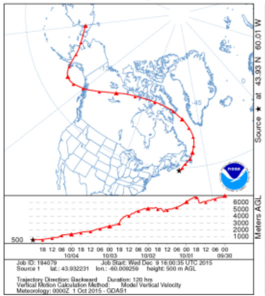

NOAA HYSPLIT MODEL
Backward trajectory ending at 1200 UTC 05 Oct 15
GDAS Meteorological Data

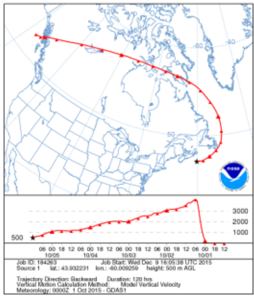

NOAA HYSPLIT MODEL
Backward trajectory ending at 0000 UTC 06 Oct 15
GDAS Meteorological Data

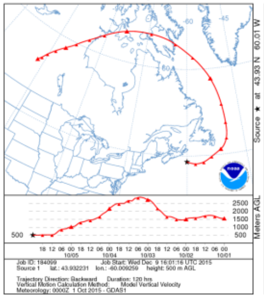

NOAA HYSPLIT MODEL
Backward trajectory ending at 1200 UTC 06 Oct 15
GDAS Meteorological Data

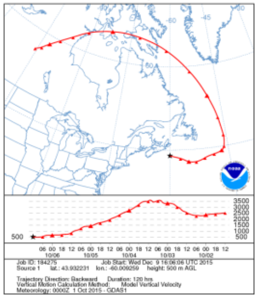

NOAA HYSPLIT MODEL
Backward trajectory ending at 0000 UTC 07 Oct 15
GDAS Meteorological Data

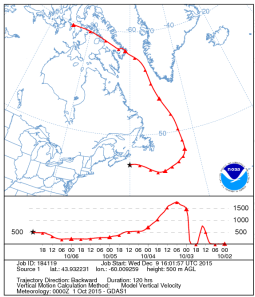

NOAA HYSPLIT MODEL
Backward trajectory ending at 1200 UTC 07 Oct 15
GDAS Meteorological Data

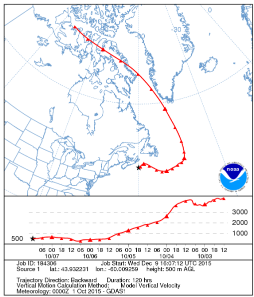

NOAA HYSPLIT MODEL
Backward trajectory ending at 0000 UTC 08 Oct 15
GDAS Meteorological Data

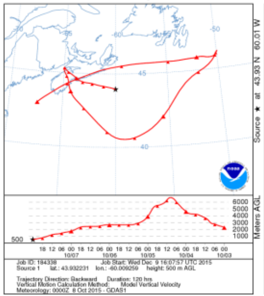

NOAA HYSPLIT MODEL
Backward trajectory ending at 1200 UTC 08 Oct 15
GDAS Meteorological Data

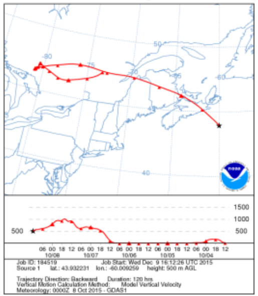

NOAA HYSPLIT MODEL
Backward trajectory ending at 0000 UTC 09 Oct 15
GDAS Meteorological Data

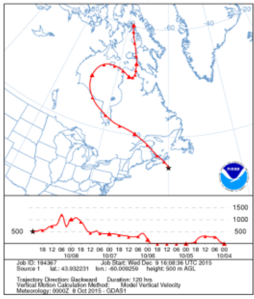

NOAA HYSPLIT MODEL
Backward trajectory ending at 1200 UTC 09 Oct 15
GDAS Meteorological Data

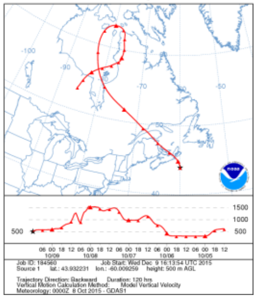

NOAA HYSPLIT MODEL
Backward trajectory ending at 0000 UTC 10 Oct 15
GDAS Meteorological Data

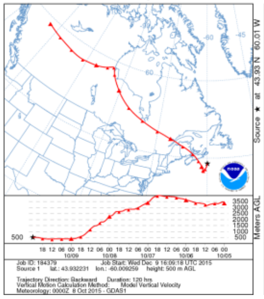

NOAA HYSPLIT MODEL
Backward trajectory ending at 1200 UTC 10 Oct 15
GDAS Meteorological Data

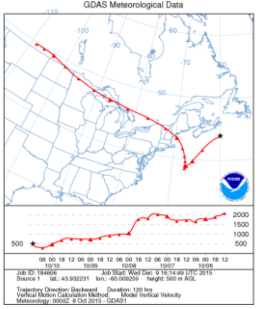

NOAA HYSPLIT MODEL
Backward trajectory ending at 0000 UTC 11 Oct 15
GDAS Meteorological Data

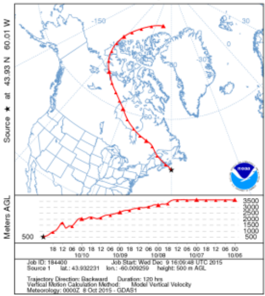

NOAA HYSPLIT MODEL
Backward trajectory ending at 1200 UTC 11 Oct 15
GDAS Meteorological Data

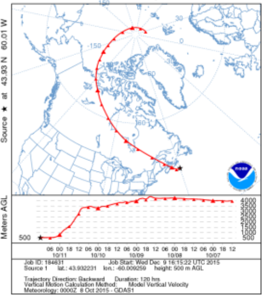

NOAA HYSPLIT MODEL
Backward trajectory ending at 0000 UTC 12 Oct 15
GDAS Meteorological Data

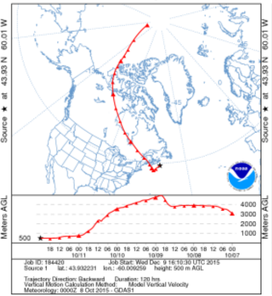

NOAA HYSPLIT MODEL
Backward trajectory ending at 1200 UTC 12 Oct 15
GDAS Meteorological Data

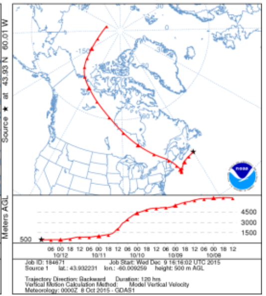

NOAA HYSPLIT MODEL
Backward trajectory ending at 0000 UTC 13 Oct 15
GDAS Meteorological Data

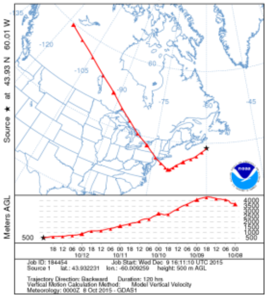

NOAA HYSPLIT MODEL
Backward trajectory ending at 1200 UTC 13 Oct 15
GDAS Meteorological Data

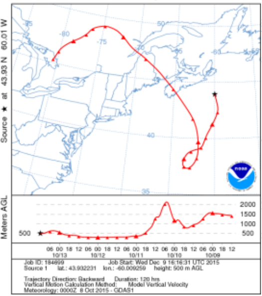

NOAA HYSPLIT MODEL
Backward trajectory ending at 0000 UTC 14 Oct 15
GDAS Meteorological Data

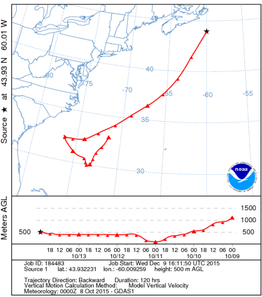

NOAA HYSPLIT MODEL
Backward trajectory ending at 1200 UTC 14 Oct 15
GDAS Meteorological Data

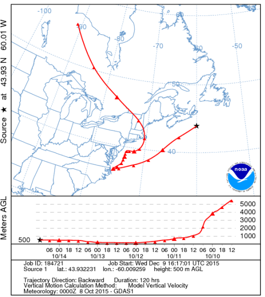

NOAA HYSPLIT MODEL
Backward trajectory ending at 0000 UTC 15 Oct 15
GDAS Meteorological Data

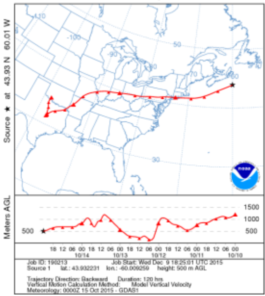

NOAA HYSPLIT MODEL
Backward trajectory ending at 1200 UTC 15 Oct 15
GDAS Meteorological Data

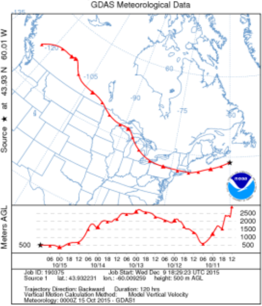

NOAA HYSPLIT MODEL
Backward trajectory ending at 0000 UTC 16 Oct 15
GDAS Meteorological Data

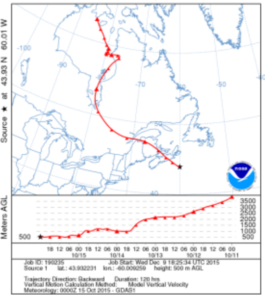

NOAA HYSPLIT MODEL
Backward trajectory ending at 1200 UTC 16 Oct 15
GDAS Meteorological Data

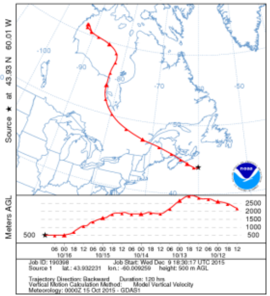

NOAA HYSPLIT MODEL
Backward trajectory ending at 0000 UTC 17 Oct 15
GDAS Meteorological Data

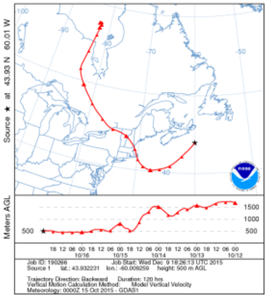

NOAA HYSPLIT MODEL
Backward trajectory ending at 1200 UTC 17 Oct 15
GDAS Meteorological Data

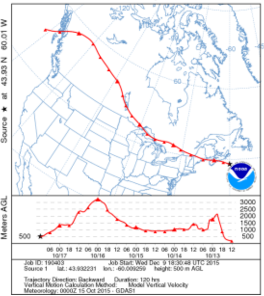

NOAA HYSPLIT MODEL
Backward trajectory ending at 0000 UTC 18 Oct 15
GDAS Meteorological Data

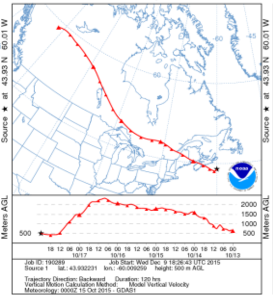

NOAA HYSPLIT MODEL
Backward trajectory ending at 1200 UTC 18 Oct 15
GDAS Meteorological Data

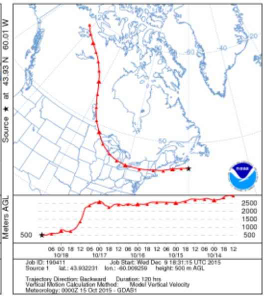

NOAA HYSPLIT MODEL
Backward trajectory ending at 0000 UTC 19 Oct 15
GDAS Meteorological Data

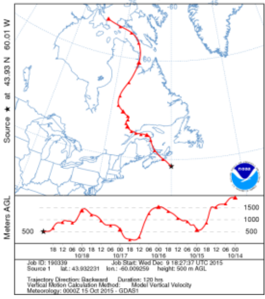

NOAA HYSPLIT MODEL
Backward trajectory ending at 1200 UTC 19 Oct 15
GDAS Meteorological Data

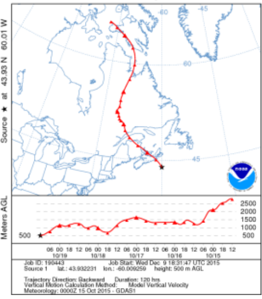

NOAA HYSPLIT MODEL
Backward trajectory ending at 0000 UTC 20 Oct 15
GDAS Meteorological Data

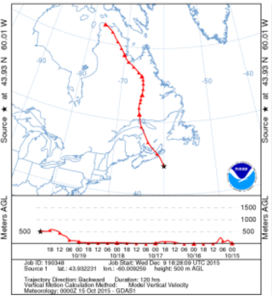

NOAA HYSPLIT MODEL
Backward trajectory ending at 1200 UTC 20 Oct 15
GDAS Meteorological Data

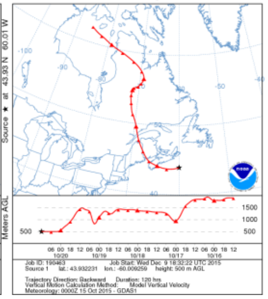

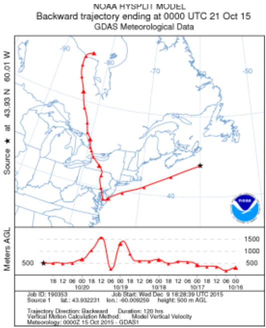
NOAA HYSPLIT MODEL
Backward trajectory ending at 0000 UTC 21 Oct 15
GDAS Meteorological Data
Source ★ at 43.93 N 60.01 W
Meters AGL

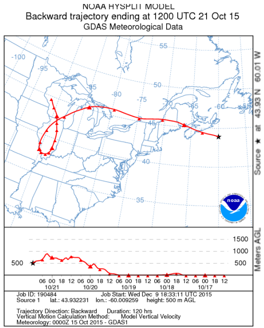
NOAA HYSPLIT MODEL
Backward trajectory ending at 1200 UTC 21 Oct 15
GDAS Meteorological Data
Source ★ at 43.93 N 60.01 W
Meters AGL

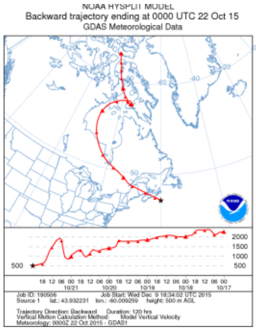
NOAA HYSPLIT MODEL
Backward trajectory ending at 0000 UTC 22 Oct 15
GDAS Meteorological Data
Source ★ at 43.93 N 60.01 W
Meters AGL

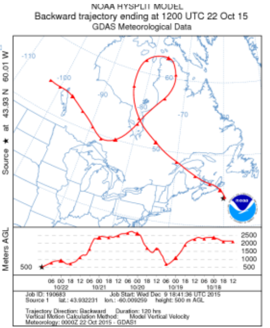
NOAA HYSPLIT MODEL
Backward trajectory ending at 1200 UTC 22 Oct 15
GDAS Meteorological Data
Source ★ at 43.93 N 60.01 W
Meters AGL

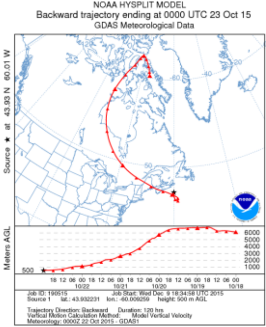
NOAA HYSPLIT MODEL
Backward trajectory ending at 0000 UTC 23 Oct 15
GDAS Meteorological Data
Source ★ at 43.93 N 60.01 W
Meters AGL

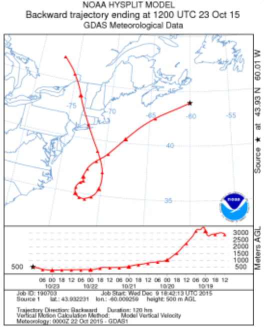
NOAA HYSPLIT MODEL
Backward trajectory ending at 1200 UTC 23 Oct 15
GDAS Meteorological Data
Source ★ at 43.93 N 60.01 W
Meters AGL

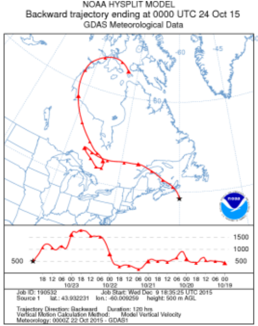
NOAA HYSPLIT MODEL
Backward trajectory ending at 0000 UTC 24 Oct 15
GDAS Meteorological Data
Source ★ at 43.93 N 60.01 W
Meters AGL

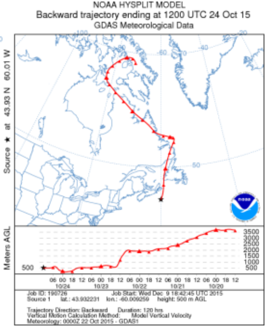
NOAA HYSPLIT MODEL
Backward trajectory ending at 1200 UTC 24 Oct 15
GDAS Meteorological Data
Source ★ at 43.93 N 60.01 W
Meters AGL

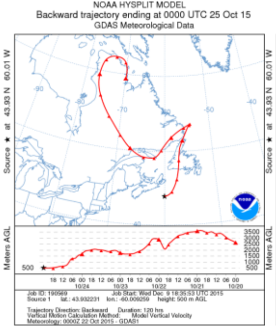
NOAA HYSPLIT MODEL
Backward trajectory ending at 0000 UTC 25 Oct 15
GDAS Meteorological Data
Source ★ at 43.93 N 60.01 W
Meters AGL

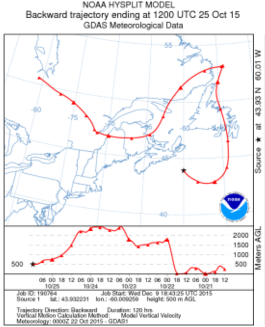
NOAA HYSPLIT MODEL
Backward trajectory ending at 1200 UTC 25 Oct 15
GDAS Meteorological Data
Source ★ at 43.93 N 60.01 W
Meters AGL

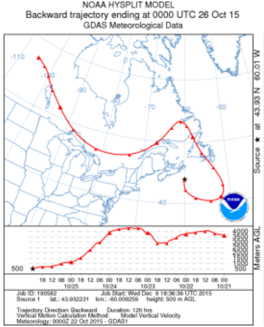
NOAA HYSPLIT MODEL
Backward trajectory ending at 0000 UTC 26 Oct 15
GDAS Meteorological Data
Source ★ at 43.93 N 60.01 W
Meters AGL

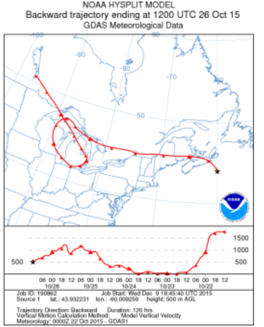
NOAA HYSPLIT MODEL
Backward trajectory ending at 1200 UTC 26 Oct 15
GDAS Meteorological Data
Source ★ at 43.93 N 60.01 W
Meters AGL

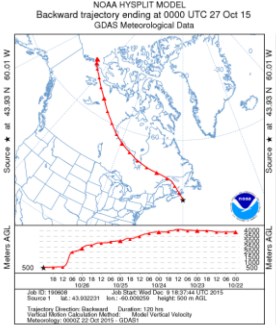
NOAA HYSPLIT MODEL
Backward trajectory ending at 0000 UTC 27 Oct 15
GDAS Meteorological Data
Source ★ at 43.93 N 60.01 W
Meters AGL

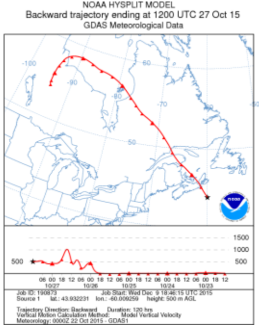
NOAA HYSPLIT MODEL
Backward trajectory ending at 1200 UTC 27 Oct 15
GDAS Meteorological Data
Source ★ at 43.93 N 60.01 W
Meters AGL

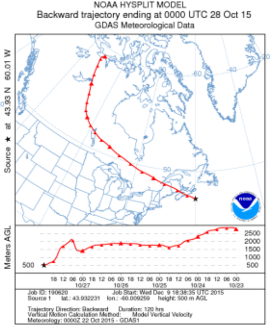
NOAA HYSPLIT MODEL
Backward trajectory ending at 0000 UTC 28 Oct 15
GDAS Meteorological Data
Source ★ at 43.93 N 60.01 W
Meters AGL

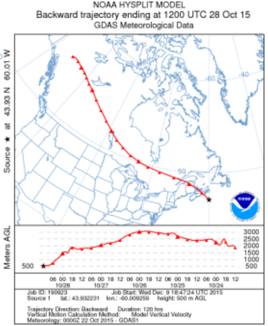
NOAA HYSPLIT MODEL
Backward trajectory ending at 1200 UTC 28 Oct 15
GDAS Meteorological Data
Source ★ at 43.93 N 60.01 W
Meters AGL

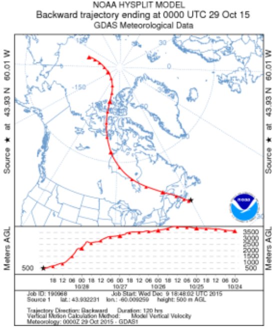
NOAA HYSPLIT MODEL
Backward trajectory ending at 0000 UTC 29 Oct 15
GDAS Meteorological Data
Source ★ at 43.93 N 60.01 W
Meters AGL

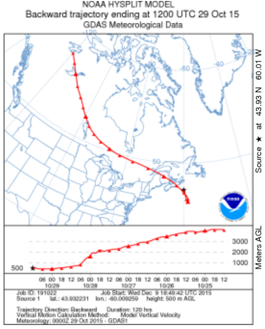
NOAA HYSPLIT MODEL
Backward trajectory ending at 1200 UTC 29 Oct 15
GDAS Meteorological Data
Source ★ at 43.93 N 60.01 W
Meters AGL

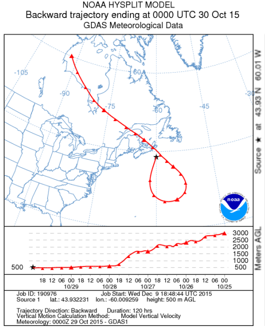
NOAA HYSPLIT MODEL
Backward trajectory ending at 0000 UTC 30 Oct 15
GDAS Meteorological Data
Source ★ at 43.93 N 60.01 W
Meters AGL

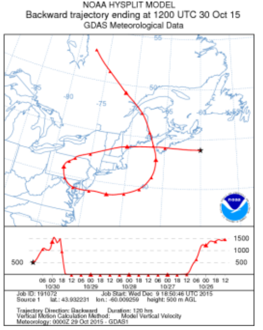
NOAA HYSPLIT MODEL
Backward trajectory ending at 1200 UTC 30 Oct 15
GDAS Meteorological Data
Source ★ at 43.93 N 60.01 W
Meters AGL

NOAA HYSPLIT MODEL
Backward trajectory ending at 0000 UTC 31 Oct 15
GDAS Meteorological Data

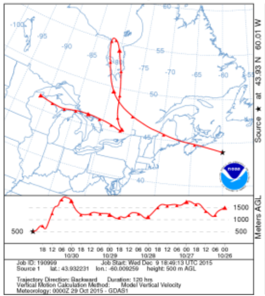

NOAA HYSPLIT MODEL
Backward trajectory ending at 1200 UTC 31 Oct 15
GDAS Meteorological Data

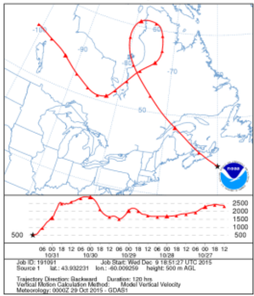

NOAA HYSPLIT MODEL
Backward trajectory ending at 0000 UTC 01 Nov 15
GDAS Meteorological Data

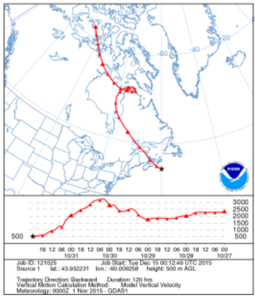

NOAA HYSPLIT MODEL
Backward trajectory ending at 1200 UTC 01 Nov 15
GDAS Meteorological Data

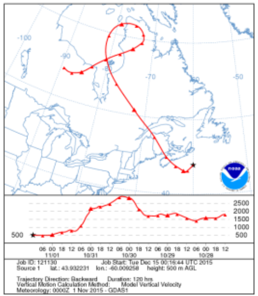

NOAA HYSPLIT MODEL
Backward trajectory ending at 0000 UTC 02 Nov 15
GDAS Meteorological Data

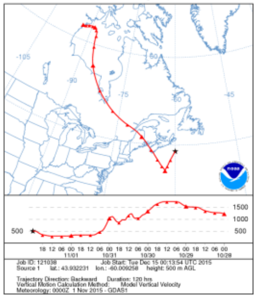

NOAA HYSPLIT MODEL
Backward trajectory ending at 1200 UTC 02 Nov 15
GDAS Meteorological Data

NOAA HYSPLIT MODEL
Backward trajectory ending at 0000 UTC 03 Nov 15
GDAS Meteorological Data

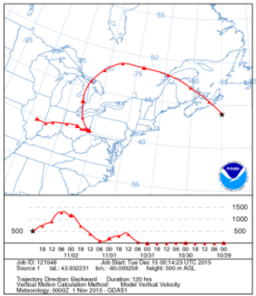

NOAA HYSPLIT MODEL
Backward trajectory ending at 1200 UTC 03 Nov 15
GDAS Meteorological Data

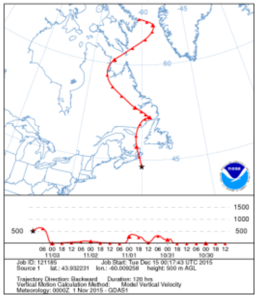

NOAA HYSPLIT MODEL
Backward trajectory ending at 0000 UTC 04 Nov 15
GDAS Meteorological Data

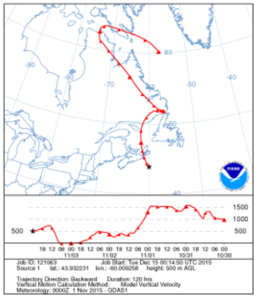

NOAA HYSPLIT MODEL
Backward trajectory ending at 1200 UTC 04 Nov 15
GDAS Meteorological Data

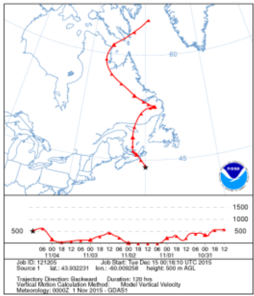

NOAA HYSPLIT MODEL
Backward trajectory ending at 0000 UTC 05 Nov 15
GDAS Meteorological Data

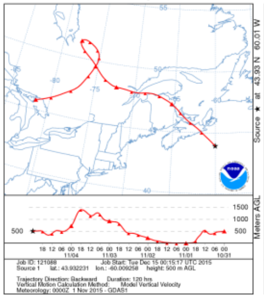

NOAA HYSPLIT MODEL
Backward trajectory ending at 1200 UTC 05 Nov 15
GDAS Meteorological Data

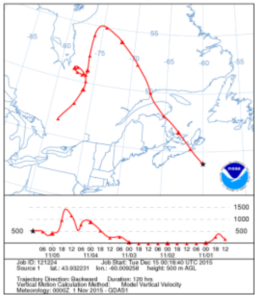

NOAA HYSPLIT MODEL
Backward trajectory ending at 0000 UTC 06 Nov 15
GDAS Meteorological Data

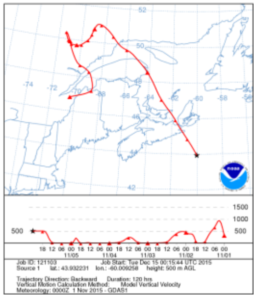

NOAA HYSPLIT MODEL
Backward trajectory ending at 1200 UTC 06 Nov 15
GDAS Meteorological Data

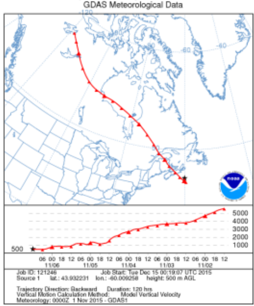

NOAA HYSPLIT MODEL
Backward trajectory ending at 0000 UTC 07 Nov 15
GDAS Meteorological Data

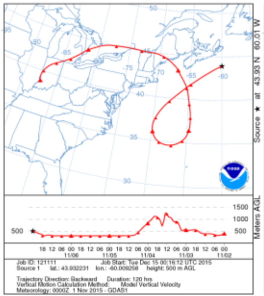

NOAA HYSPLIT MODEL
Backward trajectory ending at 1200 UTC 07 Nov 15
GDAS Meteorological Data

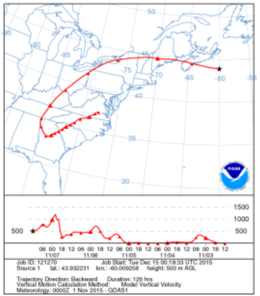

NOAA HYSPLIT MODEL
Backward trajectory ending at 0000 UTC 08 Nov 15
GDAS Meteorological Data

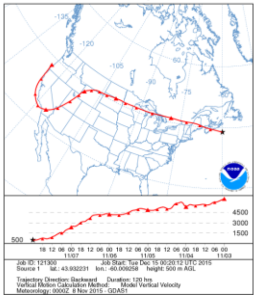

NOAA HYSPLIT MODEL
Backward trajectory ending at 1200 UTC 08 Nov 15
GDAS Meteorological Data

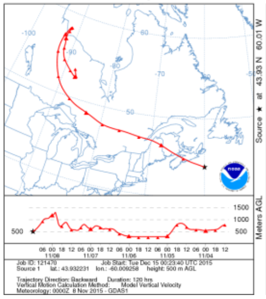

NOAA HYSPLIT MODEL
Backward trajectory ending at 0000 UTC 09 Nov 15
GDAS Meteorological Data

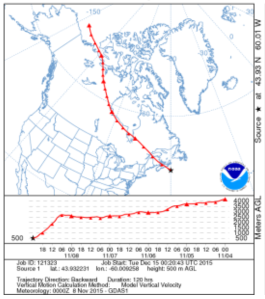

NOAA HYSPLIT MODEL
Backward trajectory ending at 1200 UTC 09 Nov 15
GDAS Meteorological Data

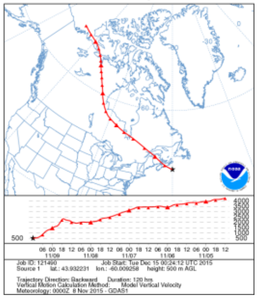

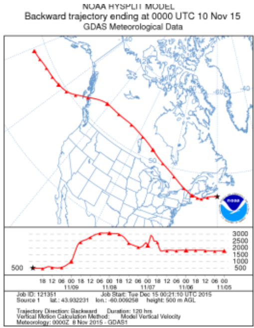
NOAA HYSPLIT MODEL
Backward trajectory ending at 0000 UTC 10 Nov 15
GDAS Meteorological Data

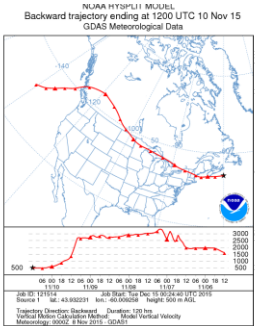
NOAA HYSPLIT MODEL
Backward trajectory ending at 1200 UTC 10 Nov 15
GDAS Meteorological Data

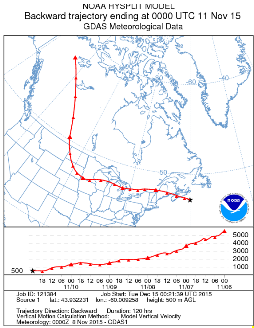
NOAA HYSPLIT MODEL
Backward trajectory ending at 0000 UTC 11 Nov 15
GDAS Meteorological Data

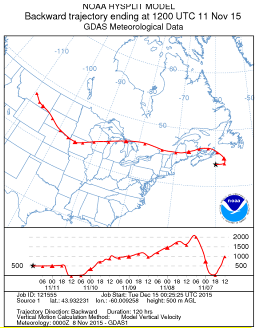
NOAA HYSPLIT MODEL
Backward trajectory ending at 1200 UTC 11 Nov 15
GDAS Meteorological Data

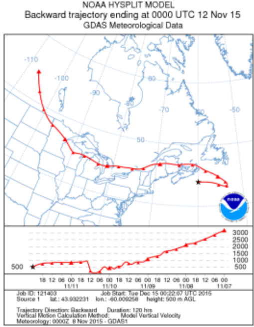
NOAA HYSPLIT MODEL
Backward trajectory ending at 0000 UTC 12 Nov 15
GDAS Meteorological Data

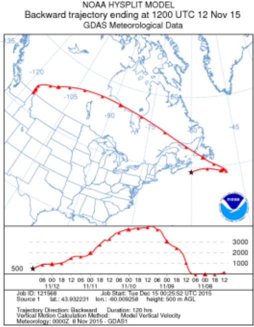
NOAA HYSPLIT MODEL
Backward trajectory ending at 1200 UTC 12 Nov 15
GDAS Meteorological Data

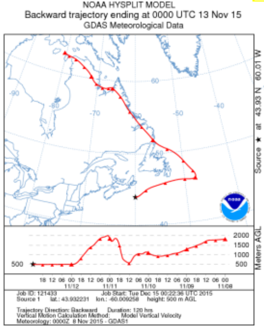
NOAA HYSPLIT MODEL
Backward trajectory ending at 0000 UTC 13 Nov 15
GDAS Meteorological Data

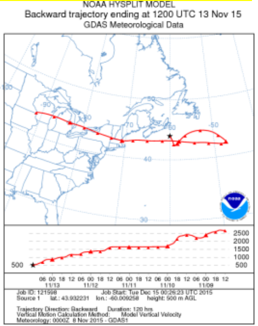
NOAA HYSPLIT MODEL
Backward trajectory ending at 1200 UTC 13 Nov 15
GDAS Meteorological Data

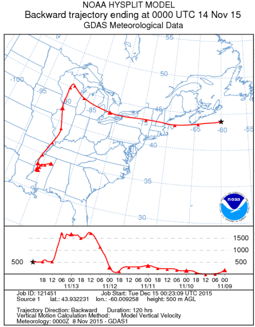
NOAA HYSPLIT MODEL
Backward trajectory ending at 0000 UTC 14 Nov 15
GDAS Meteorological Data

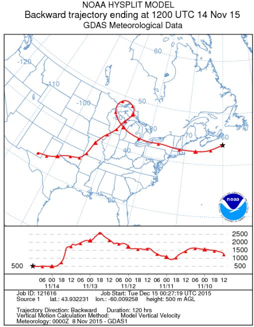
NOAA HYSPLIT MODEL
Backward trajectory ending at 1200 UTC 14 Nov 15
GDAS Meteorological Data

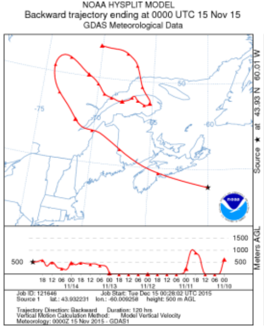
NOAA HYSPLIT MODEL
Backward trajectory ending at 0000 UTC 15 Nov 15
GDAS Meteorological Data

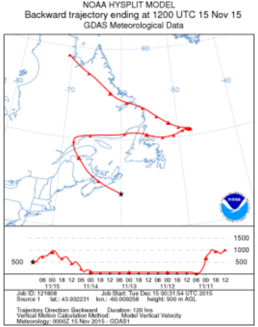
NOAA HYSPLIT MODEL
Backward trajectory ending at 1200 UTC 15 Nov 15
GDAS Meteorological Data

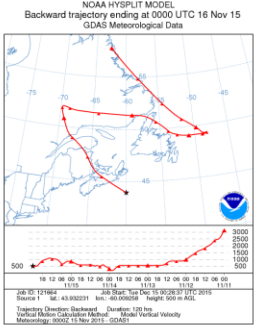
NOAA HYSPLIT MODEL
Backward trajectory ending at 0000 UTC 16 Nov 15
GDAS Meteorological Data

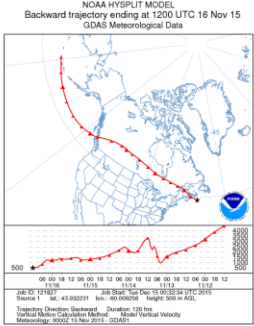
NOAA HYSPLIT MODEL
Backward trajectory ending at 1200 UTC 16 Nov 15
GDAS Meteorological Data

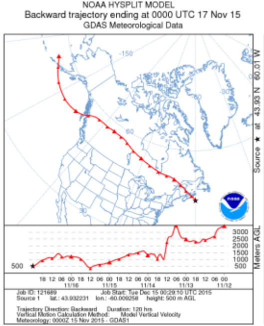
NOAA HYSPLIT MODEL
Backward trajectory ending at 0000 UTC 17 Nov 15
GDAS Meteorological Data

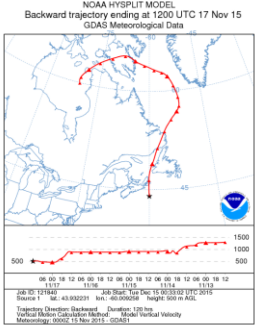
NOAA HYSPLIT MODEL
Backward trajectory ending at 1200 UTC 17 Nov 15
GDAS Meteorological Data

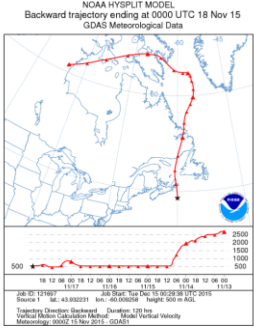
NOAA HYSPLIT MODEL
Backward trajectory ending at 0000 UTC 18 Nov 15
GDAS Meteorological Data

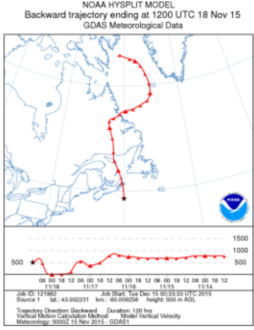
NOAA HYSPLIT MODEL
Backward trajectory ending at 1200 UTC 18 Nov 15
GDAS Meteorological Data

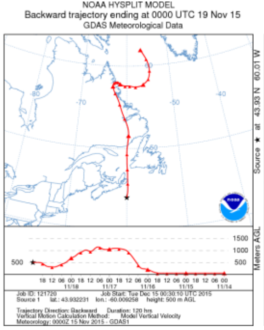
NOAA HYSPLIT MODEL
Backward trajectory ending at 0000 UTC 19 Nov 15
GDAS Meteorological Data

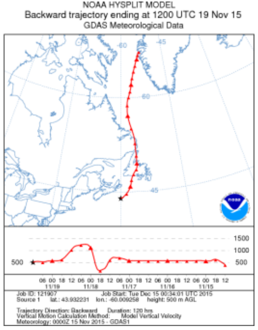
NOAA HYSPLIT MODEL
Backward trajectory ending at 1200 UTC 19 Nov 15
GDAS Meteorological Data

NOAA HYSPLIT MODEL
Backward trajectory ending at 0000 UTC 20 Nov 15
GDAS Meteorological Data

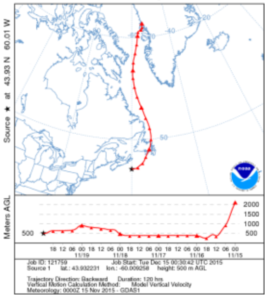

NOAA HYSPLIT MODEL
Backward trajectory ending at 1200 UTC 20 Nov 15
GDAS Meteorological Data

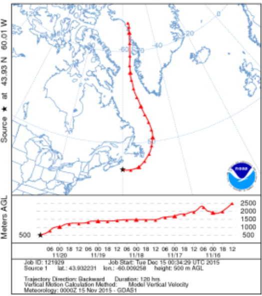

NOAA HYSPLIT MODEL
Backward trajectory ending at 0000 UTC 21 Nov 15
GDAS Meteorological Data

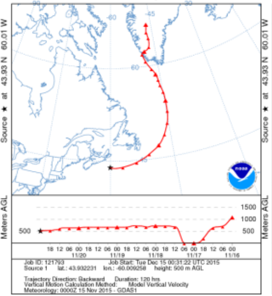

NOAA HYSPLIT MODEL
Backward trajectory ending at 1200 UTC 21 Nov 15
GDAS Meteorological Data

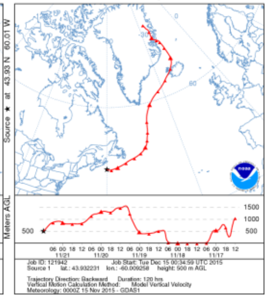

NOAA HYSPLIT MODEL
Backward trajectory ending at 0000 UTC 22 Nov 15
GDAS Meteorological Data

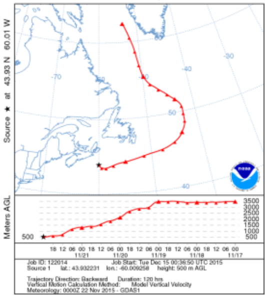

NOAA HYSPLIT MODEL
Backward trajectory ending at 1200 UTC 22 Nov 15
GDAS Meteorological Data

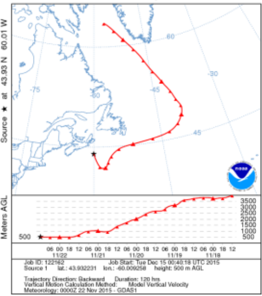

NOAA HYSPLIT MODEL
Backward trajectory ending at 0000 UTC 23 Nov 15
GDAS Meteorological Data

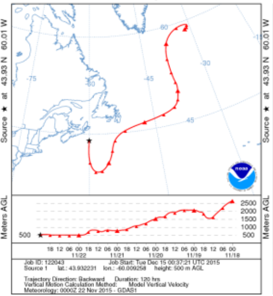

NOAA HYSPLIT MODEL
Backward trajectory ending at 1200 UTC 23 Nov 15
GDAS Meteorological Data

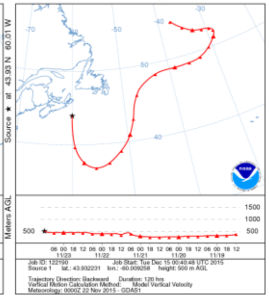

NOAA HYSPLIT MODEL
Backward trajectory ending at 0000 UTC 24 Nov 15
GDAS Meteorological Data

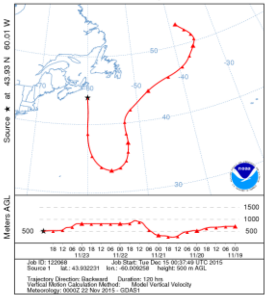

NOAA HYSPLIT MODEL
Backward trajectory ending at 1200 UTC 24 Nov 15
GDAS Meteorological Data

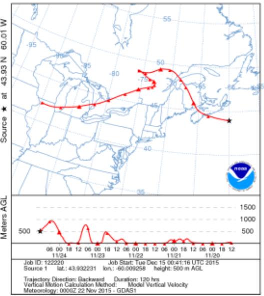

NOAA HYSPLIT MODEL
Backward trajectory ending at 0000 UTC 25 Nov 15
GDAS Meteorological Data

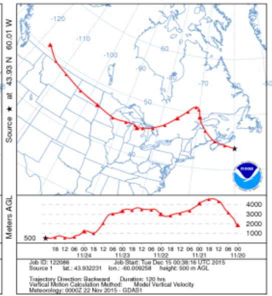

NOAA HYSPLIT MODEL
Backward trajectory ending at 1200 UTC 25 Nov 15
GDAS Meteorological Data

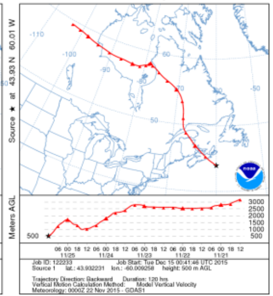

NOAA HYSPLIT MODEL
Backward trajectory ending at 0000 UTC 26 Nov 15
GDAS Meteorological Data

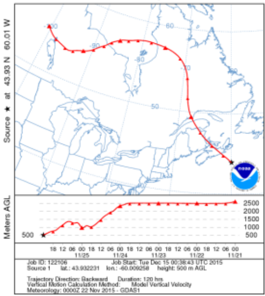

NOAA HYSPLIT MODEL
Backward trajectory ending at 1200 UTC 26 Nov 15
GDAS Meteorological Data

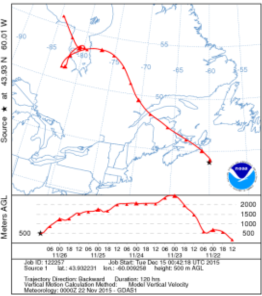

NOAA HYSPLIT MODEL
Backward trajectory ending at 0000 UTC 27 Nov 15
GDAS Meteorological Data

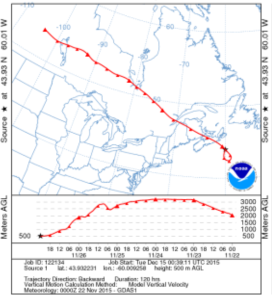

NOAA HYSPLIT MODEL
Backward trajectory ending at 1200 UTC 27 Nov 15
GDAS Meteorological Data

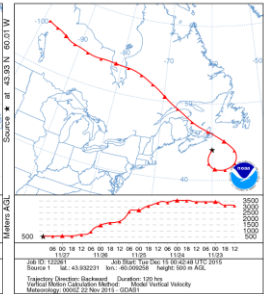

NOAA HYSPLIT MODEL
Backward trajectory ending at 0000 UTC 28 Nov 15
GDAS Meteorological Data

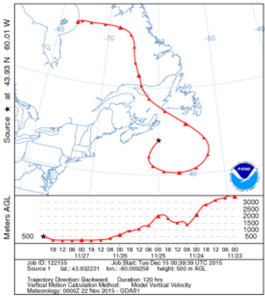

NOAA HYSPLIT MODEL
Backward trajectory ending at 1200 UTC 28 Nov 15
GDAS Meteorological Data

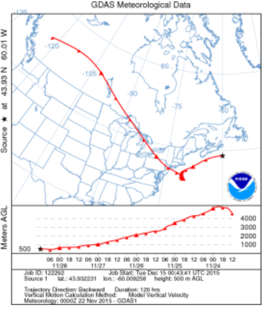

NOAA HYSPLIT MODEL
Backward trajectory ending at 0000 UTC 29 Nov 15
GDAS Meteorological Data

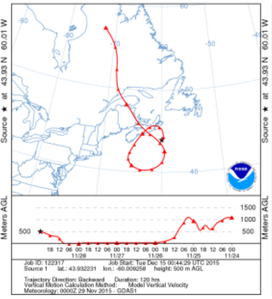

NOAA HYSPLIT MODEL
Backward trajectory ending at 1200 UTC 29 Nov 15
GDAS Meteorological Data

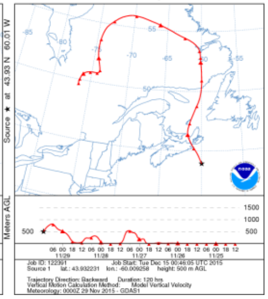

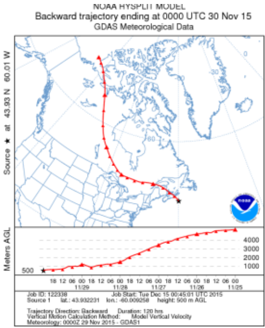
NOAA HYSPLIT MODEL
Backward trajectory ending at 0000 UTC 30 Nov 15
GDAS Meteorological Data
Source ★ at 43.93 N 60.01 W
Meters AGL

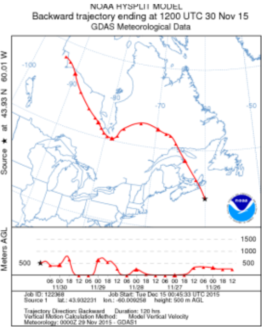
NOAA HYSPLIT MODEL
Backward trajectory ending at 1200 UTC 30 Nov 15
GDAS Meteorological Data
Source ★ at 43.93 N 60.01 W
Meters AGL

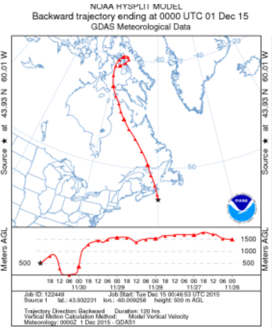
NOAA HYSPLIT MODEL
Backward trajectory ending at 0000 UTC 01 Dec 15
GDAS Meteorological Data
Source ★ at 43.93 N 60.01 W
Meters AGL

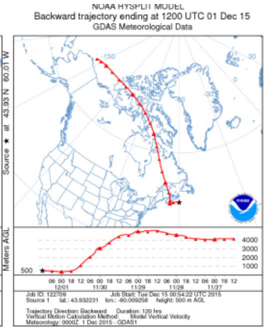
NOAA HYSPLIT MODEL
Backward trajectory ending at 1200 UTC 01 Dec 15
GDAS Meteorological Data
Source ★ at 43.93 N 60.01 W
Meters AGL

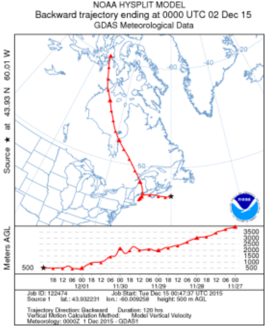
NOAA HYSPLIT MODEL
Backward trajectory ending at 0000 UTC 02 Dec 15
GDAS Meteorological Data
Source ★ at 43.93 N 60.01 W
Meters AGL

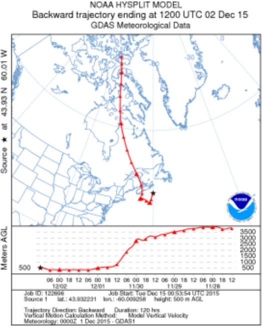
NOAA HYSPLIT MODEL
Backward trajectory ending at 1200 UTC 02 Dec 15
GDAS Meteorological Data
Source ★ at 43.93 N 60.01 W
Meters AGL

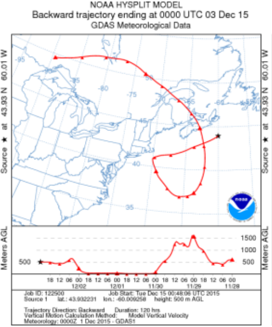
NOAA HYSPLIT MODEL
Backward trajectory ending at 0000 UTC 03 Dec 15
GDAS Meteorological Data
Source ★ at 43.93 N 60.01 W
Meters AGL

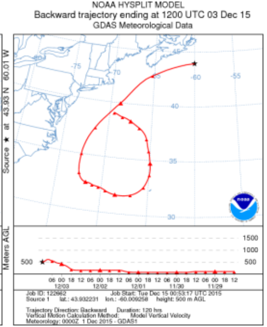
NOAA HYSPLIT MODEL
Backward trajectory ending at 1200 UTC 03 Dec 15
GDAS Meteorological Data
Source ★ at 43.93 N 60.01 W
Meters AGL

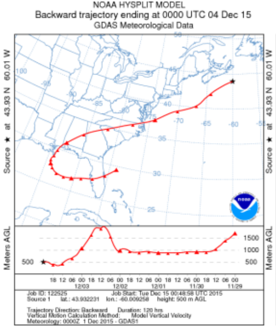
NOAA HYSPLIT MODEL
Backward trajectory ending at 0000 UTC 04 Dec 15
GDAS Meteorological Data
Source ★ at 43.93 N 60.01 W
Meters AGL

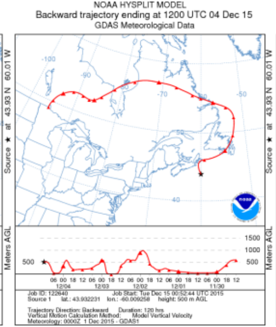
NOAA HYSPLIT MODEL
Backward trajectory ending at 1200 UTC 04 Dec 15
GDAS Meteorological Data
Source ★ at 43.93 N 60.01 W
Meters AGL

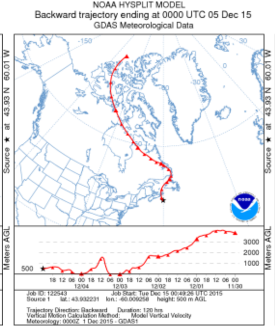
NOAA HYSPLIT MODEL
Backward trajectory ending at 0000 UTC 05 Dec 15
GDAS Meteorological Data
Source ★ at 43.93 N 60.01 W
Meters AGL

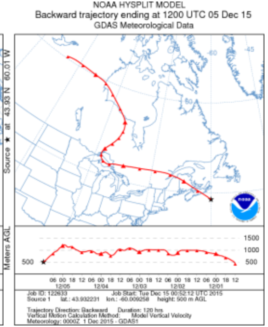
NOAA HYSPLIT MODEL
Backward trajectory ending at 1200 UTC 05 Dec 15
GDAS Meteorological Data
Source ★ at 43.93 N 60.01 W
Meters AGL

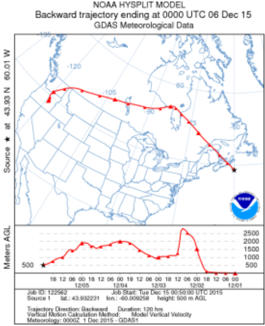
NOAA HYSPLIT MODEL
Backward trajectory ending at 0000 UTC 06 Dec 15
GDAS Meteorological Data
Source ★ at 43.93 N 60.01 W
Meters AGL

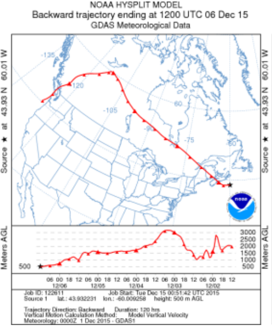
NOAA HYSPLIT MODEL
Backward trajectory ending at 1200 UTC 06 Dec 15
GDAS Meteorological Data
Source ★ at 43.93 N 60.01 W
Meters AGL

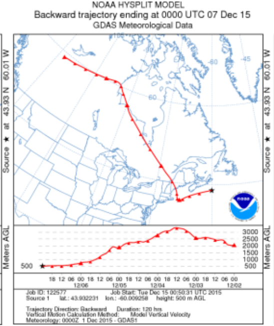
NOAA HYSPLIT MODEL
Backward trajectory ending at 0000 UTC 07 Dec 15
GDAS Meteorological Data
Source ★ at 43.93 N 60.01 W
Meters AGL

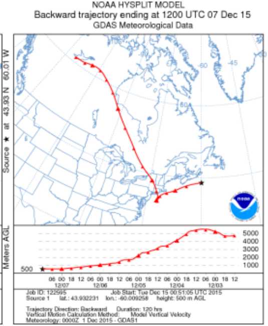
NOAA HYSPLIT MODEL
Backward trajectory ending at 1200 UTC 07 Dec 15
GDAS Meteorological Data
Source ★ at 43.93 N 60.01 W
Meters AGL

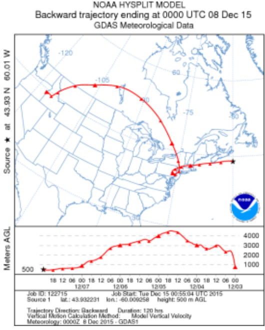
NOAA HYSPLIT MODEL
Backward trajectory ending at 0000 UTC 08 Dec 15
GDAS Meteorological Data
Source ★ at 43.93 N 60.01 W
Meters AGL

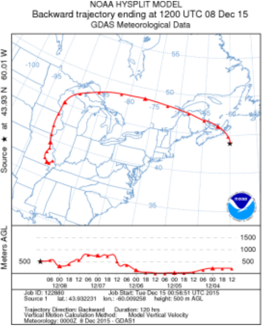
NOAA HYSPLIT MODEL
Backward trajectory ending at 1200 UTC 08 Dec 15
GDAS Meteorological Data
Source ★ at 43.93 N 60.01 W
Meters AGL

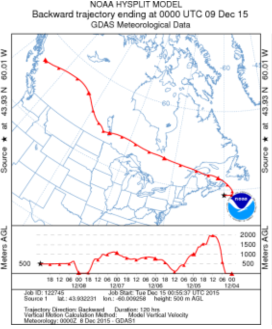
NOAA HYSPLIT MODEL
Backward trajectory ending at 0000 UTC 09 Dec 15
GDAS Meteorological Data
Source ★ at 43.93 N 60.01 W
Meters AGL

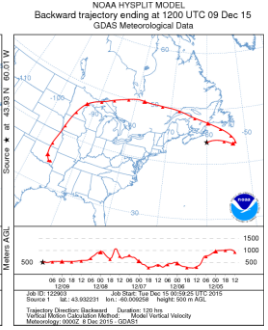
NOAA HYSPLIT MODEL
Backward trajectory ending at 1200 UTC 09 Dec 15
GDAS Meteorological Data
Source ★ at 43.93 N 60.01 W
Meters AGL

NOAA HYSPLIT MODEL
Backward trajectory ending at 0000 UTC 10 Dec 15
GDAS Meteorological Data

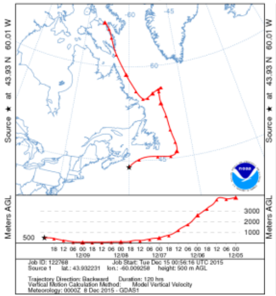

NOAA HYSPLIT MODEL
Backward trajectory ending at 1200 UTC 10 Dec 15
GDAS Meteorological Data

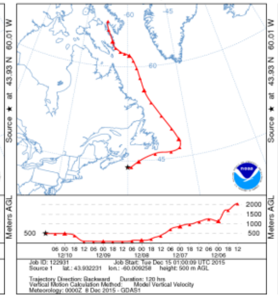

NOAA HYSPLIT MODEL
Backward trajectory ending at 0000 UTC 11 Dec 15
GDAS Meteorological Data

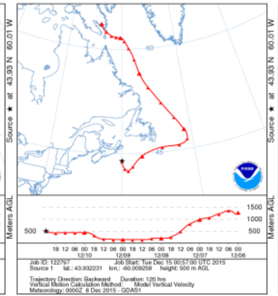

NOAA HYSPLIT MODEL
Backward trajectory ending at 1200 UTC 11 Dec 15
GDAS Meteorological Data

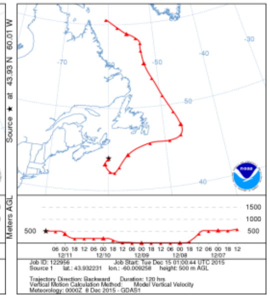

NOAA HYSPLIT MODEL
Backward trajectory ending at 0000 UTC 12 Dec 15
GDAS Meteorological Data

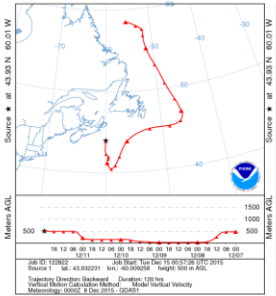

NOAA HYSPLIT MODEL
Backward trajectory ending at 1200 UTC 12 Dec 15
GDAS Meteorological Data

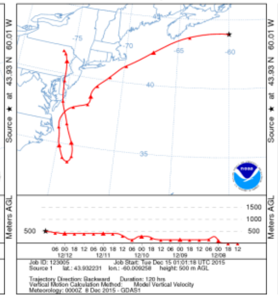

NOAA HYSPLIT MODEL
Backward trajectory ending at 0000 UTC 13 Dec 15
GDAS Meteorological Data

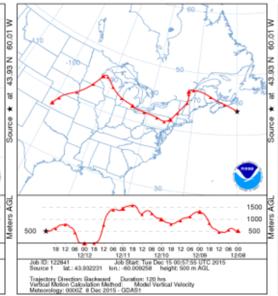

NOAA HYSPLIT MODEL
Backward trajectory ending at 1200 UTC 13 Dec 15
GDAS Meteorological Data

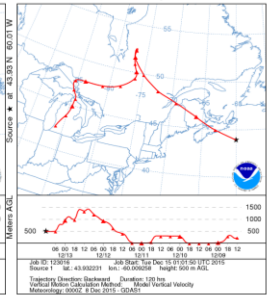

NOAA HYSPLIT MODEL
Backward trajectory ending at 0000 UTC 14 Dec 15
GDAS Meteorological Data

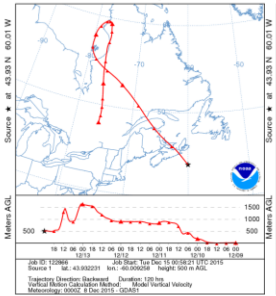

NOAA HYSPLIT MODEL
Backward trajectory ending at 1200 UTC 14 Dec 15
GDAS Meteorological Data

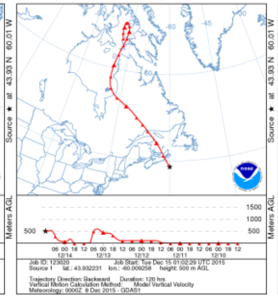

NOAA HYSPLIT MODEL
Backward trajectory ending at 0000 UTC 15 Dec 15
GDAS Meteorological Data

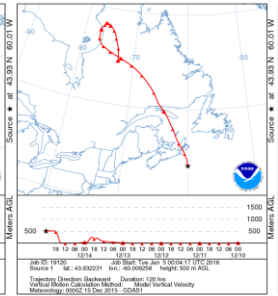

NOAA HYSPLIT MODEL
Backward trajectory ending at 1200 UTC 15 Dec 15
GDAS Meteorological Data

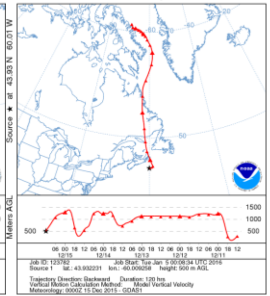

NOAA HYSPLIT MODEL
Backward trajectory ending at 0000 UTC 16 Dec 15
GDAS Meteorological Data

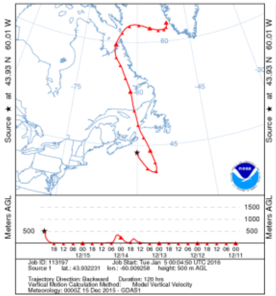

NOAA HYSPLIT MODEL
Backward trajectory ending at 1200 UTC 16 Dec 15
GDAS Meteorological Data

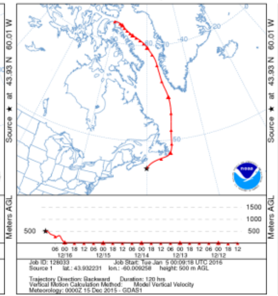

NOAA HYSPLIT MODEL
Backward trajectory ending at 0000 UTC 17 Dec 15
GDAS Meteorological Data

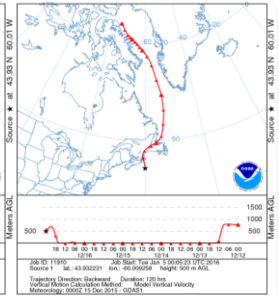

NOAA HYSPLIT MODEL
Backward trajectory ending at 1200 UTC 17 Dec 15
GDAS Meteorological Data

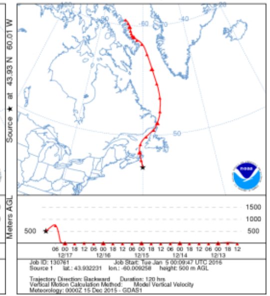

NOAA HYSPLIT MODEL
Backward trajectory ending at 0000 UTC 18 Dec 15
GDAS Meteorological Data

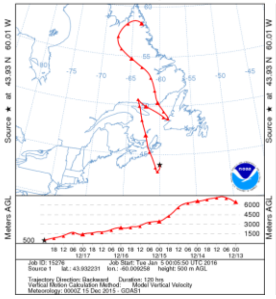

NOAA HYSPLIT MODEL
Backward trajectory ending at 1200 UTC 18 Dec 15
GDAS Meteorological Data

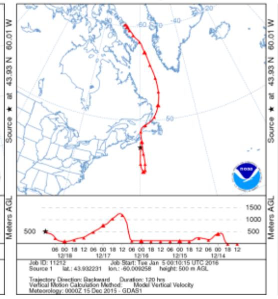

NOAA HYSPLIT MODEL
Backward trajectory ending at 0000 UTC 19 Dec 15
GDAS Meteorological Data

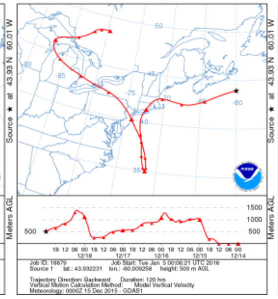

NOAA HYSPLIT MODEL
Backward trajectory ending at 1200 UTC 19 Dec 15
GDAS Meteorological Data

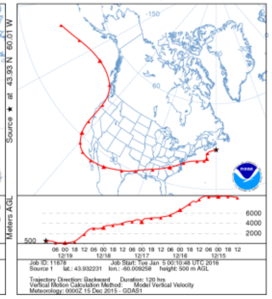

NOAA HYSPLIT MODEL
Backward trajectory ending at 0000 UTC 20 Dec 15
GDAS Meteorological Data

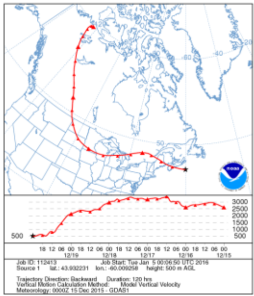

NOAA HYSPLIT MODEL
Backward trajectory ending at 1200 UTC 20 Dec 15
GDAS Meteorological Data

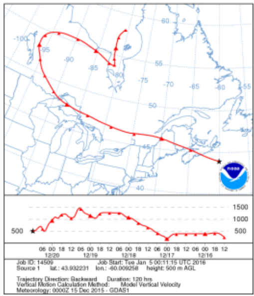

NOAA HYSPLIT MODEL
Backward trajectory ending at 0000 UTC 21 Dec 15
GDAS Meteorological Data

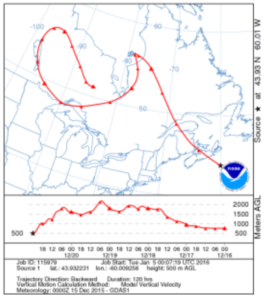

NOAA HYSPLIT MODEL
Backward trajectory ending at 1200 UTC 21 Dec 15
GDAS Meteorological Data

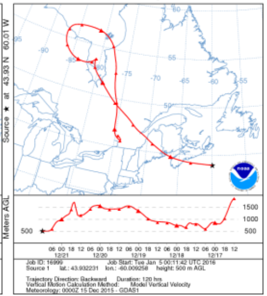

NOAA HYSPLIT MODEL
Backward trajectory ending at 0000 UTC 22 Dec 15
GDAS Meteorological Data

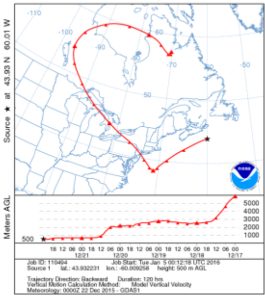

NOAA HYSPLIT MODEL
Backward trajectory ending at 1200 UTC 22 Dec 15
GDAS Meteorological Data

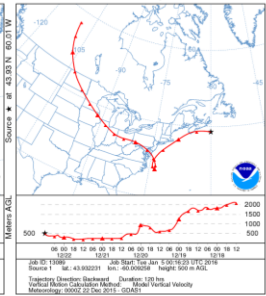

NOAA HYSPLIT MODEL
Backward trajectory ending at 0000 UTC 23 Dec 15
GDAS Meteorological Data

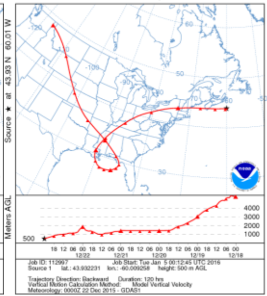

NOAA HYSPLIT MODEL
Backward trajectory ending at 1200 UTC 23 Dec 15
GDAS Meteorological Data

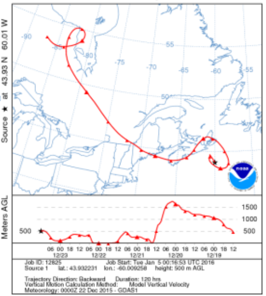

NOAA HYSPLIT MODEL
Backward trajectory ending at 0000 UTC 24 Dec 15
GDAS Meteorological Data

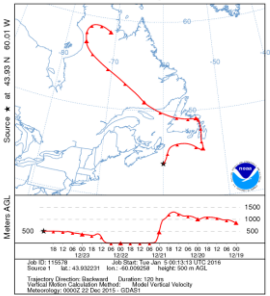

NOAA HYSPLIT MODEL
Backward trajectory ending at 1200 UTC 24 Dec 15
GDAS Meteorological Data

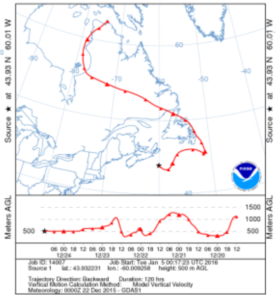

NOAA HYSPLIT MODEL
Backward trajectory ending at 0000 UTC 25 Dec 15
GDAS Meteorological Data

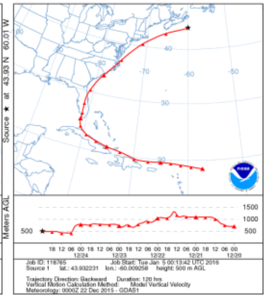

NOAA HYSPLIT MODEL
Backward trajectory ending at 1200 UTC 25 Dec 15
GDAS Meteorological Data

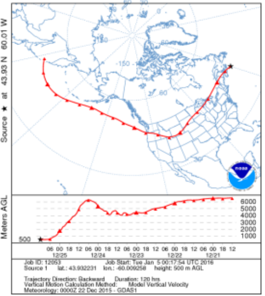

NOAA HYSPLIT MODEL
Backward trajectory ending at 0000 UTC 26 Dec 15
GDAS Meteorological Data

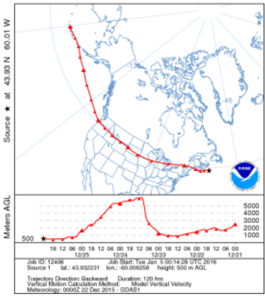

NOAA HYSPLIT MODEL
Backward trajectory ending at 1200 UTC 26 Dec 15
GDAS Meteorological Data

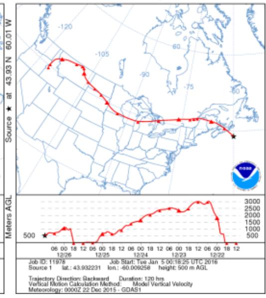

NOAA HYSPLIT MODEL
Backward trajectory ending at 0000 UTC 27 Dec 15
GDAS Meteorological Data

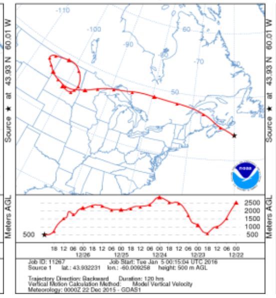

NOAA HYSPLIT MODEL
Backward trajectory ending at 1200 UTC 27 Dec 15
GDAS Meteorological Data

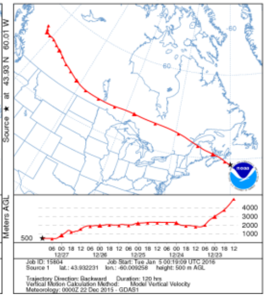

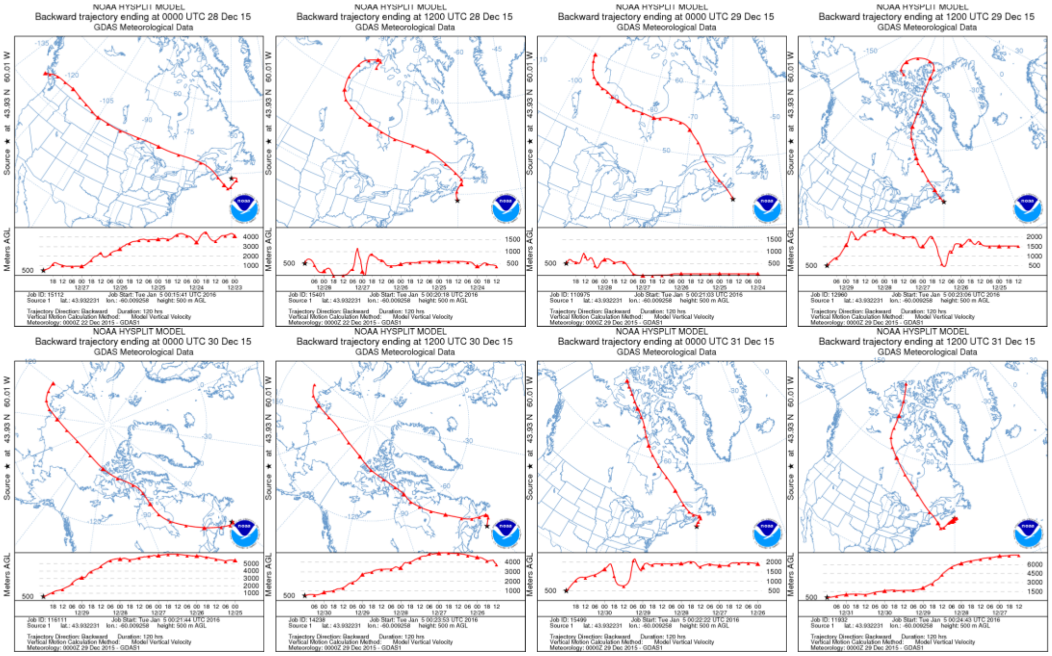

Figure 78. Daily HYSPLIT back trajectories over the sampling period October 1 to December 31, 2015